universität ulm

Josephson-Photonics Devices as Stable Sources and Detectors for Microwave Photons

Kumulative Dissertation

zur Erlangung des Doktorgrades
Dr. rer. nat.
der Fakultät für Naturwissenschaften der Universität Ulm

vorgelegt von

Lukas Danner

aus Heidenheim an der Brenz

2025

Amtierender Dekan	**Prof. Dr. Kay-Eberhard Gottschalk**
Erstgutachter	**PD Dr. Björn Kubala**
Zweitgutachter	**apl. Prof. Dr. Matthias Freyberger**
Tag der Promotion	**29. Januar 2026**

Lukas Danner
lukas.danner@dlr.de
lukas.danner@uni-ulm.de

Deutsches Zentrum für Luft- und Raumfahrt e.V.
Institut für Quantentechnologien
Abteilung Theoretische Quantenphysik
Wilhelm-Runge-Straße 10
89081 Ulm

Universität Ulm
Institut für komplexe Quantensysteme
Albert-Einstein-Allee 11
89069 Ulm

List of Presented Publications

My cumulative dissertation is based on three publications and one preprint presented in the following, as well as on three sections with related unpublished work.

(*i*) **Injection locking and synchronization in Josephson photonics devices**
Lukas Danner, Ciprian Padurariu, Joachim Ankerhold, and Björn Kubala
Physical Review B **104**, 054517 (2021)

(*ii*) **Quantum synchronization in presence of shot noise**
Florian Höhe, Lukas Danner, Ciprian Padurariu, Brecht I. C Donvil, Joachim Ankerhold, and Björn Kubala
New Journal of Physics, **27**, 023039 (2025)

(*iii*) **Quantum microwaves: Stabilizing squeezed light by phase locking**
Lukas Danner*, Florian Höhe*, Ciprian Padurariu, Joachim Ankerhold, and Björn Kubala
Physical Review B **111**, 184519 (2025)
* These authors have contributed equally to the paper.

(*iv*) **Amplification and Detection of Single Itinerant Microwave Photons**
Lukas Danner, Max Hofheinz, Nicolas Bourlet, Ciprian Padurariu, Joachim Ankerhold, and Björn Kubala
arXiv:2510.08030 (2025)

Abstract

At its heart, a Josephson-photonics device combines macroscopic superconducting electronics and microscopic quantum optics. It consists of a dc-voltage biased Josephson junction that is connected in series to one or a few microwave cavities. Cooper pairs can tunnel incoherently across the junction by depositing their energy $2eV_{\mathrm{dc}}$ in the microwave cavities, creating photonic excitations in them. Many parameters, such as the eigenfrequencies $\propto (LC)^{-1/2}$ or zero-point fluctuations $\propto (L/C)^{1/4}$ of the microwave cavities, can be experimentally designed; other parameters, such as the strength of the Josephson nonlinearity and the dc voltage are easily modified in situ. In this way, Josephson-photonics devices constitute a versatile source of microwave photons with a wide variety of features extending from the classical to the deep quantum regime. To make them of use for quantum technological applications that rely on a well-defined phase of the microwave light, a crucial drawback must be overcome. The dc voltage does not provide a stable reference phase to Josephson-photonics devices, as it is subject to experimental noise, such that all phase information is lost.
In this thesis, we develop the field of Josephson photonics in two directions:
As first main result, we resolve the issue of phase instability in Josephson photonics. The phase can be stabilized either by injection locking to a small external signal with a stable and well-defined reference phase or by mutual synchronization to a second device. An alternative approach mitigates the issue for some use cases by optimizing an ansatz to reconstruct the undiffused stationary quantum state from experiments with phase diffusion.
Secondly, we show how Josephson-photonics devices can be used for the challenging task of reliably detecting single itinerant microwave photons. The "Inelastic Cooper Pair Tunneling Photon Multiplier" exploits a resonance condition, where the energy provided by the dc voltage enables a multiplication process from one incoming to n outgoing photons. This process can be staged to reach a large number of outgoing photons. Here, we model itinerant Gaussian single-photon pulses of length T with Mølmer's approach. Further, we define a detection scheme based on heterodyne quadrature measurement of the output signal. Most importantly, we show that realistic devices can achieve a detection efficiency of 84.5% with a small dark-count rate of $10^{-3}/T$, promising to outperform competing schemes.

Contents

Introduction

The Nobel Price 2025 in physics, awarded to John Clarke, Michel Devoret and John Martinis, honored the "discovery of macroscopic quantum mechanical tunnelling and energy quantisation in an electric circuit". The recent Nobel-Prize winners have shown that the phase difference of a Josephson junction – a *macroscopic* quantity – is a quantum mechanical variable [1–3]. Thus, they demonstrated that quantum effects do not only appear in microscopic systems such as electrons, photons, or small molecules. These breakthrough experiments advanced the field of superconducting electronics, which is now firmly established as one of the leading platforms for quantum technological applications. Most prominently, novel technologies such as quantum information processing encode quantum bits in macroscopic variables of superconducting electric circuits.
The control of single *microscopic* systems, where, e.g., a quantum bit is encoded in the polarization of a single photon or in the quantum state of a single photonic mode, is the heart of many other quantum technologies. Such photonic technologies in the quantum-optics regime provide powerful tools for quantum communication, enabling protocols for quantum teleportation or quantum key distribution for secure encryption of messages. Further examples comprise quantum sensing and metrology, where, for instance, image resolution can be enhanced, precise measurement is achieved with quantum interferometry, and squeezed states are used for the detection of gravitational waves.

Recent years have witnessed a growing connection between the macroscopic quantum electronics of superconducting devices and microscopic quantum optics. On one hand, techniques from quantum optics are used for tasks in macroscopic superconducting quantum electronics with typical energy scales in the microwave regime. For instance, circuit quantum electrodynamics, which studies the interplay between microwave photons and qubits, uses techniques from quantum optics for qubit readout with microwave resonators. On the other hand, superconducting devices, especially through the development of Josephson parametric amplifiers [4], have been applied to problems and applications that originally arose in quantum optics. Using microwave photons generated by superconducting circuits, quantum teleportation has been experimentally achieved [5], Bell tests [6] can be performed,

and a microwave quantum radar [7] has used a quantum-illumination protocol and shown a true quantum advantage.

For the field of Josephson photonics, the topic of this thesis, the interplay between macroscopic superconducting quantum electronics and microscopic quantum optics is the eponymous foundational aspect. A Josephson-photonics device consists of a dc-voltage biased Josephson junction that is connected in series to one or a few microwave resonators. Cooper pairs can tunnel inelastically across the junction if they can deposit their energy $2eV_{\mathrm{dc}}$ in the microwave resonators. In 2011, pioneering work in the experimental groups of D. Estève (CEA Paris-Saclay, France) [8] and A.J. Rimberg (Dartmouth College Hanover, USA) [9] experimentally illustrated the fundamental operating principle. These experiments have since spurred further experimental and theoretical studies showing the versatility of Josephson-photonics devices by shifting the focus from the enhancement of the Cooper-pair transport to characteristics of the microwave light created in the resonators. Due to the nonlinearity of the Josephson junction, the microwave light displays features ranging from the (semi)classical to the deep quantum. Especially the quantum properties of the microwave light have sparked interest in using Josephson-photonics devices for quantum technological applications. By carefully engineering the zero-point fluctuations $\propto (L/C)^{1/4}$ of the microwave mode, high impedances can be reached. This implies that the nonlinearity of the Josephson junction becomes apparent at the few-photon level, such that the cavity ultimately behaves as an effective two-level system [10] that may constitute a single-photon source. Furthermore, two-mode squeezed microwave light [11], a key resource for quantum radars, or dissipative cat qubits [12] for quantum computation in continuous-variable systems can be created in setups that contain two microwave cavities. However, the beauty of creating nontrivial microwave light with a simple dc voltage comes with a severe drawback. A dc voltage does not provide a stable phase for the microwave light and unavoidable experimental noise perturbs its phase. As a direct consequence, the carefully created states of microwave light, such as squeezed states or cat states, are hidden from direct observation. That poses a detrimental problem for applications that fundamentally rely on an observable stable phase of light when exploiting quantum advantages.

One result of this thesis is the presentation of solutions to mitigate the issue of phase instability in Josephson photonics. The devices perform autonomous self-sustained oscillations, i.e. long-lasting oscillations whose oscillation amplitude is stable when the system is perturbed by noise. However, their oscillation phase is neutrally stable and thus easily perturbed by external noise sources. However, this drawback can also be used as an advantage: The oscillation phase is also sensitive to external stable oscillations, and a reference phase can be provided by techniques of injection locking. There, the system may synchronize its oscillations to a small reference signal with a well-defined phase. Injecting a tiny ac voltage may thus stabilize the phase of Josephson-photonics devices and protect against noise. Phase stabilization can also be achieved by mutual synchronization. When coupling two devices with neutrally stable phase, they may enter a synchronized state where their relative phase is stable and protected. Exploiting nonlinear behavior of the superconducting devices, Josephson photonics serves as an ideal platform to study

the fundamental dynamics of injection locking and synchronization from the classical to the quantum regime. Most importantly, however, we show that injection locking and synchronization enable the usage of Josephson-photonics devices as stable sources for quantum applications.

In the second part of this thesis, we utilize Josephson-photonics devices not as sources but as detectors of single microwave photons. In the optical regime, avalanche detectors or superconducting nanowire single-photon detectors exploit the impact of a single photon with energies in the order of terahertz for detection. However, microwave photons with energies in the gigahertz regime require much more sensitive detectors. Despite some recent advances, the reliable detection of single microwave photons with unknown arrival times remains an open topic. Any progress in this direction has the potential to become an important ingredient for quantum state readout, quantum communication protocols, and quantum sensing such as the quantum radar.
Here, we tackle the detection of single microwave photons using a Josephson-photonics device dubbed the "Inelastic Cooper Pair Tunneling Photon Multiplier". It takes advantage of a resonance condition for the dc voltage that involves the difference of resonator eigenfrequencies to convert one excitation in a first resonator to n excitations in a second one. A single microwave photon impinging from an input transmission line is resonantly absorbed by the device and multiplied, by the energy provided by the dc voltage, to n excitations that leak into an output transmission line. While an experiment has illustrated this basic principle of deterministic photon-number multiplication for coherent continuous-wave input signals [13], here we investigate amplification and detection of true quantum input, i.e. a temporal Gaussian input pulse in a single-photon Fock state. Specifically, we will show that the performance indicators for single-photon detection with Josephson-photonics devices compare favorably to competing schemes.

This cumulative thesis is structured as follows. In a theory part, we first explain and review fundamental principles and properties of Josephson-photonics devices in Sec. 1.3. We specifically highlight how intracavity states with interesting quantum properties, such as quantum states showing $\mathbb{Z}^k$-symmetry (see Sec. 1.4.1) or dissipative cat qubits (Sec. 1.4.2), can be created. Presenting further quantum technological applications, we show how Josephson-photonics devices are used as a single-photon source (Sec. 1.5.1) and how to generate two-mode squeezed states for a quantum radar (Sec. 1.5.2). The basic idea of the scheme for multiplication and detection of single microwave photons is reviewed in Sec. 1.6. After discussing the detrimental effect of voltage noise on phase-sensitive quantum states, like squeezed states and $\mathbb{Z}^k$-symmetric states in Sec. 1.7, the following Sec. 2 introduces basic notions and hallmark signatures of self-sustained oscillators, injection locking and synchronization. We conclude the theory part by presenting a brief theoretical description of itinerant quantum pulses of (microwave) light in Sec. 3, summarizing a recent approach introduced by K. Mølmer, and a heterodyne detection scheme by quadrature measurement of a resonator's output, which helps to understand fundamental ideas used in our publication on single-photon detection.

The results of this thesis are documented in three publications and one preprint completed during my PhD work, as well as three brief additional sections with

related unpublished work. First, we present how the phase of Josephson-photonics devices can be stabilized by injection locking and synchronization. Pub. (*i*) in Sec. 4.1.1 incorporates an additional in-series resistor forming a low-frequency environment that enables the description of self-sustained oscillations that can be injection locked and synchronized in the classical regime. In order to reduce the noise, circuit designs with other low-frequency environments may prove beneficial. In Sec. 4.1.2, containing unpublished results that constitute an extension of Pub. (*i*), we specifically discuss how the classical dynamics of injection locking is modified by a general impedance. Translating our insights to the quantum regime, Pub. (*ii*) presents how a Josephson-photonics device can be injection locked and synchronized in presence of shot noise (see Sec. 4.2.1). Pub. (*iii*) in Sec. 4.2.2 analyzes the paradigmatic example of injection locking of squeezed quantum states for technological applications. Unpublished work in Sec. 4.2.3 focuses on stabilizing cat qubits in a regime that is dominated by classical Johnson-Nyquist noise. Finally, an alternative approach can be used to mitigate the issue of phase instability in Josephson-photonics devices (c.f. unpublished results in Sec. 4.2.4). By measuring only a few experimentally accessible expectation values, the quantum state without phase diffusion can be reconstructed with an ansatz.
As a second part of the results, the amplification and detection of single microwave photons using Josephson-photonics devices is studied in Sec. 5.1. Pub. (*iv*) analyzes the device in different parameter regimes for incoming temporal Gaussian single-photon pulses of length T. We find that realistic setups can achieve a detection efficiency of 84.5% with a dark count rate of $10^{-3}/T$, promising to outperform existing approaches for single microwave-photon detection.

PART A

Fundamentals

1 Fundamentals of Josephson Photonics

A Josephson-photonics device consists of a dc-voltage biased Josephson junction that is connected in series with one or a few microwave resonators. In each superconducting part of the Josephson junction, Cooper pairs, which are pairs of electrons, exist at the Fermi energy inside the superconducting energy gap. If the Josephson junction is biased by a dc voltage below the superconducting gap and effects of an electromagnetic environment can be neglected, there is no directed Cooper-pair current. Instead, Cooper pairs can tunnel inelastically across the junction when their energy $2eV_{\mathrm{dc}}$ can be absorbed by some environment. In this regime, known as the dynamical Coulomb blockade, effects of the environment on the characteristics of the Cooper-pair current have been studied extensively [14–18]. One particular environment that enhances a directed Cooper-pair current is realized by the use of microwave resonators. Then, when the dc voltage is applied at resonance, Cooper pairs can tunnel inelastically by creating photonic excitations in the microwave cavities, which can be observed. In 2011, pioneering work in the experimental groups of D. Estève (CEA Paris-Saclay, France) [8] and A. J. Rimberg (Dartmouth College Hanover, USA) [9] has shown a first proof of this concept. This investigation of the *bright side of the Coulomb blockade* has since sparked the development of a field coined Josephson photonics with a number of experiments [8–11, 13, 19–24] and theoretical works [12, 25–52] that shift the focus from the characteristics of the Cooper-pair current to photonic properties of the microwave light in the LC-resonators. In Josephson-photonics devices, many parameters, such as the eigenfrequencies $\propto (LC)^{-1/2}$ or zero-point fluctuations $\propto (L/C)^{1/4}$ of the microwave cavities, can be specifically designed, while other parameters, like the strength of the Josephson nonlinearity and the dc voltage can easily be adjusted in situ. Hence, a variety of photonic states of the microwave cavities can be created with rich and nontrivial features ranging from the classical to the quantum.

Here, we start by describing the basic operating principle in more detail (Sec. 1.1). After providing an overview (Sec. 1.2) of different operating regimes and applications, we proceed with an in-depth theoretical description of Josephson-photonics devices operated in the semiclassical and quantum regime in Sec. 1.3, offering a mathematically sound basis. Sec. 1.4 then highlights the (steady-state) properties of the microwave cavities, where we, e.g., review in detail how cat states, which form quantum bits (qubits) in continuous-variable systems, can be generated and used for quantum computation. Further, Josephson-photonics devices can be used as microwave sources by emitting quantum microwave light. For example, they can be operated as a single-photon source emitting antibunched light [10, 22, 31, 32]. Entangled microwaves [11, 19, 36, 37], which could, for instance, be used in a quantum radar, can be generated by accessing the resonance condition for two-mode squeezing. Recent proposals have presented a scheme for amplification [20, 21, 24] and detection [13, 41] of microwave photons (also see Sec. 1.6).
However, Josephson-photonics devices suffer from a drawback. The dc voltage fluctuates due to noise and cannot provide a reference phase. As a direct consequence, the dc-voltage noise leads to instability of the phase of the quantum states in the resonators (Sec. 1.7). Providing schemes to address this shortcoming, such as phase stabilization by injection locking or the reconstruction of the quantum state by measuring very few accessible expectation values, is a central aspect of this thesis, which is discussed in Secs. 2 and 4.

1.1 Basic Operating Principle

In Josephson-photonics devices, a Josephson junction [see Fig. 1.1(a)] is commonly constructed from two superconducting metals separated by an insulating oxide region. Below a critical temperature, superconductors have an energy gap Δ around the Fermi energy, $E_F \gg \Delta$. Cooper pairs, which are pairs of (quasi-)electrons with opposite momenta and spin, condensate into a macroscopic quantum state, the ground state of the superconductor, which is energetically centered at the Fermi energy [53]. The Bardeen–Cooper–Schrieffer (BCS) ground state of a bulk superconductor is a coherent superposition of states with different numbers of Cooper pairs, such that the conjugate variable, the phase of the BCS condensate, is a well-defined macroscopic order parameter [54].

Josephson relations and the Josephson effects

Classically, the phase difference $\varphi_J = \varphi_L - \varphi_R$ between the two superconductors is related to the voltage and current across the junction by the Josephson relations

$$\frac{\mathrm{d}\varphi_J}{\mathrm{d}t} = \frac{2e}{\hbar} V_J \tag{1.1}$$

$$I_{\mathrm{CP}} = I_{\mathrm{crit}} \sin(\varphi_J)\,. \tag{1.2}$$

These relations describe the dc- and the ac Josephson effect [55]:

- dc Josephson effect

  Without applied dc voltage, the phase difference $\varphi_J = \varphi_0$ is constant, yielding a directed Cooper-pair current $I_{\mathrm{CP}} = I_{\mathrm{crit}} \sin(\varphi_0)$ across the junction [see the yellow line in Fig. 1.1(b)].

- ac Josephson effect

  An applied dc voltage that is smaller than the superconducting gap, $eV_{\mathrm{dc}} < 2\Delta$, effectively shifts the energy levels between the left and right superconductor. From the Josephson relations, we find an ac current, oscillating with frequency $\omega_{\mathrm{dc}} = 2eV_{\mathrm{dc}}/\hbar$. If the effects of an electromagnetic environment can be neglected, there is no directed Cooper-pair current [green line in Fig. 1.1(b)].

If the applied dc voltage is smaller than the superconducting gap, an electromagnetic environment capable of absorbing the energy $\hbar\omega_{\mathrm{dc}}$ enables directed Cooper-pair tunneling. This effect can be resonantly enhanced by specifically engineering microwave modes as an electromagnetic environment. In the regime of the dynamical Coulomb blockade, where the tunneling process of Cooper pairs can be treated as a perturbation, the dc current can be calculated for an arbitrary environment [14–18] by the so-called $P(E)$-theory [56, 57], which describes the ability of an environment to provide or absorb energy. An example is a resistive environment with constant impedance (in Fourier space), which can be modeled quantum mechanically as an infinite set of nondegenerate harmonic oscillators. A resistor thus allows for the absorption of any amount of energy, enabling inelastic Cooper pair tunneling. If, instead, the electrical environment consists of one or very few microwave cavities with sharp and well-defined eigenfrequencies, the Cooper pairs can tunnel inelastically when their energy $2eV_{\mathrm{dc}}$ matches these resonances, c.f. the

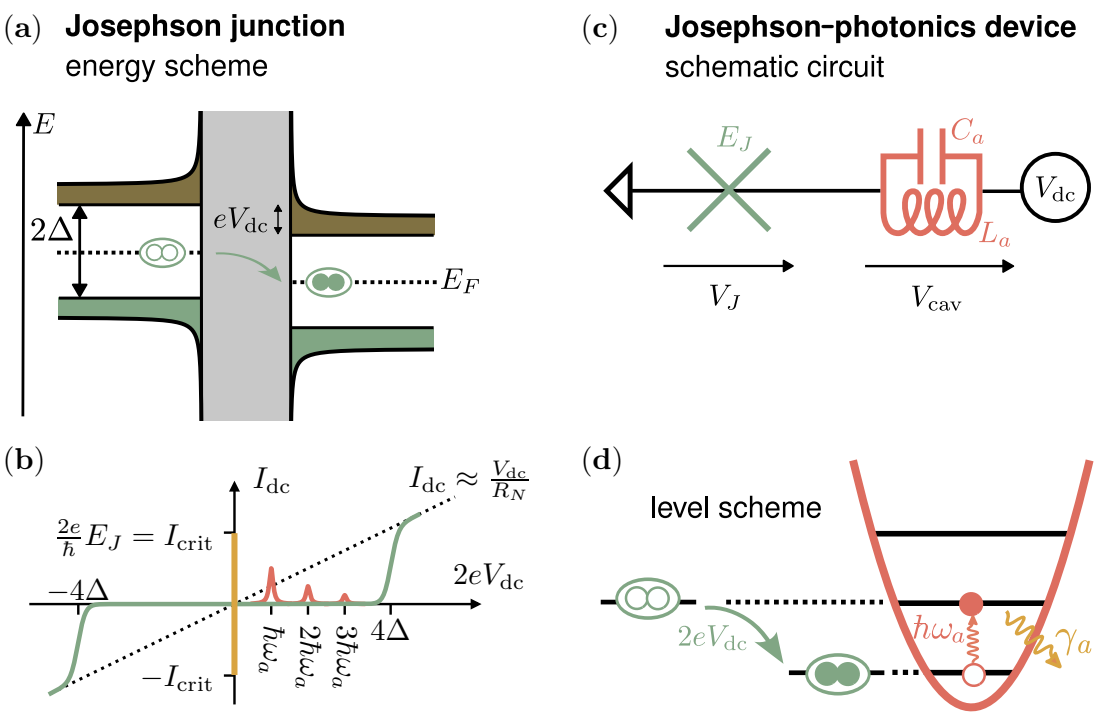

Figure 1.1: Basic operating principle of a Josephson-photonics device. (a) A Josephson junction consists of two superconducting metals, separated by an insulating region (gray). At temperature $T = 0\,\mathrm{K}$, Cooper pairs exist at the Fermi energy E_F inside an energy gap of size 2Δ. A finite dc voltage shifts the energy levels between the left and right superconductor by an amount eV_dc. (b) A directed supercurrent (yellow line) can exist without applied dc voltage and is determined by the phase difference between the junctions [compare Eqs. (1.1) and (1.2)]. A directed current (green) can only flow when $eV_\mathrm{dc} > 2\Delta$ and is at large voltages calculated from the normal state resistance R_N of the junction (compare black dashed line). (c) A single-mode Josephson-photonics device specifically fabricates a single LC-oscillator connected in series to a dc-biased Josephson junction. The microwave resonator can be quantized to a harmonic oscillator with level spacing $\hbar\omega_a$ and constitutes an electromagnetic environment of the junction. When biasing the junction well below threshold, $eV_\mathrm{dc} \ll 2\Delta$, a directed Cooper-pair current can only exist if the excess energy $2eV_\mathrm{dc}$ of an inelastically tunneling Cooper pair is resonantly absorbed by the microwave cavity. (d) Various resonances can be accessed, where each Cooper pair effectively creates k excitations in the cavity when $2eV_\mathrm{dc} \approx k\hbar\omega_a$ (here shown for $k = 1$). The microwave mode thus enables a directed Cooper-pair current even when voltage-biasing below the gap [illustrated for $k = 1, 2, 3$ (b), see red lines]. In experiments, the resonator is coupled to transmission lines and subject to single-photon loss with rate γ_a.

red curve in Fig. 1.1(b). Rather than only studying the effect of the environment on the Cooper-pair current, the focus can be shifted to the photonic side by analyzing the quantum state and emission properties of the microwave modes.

The bright side of the Coulomb blockade

In the Josephson-photonics device of Fig. 1.1(c), we consider a single LC-resonator connected in series to the Josephson junction as a specific electromagnetic environment. An LC-circuit can be described quantum mechanically by a harmonic

oscillator with eigenfrequency ω_a. Having been quantized, the phase $\hat{\varphi}$ (i.e. the integrated voltage V_{cav} across the resonator) and the charge $\hat{Q}$ on the capacitor plates are a pair of canonically conjugate variables and are therefore identified with position and momentum of the harmonic oscillator. If the applied dc voltage is tuned on resonance with the microwave cavity, $2eV_{\mathrm{dc}} \approx \hbar\omega_a$ [compare to Fig. 1.1(d)], an inelastically tunneling Cooper pair emits its excess energy into the microwave cavity and thus creates a single photonic excitation in it. In experimental setups, dissipation for the microwave resonator is introduced by capacitive coupling to a transmission line, into which it emits microwave radiation that can be measured. The competition between photon creation processes by the tunneling Cooper pairs and photon emission from the resonator into the transmission lines due to the resonator's finite lifetime $1/\gamma_a$ will eventually yield stationary states of

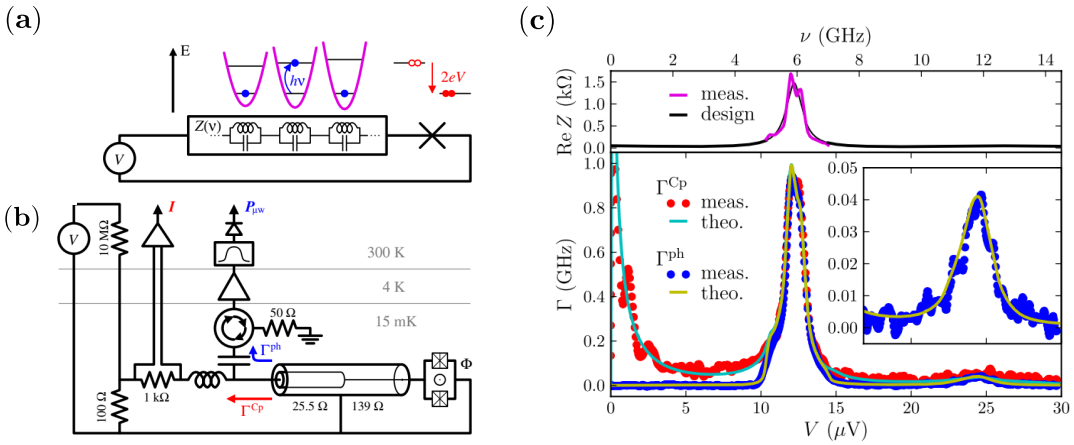

Figure 1.2: Pioneering experiment showing the *bright side of the Coulomb blockade*. (a) A dc-voltage biased Josephson junction is connected in series with an impedance $Z(\nu)$ that can be described by a series of harmonic oscillators. When biased below the gap, the energy $2eV_{\mathrm{dc}} \ll \Delta$ (in the figure, $V = V_{\mathrm{dc}}$) of an inelastically tunneling Cooper pair transfers excitations into one or several microwave cavities. (b) In the experimental setup, the Josephson energy is tunable by using a Superconducting Quantum Interference Device (SQUID). The Cooper-pair current (here called I) and the electromagnetic power $P_{\mu W}$ emitted from the cavities can be measured separately using a bias tee. The fundamental mode has a low quality factor $Q_0 \approx 9.4$, shifting the focus on the emission of the microwave resonators. (c) The fundamental mode around $\nu \approx 6\,\mathrm{GHz}$ [the impedance in the top panel corresponds to the first red peak in the IV-curve of Fig. 1.1(a)] can be excited by a tunneling Cooper pair when the circuit is biased at $V \approx h\nu_0/(2e) \approx 12\,\mu\mathrm{V}$, confirmed by the measured Cooper-pair rate Γ^{CP} and photon rate Γ^{ph} that show a pronounced peak around this voltage. A second small peak around $V \approx 24\,\mu\mathrm{V} \approx 2\nu_0$ corresponds to the resonance condition, where each tunneling Cooper pair effectively creates two excitations in the microwave cavity. Since the applied Josephson energy $E_J \approx 1.9h\nu_0/Q_0$ is small compared to the resonance, the microwave cavity stays close to equilibrium, such that $P(E)$-theory applies. Theory fits calculated by $P(E)$-theory are shown as solid lines.
[Reprinted figure with permission from M. Hofheinz, F. Portier, Q. Baudouin, P. Joyez, D. Vion, P. Bertet, P. Roche, and D. Esteve, *Physical Review Letters* **106**, 217005 (2011). Copyright (2011) by the American Physical Society; included in this thesis as reference [8].]

the microwave cavity. To observe the radiation emitted from a few-photon quantum state of the microwave resonators, a low quality factor $Q = \omega_a/\gamma_a \sim \mathcal{O}(10)$ is used in experiments [8, 11, 19].
The basic concept, that each tunneling Cooper effectively creates one photon in a microwave cavity, has been confirmed in the pioneering experiment [8] (compare Fig. 1.2). In the presented setup, the electromagnetic environment $Z(\nu)$ [top plot of Fig. 1.2(c)] consists of many harmonic modes at odd integer multiples $\nu_n = (2n+1)\nu_0$ of the fundamental mode of a microwave resonator. It uses a Superconducting Quantum Interference Device (SQUID), which is effectively a Josephson junction with tunable Josephson energy. A bias voltage of $V_{\mathrm{dc}} \approx 12\,\mu\mathrm{V}$ corresponds to the single-photon resonance of the fundamental mode $\nu_0 \approx 6\,\mathrm{GHz}$. The junction is driven weakly, i.e. the photon loss rate γ_a of the cavity [c.f. Fig. 1.1(d)] is faster than the rate of tunneling Cooper pairs, such that the resonator remains close to its ground state. Then, there is no back-action on the junction and Cooper pairs tunnel incoherently. The bias-tee shown in Fig. 1.2(b) separates the resonator's microwave radiation measurement from the low-frequency bias voltage and from the current measurement, enabling an independent measurement of the rate of emitted photons (around the fundamental resonance) and the rate of tunneled Cooper pairs. There is clear evidence that the measured photon rate matches the measured Cooper pair rate, c.f. Fig. 1.2(c). Furthermore, the voltage can be tuned to the two-photon resonance of the fundamental mode such that each tunneling Cooper pair creates two photons at once. The hallmark sig-

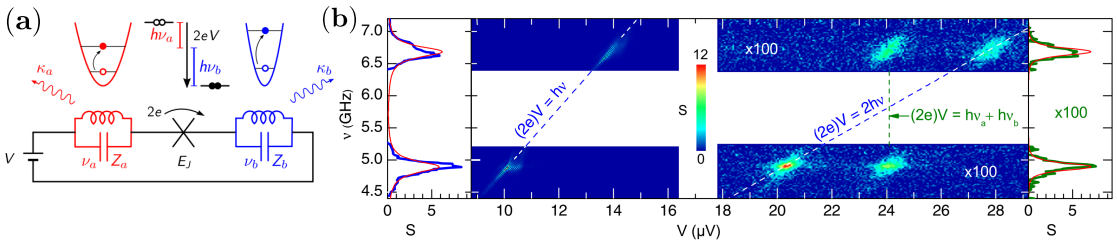

Figure 1.3: Detected power spectral density S of the emission from the microwave modes of a two-mode Josephson-photonics device [19]. (a) The Josephson-photonics device consists of two microwave modes with eigenfrequencies $\nu_a \approx 4.9\,\mathrm{GHz}$ and $\nu_b \approx 6.7\,\mathrm{GHz}$ and low quality factors $Q_a = \nu_a/\kappa_a \approx 25$ and $Q_b \approx 35$, which are connected in series to a Josephson junction, fabricated as a Superconducting Quantum Interference Device (SQUID) with tunable Josephson energy. Here, $E_J/h \approx 0.343\,\mathrm{GHz}$, such that the $P(E)$-theory is applicable. (b) The left color panel shows two clear emission peak along the line $2eV = h\nu$ (here again the dc voltage is differently named, $V = V_{\mathrm{dc}}$), which correspond to single-photon resonances of mode ν_a and mode ν_b respectively. The leftmost panel is a cut of S along $2eV = h\nu$. The right color panel shows two emission peaks along the line $2eV = 2 \cdot h\nu$, which corresponds to the two-photon resonance of a single mode ν_a (and mode ν_b, respectively). Additionally, the vertical green line $2eV = h(\nu_a + \nu_b)$ corresponds to the resonance condition, where a photon pair (one excitation in each mode) is created by an inelastically tunneling Cooper pair. The rightmost panel is a cut along the green line. Red solid lines are predictions calculated by $P(E)$-theory.
[Reprinted figure with permission from M. Westig, B. Kubala, O. Parlavecchio, Y. Mukharsky, C. Altimiras, P. Joyez, D. Vion, P. Roche, D. Esteve et al., *Physical Review Letters* **119**, 137001 (2017). Copyright (2017) by the American Physical Society; included in this thesis as reference [19].]

nature is the visible peak of the photon emission rate at $V_{\mathrm{dc}} \approx 24\,\mu\mathrm{V}$ (where there is no other mode of the resonator at $2\nu_0$), c.f. the inset of Fig. 1.2(c).

Microwave emission spectrum of Josephson-photonics devices

Ref. [19] uses a Josephson-photonics setup with two nondegenerate microwave cavities, Fig. 1.3(a). They detect the output power spectral density of the microwave cavities as a function of the frequency of the output power and of the applied dc voltage. First, emission was observed along the line $2eV_{\mathrm{dc}} \approx h\nu$ [left panel of Fig. 1.3(b)], when the applied dc voltage approximately meets the single-photon resonance condition $2eV_{\mathrm{dc}} \approx h\nu_a$ or $2eV_{\mathrm{dc}} \approx h\nu_b$, such that each tunneling Cooper pair creates one excitation in cavity a or cavity b. Further increasing the dc voltage, they also observed emission along the line $2eV_{\mathrm{dc}} \approx 2h\nu$ [right panel of Fig. 1.3(b)]. When the dc voltage is approximately $V_{\mathrm{dc}} \approx 2h\nu_a \approx 20\,\mu\mathrm{V}$, each tunneling Cooper pair creates two photons in cavity a (accordingly for $V_{\mathrm{dc}} \approx 2h\nu_b \approx 28\,\mu\mathrm{V}$ and cavity b). Finally, emission is also observed when the dc voltage is adjusted to $2eV_{\mathrm{dc}} \approx h(\nu_a + \nu_b)$. Then, the excess energy of a tunneling Cooper pair creates one excitation in cavity a and one excitation in cavity b. In the cases where two photons are created by one tunneling Cooper pair, the cavities emit these photons with random frequencies ν_1 and ν_2 that match the creation process, $2eV_{\mathrm{dc}} = h(\nu_1 + \nu_2)$. Thus, the emitted photons are frequency-correlated. For the two-photon resonance condition, this will yield quantum entanglement [11, 36, 37].

1.2 Overview of Operating Regimes and Device Applications

The combination of the nonlinearity of the Josephson junction and experimentally controllable parameters allows for a vast amount of possible parameter regimes. While the resonance frequency, the quality factor and the zero-point fluctuations of a microwave cavity can be experimentally fabricated, the dc voltage and the Josephson energy (through SQUIDs) can be tuned in situ (see Tab. 1.1).

The versatile platform and the development of a theoretical framework beyond $P(E)$-theory [25, 27] have opened the field to explore diverse and novel physical phenomena. A semiclassical regime with nearly classical high cavity occupations far from equilibrium can be reached when the Josephson energy is much larger than the photon loss rates of the high-Q cavities (where $Q \sim \mathcal{O}(10^3)$) [9, 27, 28, 33, 58, 59], whereas states deep in the quantum regime with prominent quantum effects are found for weakly driven low-Q resonators. Through the interplay of the photonic states of the microwave cavities with tunneling Cooper pairs, information and statistics about the granular charge transport across the junction can be gained by measuring microwave emission [32, 34, 38]. By increasing the inductance-to-capacitance ratio, the zero-point fluctuations can reach $\alpha_0 \sim \mathcal{O}(1)$ [10, 23]. On one hand, this enables the study of higher-order resonances with k-photon creation

Parameter	Definition	Additional remarks
Universal constants		
magnetic flux quantum	$\Phi_0 = h/2e$	
quantum of resistance	$R_Q = h/(2e)^2$	
Josephson junction		
Josephson energy	$E_J = I_{\mathrm{crit}}\Phi_0/(2\pi)$	tunable in situ by a SQUID
gap energy	Δ	$\Delta/k_B \gtrsim \mathcal{O}(1\,\mathrm{K})$
Circuit operation		
operating temperature	T	$T \sim \mathcal{O}(10\,\mathrm{mK}) \ll \frac{\hbar\omega_a}{k_B} \ll \frac{\Delta}{k_B}$
dc-voltage bias	$\omega_{\mathrm{dc}} = V_{\mathrm{dc}}\,2\pi/\Phi_0$	$\hbar\omega_{\mathrm{dc}} \ll \Delta$
Resonator		
resonance frequency	$\omega_a = 2\pi\nu_a = 1/\sqrt{L_aC_a}$	$\omega_a \sim \mathcal{O}(10\,\mathrm{GHz}) \ll \Delta/\hbar$
single-photon loss rate	γ_a	
quality factor	$Q_a = \omega_a/\gamma_a$	$Q_a \sim \mathcal{O}(10^1 \text{ to } 10^3)$
zero-point fluctuations	$\alpha_0 = \sqrt{\sqrt{L_a/C_a}\,\pi/R_Q}$	$\alpha_0 \sim \mathcal{O}(10^{-1} \text{ to } 1)$

Table 1.1: Summary of parameters and their definitions of a (single-mode) Josephson-photonics device [compare Fig. 1.1(c)] with approximate orders of magnitude that are achievable or have typically been used in experiments [8–11, 13, 19, 20, 22–24].

processes that are proportional to α_0^k and highly unlikely in quantum optics (see Sec. 1.4.1). On the other hand, specific values of zero-point fluctuations can also block specific photonic transitions to higher cavity occupations, which in turn affects the charge transfer and effectively creates a single-photon source that emits antibunched light [10, 22, 31, 32].
In this way, the platform naturally translates the study of fundamental physics to technological applications.

- Single-photon source [10, 22, 31, 32], qubits and n-level systems [44]
  Fabricating $\alpha_0 = \sqrt{2}$, the transition between Fock states $|1\rangle$ and $|2\rangle$ of the microwave cavity can be blocked, preventing higher state occupations in the microwave resonator. It now functions like a qubit and emits antibunched light. In a similar way, n-level systems can be designed, c.f. Sec.1.5.1.

- Source of entanglement [36] and (two-mode) squeezing [11, 19, 29, 33, 37]
  Two-mode squeezed microwave photons can be generated by using a photon-pair resonance condition (compare Fig. 1.3) and may be used in a quantum radar [60, 61] (see Sec. 1.5.2 for details).

- Josephson laser [59, 62]
  The superconducting cavities can enter a lasing state far from equilibrium when driven at a multi-photon resonance.

- Generation of Fock states [35]
  In a theoretical proposal of a Josephson-photonics setup with a storage and an auxiliary cavity, Fock states can be stabilized, preparing an on-demand source of them.

- Cat states for quantum computation [12, 48]
  Using two-mode Josephson-photonics devices that are biased at a resonance condition involving the difference of the resonance frequencies, two-photon driving and damping can be effectively engineered. The resulting stationary states are close to cat states. The platform is therefore a promising candidate for quantum computation (see Sec. 1.4.2).

- Amplification of microwave signals [20, 21, 24]
  Josephson-photonics devices are simple dc-powered amplifiers that allow for signal amplification close to the quantum limit.

- Microwave-photon detectors [13, 41, 51]
  Recent developments, involving a resonance condition similar to that used for the generation of cat states, realize microwave-photon detectors by photon-number multiplication. Recent developments have shown the working principle for coherent continuous-wave input signals (Sec. 1.6).

While LC resonators are typically driven by an ac signal [63], Josephson-photonics devices convert a constant voltage into microwave light. The advantage and simplicity of a dc-powered and on-chip source for microwave photons comes with the disadvantage that a constant voltage is not able to provide a reference phase of the phase-space angle for the resonators' quantum states. The effect on all phase-sensitive experiments and applications is detrimental, since many quantum

features such as entanglement (i.e. of two-mode squeezed states) or interference fringes of cat states will be hidden or destroyed by voltage noise.

In this thesis, we address two topics:

(1) Phase stabilization of Josephson-photonics devices (theory in Sec. 2 and results in Sec. 4)

We explicitly show that the platform constitutes a so-called self-sustained oscillator, which can be synchronized and injection locked to a small and external ac-signal. In this way, the phase-space angle of the quantum states can be stabilized, enabling the use of Josephson-photonics devices in technological applications, while fundamental synchronization dynamics like phase slips or the sharpening of an oscillation spectrum can be studied in both the classical and the quantum regime.

As an alternative approach to partially resolve the issue of an absent phase reference, we show how the quantum state without phase diffusion can be reconstructed by measuring only very few experimentally accessible expectation values and optimizing an ansatz for the quantum state.

(2) Single microwave-photon detection (theory in Sec. 3 and results in Sec. 5.1)

While the multiplication of an incoming classical (coherent continuous-wave) signal has been demonstrated [13], single-photon detection has not yet been achieved in Josephson-photonics devices. We combine Mølmer's approach, which theoretically describes itinerant microwave photons, with a heterodyne detection scheme to characterize the device in different parameter regimes that ensure high single-photon detection efficiencies and promise to outperform existing schemes.

In order to provide a sound background on Josephson-photonics devices, we now proceed to review their fundamental properties and some of the applications discussed above. Before that, we first offer a theoretical description with tools for an in-depth study of Josephson-photonics devices. Hence, the following Sec. 1.3 may be omitted without loss of continuity and serves as a reference for detailed mathematical derivations of the equations used throughout the thesis.

1.3 Theoretical Framework of Josephson Photonics

Before we focus on the properties of Josephson-photonics devices and their applications in more detail in the following sections, we first provide a solid theoretical foundation which comprehensively derives some of the mathematical expressions used throughout the thesis. It is not directly required for the understanding of the other following sections, and may only be used as technical support if needed.

Josephson-photonics devices are superconducting electric circuits. They can be operated in a semiclassical regime with high resonator populations, where a set of differential equations of motion describe the dynamics (see Sec. 1.3.1), and gracefully bridge the gap into the quantum regime (Secs. 1.3.2 and 1.3.3), where only a few cavity excitations are present.

1.3.1 Classical Equations of Motions for Single-Mode Devices

We consider a dc-voltage biased electric circuit, where a parallel $R_aL_aC_a$-circuit is connected in series to a Josephson junction [similar to Fig. 1.1(b) when replacing the L_aC_a-circuit therein by an $R_aL_aC_a$-circuit]. The classical equations of motion are found by applying Kirchhoff's laws and the classical Josephson relations, Eqs. (1.1) and (1.2). Using the general phase-voltage relation $\dot{\varphi} = 2eV_{\mathrm{cav}}/\hbar$ for the resonator (with analogous definitions for the total voltage V_{tot} and the voltage V_J across the junction), Kirchhoff's voltage law

$$\dot{\varphi}_{\mathrm{tot}} = \dot{\varphi}_J + \dot{\varphi} \tag{1.3}$$

can be directly integrated. The total current of the parallel $R_aL_aC_a$-circuit is fixed by the Cooper-pair current,

$$I_{\mathrm{CP}}(t) = I_{\mathrm{crit}} \sin(\varphi_J) = \frac{\hbar}{2e}\left(\frac{\dot{\varphi}}{R_a} + \frac{\varphi}{L_a} + C_a\ddot{\varphi}\right) . \tag{1.4}$$

The resulting differential equation

$$\ddot{\varphi} + \gamma_a\dot{\varphi} + \omega_a^2\varphi = \frac{2e}{\hbar}\gamma_a I_{\mathrm{crit}} R_a \cdot \sin\left(\frac{2e}{\hbar}V_{\mathrm{dc}}t - \varphi - \eta\right) \tag{1.5}$$

describes a harmonic oscillator with mass $m \propto C_a$ that is nonlinearly driven by the Josephson junction. The integration of the Kirchhoff's voltage law amounts to a constant phase η. As also shown in Tab. 1.1 of Sec. 1.2, the applied dc voltage can be associated with a driving frequency $\omega_{\mathrm{dc}} = 2eV_{\mathrm{dc}}/\hbar$ and the resonator's (angular) resonance frequency is defined as $\omega_a = (L_aC_a)^{-1/2}$. The quantum-mechanical single-photon loss rate can be related to the resistive part of the $R_aL_aC_a$-circuit with the damping constant $\gamma_a = 1/(R_aC_a)$. Most crucially, the oscillator's position variable φ appears inside a time-dependent sine function, and its classical behavior can be described as a damped motion in a potential, consisting of a time-independent harmonic part and a time-dependent modulation by a sine-wave (see Fig.1.4). While chaotic motion may be the result of large Josephson driving, we restrict the discussion throughout the thesis to the condition where the Josephson driving can be treated as a weak perturbation of the harmonic oscillator potential.

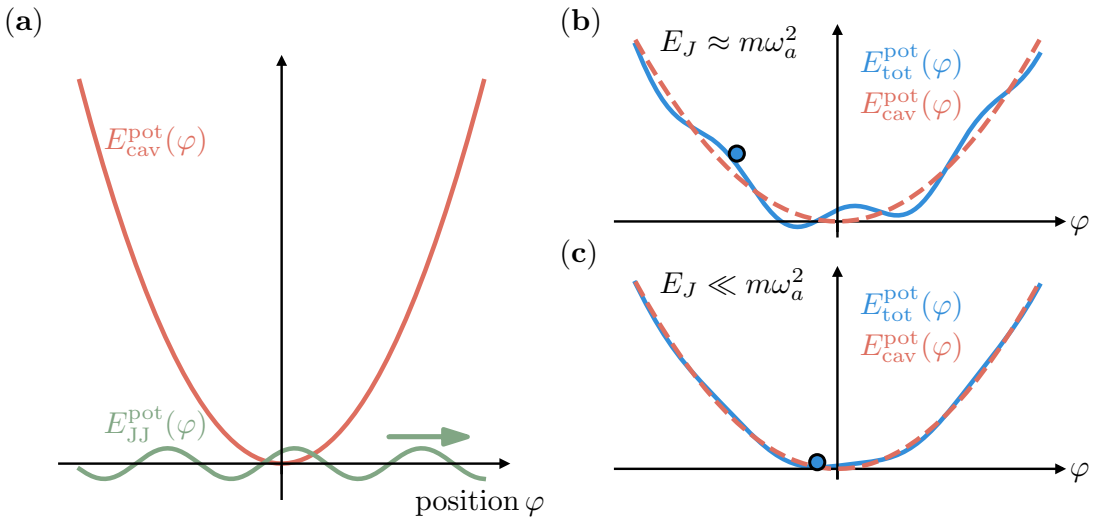

Figure 1.4: Classical potential energy of a single-mode Josephson-photonics device [compare Fig. 1.1(b)]. (a) The harmonic oscillator with position variable φ and quadratic potential $E^{\mathrm{pot}}_{\mathrm{cav}} = m\omega_a^2\varphi^2/2$ is driven by the Josephson junction [c.f. Eq.(1.5)], yielding a time-dependent potential $E^{\mathrm{pot}}_{\mathrm{JJ}} = -E_J\cos(2eV_{\mathrm{dc}}t/\hbar - \varphi)$, which is plotted at a fixed time (the explicit time-dependence is indicated by the green arrow). (b) For large $E_J \approx m\omega_a^2$, the drive of the Josephson junction leads to a complete distortion of the harmonic potential, resulting in a complex and potentially chaotic motion of the cavity phase φ. (c) When $E_J \ll m\omega_a^2$, the potential of the Josephson junction yields small wiggles on a harmonic potential. It can be interpreted as weak time-dependent and periodic perturbation of the harmonic oscillator. Throughout this thesis, we stay in parameter regimes of weak perturbations from (c).

For instance, very weak ($E_J \lll m\omega_a$) and resonant ($\omega_{\mathrm{dc}} \approx \omega_a$) driving by the Josephson junction, such that $\varphi \ll 2\pi$, yields the linear equation of motion of a driven damped harmonic oscillator

$$\ddot{\varphi} + \gamma_a\dot{\varphi} + \omega_a^2\varphi \approx \frac{2e}{\hbar}\gamma_a I_{\mathrm{crit}}R_a \cdot \sin(\omega_{\mathrm{dc}}t - \eta) \tag{1.6}$$

that will approximately perform steady-state oscillations with the driving frequency ω_{dc}. In the phase space spanned by position and momentum of the resonator, the steady state in the rotating frame is then given by a constant point with a stable amplitude and a phase-space angle that is fixed by a constant phase η. We will review the limiting case of linearly driven damped oscillation in the quantum regime, resulting in a (nearly) symmetric distribution around a fixed point (see Fig. 1.5 of Sec. 1.4.1.1). We want to emphasize already here that Josephson-photonics devices are actually self-sustained oscillators with a neutrally stable phase-space angle, whereas we explicitly note in Sec. 2.1 that a driven damped harmonic oscillator is not a self-sustained oscillator. To accurately model the physically correct behavior, the classical and quantum models derived here will be extended in Sec. 4. For this purpose, Pubs. (*i*) to (*iii*) will incorporate an additional small in-series resistor R_0, which yields a time-dependent phase $\eta \to \varphi_{R_0}(t)$. Since the phase φ_{R_0} will turn out to be the crucial missing element to describe phase diffusion and phase stabilization in Josephson-photonics devices, our derivations here explicitly include a constant phase η, which otherwise would give a physically irrelevant constant phase shift and could be omitted.

1.3.2 Single-Mode Devices in the Quantum Regime

We start with the quantum description of a single-mode Josephson-photonics device.

Quantum Hamiltonian

Within circuit quantum electrodynamics [63], a theoretical model beyond $P(E)$-theory can be derived [25, 27], yielding the quantum Hamiltonian

$$\hat{H} = \underbrace{\hbar\omega_a \hat{a}^\dagger \hat{a}}_{=\hat{H}_{\mathrm{cav}}} \underbrace{-E_J \cos\left[\omega_{\mathrm{dc}} t - \eta + \alpha_0(\hat{a}^\dagger + \hat{a})\right]}_{=\hat{H}_J} \tag{1.7}$$

that describes a cavity (with free Hamiltonian $\hat{H}_{\mathrm{cav}}$) that is nonlinearly driven by the Josephson junction (with driving Hamiltonian $\hat{H}_J$). The cavity is the quantized version of the classical L_aC_a-oscillator (for variable definitions, see Sec. 1.3.1 or Tab. 1.1 in Sec. 1.2). Its phase (i.e. the integrated voltage across the resonator) and the charge on its capacitor plates

$$\hat{\varphi} = \alpha_0(\hat{a}^\dagger + \hat{a}) \tag{1.8}$$

$$\hat{Q} = i\frac{e}{\alpha_0}(\hat{a}^\dagger - \hat{a}) \tag{1.9}$$

can be interpreted as position and momentum operators that fulfill the canonical commutation relation

$$[\hat{\varphi}, \hat{Q}] = 2ie\,. \tag{1.10}$$

Lindblad master equation

In experimental setups, the cavity is capacitively coupled to transmission lines. The sample is cooled to temperatures $T \sim \mathcal{O}(10\,\mathrm{mK})$ in a dilution refrigerator (c.f. Tab. 1.1), which is typically much smaller than the resonator's resonance frequency $\hbar\omega_a/k_B \sim \mathcal{O}(100\,\mathrm{mK})$, such that thermal excitations of the microwave cavity can be neglected to a very good approximation. In the theoretical model, it is therefore justified to describe the environment as a zero temperature heat bath (which is used throughout this thesis). Dissipation of cavity photons into transmission lines is then sufficiently well described (using the Markovian approximation) by the Lindblad operator

$$\hat{L}_a = \sqrt{\gamma_a}\,\hat{a}\,. \tag{1.11}$$

Thus, within the Born-Markov approximation, the reduced dynamics of the microwave cavity is modeled by the Lindblad master equation

$$\frac{\mathrm{d}}{\mathrm{d}t}\hat{\rho}_{\mathrm{lab}} = -\frac{i}{\hbar}[\hat{H}, \hat{\rho}_{\mathrm{lab}}] + \underbrace{\frac{\gamma_a}{2}\left(2\hat{a}\hat{\rho}_{\mathrm{lab}}\hat{a}^\dagger - \hat{a}^\dagger\hat{a}\hat{\rho}_{\mathrm{lab}} - \hat{\rho}_{\mathrm{lab}}\hat{a}^\dagger\hat{a}\right)}_{=\mathcal{D}_{\hat{L}_a}[\hat{\rho}_{\mathrm{lab}}]}, \tag{1.12}$$

where $\hat{\rho}_{\mathrm{lab}}$ describes the density matrix in the laboratory frame.

The Hamiltonian (1.7) is not only nonlinear but also explicitly time-dependent. Specific resonance conditions allow us to simplify the theoretical description by

moving to a rotating frame and performing a rotating-wave approximation of the driving Hamiltonian $\hat{H}_J$, for which the dynamics on fast time scales are neglected. The rotating-wave approximation is justified for weak driving, i.e. when $E_J \ll \hbar\omega_a$, which is a typical parameter regime considered in the experiments.

Rotating-frame transformation

A transformation of the Lindblad master equation to the rotating frame (with a unitary $\hat{U}_a$) modifies all operators involved. The density matrix

$$\hat{\rho} = \hat{U}_a \, \hat{\rho}_{\text{lab}} \, \hat{U}_a^\dagger \tag{1.13}$$

describes the quantum state of the system in the rotating frame and will be used throughout this thesis if not explicitly stated otherwise. The transformation to the rotating frame is summarized in Box 1.1. With analogous calculations, the dissipative term $\mathcal{D}_{\hat{L}_a}[\hat{\rho}]$ remains formally unchanged by the transformation.

Box 1.1: Rotating-Frame Transformation for $\hat{H}$

Rotating-Frame Hamiltonian

$$\hat{H}_{\text{rot}} = \hbar\,\delta\,\hat{a}^\dagger\hat{a} + E_J^*\left(\hat{h}_{\text{rot}}^\dagger + \hat{h}_{\text{rot}}\right) \tag{1.14}$$

$$\begin{aligned}\hat{h}_{\text{rot}} &= -\frac{1}{2}e^{i(\omega_{\text{dc}}t-\eta)}e^{i\alpha_0\hat{a}^\dagger \exp[i\phi_{a,\text{rot}}]}\,e^{i\alpha_0\hat{a}\exp[-i\phi_{a,\text{rot}}]} \\ &= -\frac{1}{2}\sum_{l=0}^{\infty}\sum_{m=0}^{\infty}\frac{(i\alpha_0)^{l+m}}{l!\cdot m!}\hat{a}^{\dagger l}\hat{a}^m\, e^{i(\omega_{\text{dc}}t-\eta)}e^{i(l-m)\phi_{a,\text{rot}}}\end{aligned} \tag{1.15}$$

phase of rotating frame	detuning	renormalized Josephson energy
$\phi_{a,\text{rot}}(t) = \omega_{a,\text{rot}}t + \phi_{a,0}$	$\delta = \omega_a - \omega_{a,\text{rot}}$	$E_J^* = E_J\, e^{-\alpha_0^2/2}$

rewrite the driving Hamiltonian $\hat{\mathbf{H}}_\mathbf{J}$

- $\hat{H}_J = -\frac{E_J}{2}e^{i(\omega_{\text{dc}}t-\eta)}e^{i\alpha_0(\hat{a}^\dagger+\hat{a})} + \text{h.c.}$ (Euler formula)
- $E_J e^{i\alpha_0(\hat{a}^\dagger+\hat{a})} = \underbrace{E_J e^{-[i\alpha_0\hat{a}^\dagger, i\alpha_0\hat{a}]/2}}_{\Rightarrow E_J^* = E_J e^{-\alpha_0^2/2}}\, e^{i\alpha_0\hat{a}^\dagger}\, e^{i\alpha_0\hat{a}}$ (Baker-Campbell-Hausdorff)

$$\Rightarrow \hat{H}_J = -\frac{E_J^*}{2}e^{i(\omega_{\text{dc}}t-\eta)}\, e^{i\alpha_0\hat{a}^\dagger}\, e^{i\alpha_0\hat{a}} + \text{h.c.} = E_J^*\left(\hat{h} + \hat{h}^\dagger\right)$$

definition and action of the unitary transformation

$\hat{U}_a = e^{i\phi_{a,\text{rot}}\hat{a}^\dagger\hat{a}}$ $\Rightarrow$

$\hat{A}$	$\hat{a}$	$\hat{a}^\dagger\hat{a}$	$e^{i\hat{a}}$
$\hat{U}_a\,\hat{A}\,\hat{U}_a^\dagger$	$\hat{a}\,e^{-i\phi_{a,\text{rot}}}$	$\hat{a}^\dagger\hat{a}$	$e^{i\hat{a}\exp[-i\phi_{a,\text{rot}}]}$

$\Rightarrow$ calculation of $\hat{H}_{\text{rot}} = \hat{U}_a(\hat{H}_{\text{cav}} + \hat{H}_J)\hat{U}_a^\dagger + i\hbar\dot{\hat{U}}_a\hat{U}_a^\dagger$ yields the main results

Rotating-wave approximation (RWA)

The Hamiltonian can become time independent for specific resonance conditions of the dc-voltage drive. When a dc voltage

$$2eV_{\mathrm{dc}} \approx k\,\hbar\omega_a \quad (k \in \mathbb{N}_0) \tag{1.16}$$

is applied, each tunneling Cooper pair effectively creates k excitations in the cavity.

Box 1.2: Rotating Wave Approximation (RWA) of the Hamiltonian

RWA-Hamiltonian in the Rotating Frame

$$\hat{H}_{\mathrm{RWA}} = \hbar\delta\,\hat{a}^\dagger\hat{a} - \frac{E_J^*\alpha_0^k}{2k!} :\!\left[i^k e^{-i\eta}\hat{a}^k + (-i)^k e^{i\eta}\hat{a}^{\dagger k}\right] \frac{J_k\left(2\alpha_0\sqrt{\hat{a}^\dagger\hat{a}}\right)\cdot k!}{(\alpha_0\sqrt{\hat{a}^\dagger\hat{a}})^k} :\!, \tag{1.17}$$

$$\approx \hbar\delta\,\hat{a}^\dagger\hat{a} - \frac{E_J^*\alpha_0^k}{2k!}\left[i^k e^{-i\eta}\hat{a}^k + (-i)^k e^{i\eta}\hat{a}^{\dagger k}\right] \quad (\text{if } \alpha_0^2\langle\hat{a}^\dagger\hat{a}\rangle \ll 1) \tag{1.18}$$

k-photon resonance	frequency of rotating frame
$\omega_{\mathrm{dc}} \approx k\,\omega_a$	$\omega_{a,\mathrm{rot}} = \frac{\omega_{\mathrm{dc}}}{k} = \omega_a - \delta$

RWA (neglecting fast oscillating terms in $\hat{h}_{\mathrm{rot}}$ yields the condition $m = k + l$)

$\Rightarrow \hat{h}_{\mathrm{RWA}} = \frac{-i^k}{2} e^{-i\eta} \sum_{l=0}^{\infty} (-1)^l \frac{\alpha_0^{2l+k}}{(l+k)!\cdot l!} \hat{a}^{\dagger l}\hat{a}^{l+k}$ [in frame defined by $\phi_{a,\mathrm{rot}}(t) = \frac{\omega_{\mathrm{dc}}}{k}t$]

closed expression for $\hat{h}_{RWA}$

- ∘ use normal ordering of operators: $\hat{a}^{\dagger l}\hat{a}^{l+k} =: \sqrt{\hat{a}^\dagger\hat{a}}^{2l+k} \frac{a^k}{\sqrt{\hat{a}^\dagger\hat{a}}^k} :$
- ∘ compare to Bessel function: $J_k(x) = \sum_{l=0}^{\infty} \frac{(-1)^l}{(l+k)!\cdot l!} \left(\frac{x}{2}\right)^{2l+k}$
  - ⇒ in lowest order: $\approx \frac{1}{k!}\left(\frac{x}{2}\right)^k$ for $x \ll 1$

Starting from the Hamiltonian in Eq. (1.14), we perform a rotating wave approximation. Box 1.2 summarizes the main steps to find the closed form, Eq. (1.17), that elegantly highlights the imposed resonance condition. Fundamentally, it describes the creation $\propto \hat{a}^{\dagger k}$ (annihilation processes $\propto \hat{a}^k$) of k photons in the microwave cavity by a single forward (backward) coherently tunneling Cooper pair. This theoretical model can also be applied to the stronger driving regime, where the cavities are driven far out of equilibrium, which cannot be captured by $P(E)$-theory. The nonlinearity of the Josephson junction gives rise to higher-order processes, where the tunneling process of a single Cooper pair is accompanied by the creation and subsequent annihilation of multiple virtual cavity photons without changing the total number k of effectively created photons. They are captured by normally-ordered Bessel functions of the first kind [64]. (The normal ordering, signaled by colons, means that all creation operators are positioned to the left of all annihilation operators.) In the limit of small Bessel function arguments, such that higher-order processes can be neglected, the Hamiltonian takes a simple form, Eq. (1.18).

It reduces to a coherently driven damped cavity ($k = 1$) and single-mode squeezing (for $k = 2$) known from quantum optics [65, 66] and serves as accessible starting points (see Sec. 1.4.1) to introduce the dynamics in Josephson-photonics devices.

1.3.3 Two-Mode Devices in the Quantum Regime

In principle, multiple cavities can be connected in series to a Josephson junction. Since this thesis only analyzes single- or two-mode devices, we briefly summarize the results for two cavities and avoid showing results for a general Hamiltonian with N modes. All derivations are straightforward and follow the steps shown in Box 1.1 and 1.2 of Sec. 1.3.2.
Let us consider a dc-voltage biased Josephson junction that is connected in series to two nondegenerate cavities with eigenfrequencies ω_ξ, single-photon loss rates γ_ξ ($\xi = a, b$) and zero-point fluctuations α_0 and β_0, which are defined analogously to the single-mode case.

Lab-frame and rotating-frame Hamiltonian

The two-mode Hamiltonian

$$\hat{H} = \hbar\omega_a \hat{a}^\dagger \hat{a} + \hbar\omega_b \hat{b}^\dagger \hat{b} - E_J \cos[\omega_{\mathrm{dc}} t - \eta + \alpha_0(\hat{a}^\dagger + \hat{a}) + \beta_0(\hat{b}^\dagger + \hat{b})] \tag{1.19}$$

is transformed to the rotating frame

$$\hat{H}_{\mathrm{rot}} = \hbar\delta_a \hat{a}^\dagger \hat{a} + \hbar\delta_b \hat{b}^\dagger \hat{b} + E_J^*(\hat{h}_{\mathrm{rot}} + \hat{h}_{\mathrm{rot}}^\dagger) \tag{1.20}$$

$$\hat{h}_{\mathrm{rot}} = -\frac{1}{2} \sum_{\substack{l_a=0 \\ m_a=0}}^{\infty} \sum_{\substack{l_b=0 \\ m_b=0}}^{\infty} \left\{ \frac{(i\alpha_0)^{l_a+m_a}}{l_a! \cdot m_a!} \frac{(i\beta_0)^{l_b+m_b}}{l_b! \cdot m_b!} \hat{a}^{\dagger l_a} \hat{a}^{m_a} \hat{b}^{\dagger l_b} \hat{b}^{m_b} \cdot \right.$$
$$\left. e^{i\left[\omega_{\mathrm{dc}} t - \eta + (l_a - m_a)\phi_a^{\mathrm{rot}} + (l_b - m_b)\phi_b^{\mathrm{rot}}\right]} \right\} \tag{1.21}$$

using the unitary transformation[1] $\hat{U} = \hat{U}_a \otimes \hat{U}_b$. Here, we have defined the renormalized Josephson energy $E_J^* = E_J e^{-(\alpha_0^2+\beta_0^2)/2}$ (compared to $E_J^* = E_J e^{-\alpha_0^2/2}$ for the single-mode case) and detunings $\delta_\xi = \omega_\xi - \omega_{\xi,\mathrm{rot}}$ between the resonance frequencies and the rotating-frame frequencies.

Lindblad master equation

Both cavities are coupled to zero-temperature heat baths, yielding a Lindblad master equation (in the rotating frame)

$$\frac{\mathrm{d}}{\mathrm{d}t}\hat{\rho} = -\frac{i}{\hbar}[\hat{H}_{\mathrm{rot}}, \hat{\rho}] + \mathcal{D}_{\hat{L}_a}[\hat{\rho}] + \mathcal{D}_{\hat{L}_b}[\hat{\rho}] \tag{1.22}$$

with Lindblad collapse operators $\hat{L}_\xi = \sqrt{\gamma_\xi}\hat{\xi}$.

Rotating-wave approximation

A rotating wave approximation is performed for the resonance conditions[2] $\omega_{\mathrm{dc}} \approx k_a\omega_a + k_b\omega_b$, where each tunneling Cooper pair effectively creates k_a photons in

[1] $\hat{U}_\xi = \exp[i\phi_{\xi,\mathrm{rot}}\xi^\dagger\xi]$ and $\phi_{\xi,\mathrm{rot}} = \omega_{\xi,\mathrm{rot}}t + \phi_{\xi,0}$ for $\xi = a, b$ are defined as in Sec. 1.3.2
[2] $k_a, k_b \in \mathbb{N}_0$, $k_a + k_b \neq 0$ and $k_b\omega_b - k_a\omega_a > 0$

cavity $\hat{a}$ and k_b photons in cavity $\hat{b}$. Recently, ideas emerged beyond simple multi-photon creation processes [12, 13, 20, 21, 24, 41, 48, 51], which consider processes at frequency differences, like $\omega_{\rm dc} \approx k_b\omega_b - k_a\omega_a$ (where each tunneling Cooper pair and k_a photons from cavity $\hat{a}$ create k_b photons in cavity $\hat{b}$). Box 1.3 thus summarizes the results for both resonance conditions

$$\omega_{\rm dc} \approx \begin{cases} k_b\omega_b + k_a\omega_a & \text{case 1} \\ k_b\omega_b - k_a\omega_a & \text{case 2} \end{cases} . \tag{1.23}$$

Box 1.3: RWA in Two-Mode Josephson-Photonics Devices

RWA for Case 1: $\omega_{\rm dc} \approx k_b\omega_b + k_a\omega_a$

$$\hat{H}_{\rm RWA} = \frac{\hbar\delta}{k_a+k_b}\left(\hat{a}^\dagger\hat{a} + \hat{b}^\dagger\hat{b}\right) + E_J^*\left(\hat{h}_{\rm RWA} + \hat{h}_{\rm RWA}^\dagger\right) \tag{1.24}$$

$$\hat{h}_{\rm RWA} = -\frac{\alpha_0^{k_a}\beta_0^{k_b}}{2k_a!k_b!} i^{k_a+k_b} e^{-i\eta} : \hat{a}^{k_a}\hat{b}^{k_b} \frac{J_{k_a}\left(2\alpha_0\sqrt{\hat{a}^\dagger\hat{a}}\right) k_a!}{\alpha_0^{k_a}\sqrt{\hat{a}^\dagger\hat{a}}^{k_a}} \frac{J_{k_b}\left(2\beta_0\sqrt{\hat{b}^\dagger\hat{b}}\right) k_b!}{\beta_0^{k_b}\sqrt{\hat{b}^\dagger\hat{b}}^{k_b}} : \tag{1.25}$$

$$\approx -\frac{\alpha_0^{k_a}\beta_0^{k_b}}{2k_a!k_b!} i^{k_a+k_b} e^{-i\eta}\ \hat{a}^{k_a}\,\hat{b}^{k_b} \quad (\text{if } \alpha_0^2\langle\hat{a}^\dagger\hat{a}\rangle, \beta_0^2\langle\hat{b}^\dagger\hat{b}\rangle \ll 1) \tag{1.26}$$

resonance condition	rotating-frame frequencies	detunings
$\omega_{\rm dc} = k_b\,\omega_b + k_a\omega_a - \delta$	$k_b\omega_{b,\rm rot} + k_a\omega_{a,\rm rot} = \omega_{\rm dc}$	$\delta_a = \delta_b = \frac{\delta}{k_a+k_b}$

RWA for Case 2: $\omega_{\rm dc} \approx k_b\omega_b - k_a\omega_a$

$$\hat{H}_{\rm RWA} = \frac{\hbar\delta}{k_a+k_b}\left(\hat{b}^\dagger\hat{b} - \hat{a}^\dagger\hat{a}\right) + E_J^*\left(\hat{h}_{\rm RWA} + \hat{h}_{\rm RWA}^\dagger\right) \tag{1.27}$$

$$\hat{h}_{\rm RWA} = -\frac{\alpha_0^{k_a}\beta_0^{k_b}}{2k_a!k_b!} i^{k_a+k_b} e^{-i\eta} : \hat{a}^{\dagger k_a}\hat{b}^{k_b} \frac{J_{k_a}\left(2\alpha_0\sqrt{\hat{a}^\dagger\hat{a}}\right) k_a!}{\alpha_0^{k_a}\sqrt{\hat{a}^\dagger\hat{a}}^{k_a}} \frac{J_{k_b}\left(2\beta_0\sqrt{\hat{b}^\dagger\hat{b}}\right) k_b!}{\beta_0^{k_b}\sqrt{\hat{b}^\dagger\hat{b}}^{k_b}} : \tag{1.28}$$

$$\approx -\frac{\alpha_0^{k_a}\beta_0^{k_b}}{2k_a!k_b!} i^{k_a+k_b} e^{-i\eta}\ \hat{a}^{\dagger k_a}\,\hat{b}^{k_b} \quad (\text{if } \alpha_0^2\langle\hat{a}^\dagger\hat{a}\rangle, \beta_0^2\langle\hat{b}^\dagger\hat{b}\rangle \ll 1) \tag{1.29}$$

resonance condition	rotating-frame frequencies	detunings
$\omega_{\rm dc} = k_b\,\omega_b - k_a\omega_a - \delta$	$k_b\omega_{b,\rm rot} - k_a\omega_{a,\rm rot} = \omega_{\rm dc}$	$\delta_a = -\delta_b = -\frac{\delta}{k_a+k_b}$

The result of Eq. (1.25) illustrates the resonance condition of case 1, where k_a photons in cavity $\hat{a}$ and k_b photons in cavity $\hat{b}$ are created by each tunneling Cooper pair. These processes are again renormalized by higher-order processes involving multiple cavity photons (indicated by normally-ordered Bessel functions). In the limit of small Bessel-function arguments and for $k_a = k_b = 1$, the Hamiltonian reduces to the quantum optical version of two-mode squeezing (see Sec. 1.5.2).
If, on the other hand, the applied dc-voltage is resonant to the process where each

tunneling Cooper pair annihilates k_a photons from cavity $\hat{a}$ and creates k_b photons in cavity $\hat{b}$, we find Eq. (1.28). Photon amplification and photon multiplication schemes (see Sec. 1.6) as well as the generation of cat states, Sec. 1.4.2, use resonant driving at frequency differences.

1.4 Intracavity States Created by Josephson-Photonics Devices

The versatility of Josephson-photonics devices enables the creation of microwave light with properties ranging from (nearly) classical to the deep quantum regime. To illustrate these properties, we focus on the internal resonator dynamics for cases where the dc-voltage is adjusted to specific resonance conditions of different nontrivial photon creation processes. In the long-time limit, the system will eventually reach a stationary state (which is constant in the rotating frame) where the microwave resonators internally exhibit nontrivial properties, like k-fold symmetric quantum states (discussed in Sec. 1.4.1) or cat states (Sec. 1.4.2) that can be used for quantum applications. Understanding how intracavity state properties manifest in the properties of the emitted radiation is often a more complex issue.

1.4.1 k-Photon Resonances in Single-Mode Devices

When the dc voltage is adjusted to the resonance condition

$$2eV_{\rm dc} \approx k\,\hbar\omega_a \quad (k \in \mathbb{N}_0)\,, \tag{1.30}$$

each tunneling Cooper pair will effectively create k excitations in a single microwave cavity. Such k-photon creation processes are proportional to the k-th power of the zero-point fluctuations, α_0^k (c.f. Box 1.2 in Sec. 1.3.2 for technical details). In contrast to quantum optics, where k-photon creation processes are proportional to the k-th power of the fine structure constant, $\alpha^k \approx 137^{-k}$ and hence are strongly suppressed for larger k, Josephson-photonics devices can be designed with large zero-point fluctuations $\alpha_0 \sim 1$ [10, 23], such that multi-photon resonances up to $k = 6$ have been experimentally observed [23].
Since the cavity is coupled to transmission lines, dissipation from the cavity (with mean life time $1/\gamma_a$) will balance out the k-fold photon creation process, and a stationary state is reached that can exhibit strong quantum properties. The k-photon resonant drive will manifest itself in a $\mathbb{Z}^k$-symmetry of the microwave resonator, which can be illustrated by the steady-state Wigner function in the phase space of the cavity.

1.4.1.1 $k = 1$: Coherent States and Their Modifications

For the single-photon resonance condition ($k = 1$), each tunneling Cooper pair effectively creates one excitation in the microwave cavity [c.f. Fig.1.1(d) in Sec. 1.1]. On resonance, $\omega_{\rm dc} = \omega_a$, and in the frame rotating with $\omega_{\rm dc}$, the Hamiltonian (see Eq. (1.17) in Sec. 1.3.2)

$$\hat{H}_{\rm RWA} = \frac{E_J^*\alpha_0}{2} : (ie^{i\eta}\hat{a}^\dagger - ie^{-i\eta}\hat{a}) \frac{J_1(2\alpha_0\sqrt{\hat{a}^\dagger\hat{a}})}{\alpha_0\sqrt{\hat{a}^\dagger\hat{a}}} : \tag{1.31}$$

$$\approx \frac{E_J^*\alpha_0}{2}(ie^{i\eta}\hat{a}^\dagger - ie^{-i\eta}\hat{a}) \quad (\text{if } \alpha_0^2\langle\hat{a}^\dagger\hat{a}\rangle \ll 1) \tag{1.32}$$

crucially contains a coherent drive term $\propto E_J^*\alpha_0\hat{a}^\dagger + \text{h.c.}$, which is amended by a Bessel function (the colons signal normal ordering of operators).

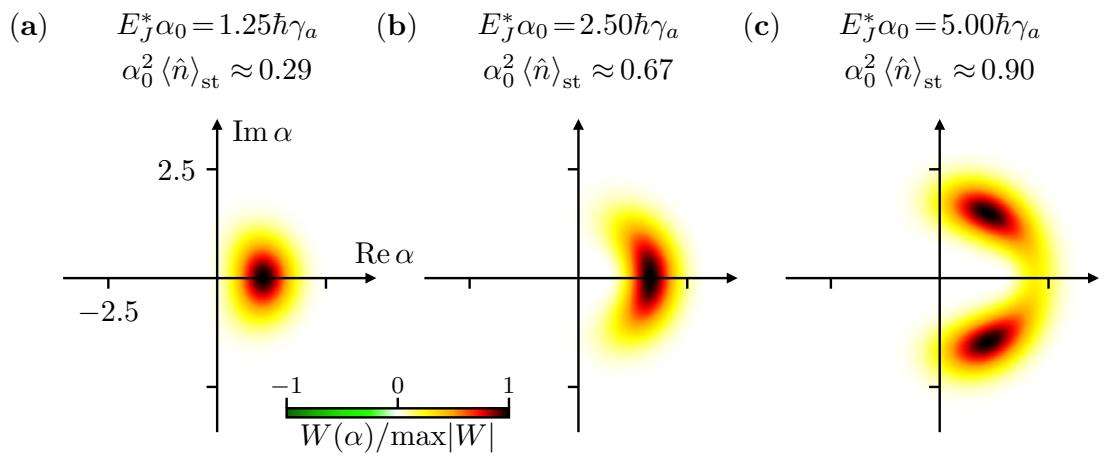

Figure 1.5: Steady-state Wigner functions for the single-photon resonance, $2eV_{\rm dc} = \hbar\omega_a$. A single-mode Josephson-photonics device is simulated under rotating wave approximation and in the rotating frame. The Wigner functions are plotted in the phase space defined by $\alpha = x+ip$ of the microwave cavity with zero-point fluctuations $\alpha_0 = 1/2$. (a) Weak driving results in a near-coherent stationary state. In this limit, the steady-state cavity occupation $\langle\hat{n}\rangle_{\rm st} \approx 1.16$ stays small, such that nonlinear effects may be neglected and the dynamics is governed to good approximation by Eq. (1.32) with the steady state $\hat{\rho} \approx |\alpha_{\rm st}\rangle\langle\alpha_{\rm st}|$ (compare main text). The phase-space angle of the steady state is determined by the phase of the drive, $\phi_\alpha = \eta = 0$. (b) An increased drive results in steady-state Wigner functions that are distorted in angular direction due to nonlinear corrections of the Bessel functions [compare Eq. (1.31) and the explanation given in the main text]. (c) A bifurcation, where two fixed points branch out along a circle, occurs when driving beyond a threshold (see main text). In all cases, the steady-state Wigner function shows a $\mathbb{Z}^{k=1}$-symmetry in the phase space.

For weak drive, cavity occupations remain small such that the fraction with the Bessel function can be approximated to $\mathbb{1}$. Then, the Hamiltonian reduces to a coherently driven damped harmonic oscillator known from quantum optics [65, 66]. Consequently, the steady state is a coherent state [compare Fig. 1.5(a)] with amplitude

$$\alpha_{\rm st} = \frac{E_J^*\alpha_0}{\hbar\gamma_a}\, e^{i\phi_\alpha}\,. \tag{1.33}$$

The angular direction, i.e. the phase-space angle ϕ_α of the coherent state, is fixed by the phase η of the driving term. Increasing the effective drive of the approximated Hamiltonian shifts the coherent state further away from the origin of the phase space with a steady-state cavity occupation of $\langle\hat{n}\rangle_{\rm st} = |\alpha_{\rm st}|^2$. Josephson-photonics devices with small zero-point fluctuations of a high-Q cavity that are strongly driven, $E_J^*\alpha_0 \gg \hbar\gamma_a$, can reach a regime with a (nearly classical) coherent stationary state far from the origin [9, 27, 28, 33, 58, 59].

The nonlinearity of the full model limits the growth $\alpha_{\rm st} \propto E_J^*\alpha_0$ of the approximated Hamiltonian. Fig. 1.5(b) shows that stronger driving will not merely shift a coherent state to larger amplitudes. First, increasing the drive results in steady-state Wigner functions whose amplitude $\alpha_{\rm st}$ grows linearly with $E_J^*\alpha_0$. Due to increased cavity occupations, Bessel-function arguments grow and their nonlinear corrections become more important [compare Eq. (1.31)] and distort the previously

near-symmetric phase-space distribution in angular direction.

When driving is further increased, there exists a critical point $\frac{E_J^*\alpha_0^2}{\hbar\gamma_a} = z_1/[4J_0(z_1)]$ [$z_1 \approx 1.84$ is the position of the first maximum of $J_1(z)$] [27], where the steady-state occupation number saturates and beyond which the phase-space distribution is broadened in the angular direction [38]. The phase-space distribution then splits into an equal mixture of two components with opposite momenta [Fig. 1.5(c)]. Nevertheless, all steady-state distributions show a $Z^{k=1}$ symmetry in phase space.

1.4.1.2 $k = 2$: Single-Mode Squeezing

By tuning the dc voltage to the two-photon resonance ($k = 2$ and $\omega_{\mathrm{dc}} = 2\omega_a$), the drive yields the RWA-Hamiltonian

$$\hat{H}_{\mathrm{RWA}} = \frac{E_J^*\alpha_0^2}{4} : (e^{i\eta}\hat{a}^{\dagger 2} + e^{-i\eta}\hat{a}^2)\frac{2 \cdot J_2(2\alpha_0\sqrt{\hat{a}^\dagger\hat{a}})}{(\alpha_0\sqrt{\hat{a}^\dagger\hat{a}})^2} : \tag{1.34}$$

$$\approx \frac{E_J^*\alpha_0^2}{4}(e^{i\eta}\hat{a}^{\dagger 2} + e^{-i\eta}\hat{a}^2) \quad (\text{if } \alpha_0^2\langle\hat{a}^\dagger\hat{a}\rangle \ll 1)\ . \tag{1.35}$$

The approximate form is also well known from quantum optics and describes a driven damped parametric amplifier. The resulting steady state (in a frame rotating with ω_a) shows squeezed states in phase space. Fig. 1.6(a) illustrates a squeezed state where the fluctuations in the quadrature $p = \mathrm{Im}\,\alpha$ are smaller than vacuum fluctuations (squeezed quadrature). Fluctuations in the other quadrature $x = \mathrm{Re}\,\alpha$ are enhanced (anti-squeezed), such that the quantum state fulfills Heisenberg's uncertainty relation. As in the case of single-photon resonance ($k = 1$), the direction of the squeezing ellipse in the phase space is determined by the phase η of the drive. The effective driving strength $E_J^*\alpha_0^2/\hbar\gamma_a$ is the squeezing parameter that fixes the amount of squeezing in the steady state. When driving beyond the threshold $E_J^*\alpha_0^2 \geq \hbar\gamma_a$, the approximate squeezing Hamiltonian becomes unphysical. Maximal squeezing can be reached, where the fluctuations in one quadrature are reduced by 3dB below vacuum noise [67], when the approximate Hamiltonian is driven at threshold. A damped classical harmonic oscillator that is parametrically driven below threshold does not exhibit steady-state oscillations, with vanishing amplitude $\alpha_{\mathrm{st}} = 0$. However, the amplitude $\alpha_{\mathrm{st}} = 0$ is the stable fixed point of the quantum mechanical squeezing ellipse.

The Bessel nonlinearity of the full Hamiltonian regularizes the unphysical behavior of the driven damped parametric amplifier. Close to the threshold, the shape of the Wigner function appears more stretched than a mathematical ellipse [see Fig. 1.6(b)], before it splits into two components with stable fixed points when increasing the drive beyond the threshold [Fig. 1.6(c)].
Above a second critical threshold at $E_J^*\alpha_0^2 = \hbar\gamma_a z_2/[4J_1(z_2)]$ [where $z_2 \approx 3.05$ is the maximum of $J_2(z)$] [27], these two components will split again [c.f. Fig. 1.6(d)]. This overall behavior is comparable to the single-photon resonance, where the steady-state Wigner functions now exhibit a $Z^{k=2}$ symmetry in the phase space.

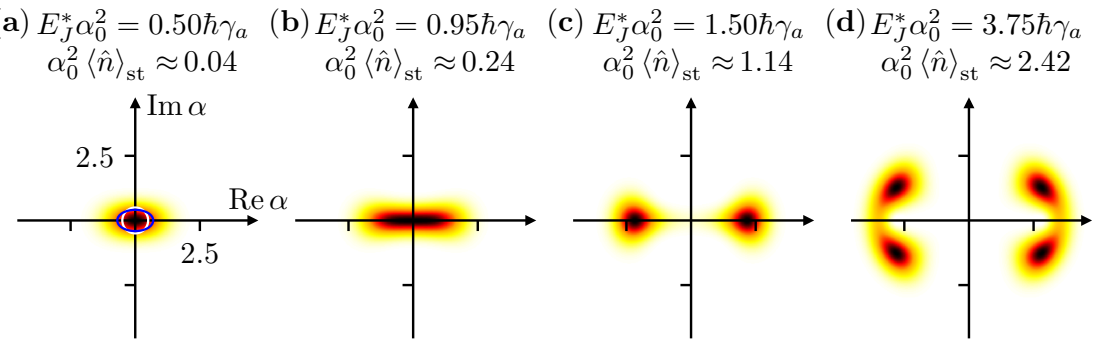

Figure 1.6: Steady-state Wigner functions (as in Fig. 1.5) of a Josephson-photonics device with $\alpha_0 = 1/2$ driven at the two-photon resonance, $2eV_{\rm dc} = 2\cdot\hbar\omega_a$. (a) For weak driving, the Bessel function arguments remain small and the system can be approximated by the Hamiltonian Eq. (1.35). The steady state is squeezed, where the standard deviation in one quadrature (here the quadrature $p = \mathrm{Im}\,\alpha$) is smaller than the vacuum noise, while the fluctuations in the other (anti-squeezed) quadrature exceed the vacuum fluctuations [compare the solid blue ellipse to the vacuum fluctuations (white circle)]. The squeezing angle is determined by the phase of the drive, here $\eta = \pi/2$. (b) Close to the first threshold $E_J^*\alpha_0^2 = \hbar\gamma_a$, the Wigner function starts to split into two parts, resulting in an elongated shape. (c) Above the first threshold, two stable fixed points form at opposite directions in phase-space, (d) which themselves split and branch out along a circle when driving beyond a second threshold (given in the main text). All steady-state Wigner functions are $\mathbb{Z}^{k=2}$-fold symmetric (c.f. Figs. 1.5 and 1.7).

1.4.1.3 $\mathbb{Z}^k$-Symmetry in Phase Space

Higher resonances ($k > 2$) with the RWA-Hamiltonian

$$\hat{H}_{\rm RWA} = \hbar\delta\,\hat{a}^\dagger\hat{a} - \frac{E_J^*\alpha_0^k}{2k!}:\!\left[i^k e^{-i\eta}\hat{a}^k + (-i)^k e^{i\eta}\hat{a}^{\dagger k}\right]\frac{J_k\left(2\alpha_0\sqrt{\hat{a}^\dagger\hat{a}}\right)\cdot k!}{(\alpha_0\sqrt{\hat{a}^\dagger\hat{a}})^k}\!: \tag{1.31}$$

will result in higher-order squeezed states, i.e. stationary states with a Wigner function that shows a $\mathbb{Z}^k$-symmetry in phase space. While the action of the higher-order squeezing operator

$$\hat{D}_k(r) = \exp\left[r\hat{a}^{\dagger k} - r^*\hat{a}^k\right] \tag{1.36}$$

on the vacuum state diverges for $k > 2$ [68–71], we have observed similar convergence problems for the time evolution towards a stationary state of a driven and damped system described by the approximated Hamiltonian. This suggests that single-photon damping might not be strong enough to reach a stationary state. However, the full Josephson-photonics model with Bessel nonlinearities can limit the drive, and a stationary state can be reached despite mere single-photon loss. Fig. 1.7 shows such steady states for $k = 3$ and illustrates that a simple change of the Josephson energy can create complex stationary states in the microwave resonator, while the dc bias changes the character of the microwave states.

The immediate technological advantage of higher-order single-mode squeezed states ($k \geq 3$) in Josephson-photonics devices is left for further research, whereas similar higher-order resonances are, for instance, used in two-mode Josephson-photonics

devices to generate cat states (Sec. 1.4.2 and Sec.4.2.3) and to achieve photon multiplication and detection of single microwave photons [Sec. 1.6 and Pub. (*iv*) in Sec. 5.1].

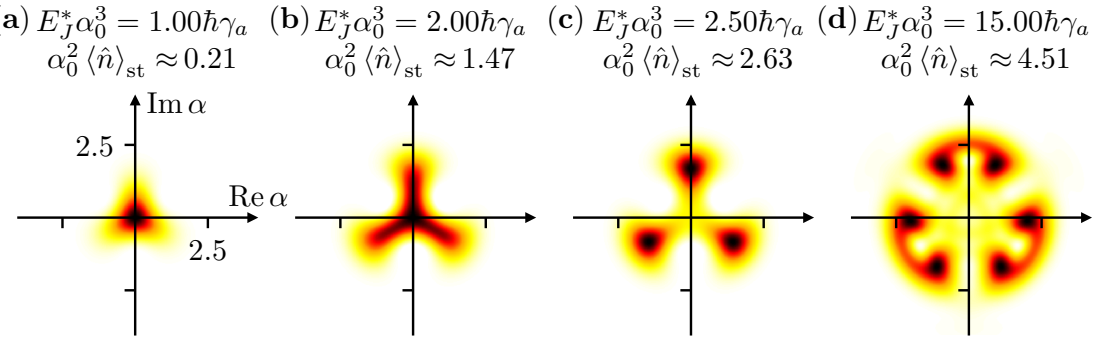

Figure 1.7: Steady-state Wigner functions (as in Fig. 1.5) of a Josephson-photonics device with zero-point fluctuations $\alpha_0 = 1$ for the k-photon resonance, $2eV_{\rm dc} = k \cdot \hbar\omega_a$, where here $k = 3$. Increasing the drive from (a) to (d), the system first shows (a) weak, then (b) more strongly pronounced three-fold symmetric Wigner functions centered around the phase-space origin. (c) Increasing the drive beyond a first threshold will result in three (in general k) fixed points on a circle. (d) Each fixed point splits into two when the system is driven beyond a second threshold. In general, k-photon resonance conditions will yield $\mathbb{Z}^k$-symmetric Wigner functions in the phase space, where the orientation is fixed by the phase η of the drive.

1.4.2 Dissipative Cat Qubits for Quantum Computation

Quantum computers manipulate quantum bits (qubits) to encode and process information in ways that classical computers cannot. Fundamental quantum properties, such as entanglement or superposition, can only be used when the qubits have a sufficiently long coherence time. However, in order to perform quantum computations, the qubits cannot be isolated and any environment induces decoherence and different error channels in the qubits [72].
One countermeasure is quantum error correction [73, 74] that uses many physical qubits to redundantly encode the information of a single logical qubit. Different error channels yield distinguishable signatures (error syndromes). It is possible to identify and correct specific types of errors, such as bit-flip and phase-flip errors, without collapsing the quantum state. Nevertheless, quantum error correction has two major limitations:

- Adding physical bits possibly introduces new decoherence channels.
- The need of multiple physical qubits significantly increases the hardware overhead.

Using a continuous-variable system, like a harmonic oscillator, the two coherent states $|0\rangle = |+\alpha\rangle$ and $|1\rangle = |-\alpha\rangle$ (with the same amplitude $|\alpha|$ but opposite phase) can define the computational basis states of a qubit. The cat states

$$|C_\alpha^\pm\rangle \propto |\alpha\rangle \pm |\alpha\rangle \tag{1.37}$$

then form the complementary basis $|\pm\rangle$. Attractive advantages of using a cavity mode to encode qubits emerge [75–78]:

+ The infinite-dimensional Hilbert space of a resonator can be used to redundantly encode quantum information.

+ When $|\alpha|^2$ is large, the two computational basis states are delocalized in a resonator's phase space.

This delocalization directly leads to the fact that, for cat qubits, bit-flip errors (associated with the Pauli matrix σ_x), where the quantum state of a qubit changes between $|0\rangle \leftrightarrow |1\rangle$, can be exponentially suppressed [78–81]

$$\Gamma_{|0\rangle\leftrightarrow|1\rangle} \propto |\alpha|^2 e^{-2|\alpha|^2} \tag{1.38}$$

when increasing the number of photons $\sim |\alpha|^2$ of the computational basis states. State-of-the-art proposals reach bit-flip times that exceed ten seconds [82]. Consequently, there is less need to correct bit-flip errors, which significantly reduces the hardware overhead of error correction codes [83, 84].

The focus of error correction in cat-qubit systems is thus on correcting phase-flip errors. Such errors are associated with the Pauli matrix σ_z and flip the cat states $|C_\alpha^+\rangle \leftrightarrow |C_\alpha^-\rangle$. Single-photon loss of the resonator induces such phase flips and is the dominant dissipation channel of resonators coupled to an environment. However, it has been shown that the rate of phase flips increases only linearly with the number of photons [78–81],

$$\Gamma_{|C_\alpha^+\rangle\leftrightarrow|C_\alpha^-\rangle} \propto |\alpha|^2 \,. \tag{1.39}$$

Thus, it is beneficial to have a large number of photons, $|\alpha| \gg 1$, which exponentially suppresses bit-flip errors. As an immediate disadvantage, phase-flip errors due to single-photon losses grow linearly and become the dominant type of error. It is possible to stabilize and correct the phase-flip errors of cat states by continuous parity measurements [85, 86]. Nevertheless, the cat mode should have a high quality factor to suppress single-photon losses.

In the following, we will start by defining cat states in more detail and summarize their main properties (Sec. 1.4.2.1). While cat states occur naturally as the ground states of parametric Kerr oscillators [87–89], we focus on dissipative cat states, which emerge as stationary states of a driven damped system (see Sec. 1.4.2.2). In Sec. 1.4.2.3, we will explain why Josephson-photonics devices are an attractive platform for cat qubits states.

1.4.2.1 Cat States Form Qubits for Quantum Computation

The two-legged cat states used for universal quantum computation [76, 77, 90]

$$|C_\alpha^+\rangle = \mathcal{N}_+ \left(|\alpha\rangle + |-\alpha\rangle\right) = \frac{e^{-|\alpha|^2/2}}{\sqrt{2(1+\exp\{-2|\alpha|^2\})}} \sum_{n=0}^{\infty} \frac{2\alpha^{2n}}{\sqrt{(2n)!}} |2n\rangle \tag{1.40}$$

$$|C_\alpha^-\rangle = \mathcal{N}_- \left(|\alpha\rangle - |-\alpha\rangle\right) = \frac{e^{-|\alpha|^2/2}}{\sqrt{2(1-\exp\{-2|\alpha|^2\})}} \sum_{n=0}^{\infty} \frac{2\alpha^{2n+1}}{\sqrt{(2n+1)!}} |2n+1\rangle \tag{1.41}$$

are superpositions of two coherent states

$$|\alpha\rangle = e^{-|\alpha|^2/2} \sum_{n=0}^{\infty} \frac{\alpha^n}{\sqrt{n!}} |n\rangle \tag{1.42}$$

with the same amplitude $|\alpha|$ but opposite phase. They differ in their even and odd photon-number parity [compare Fig. 1.8(d)], which is measured by the parity operator

$$\hat{\Pi} = \sum_{n=0}^{\infty} (-1)^n |n\rangle \langle n| \ . \tag{1.43}$$

Its expectation value is equal to the value of the Wigner function at the origin [compare Fig. 1.8(b,c)]. Two coherent states with the same amplitude but opposite phases are approximately orthonormal when their amplitude is sufficiently large,

$$\langle \alpha | -\alpha \rangle = e^{-2|\alpha|^2} \to 0 \quad (|\alpha| \to \infty) \, . \tag{1.44}$$

Then, they define the two computational basis states

$$|0\rangle_\alpha = \frac{|C_\alpha^+\rangle + |C_\alpha^-\rangle}{\sqrt{2}} \approx |\alpha\rangle \tag{1.45}$$

$$|1\rangle_\alpha = \frac{|C_\alpha^+\rangle - |C_\alpha^-\rangle}{\sqrt{2}} \approx |-\alpha\rangle \tag{1.46}$$

of a logical qubit, with the cat states as the complementary basis $\{|\pm\rangle = |C_\alpha^\pm\rangle\}$.

1.4.2.2 Cat Qubits in Dissipative Systems

In order to generate cat states, a resonator mode $\hat{c}$ must be subject to an effective two-photon drive by a Hamiltonian

$$\hat{H}_{\text{2ph}} = \epsilon_2 (\hat{c}^{\dagger 2} + \hat{c}^2) \, , \tag{1.47}$$

and to an effective two-photon loss with the Lindblad dissipator $\hat{L}_2 = \sqrt{\gamma_2}\hat{c}^2$ [76]. It is easy to see that the coherent states $|\pm\alpha\rangle$ (and all superpositions $c_+ |\alpha\rangle + c_- |-\alpha\rangle$) with

$$\alpha = \sqrt{\frac{2\epsilon_2}{\hbar\gamma_2}} e^{-i\pi/4} \tag{1.48}$$

are the stationary states of the Lindblad master equation that incorporates the two-photon drive and two-photon dissipation. This can be achieved by coupling the cat mode $\hat{c}$ to a buffer mode $\hat{b}$ that is additionally linearly driven by an ac microwave signal. The effective Hamiltonian

$$\hat{H}_{\text{2ph}}^{\text{eff}} = (\hbar g_2 \hat{b} \hat{c}^{\dagger 2} + E_{mw} \hat{b}^\dagger) + \text{h.c.} \tag{1.49}$$

engineers two-photon drive and two-photon loss for the high-Q cat mode $\hat{c}$ (hosting long-living cat states):

- Two photons can be created in resonator $\hat{c}$ by annihilation of a photon in mode $\hat{b}$. This process is possible because $\hat{b}$ is driven by a microwave signal and therefore weakly occupied. Without the drive, the buffer mode would be in the ground state and the Hamiltonian processes would be absent.
- The reverse Hamiltonian process $\propto \hat{b}^\dagger \hat{c}^2$ annihilates two photons by creating one excitation in resonator $\hat{b}$. Since $\hat{b}$ has a low quality factor, it directly emits the excitation into the environment with single-photon loss rate γ_b and engineers a two-photon loss of the cat mode $\hat{c}$ with an effective rate

$$\gamma_2 = \frac{4g_2^2}{\gamma_b}\,. \tag{1.50}$$

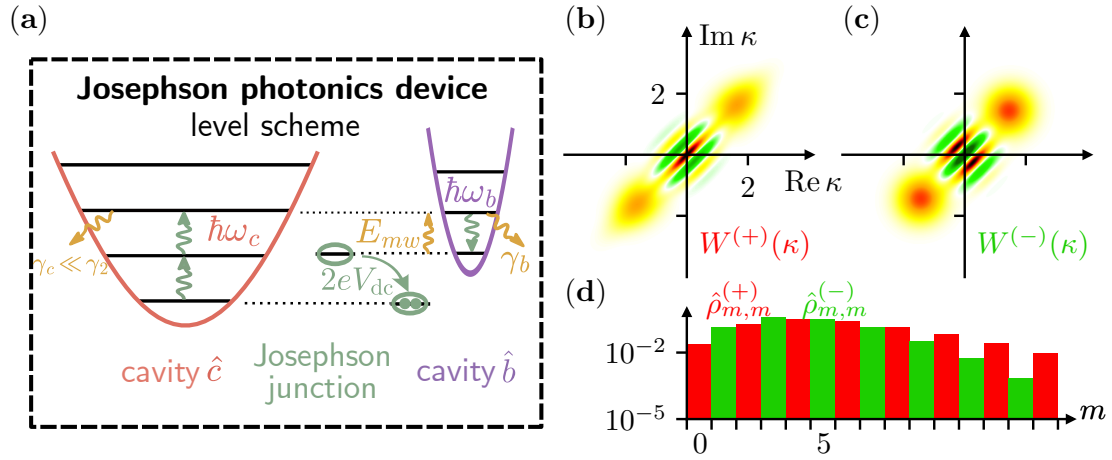

Figure 1.8: Creation of cat states with Josephson-photonics devices. (a) When the dc voltage is set to $2eV_{\rm dc} \approx 2\omega_c - \omega_b$, each tunneling Cooper pair creates two photons in the cat cavity $\hat{c}$ by annihilating one photon from the buffer mode $\hat{b}$, which is directly driven by a resonant microwave signal with strength E_{mw} sent through the transmission line. The direct microwave drive enables the forward tunneling process of Cooper pairs, creating an effective two-photon drive of the high-Q cat cavity. The back-tunneling process enables an effective two-photon loss (with rate $\gamma_2 \gg \gamma_a$, see main text) by the annihilation of two $\hat{c}$-photons together with the creation and fast emission of a photon in the low-Q buffer mode (with large single-photon loss rate γ_b). The steady-state Wigner function $W(\kappa)$ of the cat cavity in the phase-space (spanned by $\kappa = x_c + ip_c$) is close to (b) the $|C_\alpha^+\rangle$ cat state when starting in the ground state, $|0\rangle_c\,(t=0)$, or (c) the $|C_\alpha^-\rangle$ cat state when starting in the state $|1\rangle_c\,(t=0)$. In (b), larger zero-point fluctuations $\kappa_0 = 0.4$ show a weak deformation of the distribution around the fixed points with opposite phase, which is nearly not noticeable in (c) where $\kappa_0 = 0.15$. The even/odd parity of the state $W^{(\pm)}(\kappa)$ is directly connected to the value $\pi\hbar W^{(\pm)}(\kappa=0) = \langle\hat{\Pi}\rangle = \pm 1$ at the origin and (d) to the population of only even/odd Fock states.
[Other parameters: $E_{mw} = E_J^*\kappa_0^2\beta_0 = 0.135\hbar\gamma_b$, $\delta_{\rm dc} = \delta_{mw} = 0$, $\eta = \phi_{mw} = 0$, $\beta_0 = 0.3$. (See Fig. 1.5 for color scale of Wigner functions.)]

1.4.2.3 Dissipative Cat Qubits in Josephson-Photonics Devices

Cat states can be realized in Josephson-photonics devices (see Fig. 1.8) by a circuit that consists of a low-Q buffer mode $\hat{b}$ (with eigenfrequency ω_b, loss-rate γ_b and

zero-point fluctuations β_0) and a high-Q cat cavity $\hat{c}$ (with eigenfrequency ω_c, loss-rate γ_c and zero-point fluctuations κ_0). The effective two-photon processes can be created by applying the resonance condition [12, 48]

$$2eV_{\rm dc} \approx \hbar(2\omega_c - \omega_b)\,, \tag{1.51}$$

such that each tunneling Cooper pair will effectively create two photons in cavity $\hat{c}$ by annihilating one excitation from cavity $\hat{b}$. An additional microwave drive for the buffer mode can be realized by sending an ac signal through the transmission line, such that the coupling scenario corresponds to a Hamiltonian contribution of the form

$$\hat{x}_{mw} \propto \left[\hat{m}^\dagger e^{i(\omega_{mw}t+\phi_{mw})} + \hat{m}e^{-i(\omega_{mw}t+\phi_{mw})}\right]\,. \tag{1.52}$$

Within rotating-wave approximation, the Hamiltonian of a Josephson-photonics device then takes the form (compare Sec. 1.3.3)

$$\begin{aligned}\hat{H}_{\rm cat} =& \hbar\delta_{mw}\hat{b}^\dagger\hat{b} + \hbar\frac{\delta_{\rm dc}+\delta_{mw}}{2}\hat{c}^\dagger\hat{c} + E_{mw}(e^{-i\phi_{mw}}\hat{b}^\dagger + e^{i\phi_{mw}}\hat{b}) \\ &+ \frac{E_J^*\beta_0\kappa_0^2}{4} : (ie^{-i\eta}\hat{b}^\dagger\hat{c}^2 - ie^{i\eta}\hat{b}\hat{c}^{\dagger 2})\frac{J_1(2\beta_0\sqrt{\hat{b}^\dagger\hat{b}})}{\beta_0\sqrt{\hat{b}^\dagger\hat{b}}}\frac{J_2(2\kappa_0\sqrt{\hat{c}^\dagger\hat{c}})\cdot 2}{\kappa_0^2\sqrt{\hat{c}^\dagger\hat{c}}^2} :\,,\end{aligned} \tag{1.53}$$

where $E_J^* = E_J e^{-(\beta_0^2+\kappa_0^2)/2}$. The detuning of the microwave drive and the dc voltage, respectively, are defined by $\delta_{mw} = \omega_b - \omega_{mw}$ and $\delta_{\rm dc} = 2\omega_c - \omega_b - \omega_{\rm dc}$.

In order to implement a stable cat state and fast quantum gates [76], the platform should ideally have the following properties:

- The effective two-photon loss rate γ_2 should be large.
- Since single-photon losses induce phase flips, the cat mode $\hat{c}$ should exhibit a low single-photon loss rate $\gamma_c \ll \gamma_2$.
- Kerr and cross-Kerr terms introduce amplitude-dependent dephasing and distortions. Thus, they are among the most harmful parasitic processes that hamper cat-state generation and should be carefully suppressed.

Proposal	**Amplitude g_2**	**Parasitic Kerr terms**
transmon	$\propto \frac{E_J\beta_0\kappa_0^2}{\hbar}\epsilon_p$	$\hat{c}^{\dagger 2}\hat{c}^2$, $\hat{b}^{\dagger 2}\hat{b}^2$, $\hat{b}^\dagger\hat{b}\hat{c}^\dagger\hat{c}$
asymmetrically-threaded SQUID	$\propto \frac{E_J\beta_0\kappa_0^2}{\hbar}\epsilon_p$	suppressed by symmetries
autoparametric	$\propto \frac{E_J\beta_0\kappa_0^2}{2\hbar}$	$\hat{c}^{\dagger 2}\hat{c}^2$, $\hat{b}^{\dagger 2}\hat{b}^2$, $\hat{b}^\dagger\hat{b}\hat{c}^\dagger\hat{c}$
Josephson-photonics devices	$\propto \frac{E_J\beta_0\kappa_0^2}{\hbar}$	no parasitic Kerr terms

Table 1.2: State of the art of dissipative cat qubits. Proposals either use a transmon configuration [77], an asymmetrically-threaded SQUID [78], or an autoparametric superconducting circuit [79] to create the effective Hamiltonian from Eq. (1.49). Except for Josephson-photonics devices [12, 48], the proposal are either constrained by an ac pump signal $\epsilon_p \ll 1$, strongly limiting the effective two-photon driving amplitude g_2, or they introduce parasitic Kerr terms.

In the Josephson-photonics platform, the driving strength $g_2 = E_J^* \beta_0 \kappa_0^2 / \hbar$ of the two-photon generation and dissipation process is not limited by a small pump power $\epsilon_p \leq 1/10$, unlike other systems, c.f. Tab. 1.2. As a direct advantage, according to the arguments presented in [48], the two-photon loss rate can be increased by a factor of 100 compared to other setups, such that the two-photon loss can be engineered 1000 times larger than the single-photon loss rate, $\gamma_2 \sim 10^3 \gamma_c$, significantly reducing phase-flip errors. Also, Kerr terms do not exist, such that the dc-driven cat qubit is protected against such parasitic nonlinearities. However, Josephson-photonics devices suffer from a detrimental drawback (see Sec. 1.7). The dc voltage lacks a stable reference phase. Due to voltage noise, the microwave cavities have a neutrally stable phase-space angle, and the Josephson-photonics device therefore suffers from dephasing. In Sec. 4.2.3, we thus use injection locking (compare Sec. 2.1) to stabilize the phase of a cat state, enabling their usage in quantum computing.

1.5 Josephson-Photonics Devices as Versatile Sources of Microwave Photons

Josephson-photonics devices can generate stationary states with strong quantum properties in the resonators. In addition, the photons emitted from the microwave cavities have interesting quantum features and can be used in applications. Here, we first highlight the application of Josephson-photonics devices as a signal photon source emitting antibunched photons (Sec. 1.5.1), which will show the influence of zero-point fluctuation on the internal system dynamics. Additionally, we show in Sec. 1.5.2 how photons emitted by two-mode squeezed states can be used in a quantum radar.

1.5.1 Single-Photon Source and the Role of Zero-Point Fluctuations

The k-photon resonance condition, where each forward (backward) tunneling Cooper pair effectively creates (annihilates) k excitations in the cavity, is nicely reflected in the powers of creation and annihilation operators, $\left(\hat{a}^k + \hat{a}^{\dagger k}\right)$ in the Hamiltonian. These operators are amended by normally-ordered Bessel functions, which themselves are diagonal in the Fock basis and describe nonlinear higher-order processes involving multiple virtual cavity photons. The nonlinear driving terms can be understood by analogy to the Franck-Condon effect that describes vibronic transitions in molecules [see Fig. 1.9(a)]. The Josephson driving Hamiltonian of a single-mode device can be expressed as a displacement operator

$$\hat{H}_J \propto \hat{D}_1(i\alpha_0) + \hat{D}_1^\dagger(i\alpha_0) \tag{1.54}$$

with $\hat{D}_1(i\alpha_0) = e^{i\alpha_0(\hat{a}^\dagger + \hat{a})}$. As explained in Fig. 1.9(a), the intensity of transitions between two vibronic energy states ν and ν' depends on the overlap of their displaced wave functions, $I \propto |\langle \nu'| \hat{D}_1(\Delta q) |\nu\rangle|^2$, where Δq is the relative distance between the two nuclei of the molecule. For the Josephson driving Hamiltonian, we can equivalently calculate the overlap $\langle n| \hat{D}_1(i\alpha_0) |m\rangle$ between two Fock states. Here, the zero-point fluctuations assume the role of the shift in distance between the nuclei of the molecule in Fig. 1.9(a). For specific values of the zero-point fluctuations, the transitions between different energy levels can be blocked in Josephson-photonics devices. To be precise, we calculate the nonzero (normalized) transition matrix elements

$$T_{m+k,m} = \langle m+k| : \hat{a}^{\dagger k} \frac{J_k(2\alpha_0\sqrt{\hat{a}^\dagger \hat{a}}) \cdot k!}{\alpha_0^k \sqrt{\hat{a}^\dagger \hat{a}}^k} : |m\rangle = \frac{L_m^{(k)}(\alpha_0^2)}{L_m^{(k)}(0)} \cdot \langle m+k| \hat{a}^{\dagger k} |m\rangle \tag{1.55}$$

for the k-photon resonance condition of a single-mode Josephson-photonics device. We find that the matrix entries of the powers of the creation operator, $\langle m+k| \hat{a}^{\dagger k} |m\rangle = \sqrt{(m+k)!/m!}$ are modified by generalized Laguerre polynomials.

Specifically, we choose the single-photon resonance condition ($k = 1$), where each tunneling Cooper pair creates one photonic excitation in the microwave cavity, Fig. 1.9(b). The Hamiltonian drives transitions between neighboring Fock states $|m\rangle$ and $|m+1\rangle$. While the transition between the ground state $|0\rangle$ and the first excited state $|1\rangle$ depends only trivially on the zero-point fluctuations, $T_{1,0} = 1$,

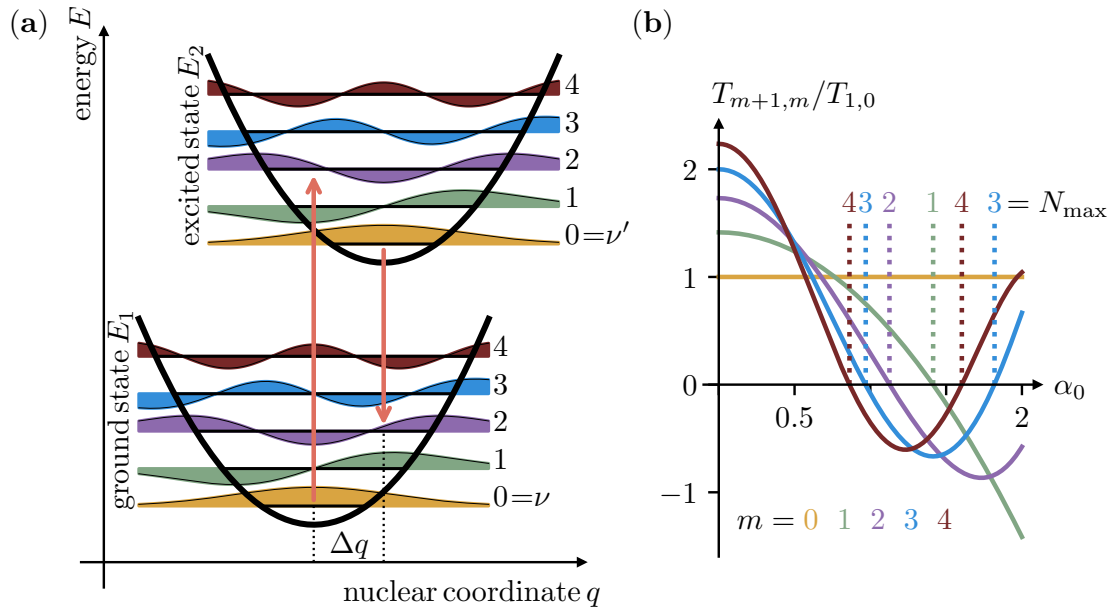

Figure 1.9: (a) Franck-Condon principle. The electronic ground state E_1 and excited state E_2 of a molecule is depicted. Its internal energy can be changed by vibronic excitations (labeled with ν for the electronic ground state and ν' for the first electronic excited state) describing oscillations of the nuclei. The vibronic states are here approximated as wave functions of a harmonic oscillator. Electronic transitions occur at a significantly faster rate than vibronic transitions due to the heavy mass of the nuclei compared to electrons, such that during an electronic transition the distance between the nuclei can be assumed constant. The electronic transitions can therefore be drawn as a vertical arrow in the energy diagram and involve vibronic transitions between states ν of the electronic ground state and ν' of the electronic excited state. The Franck-Condon principle explains that the intensity $I \propto |\langle \nu' | \hat{D}(\Delta q) | \nu \rangle|^2$ of an electronic transition strongly depends on the overlap between the involved vibronic energy levels. Since the ground state of a harmonic oscillator ($\nu = 0$) has no nodes, its overlap with any other Fock state is always nonzero. In contrast, vibronic transitions that do not involve the ground state can have zero overlap and may be blocked at specific nuclear distances. (b) Hamiltonian transition matrix elements $T_{m+k,m} = \langle m+k | \hat{D}(i\alpha_0) | m \rangle$ of a Josephson-photonics device [here shown for the single-photon resonance, $k = 1$, c.f. Eq.(1.55)] depend, analogously to Franck-Condon physics, on the overlap between displaced Fock states. The strength of the zero-point fluctuations determine the transition amplitude to higher Fock states, which can be blocked when α_0 is a root of the respective matrix element (indicated by dashed vertical lines). The Josephson-photonics device reduces to an effective $(N_{\max}+1)$-level system, when the cavity is initially in the ground state. An effective two-level system can be engineered by a microwave cavity with $\alpha_0 = \sqrt{2}$ (green line).

all other transition matrix elements between neighboring Fock states depend on Laguerre polynomials.

For instance, the transition between the first and second excited state

$$T_{2,1} = \sqrt{2}\frac{L_1^{(1)}(\alpha_0^2)}{L_1^{(1)}(0)} = \frac{2-\alpha_0^2}{\sqrt{2}}$$

can be blocked by fabricating $\alpha_0 = \sqrt{2}$. Compared with Fig. 1.9(a), this means

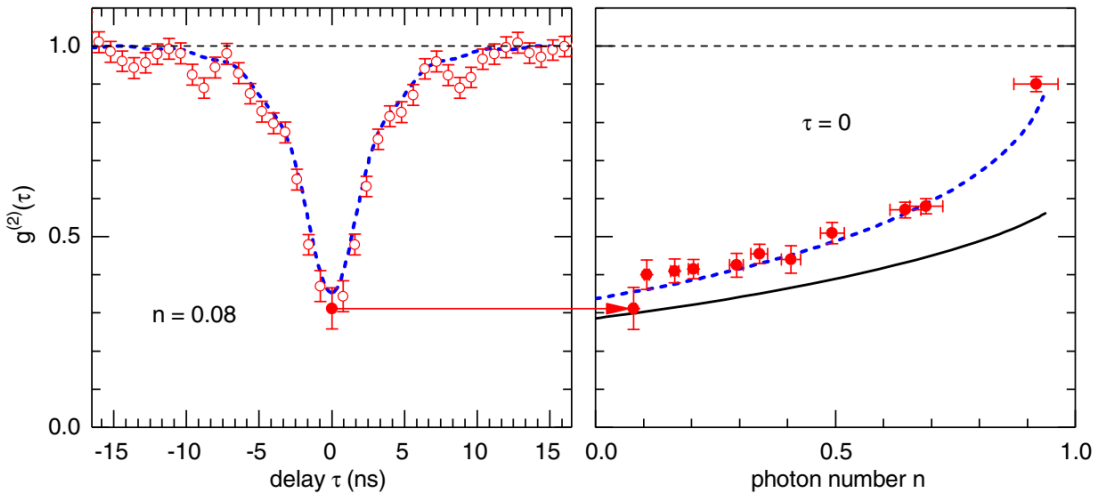

Figure 1.10: (Left) The measured (red dots) and theoretical (blue dashed line) intensity correlation function $g^{(2)}(\tau) = \langle \hat{a}^\dagger(0)\hat{a}^\dagger(\tau)\hat{a}(\tau)\hat{a}(0)\rangle / \langle \hat{a}^\dagger\hat{a}\rangle^2$ for a Josephson-photonics device with a single microwave cavity with zero-point fluctuations $\alpha_0 \approx 0.98$ and mean steady-state occupation of $n = \langle \hat{a}^\dagger\hat{a}\rangle = 0.08$ shows a strong suppression at $\tau = 0$, which indicates photon antibunching. (Right) The value $g^{(2)}(\tau = 0)$ as a function of mean cavity occupation n. The black line is a theoretical prediction without accounting for the finite detection bandwidth of the experiment.
[Reprinted figure with permission from C. Rolland, A. Peugeot, S. Dambach, M. Westig, B. Kubala, Y. Mukharsky, C. Altimiras, H. le Sueur, P. Joyez et al., *Physical Review Letters* **122**, 186804 (2019). Copyright (2019) by the American Physical Society; included in this thesis as reference [10].]

that the state $|\nu' = 1\rangle$ is shifted by just the right amount, such that its overlap with the state $|\nu = 2\rangle$ vanishes. When the system is initially prepared in the ground state, the only accessible energy levels are the Fock states $|0\rangle$ and $|1\rangle$. It thus behaves like a qubit that is well protected from unwanted excitations to higher energy levels.

A signature of this effect is the suppression of the two-time intensity correlation function $g^{(2)}(t + \tau, t)$ [65] at zero time delay $\tau = 0$ (see Fig. 1.10), which means that the probability of two photon detection events at the same time is strongly reduced. The system thus emits antibunched photons and thus constitutes a bright but non-deterministic single-photon source [10, 22, 31, 32]. However, compared to alternative schemes based on superconducting qubits [91–96], Josephson-photonics devices do not require a complex pulse sequence to generate antibunched photons. By choosing specific roots of higher-order Laguerre polynomials, $L^{(1)}_{N_{\max}}(\alpha_0^2)$, an $(N_{\max} + 1)$-level system can be fabricated [10, 37, 44]. The advantage of the possibility of blocking specific Hamiltonian transitions will, for example, be exploited in Pub. (*iv*) (see Sec. 5.1.1) in order to be able to detect single microwave photons.

1.5.2 Quantum Radar as an Application of Two-Mode Squeezing

When the dc voltage is tuned to the resonance condition $2eV_{\mathrm{dc}} \approx \hbar(\omega_a + \omega_b)$ [see Fig. 1.11(a)] in a Josephson-photonics device containing two resonators $\hat{a}$ and $\hat{b}$, the Hamiltonian is given by

$$\hat{H} \approx \hbar\delta_{\mathrm{dc}} \frac{\hat{a}^\dagger\hat{a}+\hat{b}^\dagger\hat{b}}{2} + \frac{E_J^*\alpha_0\beta_0}{2} :\left(\hat{a}\hat{b}e^{-i\eta}+\hat{a}^\dagger\hat{b}^\dagger e^{+i\eta}\right) \frac{J_1\left(2\alpha_0\sqrt{\hat{a}^\dagger\hat{a}}\right)}{\alpha_0\sqrt{\hat{a}^\dagger\hat{a}}} \frac{J_1\left(2\beta_0\sqrt{\hat{b}^\dagger\hat{b}}\right)}{\beta_0\sqrt{\hat{b}^\dagger\hat{b}}}: \,. \tag{1.56}$$

A tunneling Cooper pair creates two photons with frequency $\omega_1 \approx \omega_a$ in cavity $\hat{a}$ and $\omega_2 \approx \omega_b$ in cavity $\hat{b}$. Although the frequencies ω_1 and ω_2 of the two photons vary for each tunneling process, their sum is fixed and exactly matches the excess energy of each tunneling event, $\omega_1 + \omega_2 = 2eV_{\mathrm{dc}}$. The Cooper pairs therefore create correlations and, indeed, frequency entanglement between the resonators. The stationary states of the resonators are two-mode squeezed and thus number-correlated [11, 19, 29, 33, 36, 37]. Two-mode squeezed microwave light is more commonly generated by three- or four-wave mixing in Josephson parametric amplifiers, Josephson parametric converters, or Josephson traveling wave parametric amplifiers that require an ac-pump signal and parametric downconversion [4, 97, 98]. Instead, a Josephson-photonics device uses a dc voltage to generate entangled states of light.

An entanglement witness is the visible squeezing in the phase space. The total Wigner function depends on two quadratures of both cavities and is defined on a four-dimensional phase space. For visualization purposes, six two-dimensional marginal phase spaces can be defined by integrating the total Wigner function over the other two quadrature variables [compare Figs. 1.11(b,c)]. The Hamiltonian process contains a two-mode squeezing operation $\propto \hat{a}^\dagger\hat{b}^\dagger e^{i\eta} + \mathrm{h.c.}$ that depends on the relative phase η and acts in the joined Hilbert space of both microwave modes. Thus, it entangles their quantum states. Since no processes that act only on a single mode, such as a single-mode squeezing operation $\propto \hat{a}^{\dagger 2} + \mathrm{h.c.}$, are present, the reduced quantum state of both cavities is rotationally symmetric; in fact, it is a thermal state with fluctuations larger than the vacuum state, c.f. Fig. 1.11(b). Therefore, no information about entanglement can be accessed through the marginal Wigner function of each individual resonator. Instead, squeezing is only visible in a mixed marginal phase space, Fig. 1.11(c).

Beyond their application in parametric amplifiers [99], this fact enables the usage of two-mode squeezed states for a wide range of quantum information tasks, such as in protocols for quantum key distribution [100, 101], quantum sensing [102, 103], quantum teleportation [5, 104] and secure remote state preparation [105]. Here, we want to present one specific possible application, the quantum radar [60, 61].

A (classical) radar sends out microwaves that are reflected by an object and recorded. From the received signal, information about the distance, the direction and the velocity of the object can be obtained. In a classical radar, the recorded signal (with frequency $\sim \nu_{mw}$ in the microwave range) is strongly overlayed by

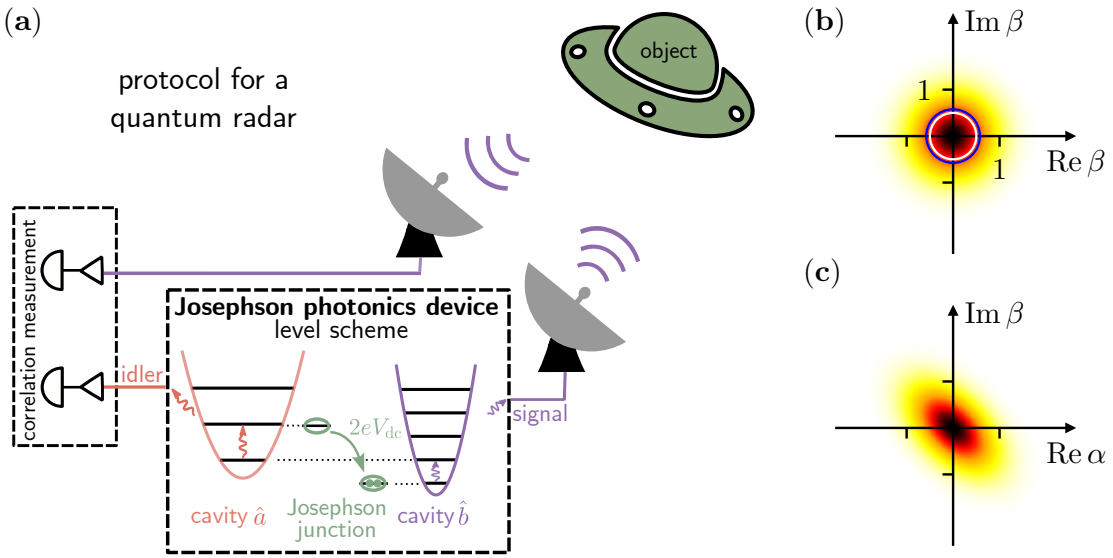

Figure 1.11: Quantum radar as application of two-mode squeezing. (a) A Josephson-photonics device, where two microwave modes with eigenfrequencies $\omega_{a/b}$ and effective single-photon loss rates $\gamma_{a/b}$ are connected to a Josephson junction, is dc-voltage biased at the resonance condition $2eV_{\rm dc} \approx \hbar(\omega_a + \omega_b)$. Each tunneling Cooper pair then effectively creates one excitation in each cavity. Photons leaking from the cavities could be used in a protocol for a quantum radar. While an idler photon (leaked from cavity $\hat{a}$) is kept, a photon from cavity $\hat{b}$ is emitted by an antenna as signal into the environment. When reflected by an object, the signal photon can be absorbed. When signal and idler are simultaneously measured, the quantum radar can theoretically achieve a 6 dB signal-to-noise improvement compared to classical radars, which send/receive a strong electromagnetic wave. (b) The steady-state Wigner function of a single cavity (here the signal cavity $\hat{b}$) shows a thermal distribution with larger quadrature standard deviation (c.f. blue circle) than vacuum fluctuations (white circle). The sent thermal state appears for the object as part of the background radiation. (c) Squeezing, that arises from the photon-pair production in different cavities by a single tunneling Cooper pair, is hidden in the mixed phase space. Its phase-space angle depends on the relative phase η of the coherent Hamiltonian process. Squeezing is only observable upon correlation measurement of signal and idler.
[Parameters: $\gamma_a = \gamma_b$, $\alpha_0 = \beta_0 = 1/10$, $E_J^* = 500\hbar\gamma_a$, $\delta = 0 = \eta$. (See Fig. 1.5 for color scale of Wigner functions.)]

thermal background radiation at room temperature $T_{\rm RT}$ because $k_B T_{\rm RT} \gg h\nu_{mw}$. This implies that a strong signal must be used. Thus, a classical radar of this type cannot be used for covert detection. The object being monitored can detect the signal and implement countermeasures. In addition, jamming of the signal frequency with other electromagnetic radiation becomes possible.
To understand the principle of a quantum radar, we first consider a single entangled pair of photons [see Fig. 1.11(a)]. One photon is sent out (signal photon) like in a classical radar, but the second photon (idler) is kept. Upon receiving a signal, the sent signal photon can be identified by a coincidence measurement with the idler photon, whereby background photons arriving at other times can be eliminated. The theoretically proposed quantum illumination protocols use two-mode squeezed states that can be created, for instance, by a Josephson-photonics device, where the

quantum states of the microwave cavities are emitted into transmission lines, and the signal line is fed onto the object. The quantum state of each individual mode looks thermal, and entanglement is hidden in the mixed marginal phase space. As a first direct advantage, true covert observation becomes possible because the object cannot distinguish the sent signal from the background radiation. To exploit the full quantum advantage, a correlation measurement of signal and idler is required.

Early-stage experimental realizations of quantum radars present a proof of concept of the protocols and can claim to show quantum advantage [7], but also suffer from technological challenges [106–111]:

+ Improved signal-to-noise ratio for weak signal strengths

  Quantum radars show enhanced detection efficiency when operated in environments with weak signal strength compared to a bright background noise by exploiting quantum entanglement. Therefore, they are only marginally affected by signal jamming. The advantage is still preserved by residual quantum correlations even when entanglement is mainly lost.

+ No possibility of interception

  Since entanglement is hidden in the mixed phase space, the sent signal looks thermal and covert observation is possible because the monitored object cannot distinguish the signal from background radiation.

+ Increased information per measurement

  Exploiting quantum correlations, a measurement in quantum radars can potentially gather more information than in classical radars.

− Technological effort

  The generation of two-mode squeezed states requires quantum systems controlled in cryostats at millikelvin temperatures. Sending entangled microwaves into and receiving them from a room-temperature environment without heating the cryostat is a pressing issue. The need of quantum memories to store the idler state, while the signal travels to the object and back, increase the technological effort.

− Recent experiments only allow short-range detection

  The maximal achievable coherence times of quantum memories significantly limit the detection distance. Recent experiments with an object at room temperature could demonstrate a working setup in detection ranges of approximately one meter [107], using a simple delay line instead of a quantum memory.

− Unknown signal arrival time

  To exploit quantum advantage, the signal and idler photon should be measured at the same time. Quantum radars, therefore, typically require knowledge of the expected arrival time or have to perform sweeps prolonging the time till an object can be detected. Current experiments only use quantum radars to determine whether an object is present in a specific position of interest.

1.6 Josephson-Photonics Devices as Detectors of Microwave Photons

The reliable detection of single microwave photons is an open topic. Typical energy scales are in the gigahertz range, and thus multiple orders of magnitude smaller than optical photons with energies in the order of terahertz. Whereas optical detectors, such as avalanche photodiodes or superconducting nanowire single-photon detectors [112, 113] rely on the strong impact of a single impinging optical photon and operate at room temperature, microwave photon detection is fundamentally more challenging. The weaker impact of microwave photons requires highly sensitive detectors that have to operate at millikelvin temperatures and low noise levels. Single-photon detectors in the microwave regime are an essential ingredient to enable a number of protocols of quantum information, quantum communication, and quantum sensing, such as improved sensing of signals from electron-spin resonance [114, 115], the detection of Josephson radiation [116], the measurement-based remote entanglement [117] and readout [118, 119] of superconducting qubits and the fundamental physics quest for detecting axions [120–122].

Various schemes for single microwave-photon detection have been proposed and experimentally implemented (for more information, see the reviews in [123–125]). They comprise threshold detectors, where an impinging photon switches a current biased Josephson junction into the resistive state [122, 126–130], and various setups where the photon is absorbed in a microwave cavity and interacts with a quantum system whose state can be measured [131–135]. The properties of these schemes are tailored to meet various requirements. However, each scheme has their individual drawback: Nonlinear or non-unitary detectors map all incoming states onto the same output state and are typically gated or must be reset. Therefore, they suffer from dead time and lack photon-number sensitivity. The latter is currently also true for more linear bolometers [116, 119, 136–138]. Only for pulses arriving at a predetermined time, it has been possible to distinguish between different photon-number states. Likewise, different schemes report different achievable efficiencies of photon detection, dark count rates or dead time and may excel in some of these criteria, while lacking in others.

Recently, a Josephson-photonics setup, known as the Inelastic Cooper Pair Tunneling Photon Multiplier (ICTPM) [13, 41, 51], has been put forward as a promising candidate for single microwave-photon detection. Number multiplication has been studied theoretically and implemented for continuous coherent-wave input that uses two microwave modes which are connected in series to a dc-biased Josephson junction and coupled to transmission lines, Fig. 1.12. Similarly to the idea of cat-state generation in Sec. 1.4.2 (for details, see Secs. 1.3.2 and 1.3.3), a dc voltage bias at $2eV_{\mathrm{dc}}/\hbar = n\omega_b - \omega_a$ yields the Hamiltonian

$$\hat{H} \approx \frac{E_J^* \alpha_0 \beta_0^n}{2n!} (\hat{a}\hat{b}^{\dagger n} + \hat{a}^\dagger \hat{b}^n) \,. \tag{1.57}$$

In the steady state, both cavities are in the vacuum state. The Josephson junction only drives photon conversion processes between the two resonators and no direct photon excitations. When a single resonant microwave photon impinges from the left transmission line onto the system, it can be resonantly absorbed by cavity $\hat{a}$,

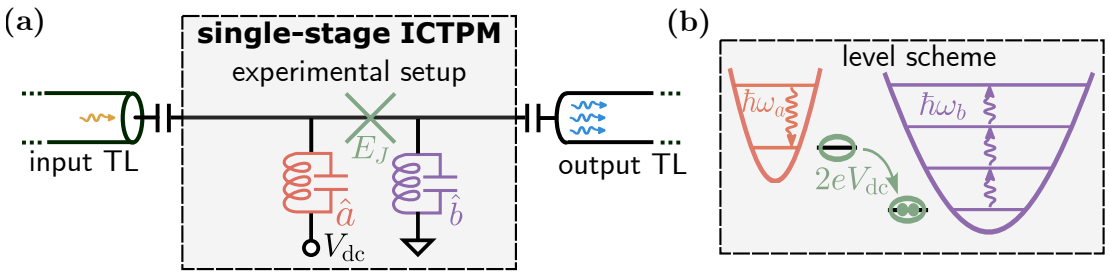

Figure 1.12: (a) The single-stage Inelastic Cooper Pair Tunneling Photon Multiplier (ICTPM) consists of two microwave cavities, which are connected in series to a dc-voltage biased Josephson junction. Both cavities are capacitively coupled to transmission lines (TL). (b) When the circuit is biased at resonance $2eV_{\mathrm{dc}} + \hbar\omega_a \approx n\omega_b$ (shown for $n = 3$), a tunneling Cooper pair converts one excitation in cavity $\hat{a}$ into n excitations in cavity $\hat{b}$. Without input, both cavities are in the ground state. When a single microwave photon impinges on the system from the input transmission line, it can be resonantly absorbed by cavity $\hat{a}$ and the conversion process driven by the junction transfers the excitation to cavity $\hat{b}$, which emits n photons in the output transmission line. Deterministic conversion to n outgoing photons (with vanishing reflection of the photon at cavity $\hat{a}$) can be achieved for resonant input [41].

which enables a photon multiplication process driven by the Josephson junction: a tunneling Cooper pair annihilates one photon from cavity $\hat{a}$ and creates n photons in cavity $\hat{b}$. Photons can then leak from cavity $\hat{b}$ into the right transmission line and subsequently be measured in an experiment by heterodyne detection of the quadratures (compare Sec. 3).

In order to enhance photon detection efficiency, the photon multiplication process must be efficient such that a high probability of photon conversion is achieved, leading to the following considerations:

- Direct reflection of the incoming signal at cavity $\hat{a}$ must be avoided.
- When cavity $\hat{b}$ has leaked one photon into the right transmission line, the reverse Hamiltonian process, where Cooper pairs tunnel against the bias and (re)-create a photon in cavity $\hat{a}$ by annihilating n photons from cavity $\hat{b}$, is off-resonant and energetically forbidden. Resonator $\hat{b}$ then emits all n photons into the right transmission line.
- Before the cavity $\hat{b}$ emits a photon, the reverse conversion process is possible, where a photon in cavity $\hat{a}$ is created and n cavity-$\hat{b}$ photons are annihilated. Subsequent photon emission from cavity $\hat{a}$ into the left transmission line will lead to signal loss and must be avoided.
- An analysis [41] has shown that perfect photon conversion is possible for an impinging weak and perfectly resonant continuous-wave microwave signal. An impedance-matching argument yields the optimal Josephson-driving strength

$$E^*_{J,\mathrm{opt}} = \frac{\hbar\sqrt{\gamma_a\gamma_b}}{\alpha_0\beta_0^n}\sqrt{n\cdot n!}\,, \tag{1.58}$$

for which such perfect photon conversion is realized.

- For single-photon input, both resonators can effectively be treated as two-level systems with states $\{|0\rangle_a, |1_a\rangle\}$ and $\{|0_b\rangle, |n_b\rangle\}$. An analytic expression for the frequency-dependent transmission function can then be derived [41].

Multiplication factors $n \leq 4$ are realistic for experiments. For larger n, the dc voltage becomes much larger than the eigenfrequencies involved and spontaneous excitation of the modes becomes more likely. This in turn triggers the Hamiltonian multiplication process without an incoming signal and would result in a dramatic increase of dark counts. The problem can be circumvented by implementing a device with two or more multiplication stages.

The two-stage ICTPM extends the single-stage multiplier by a second circuit (see Fig. 9 from Pub. (*iv*) in Sec. 5.1.1). In the first circuit, photon multiplication with a factor n_1 is achieved between cavities $\hat{a}$ and a high-quality central resonator $\hat{c}$. The second multiplication stage converts each excitation from $\hat{c}$ to n_2 excitations in $\hat{b}$. Again, perfect photon conversion can be achieved by tuning the Josephson energies [41]. In contrast to single-stage multiplication, where the Bessel nonlinearities in Eq. (1.57) can be neglected (compare Sec. 1.5.1 where we show that the transition from vacuum to the level $|n_b = n\rangle$ is unaffected for a driving $\propto \hat{b}^{\dagger n} + \text{h.c.}$), cavity $\hat{c}$ is occupied up to Fock state $|n_c = n_1\rangle$. The transitions between cavity $\hat{c}$ and $\hat{b}$ are influenced by zero-point fluctuations even for single-photon input into cavity $\hat{a}$. Internal dynamics, such as Rabi oscillations of excitations between cavities $\hat{b}$ and $\hat{c}$ yields markedly different physics and more complicated dynamics.

The fundamentally novel scheme for photon detection in an ICTPM has so far only been studied for classical input, i.e. coherent continuous-wave signals. Pub. (*iv*) (see Sec. 5.1.1) analyzes the single- and two-stage device for true quantum input (single-photon wavepackets) and presents a scheme for the detection of Gaussian single-photon pulses by heterodyne quadrature measurement. The theoretical ingredients to simulate temporal quantum pulses and heterodyne quadrature measurement are summarized in Sec. 3. The ICTPM can be combined with other novel detection schemes in Josephson-photonics devices, where (higher-order) resonances similar to the condition above mimic photon avalanches, or in setups that involve a spectator cavity and realize strong projective measurement of a resonator, and thus promise to outperform existing microwave photon detection schemes.

1.7 Phase Instability in Josephson Photonics

The applications and quantum states discussed above, e.g., cat states (Sec. 1.4.2), k-fold symmetric states (Sec. 1.4.1), or two-mode squeezed states for a quantum radar (Sec. 1.5.2) crucially rely on a stable phase-space angle of the quantum states in order to exploit quantum properties like entanglement or coherent superpositions. For instance, the symmetry of the k-fold symmetric quantum states manifests itself in finite expectation values $\langle \hat{a}^k \rangle$, while two-mode squeezed states possess finite expectation values like $\langle \hat{a}\hat{b} \rangle$ that depend on the relative phase between the cavities. The phase-space angle for $k = 1$ or the squeezing direction for $k = 2$ are directly related to the phase of expectation values $\langle \hat{a} \rangle$ or $\langle \hat{a}^2 \rangle$, respectively.

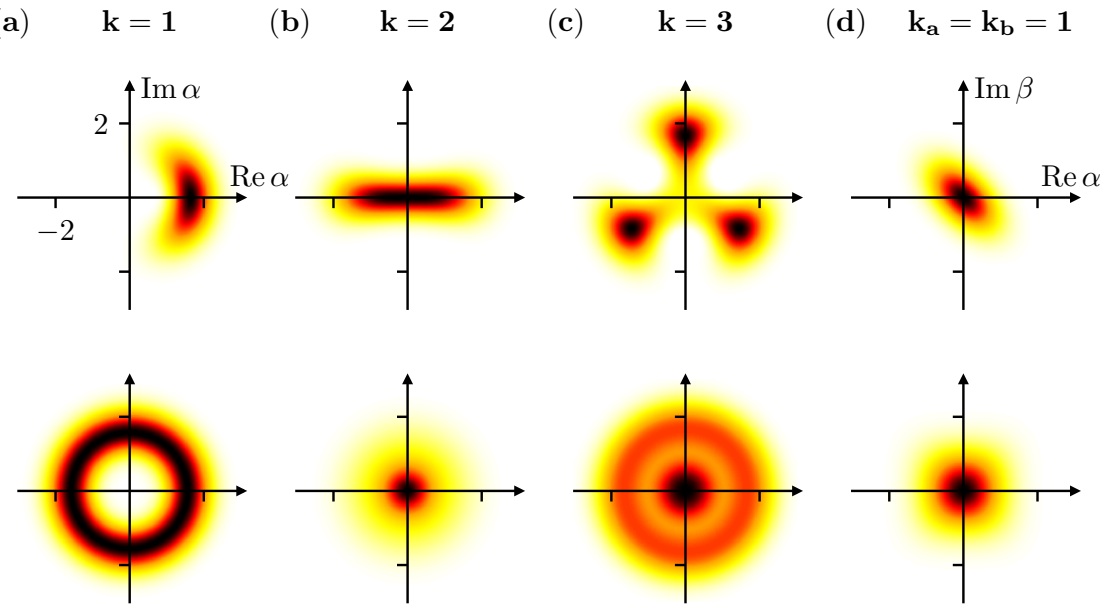

Figure 1.13: Phase instability in Josephson photonics. (Top row) A fixed dc voltage is associated with a driving phase $2eV_{\mathrm{dc}}t/\hbar - \eta$, which becomes the constant η in the rotating frame that defines the orientation, i.e. the phase-space angle, of the steady-state Wigner functions. (Bottom row) Due to fluctuations δV of the dc voltage, the phase-space angle of the Wigner functions is effectively averaged, $\eta \to \eta(t) \propto \int_0^t \delta V(\tau)\,\mathrm{d}\tau$. As a direct consequence, the quantum mechanical steady-state under influence of voltage noise is a diagonal density matrix. (a)-(c) For the k-photon resonance (of single-mode devices), the $\mathbb{Z}^k$-symmetry of the Wigner functions (in top row) is lost and the experimental steady-state Wigner functions are rotationally symmetric. (d) Due to integration over two phase-space quadratures, the noise-averaged squeezing ellipse of a two-mode squeezed state can assume a more rectangular shape.
[Methods: The steady-state Wigner functions under influence of voltage noise (bottom row) were obtained by assuming quasistatic Gaussian noise (see main text) and averaging manysteady-state solutions for randomly sampled, Gaussian distributed detunings δ around the mean $\delta = 0$ with standard deviation $\sigma = \gamma_a/10$.
The Wigner functions (for color scale see Fig. 1.5) from the top row have been shown in Fig. 1.5(b), Fig. 1.6(b), Fig. 1.7(c) and Fig. 1.11(c)]

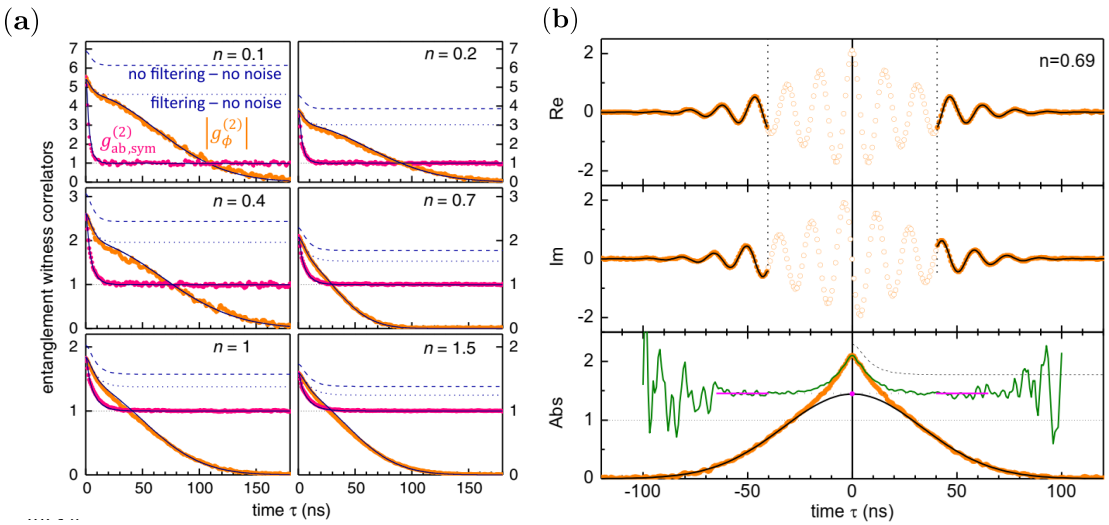

Figure 1.14: Reconstruction of expectation values from experiments with phase diffusion.
(a) Experimental measurement of the normalized two-time correlation functions $g^{(2)}_{\phi}(\tau)$ [c.f. Eq. (1.59)] and $g^{(2)}_{ab,\mathrm{sym}}(\tau)$ (similarly defined) of the output fields of a Josephson-photonics setup with two microwave cavities $\hat{a}$ and $\hat{b}$. Several plots are shown for different steady-state resonator populations $n = (\langle\hat{a}^\dagger\hat{a}\rangle\langle\hat{b}^\dagger\hat{b}\rangle)^{1/2}$. The starting time of the measurement is always the steady-state. In the long-time limit, $g^{(2)}_{\phi}$ should (theoretically without voltage noise) approach a nonzero constant value, $g^{(2)}_{\phi,\infty}$. Instead, $g^{(2)}_{\phi}(\tau)$ experimentally decays on short times to a shoulder value and completely decays to $g^{(2)}_{\phi,\infty} = 0$ in the long-time limit. The latter decay is caused by the fluctuations of the applied dc voltage. (b) The value $g^{(2)}_{\phi,\infty}$ can be recovered by fitting a Gaussian $g_\infty \cdot e^{-2(\pi\sigma\tau)^2}$ to the experimental data outside the shoulder region (indicated by dashed vertical lines in the two top panels). The fitted Gaussian (black line) in the bottom panel correctly describes the experimental decay of $|g^{(2)}_{\phi}(\tau)|$ outside the shoulder region. The fitted height of the shoulder (magenta dot) recovers the long-time value $g_\infty \approx g^{(2)}_{\phi,\infty}$ without phase diffusion. The experimental data can be divided by the fitted Gaussian (green curve). The height of the lateral constant region (magenta lines) are an alternative estimate of $g^{(2)}_{\phi,\infty}$ without phase diffusion.
[Reprinted figure with permission from A. Peugeot, G. Ménard, S. Dambach, M. Westig, B. Kubala, Y. Mukharsky, C. Altimiras, P. Joyez, D. Vion et al., *Physical Review X* **11**, 031008 (2021). Copyright (2021) by the American Physical Society; included in this thesis as reference [11].]

A significant impact of biasing the devices with a dc voltage is the lack of a reference phase. Consequently, Josephson-photonics devices generate quantum states with neutrally stable phase-space angle which can be easily affected by noise. Small fluctuations of the dc voltage then effectively average the phase-space angle of the stationary quantum state and mask its quantum properties. Fig. 1.13 shows the effect of noise on k-fold symmetric states and on squeezing in the mixed phase space for two-mode squeezed states. Information about the phase, like the direction of the coherent state, the squeezing angle or the orientation of the three-fold symmetric shape, is inevitably lost. Instead, the effective phase-averaged quantum states are rotationally symmetric in the total phase space [resulting in possibly

rectangular Wigner densities in the mixed phase space for two-mode squeezing, c.f. Fig. 1.13(d)] and expectation values like $\langle \hat{a}^k \rangle$ or $\langle \hat{a}\hat{b} \rangle$ vanish.

In Josephson-photonics devices that generate two-mode squeezed light, one experimentally observable quantity is the two-time correlation function

$$G_{\phi}^{(2)}(\tau) = \langle \hat{a}^{\dagger}(\tau)\hat{b}^{\dagger}(\tau)\, \hat{a}(0)\hat{b}(0) \rangle \to |\langle \hat{a}\hat{b} \rangle_{\mathrm{st}}|^2 \text{ (if } \tau \to \infty), \tag{1.59}$$

from which the steady-state expectation value $|\langle \hat{a}\hat{b} \rangle_{\mathrm{st}}|^2$ can be extracted (starting at some arbitrary time $t = 0$ in the steady-state). Instead, measurements [see Fig. 1.14(a)] show a decay of $G_{\phi}^{(2)}(\tau \to \infty) \to 0$, proving the loss of phase information and entanglement [11].

In this thesis, we present two solutions to overcome the issue of the neutrally stable phase, which are either able to partially recover lost phase information or completely stabilize the phase-space angle.

- Phase stabilization by injection locking and synchronization (Sec. 4)

  The neutrally stable phase can not only be perturbed by noise but also be adjusted by other external signals. The phase-space angle can be stabilized by providing a reference phase, either by mutual synchronization between two devices or by injecting a phase-stable external signal. As one central result of this thesis, we show how to extend the model of Josephson-photonics devices to enable a theoretical description of injection locking and synchronization. By including a finite in-series resistance into the model, the device becomes a self-sustained oscillator with a realistically fluctuating voltage source which is susceptible to injection locking and synchronization.

- Reconstruction of expectation values (Sec. 4.2.4)

  A fluctuating voltage, e.g., for the case of two-mode squeezing with the Hamiltonian

  $$\hat{H} \approx \hbar\delta_{\mathrm{dc}} \frac{\hat{a}^{\dagger}\hat{a} + \hat{b}^{\dagger}\hat{b}}{2} + \frac{E_J^* \alpha_0 \beta_0}{2} (\hat{a}\hat{b}e^{-i\eta} + \hat{a}^{\dagger}\hat{b}^{\dagger}e^{+i\eta}),$$

  results in a slowly time-dependent phase $\eta \to \eta(t)$ when fixing the rotating frame to the theoretically perfect dc-voltage. Alternatively, the rotating frame could be adapted [resulting in a time-dependent detuning $\delta_{\mathrm{dc}}(t)$]. Assuming quasistatic Gaussian noise, the influence of fluctuations can then be modeled by sampling values for δ_{dc} from a Gaussian distribution and averaging all results in the same rotating frame. The lost expectation value $|\langle \hat{a}\hat{b} \rangle_{\mathrm{st}}|^2$ can be recovered by fitting the decaying $G_{\phi}^{(2)}(\tau)$ with an envelope $e^{-2(\pi\sigma\tau)^2}$ that captures the effect of this averaging. Extracting in a similar manner from the measurements a few lost expectation values and using an ansatz, the full Wigner function of the steady state without phase diffusion can be reconstructed in some parameter regimes.

Phenomenology of Injection Locking and Synchronization

2

In 1665, Christiaan Huygens discovered synchronization in pendulum clocks [139]. When weakly coupled by a shared support (compare Fig. 2.1), two pendulum clocks can adjust their rhythm over time, leading to long-lasting and stable synchronized oscillations.
Since then, the nonlinear phenomenon has been studied in both natural and engineered systems in all fields of science [140–144]. In biology and neuroscience, synchronization has been observed, for example, in synchronously flashing fireflies [145], pacemaker cells of the heart [146], neurons of the brain [147], or the circadian rhythm regulating the sleep-wake cycle of animals and plants [148]. The adjustment of rhythms is also a widespread phenomenon in music, where people synchronize when singing, dancing, or giving applause. Further examples range from chemistry, where oscillating enzyme and autocatalytic reactions are studied [149], and climate research (seasons, monsoon cycles and El Niño), to technological applications like clock synchronization, electrical oscillators, and beyond.

definition

Synchronization and Injection Locking
Synchronization is the adjustment of rhythms between two or more self-sustained periodic oscillators due to weak interaction.

Injection locking is a variant of synchronization, where the frequency and phase of self-sustained oscillators are entrained to an external stable signal.

Synchronization can occur only in self-sustained oscillators, i.e. oscillators that perform long-lasting autonomous oscillations driven by an internal energy source. These oscillations do not have a preferred phase, resulting in a neutrally stable oscillation that is sensitive to perturbations.

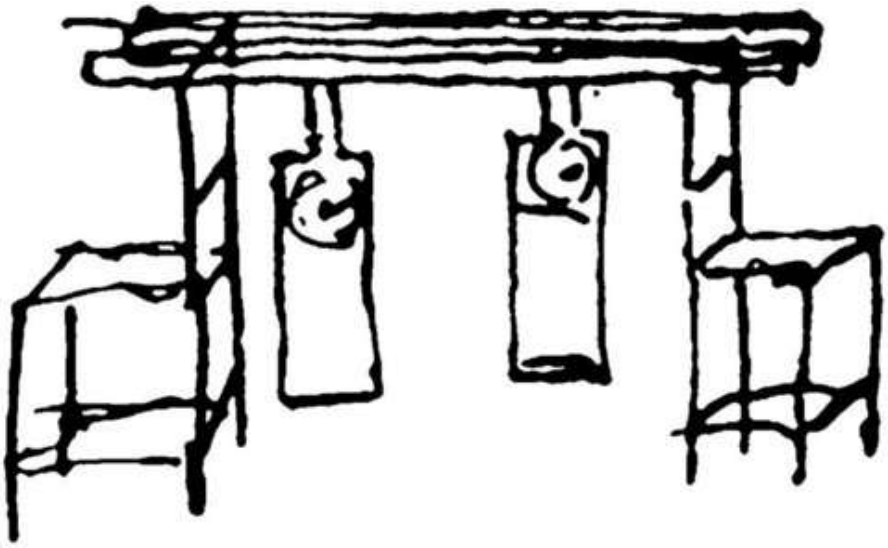

Figure 2.1: Experimental sketch from Huygens illustrating the synchronization of pendulum clocks. Both clocks are attached to a shared support, which weakly couples the two pendulum clocks. The way of coupling may lead to synchronization of the oscillations of the pendulum clocks. In contrast, directly connecting both pendulums by a rigid rod also leads to the same oscillation of both pendulums, but the coupling would then be too strong to describe the dynamics by synchronization.
[Original drawing from C. Huygens, Oeuvres complètes de Christiaan Huygens, "Publiées par la Société hollandaise des sciences", Vol. **1**, p. 658 (La Haye, M. Nijhoff, 1888-1950); included in this thesis as reference [139].
Reproduced from Arkady Pikovsky, Michael Rosenblum, and Jürgen Kurths, "Synchronization: A Universal Concept in Nonlinear Sciences", (Cambridge University Press, 2001); included in this thesis as reference [140].]

Phase stabilization and frequency pulling (Sec. 2.2.1) are well known in laser physics [150, 151]. Several generic models exist, such as the van der Pol oscillator [152–160], which exhibits self-sustained oscillations, while the Kuramoto model [161, 162] and Adler's theory [163] reduce the full dynamical description by equations of motion for all phase-space variables to the behavior of the differences between the involved oscillation phases. For many years, synchronization and injection locking have only been observed in nonlinear classical systems. The ability to control individual quantum systems has paved the way for studying systems in the quantum regime that classically show synchronization behavior, like the van der Pol oscillator, and systems [164–172], such as spins and mechanisms [173–179] without classical analogs.
Josephson-photonics devices, operable in both the semiclassical and the deep quantum regime, provide a platform well-suited to study how classical synchronization dynamics and its signatures are transferred to the quantum realm. They are self-sustained oscillators with a neutrally stable phase-space angle that can be perturbed by dc-voltage fluctuations due to shot noise of the tunneling Cooper pairs (see Sec. 1.7). Previously, locking experiments have been performed in a multi-mode Josephson-photonics setup [59, 62]. In order to provide an in-depth theory (see Sec. 4), we give a comprehensive summary of the phenomenology of injection locking and synchronization in the following sections. In Sec. 2.1, we will define self-sustained oscillators and stress why only this family of oscillators

can be injection locked and synchronized. After reviewing the most important hallmarks of injection locking in Sec. 2.2.1, we specifically discuss the Adler theory in Sec. 2.2.2. Although synchronization and injection locking are closely linked to noise, the Adler theory and the phenomenological description of the hallmarks do not include perturbations. Effects of noise, such as phase slips, are therefore briefly summarized in Sec. 2.2.3.

2.1 Self-Sustained Oscillators

The effect of synchronization can only be observed in special oscillatory systems, called self-sustained oscillators (SSOs), which undergo autonomous limit-cycle oscillations in their steady-state. Their stability property with a stable oscillation amplitude but a neutrally stable oscillation phase is crucial for synchronization.

definition

Self-Sustained Oscillator (SSO)
A self-sustained oscillator is a nonlinear system that autonomously performs a periodic and long-lasting oscillatory motion.

Limit-cycle oscillations

The long-lasting periodic motion of an SSO is typically described in the phase space spanned by its position and momentum variables, where it follows a closed loop, the **limit cycle**. After each time period $T = 2\pi/\omega_0$, a classical SSO (with the oscillation frequency ω_0) reaches the same point in the phase space. Here, we restrict the explanation to one spatial dimension and dimensionless phase-space variables $\{\tilde{x}, \tilde{p}\}$. Then a general limit cycle can be parametrized by the complex amplitude $a(t) = r(t)e^{i\phi(t)}$, consisting of a periodic radial component $r(t) = r(t+T)$ and the phase of the oscillation $\phi(t)$. Although arbitrary shapes of the limit cycle are possible, the position and momentum of an SSO (with mass m) can, in the simplest case, be expressed as

$$x(t) = x_0 \sin(\omega_0 t + \phi_0) \tag{2.1}$$

$$p(t) = m x_0 \omega_0 \cos(\omega_0 t + \phi_0)\,, \tag{2.2}$$

where the limit cycle is a circle in dimensionless coordinates, $\tilde{x} = x/x_0$ and $\tilde{p} = p/m x_0 \omega_0$ [compare Fig. 2.2(b)]. Here, the radial component is trivially constant, $r(t) = 1$, and the phase of the oscillation increases linearly with time, $\phi(t) = \omega_0 t + \phi_0$. In the frame, which rotates with ω_0, the motion can easily be described by a constant vector with phase-space angle ϕ_0.

Stability properties of the oscillation

The **stability** of an SSO is crucial to observe synchronization effects. We consider an SSO in its steady-state, which is subject to a small external perturbation [Fig. 2.2(b)]. In the rotating frame, its oscillation amplitude and phase are then weakly disturbed by a small amount, $r \to r + \delta r$ and $\phi_0 \to \phi_1 = \phi_0 + \delta\phi$. After a long time, the SSO re-establishes its original amplitude, which is stable against small perturbations. However, the phase-space angle of the oscillation does not return to its original value. It is neutrally stable, such that all points on the limit cycle are equivalent. Although the general form of the oscillation (as characterized by x_0 and ω_0 above) is independent of how the SSO was initially brought into motion, its phase-space angle indeed depends on the initial conditions. Noise can effectively move the SSO along its limit cycle, leading to perturbations in the oscillation frequency, which is now only on average given by ω_0. The property of an easily adjustable, neutrally stable phase makes an SSO vulnerable to perturbation, but also enables it to be synchronized to other systems.

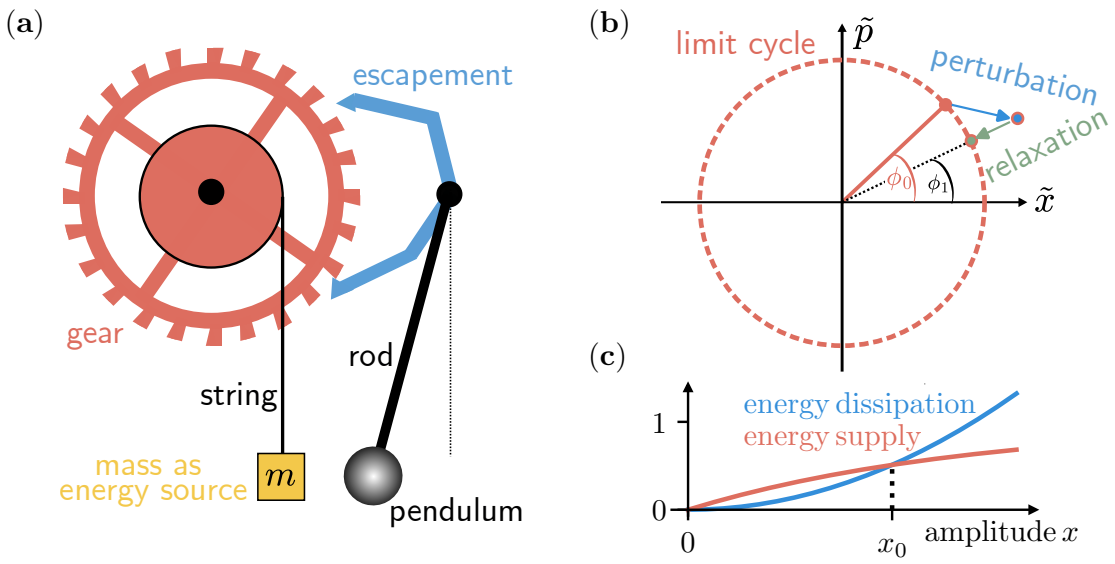

Figure 2.2: (a) Schematic sketch of a pendulum clock. A rod pendulum is connected to an escapement mechanism that rotates as the pendulum oscillates. A gear, around which a string with a suspended mass is wound, tends to rotate as the mass descends due to earth's gravitational pull. The bottom (top) arm of the escapement can stop the rotation of the gear at times when the pendulum is at the most left (right) position of its oscillations (here shown for the bottom arm), allowing the gear to rotate only by one tooth at a time. In between, the mass descends and releases potential energy, part of which is transferred to the pendulum in form of a small kick when the gear is stopped by the escapement. The resulting pendulum oscillation is long-lasting due to the internal energy source from the descending mass.
(b) In its steady state, the pendulum (or any SSO) performs an autonomous periodic oscillation. In the phase-space, spanned by position and momentum of the SSO, the motion of the phase-space point can be described by a closed loop, the limit cycle. In the simplest case, e.g., for the motion of a pendulum clock shown here, the closed loop is a circle with constant amplitude. Then, in a co-rotating frame, the phase-space point is fixed on the limit cycle with constant phase-space angle ϕ_0. External noise may perturb the amplitude and phase-space angle (still considered in the rotating frame). After some time, the SSO will return to its original stable amplitude. Since the phase is neutrally stable, the phase-space angle after relaxation is different from ϕ_0. (c) Schematic interplay between internal energy supply and energy dissipation of a self-sustained oscillation. At steady-state oscillation amplitude x_0, the energy dissipation balances the energy supply. If the oscillation amplitude is increased, $x > x_0$ due to some perturbation, the energy dissipation is stronger than the supplied energy and the oscillation amplitude decreases again to x_0. Analogously, the energy supply is dominating over the dissipated energy when a perturbation decreases the oscillation amplitude $x < x_0$. As result, the amplitude x_0 is re-established. At zero amplitude, the energy supply and the dissipated energy vanish. The two curves can only intersect at $x = 0$ and at x_0 when the dynamical equations of motion are nonlinear.

Key features of an SSO

In order to show the properties described above, an SSO must have the following key features:

- **Internal energy source and dissipation**
  Any physical system interacting with its environment is subject to dissipa-

tion. Energy that is dissipated to the environment inevitably leads to decay of an oscillation. In order to show long-lasting and autonomous oscillations, an SSO must possess an internal energy source that balances the dissipated energy. An example is the pendulum clock, where the energy supplied by a mass attached to a string [see the explanation in Fig. 2.2(a)] balances the dissipation suffered by other components.

- **Nonlinearity**
  The internal energy supply and the dissipated energy strongly depend on the oscillation amplitude [Fig. 2.2(c)]. At some finite oscillation amplitude x_0, dissipation compensates the internal energy supply of an SSO.
  - When an external perturbation increases the oscillation amplitude, $x > x_0$, dissipation dominates over the internal energy supply. Consequently, the oscillation amplitude decreases to x_0.
  - When an external perturbation decreases the oscillation amplitude, $x < x_0$, then the supplied energy is stronger than dissipation and the oscillation amplitude increases to x_0.

  The amplitude x_0 is thus the steady-state amplitude of the SSO that is stable against perturbations. At zero oscillation amplitude $x = 0$, no energy is supplied or dissipated. The two curves of the supplied energy and the dissipated energy can only intersect at $x = 0$ and at x_0 when the system dynamics is governed by nonlinear equations of motion.

Counterexamples: Systems without self-sustained oscillations

At first glance, some systems may appear to show self-sustained oscillations because their stationary state is similar to Eqs. (2.1) and (2.2). However, the crucial property of an SSO is its stable amplitude and its neutrally stable phase. Here, we briefly discuss simple counterexamples that do not show self-sustained oscillations.

- The undriven and undamped harmonic oscillator

$$\ddot{x} + \omega_0^2 x = 0 \tag{2.3}$$

  performs steady-state oscillations $x(t) = x_0 \sin(\omega_0 t + \phi_0)$. However, the oscillation amplitude is not stable because $f \cdot x(t)$ for any real factor f also solves the linear equations of motion. The steady-state oscillation amplitude depends on the initial conditions. Hence, the system is not an SSO.

- A damped harmonic oscillator

$$\ddot{x} + \gamma\dot{x} + \omega_0^2 x = 0 \tag{2.4}$$

  will reach the steady-state solution $x(t) = 0$. It can not be an SSO, since there is no long-lasting steady-state oscillation.

- The driven damped harmonic oscillator

$$\ddot{x} + \gamma\dot{x} + \omega_0^2 x = F_0 \sin(\omega_J t) \tag{2.5}$$

has the steady-state solution

$$x(t) = x_0 \sin(\omega_J t + \phi_0)\,.$$

Although the system is damped with loss rate γ, energy is supplied by the drive with strength F_0 and the steady-state solution itself looks similar to the case discussed above: both the amplitude

$$x_0 = \frac{F_0}{\sqrt{(\omega_J^2 - \omega_0^2)^2 + \gamma^2 \omega_J^2}}$$

and the phase-space angle

$$\phi_0 = \arctan\left(\frac{\gamma\omega_J}{\omega_J^2 - \omega_0^2}\right)$$

are fixed by the drive, and hence are stable. This oscillation is forced and not self-sustained, such that synchronization cannot occur.

2.2 Hallmark Signatures of Injection Locking and Synchronization

In Sec. 4, we will focus mainly on injection locking of a Josephson-photonics device to an external signal with stable reference phase. To illustrate the signatures of injection locking and synchronization, here we study the case of an SSO that is injection-locked to an external drive. We specifically consider an SSO that performs steady-state oscillations $x(t) \propto \sin(\omega_0 t + \phi_0)$ and a weak periodic locking drive $\propto \epsilon \sin(\Omega t + \phi_\epsilon)$ with a frequency that is close to the oscillation frequency of the SSO, $\Omega \approx \omega_0$. These sections first explain how and why the oscillation frequency of an SSO is pulled towards the locking frequency, and under which conditions injection-locked states can exist. Although injection locking stabilizes the oscillation phase of the SSO against noise, the phenomenological description of injection locking in Secs. 2.2.1 and 2.2.2 does not account for external perturbations. Noise (included in Sec. 2.2.3) is effectively able to drive the system out of the stabilized state.

Without a locking drive, $\epsilon = 0$, there is an initial detuning between the frequency of the locking drive and the oscillation frequency of the SSO,

$$\nu_0 = \Omega - \omega_0 \,. \tag{2.6}$$

When a locking signal is applied, the steady-state oscillation frequency of the SSO becomes dependent on the strength ϵ of the signal and on the initial detuning, $\omega_0 \to \omega_0(\epsilon, \nu_0)$. The SSO is said to be injection locked to the external drive if the frequency mismatch

$$\nu(\epsilon, \nu_0) = \Omega - \omega_0(\epsilon, \nu_0) \tag{2.7}$$

between the locking signal and the new steady state of the SSO vanishes (compare Fig. 2.3).

Mutual synchronization, e.g., between two SSOs, can be described analogously. Then ν_0 describes the initial frequency mismatch and ϵ the coupling strength between the SSOs. The frequency mismatch $\nu(\epsilon, \nu_0)$ after coupling arises from the difference between the SSOs' oscillation phases.

2.2.1 Locking Region, Frequency Pulling and the Arnold Tongue

Locking region

We fix the strength of the locking drive and analyze the dependence of the frequency mismatch $\nu(\epsilon, \nu_0)$ on the initial detuning ν_0:

- $\epsilon = 0$: The locking signal is turned off.
  The frequency mismatch is trivially given by $\nu = \nu_0$ [see brown line in Fig. 2.3(a)].

- $\epsilon > 0$: The locking signal is turned on.
  We fix the strength of the locking signal [ϵ_1 and ϵ_2 in Fig. 2.3(a)]. If the initial detuning between the locking drive and the oscillation frequency of the SSO is sufficiently large compared to the locking amplitude, the system

cannot be synchronized. The locking signal is then barely able to influence the oscillation frequency of the SSO, resulting in $\nu \approx \nu_0$ [c.f. the yellow and blue lines of Fig. 2.3(a) at large ν_0]. However, the locking strength is strong enough to obtain an injection locked state, $\nu = 0$, for smaller initial detunings. For each fixed strength of the locking drive, there exists a critical detuning $\nu_c(\epsilon)$, at which a sharp transition occurs between the locked and unlocked state. The **locking region**, $|\nu_0| < \nu_c(\epsilon)$, expands as the strength of the locking drive increases.

Frequency pulling

We now consider a fixed initial detuning ν_0, such that the locking drive is still nearly resonant with the oscillation frequency of the SSO, $\nu_0 \ll \omega_0$. In Fig. 2.3(b), the locking strength ϵ is varied. Above a critical (but still weak) locking amplitude $\epsilon_c(\nu_0)$, the SSO becomes injection locked to the external signal. Below the critical locking amplitude, $\epsilon < \epsilon_c$, the oscillation frequency of the SSO is modified but not completely shifted to the locking frequency. The oscillation frequency of the SSO is pulled towards the locking frequency when increasing ϵ.

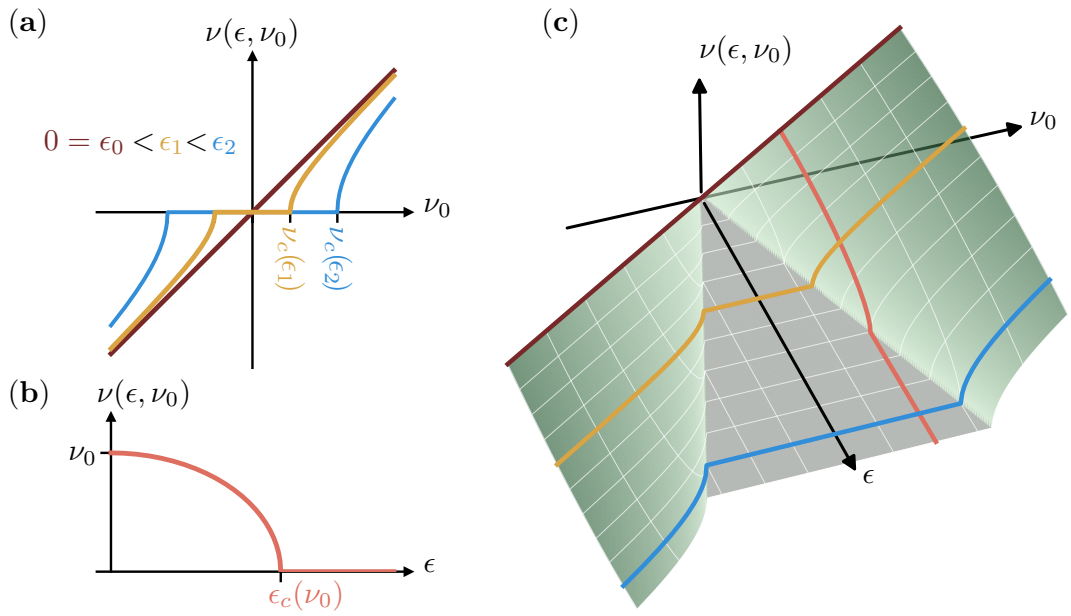

Figure 2.3: Hallmarks of injection locking (weakly coupling an SSO to an external reference) and synchronization (weakly coupling two SSOs). (a) Fixing a coupling strength ϵ, the frequency mismatch a long time after coupling, $\nu(\epsilon,\nu_0)$, depends on the initial detuning ν_0. In the uncoupled case (brown), $\nu(0,\nu_0) = \nu_0$. A coupling strength weak compared to the initial detuning ν_0 merely modifies the frequency mismatch after coupling, $\nu(\epsilon,\nu_0) \approx \nu_0$ (yellow and blue curve at large ν_0). At sufficiently small initial detunings below a critical detuning ν_c, an injection locked (or synchronized) region appears with $\nu(\epsilon,\nu_0) = 0$. The locking region grows with larger ϵ. (b) Fixing the initial detuning, a small locking signal merely changes the frequency mismatch. A critical locking strength exists where the SSO is injection locked to the external signal (or where two SSOs synchronize). The frequency of the SSO is then pulled towards the frequency of the injected signal. (c) The two-dimensional plots from (a) and (b) are cuts (colored lines) in specific directions of $\nu(\epsilon,\nu_0)$. The injection locked (or synchronized) region, where $\nu(\epsilon,\nu_0) = 0$ (gray shaded), is called the Arnold tongue.

Arnold tongue

Summarizing the above findings in a three dimensional plot of $\nu(\epsilon, \nu_0)$ gives a complete description of the parameters for which the SSO can be injection locked. The region where $\nu(\epsilon, \nu_0) = 0$ [gray shaded in Fig. 2.3(c)] is called the Arnold tongue.

2.2.2 Reduced Description of Locking with Adler's Theory

Since the amplitude of the SSO is stable, the dynamics of injection locking can be reduced from the full equations of motion to a description that only involves the oscillation phases [163]. In the injection-locked state, the oscillation frequency of the SSO equals the frequency of the locking drive. Defining the phase difference

$$\psi(t, \epsilon, \nu_0) = [\Omega t + \phi_\epsilon] - [\omega_0(\epsilon, \nu_0) + \phi_0] \tag{2.8}$$

between the oscillation phase of the injected signal and of the SSO, a locked state corresponds to the condition that ψ becomes constant in time, $\dot{\psi}(t) = 0$.

Adler equation

In general, $\omega_0(\epsilon, \nu_0)$ is a nonlinear function with a nontrivial time derivative, such that exact calculations of its time derivative strongly depend on the specific problem. Assuming a weak and resonant locking signal, a calculation of the time derivative [140, 163] yields the Adler equation

$$\frac{\mathrm{d}}{\mathrm{d}t}\psi = \nu_0 + \epsilon \cdot q(\psi) \tag{2.9}$$

with a general periodic function $q(\psi)$. For the moment, we restrict ourselves to the simplest case where $q(\psi) = \sin(\psi)$, such that the Adler equation simplifies

$$\frac{\mathrm{d}}{\mathrm{d}t}\psi = \nu_0 + \epsilon \cdot \sin(\psi)\,. \tag{2.10}$$

When $\epsilon \geq \epsilon_\mathrm{c} = \nu_0$, there exist constant solutions, where $\dot{\psi} = 0$. From Eq. (2.10), these are given by $\psi_\mathrm{locked} = \pi + \arcsin(\nu_0/\epsilon) \pmod{2\pi}$ [c.f. Fig.2.4(b)] and fix the position of the now stabilized phase-space angle ϕ_0 of the SSO with respect to the locking phase.

Adler potential

Eq. (2.10) can be interpreted as the motion of a massless fictitious phase particle with position ψ in a tilted "washboard" potential

$$V_\mathrm{WB}(\psi) = -\int \dot{\psi}\,\mathrm{d}\psi = -\nu_0\psi + \epsilon\cos(\psi)\,, \tag{2.11}$$

as shown in Fig. 2.4. Due to the missing second derivative in Eq. (2.10), the motion is overdamped and the critical locking drive ϵ_c defines the onset of minima ψ_locked in the potential, in which the fictitious particle is trapped. If the locking strength is too small, $\epsilon < \nu_0$, such that the potential does not exhibit any minima, there

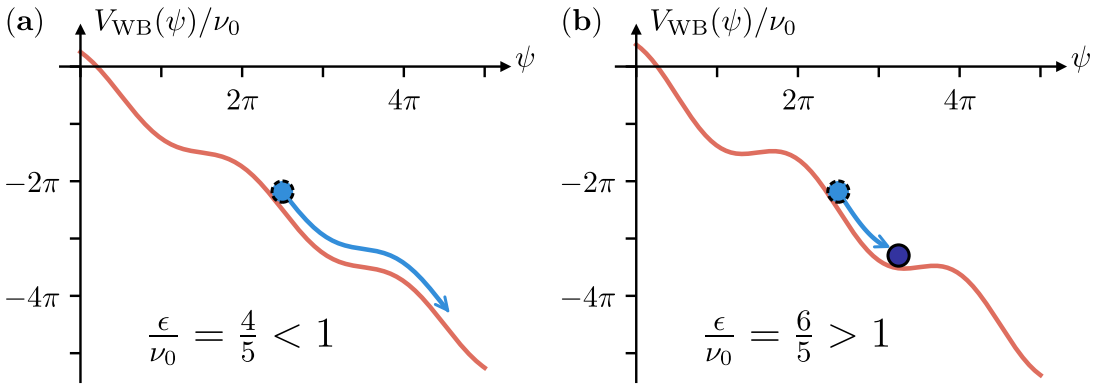

Figure 2.4: Motion of the effective massless phase particle with position ψ in a washboard potential. (a) For $\epsilon < \nu_0$, the potential does not exhibit minima, allowing the phase particle to glide down the slope. Since ψ is the difference between the oscillation phase of the SSO and the injection signal, the SSO is not injection locked. At times, the increase of ψ is slower (faster), when the phase particle moves through shallow (steeper) potential regions. (b) When $\epsilon > \nu_0$, potential minima form at ψ_{locked} (see main text), in which the initially moving phase particle will be trapped. Then, $\dot{\psi} = 0$ and the SSO is injection locked to the external signal.

is no locked solution. The motion of the fictitious particle is then described by a quasi-periodic function, fulfilling $\psi(t+T) = \psi(t) + 2\pi$ with some period T. By separation of variables in Eq. (2.10) and integration over one period

$$\int_0^{2\pi} \frac{\mathrm{d}\psi}{1 + \frac{\epsilon}{\nu_0}\sin(\psi)} = \int_0^{T} \nu_0 \,\mathrm{d}t \tag{2.12}$$

we calculate the corresponding frequency

$$\nu(\epsilon, \nu_0) = 2\pi/T = \sqrt{\nu_0^2 - \epsilon^2}\,. \tag{2.13}$$

The phase particle moves faster on steeper parts of the potential and slower on flat regions. On average, the particle moves with velocity $\nu(\epsilon, \nu_0)$, which can therefore be interpreted as the frequency difference between the locking drive and the oscillation frequency of the SSO in the unlocked scenario (compare Fig. 2.3).

2.2.3 Effects of Noise

Until now, the description of injection locking and synchronization has been limited to a discussion without the explicit influence of noise induced by the environment. Noise is always present in real physical systems, which will modify the theoretical description of injection locking and synchronization.
To illustrate the effect of noise, we discuss specific observable phenomena shown in Fig. 2.5.

a) Broadening of the phase-space distribution

Without locking signal, the Adler potential is linear. When choosing specifically $\Omega = \omega_0$, it is constant, since here trivially $\dot{\psi} = 0$. The steady-state of ψ (and

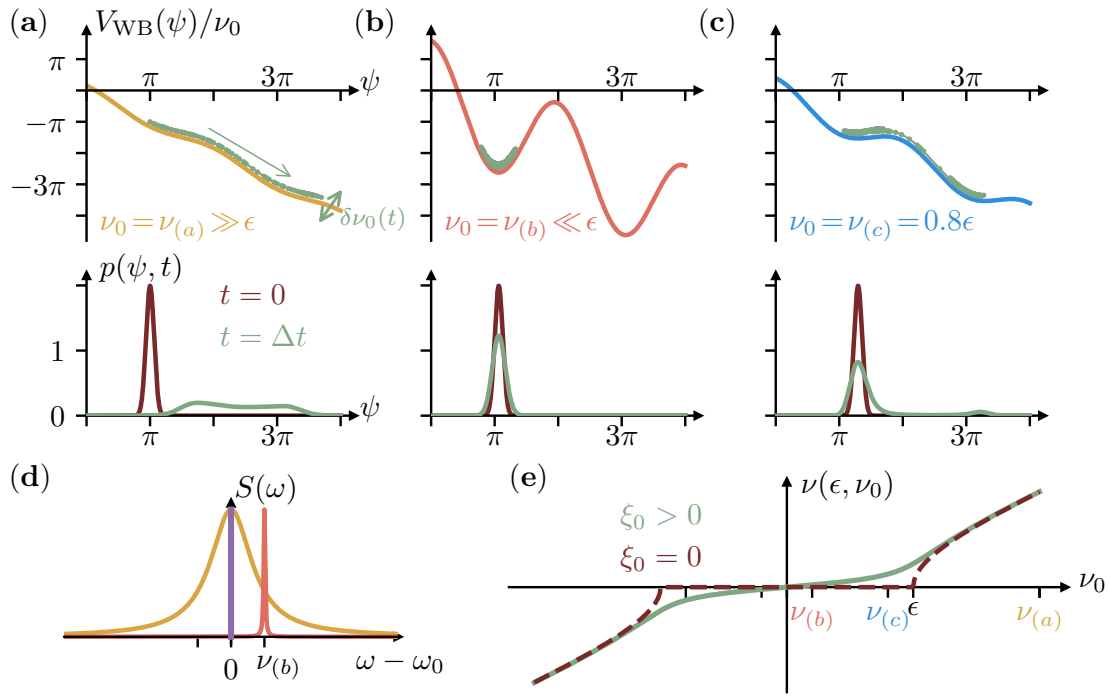

Figure 2.5: Effects of noise on the injection-locking dynamics of an SSO. (a) When the locking signal is located far away from the zero-noise locking region [brown curve in (e)], the phase particle descends even without noise in the washboard potential (top plot). The oscillation spectrum $S(\omega)$ [see (d)] of the SSO is nearly unmodified (purple delta-peak). Noise yields random time-dependent tilts $\delta\nu_0$ of the potential. Alternatively, this can be described by diffusion of the phase particle in a nearly linearly decreasing potential that is constant in time [motion shown in green in top plot of (a)]. An initial probability distribution of the phase-particle's position $p(\psi, 0)$ [bottom plot of (a)] will not only descend, but its variance is growing due to noise. This gives a broadened oscillation spectrum of the SSO [yellow curve in (d)]. (b) Deep in the locking region [see $\nu_{(b)}$ in (e)], the locking signal confines the phase ψ, which diffuses around the minimum. Weak noise ξ_0 is not strong enough to push the phase particle out of the potential well. An initial phase distribution will stay in the minimum and will be broadened only marginally. The SSO stays injection locked, resulting in a sharp peak of the oscillation spectrum (red line) at $\Omega = \omega_0 + \nu_{(b)}$. (c) Close to the boundary (but inside) of the zero-noise locking region [see $\nu_{(c)}$ in (e)], noise is able to push the particle out of the potential minimum. The phase stays confined to a minimum for a long time (green points in top plot). It can however slip quickly into the next potential minimum, where it again stays confined for long times. The hallmark of phase slips is the emergence of peaks of $p(\psi, t)$ at other minima [bottom plot of (c)]. (d) Due to noise, the sharp transition between locked and unlocked regime at $\nu_0 = \epsilon$ is smoothened, such that $\nu(\epsilon, \nu_0)$ is not vanishing close to the boundaries of the locking region.

the phase-space angle of the SSO) is fixed to a specific value that depends on the initial conditions. However, it is neutrally stable, as illustrated by the flat potential. Noise will effectively perturb the oscillation phase of the SSO by slightly tilting the potential randomly in time. This causes the frequency of the SSO to fluctuate, $\omega_0 \to \omega(t)$, leading to a broadened oscillation spectrum. The phase ψ undergoes a random walk induced by the noise force $\dot{\psi} \sim \omega_0 - \omega(t)$. Consequently, $\psi \,(\mathrm{mod}\, 2\pi)$ is equally distributed in the steady state and any information about

the phase-space angle is lost.

Far away from the (zero-noise) locking region, [Fig. 2.5(a)], the SSO is merely affected by the locking signal even when considering no external perturbations. Noise then only marginally changes the motion of the phase particle. The Adler potential mainly exerts a force $\dot{\psi} \sim \nu_0$ leading to a descending phase particle ψ. A small additional force from the external noise slightly slows down the motion at some times and accelerates it at other times.

b) Protecting the phase-space angle against weak noise

Deep in the locking regime [c.f. Fig. 2.5(b)], the phase particle is trapped inside one of the minima and would stay there when external perturbations can be neglected. Weak noise results in a marginal broadening of the phase distribution $p(\psi)$. The system remains injection locked and is protected against weak noise. To estimate how well the system is protected, the effective noise strength can be compared to the height of the potential well.

c) Phase slips

Inside, but close to the boundary of the zero-noise locking region, the Adler potential exhibits shallow minima, in which the phase particle ψ would be trapped without external perturbations. If the potential well is small enough, such that noise can drag ψ over the potential barrier, a fast slipping motion of ψ can occur until it may be re-trapped in the next potential minimum. Such quick changes of ψ by (multiples of) 2π are called phase slips. The dynamics of the SSO can be divided into an injection locked state, where fluctuations of ψ stay small for a long time, which is interrupted by short phase slips.

Locking region

The three cases discussed above correspond to different regimes of the locking curve in Fig. 2.5(e).

a) When a detuned locking signal is too weak to lock the system, noise will only marginally modify the motion of the phase particle. The frequency difference with applied locking signal is approximately given by the initial detuning.

b) A strongly locked system is protected against weak noise. Deep in the locking regime, the average frequency difference $\dot{\psi} = \nu(\epsilon, \nu_0)$ with applied locking signal is still vanishing (to a good approximation).

c) Without noise, the application of an injection locking signal results in a sharp transition between the locked and unlocked regions (c.f. Fig. 2.3). Noise smoothens the crossover between the two different regions. At the borders of the locking region, the average velocity no longer vanishes, since noise leads to phase slips. A stronger locking signal results in fewer phase slips and in better protection of the SSO's phase-space angle against noise.

3 Itinerant Microwave Photons

Itinerant microwave pulses are temporally confined propagating electromagnetic fields. By carrying and transporting quantum information, they open the door for various tasks and applications in quantum information processing, quantum sensing and quantum communication [123, 124]. Naming only a few examples, the vast amount of applications includes the generation of quantum states for quantum teleportation [5, 104] and quantum key distribution [100, 101], or state readout [180] and state transfer [181] used for quantum computational tasks. Further, they enable the characterization of physical properties of open quantum systems, such as frequency-dependent transmission and reflection coefficients.

In this thesis, we specifically focus on the detection of itinerant single-photon pulses in the microwave regime that travel through a transmission line and interact with a Josephson-photonics device, as described in Sec. 1.6 and Pub. (*iv*) in Sec. 5.1.1. The device is designed to convert single-photon pulses impinging from an input transmission line into pulses of n leaking photons into the output transmission line. Such a photon-multiplication scheme can enhance detection efficiency of the single-photon microwave pulse. Since the photon pulses in this case fall comfortably within the broader frequency range supported by the transmission line, any dispersion within the line can be ignored. It is thus sufficient to introduce temporal modes of quantum light in Sec. 3.1. Further, we review Mølmer's approach, which theoretically describes the interaction of quantum pulses of light with a generic quantum system. Finally, we introduce the stochastic Schrödinger equation, which unravels the Lindblad master equation and describes heterodyne detection (Sec. 3.3) of the quadratures of quantum fields leaking from a quantum system.

3.1 Itinerant Photon Pulses

We focus on the case where our quantum system (i.e. the Josephson-photonics device) interacts at a single coupling point with a microwave field travelling in a transmission line and assume a frequency range where dispersion in the transmission lines can be ignored. This interaction can then be modeled using temporal pulses [182–184] that are either sent to or received from the system via the transmission lines. Since the transmission lines support a wide range of microwave frequencies, an oftentimes convenient mode decomposition is given by the basis of plane waves. Then the time-dependent creation operator $\hat{a}^\dagger(t)$, which is now the field of the transmission line at some arbitrary point, is decomposed into an infinite set of harmonic-oscillator modes

$$\hat{a}^\dagger_\omega = \frac{1}{\sqrt{2\pi}} \int_{-\infty}^{\infty} e^{i\omega t}\, \hat{a}^\dagger(t)\, \mathrm{d}t \tag{3.1}$$

with orthonormal basis functions $\{e^{i\omega t}/\sqrt{2\pi} : \omega \in (-\infty, \infty)\}$ such that

$$\delta(\omega - \omega') = \frac{1}{2\pi} \int_{-\infty}^{\infty} e^{-i\omega' t} e^{i\omega t}\, \mathrm{d}t\,. \tag{3.2}$$

Each mode $\hat{a}^\dagger_\omega$ therefore describes a monochromatic electromagnetic wave with frequency ω, which is continuous in time (i.e. an infinitely long pulse).

Alternatively, any different set of orthonormal basis functions $\{u_k(t) : k \in \mathbb{N}_0\}$ can be used, which can be linked to the plane-wave basis by a unitary transformation. Itinerant quantum pulses with a given temporal mode envelope $u(t)$ can therefore be expressed as some superposition of basis functions

$$u(t) = \int_{-\infty}^{\infty} f(\omega)\, e^{i\omega t}\, \mathrm{d}\omega = \sum_{k=0}^{\infty} g_k\, u_k(t) \tag{3.3}$$

with amplitudes $f(\omega)$ or g_k respectively. In this context, the bosonic operator defined by

$$\hat{a}^\dagger_u = \int_0^{\infty} \hat{a}^\dagger(t)\, u(t)\, \mathrm{d}t \tag{3.4}$$

creates a single excitation in a mode with temporal envelope $u(t)$.

Having introduced a vector space for the modes, we want to highlight two sides of quantum optics.

1) The temporal envelope of the pulses of (microwave) light is defined in the modal vector space. Its relationship to the wave description of light within classical optics is governed by Maxwell equations, which are linear, ensuring that the superposition principle holds for electromagnetic waves.

2) The operator $\hat{a}^\dagger_u$ is defined in the linear (quantum mechanical) Hilbert space. Fock states are often used as a convenient basis for describing photons.

This double linearity of quantum optics enables a description of the same system state from different perspectives.

3.1.1 Entanglement and the Temporal Mode Basis

The close connection between the classical mode description and quantum mechanics can be explained by a simple example. We consider two orthonormal modes u_1 and u_2. The quantum state

$$|\psi\rangle = |1_{u_1}\rangle\,|1_{u_2}\rangle = \hat{a}^\dagger_{u_1} \otimes \hat{a}^\dagger_{u_2}\,|\mathrm{vac}\rangle \tag{3.5}$$

is factorizable and contains a photon in each mode, created by application of the respective creation operators on the (multi-mode) vacuum state $|\mathrm{vac}\rangle$. Two different orthogonal modes $u_\pm = \frac{u_1 \pm u_2}{\sqrt{2}}$ can be defined. Written in this basis, the quantum state is obviously entangled,

$$|\psi\rangle = \frac{|2_{u_+}\rangle\,|0_{u_-}\rangle - |0_{u_+}\rangle\,|2_{u_-}\rangle}{\sqrt{2}}\,. \tag{3.6}$$

Quantum entanglement thus depends on the choice of the classical mode basis.

3.1.2 Coherence Property of Temporal Modes

The coherence property of photons within a mode is related to the first-order two-time correlation function. A propagating quantum field is said to be coherent if the first-order correlation function

$$G^{(1)}(t_1, t_2) = \langle \hat{a}^\dagger(t_1)\hat{a}(t_2)\rangle = n_0 \cdot u_0^*(t_1)u_0(t_2) \tag{3.7}$$

is factorizable into a single mode $u_0(t)$ [65, 185]. Once again, the parallel between classical optics and quantum mechanics becomes evident: evaluating the quantum expectation value yields the complex solution u_0 of Maxwell's wave equation.

definition

Eigenmode Decomposition of the First-Order Correlation Function

$$G^{(1)}(t_1, t_2) = \langle \hat{a}^\dagger(t_1)\hat{a}(t_2)\rangle = \sum_k \langle \hat{a}^\dagger_{u_k}\hat{a}_{u_k}\rangle\, u_k^*(t_1)u_k(t_2) \tag{3.8}$$

- u_k are orthonormal eigenmode-functions
- $\langle \hat{a}^\dagger_{u_k}\hat{a}_{u_k}\rangle$ is the mean occupation of mode u_k

A set of eigenmodes of a temporal field can be found by diagonalization of the first-order two-time correlation function, Eq. (3.8). Any single-photon pulse is first-order coherent and can be described by a single mode [185].

3.1.3 Exponential Modes of a Harmonic Oscillator

Let us, for instance, consider a single harmonic oscillator coupled to a zero temperature heat bath, such that its time evolution can be described by a Lindblad master equation with the rotating-frame Hamiltonian $\hat{H} = \hbar\delta\hat{a}^\dagger\hat{a}$ (with detuning $\delta = \omega_a - \omega_{\mathrm{rot}}$) and collapse operator $\hat{L}_a = \sqrt{\gamma_a}\hat{a}$, where γ_a is the single-photon loss rate. Initially, at time $t = 0$, it shall be prepared in some quantum state $\hat{\rho}_0$ with mean occupation $\langle \hat{a}^\dagger\hat{a}\rangle_0$.

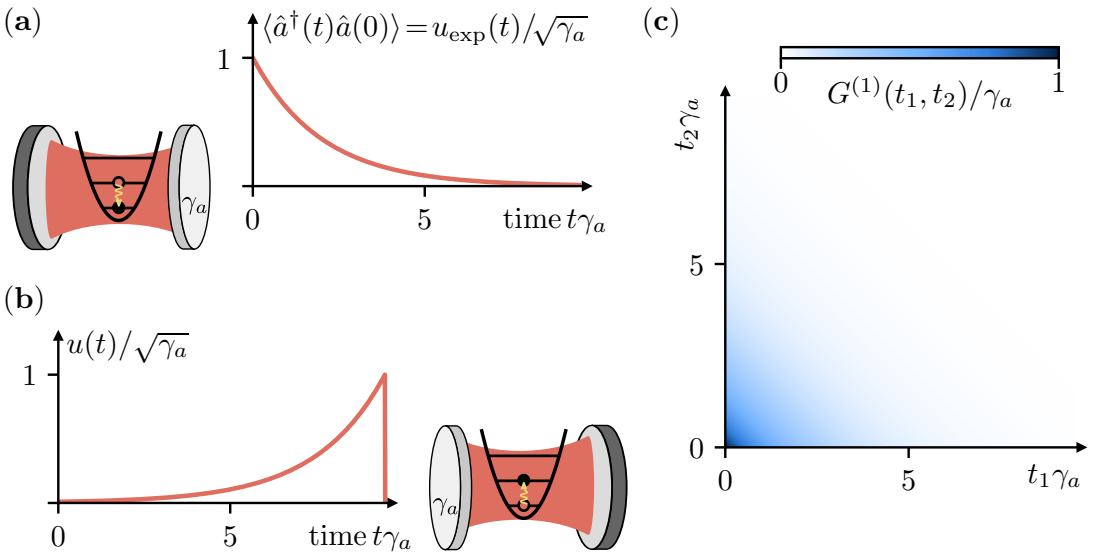

Figure 3.1: Exponential mode of a harmonic oscillator. (a) A cavity, coupled to a zero temperature heat bath (with effective constant single-photon loss rate γ_a) is initially at time $t = 0$ prepared in Fock state $|1\rangle$. It will emit the photon, resulting in an exponential two-time correlation function $\langle \hat{a}^\dagger(t)\hat{a}(0)\rangle$. (b) A single photon in a time-reversed exponential pulse $u_{\rm exp}(t)$ sent to the cavity, initially in the ground state, will be perfectly absorbed [186]. (c) The two-time correlation function for the situation in (a) can be diagonalized. The single eigenfunction is the exponential eigenmode shown in (a), while the eigenvalue is the initial population $\langle \hat{a}^\dagger\hat{a}\rangle(t=0)$ of the cavity [c.f. Eq. (3.11)].

Using the quantum regression theorem [65], the set of equations

$$\frac{\mathrm{d}}{\mathrm{d}t}\langle \hat{a}^\dagger\hat{a}\rangle(t) = -\gamma_a\langle \hat{a}^\dagger\hat{a}\rangle(t) \tag{3.9}$$

$$\frac{\mathrm{d}}{\mathrm{d}t_1}\langle \hat{a}^\dagger(t_1)\hat{a}(t_2)\rangle = -\left(\frac{\gamma_a}{2} - i\delta\right)\langle \hat{a}^\dagger(t_1)\hat{a}(t_2)\rangle \quad (\text{if } t_1 \geq t_2) \tag{3.10}$$

yields the first-order correlation function of the output field of the harmonic oscillator,

$$G^{(1)}(t_1,t_2) = \gamma_a\,\langle \hat{a}^\dagger(t_1)\hat{a}(t_2)\rangle = \gamma_a e^{-\frac{\gamma_a}{2}(t_1+t_2)}e^{i\delta(t_1-t_2)}\cdot\langle \hat{a}^\dagger\hat{a}\rangle_0\,. \tag{3.11}$$

It can be diagonalized [compare Eq. (3.8)] into a single exponential eigenmode

$$u_{\rm exp}(t) = \sqrt{\gamma_a}e^{-(\frac{\gamma_a}{2}+i\delta)t}\begin{cases}1 & \text{if } t \geq 0\\ 0 & \text{else}\end{cases} \tag{3.12}$$

with occupation $\langle \hat{a}^\dagger\hat{a}\rangle_0$ [c.f. Fig. 3.1(a,c)]. The mode $u_{\rm exp}(t)$ describes the electromagnetic field emitted by the resonator at the coupling point. Initially, at time $t = 0$, the decaying quantum state yields a large signal, which decreases exponentially with time. In turn, a harmonic oscillator can perfectly absorb an impinging time-reversed exponential mode [see Fig. 3.1(b)], which has also been shown experimentally [186]. Then, the signal sent to the quantum system grows exponentially before it stops at some time t_f.

3.2 Interaction of Itinerant Quantum Fields with Quantum Systems

The interaction between itinerant microwave fields and quantum systems can be modeled using a cascaded Lindblad master equation following Mølmer's approach. In this framework, harmonic oscillators are auxiliary sources that generate itinerant photon pulses. The method combines input-output theory, describing the interaction between itinerant fields and quantum systems, with the idea of cascaded quantum systems, that captures the unidirectional influence of one system on a second one.

3.2.1 Input-Output Theory

Input-output theory [65, 67, 187] is a theoretical framework of quantum optics that describe the interaction of a quantum system with traveling quantum fields. While the Lindblad master equation is a reduced equation of motion for the internal state of a quantum system in a large environment, input-output theory connects the system dynamics to experimentally measurable quantum fields. It is a powerful tool for studying, e.g., how incoming signals are modified by a quantum system, the system's reaction to incoming quantum fields, as well as its transmission and reflection properties (c.f. Fig. 3.2).

Input-Output Equation of Motion ($\hat{z}$ is an arbitrary system operator)

$$\frac{\mathrm{d}}{\mathrm{d}t}\hat{z} = -\frac{i}{\hbar}[\hat{z}, \hat{H}] - [\hat{z}, \hat{a}^\dagger]\left(\frac{\gamma_a}{2}\hat{a} + \sqrt{\gamma_a}\hat{a}_{\mathrm{in}}\right) + \left(\frac{\gamma_a}{2}\hat{a}^\dagger + \sqrt{\gamma_a}\hat{a}_{\mathrm{in}}^\dagger\right)[\hat{z}, \hat{a}] \tag{3.13}$$

$$\hat{a}_{\mathrm{out}} = \sqrt{\gamma_a}\hat{a} + \hat{a}_{\mathrm{in}} \tag{3.14}$$

The input-output equations follow from the Heisenberg equations of motion of the total Hamiltonian $\hat{H}_{\mathrm{tot}} = \hat{H} + \hat{H}_{\mathrm{bath}} + \hat{H}_{\mathrm{int}}$, modeling a system with Hamiltonian $\hat{H}$ coupled to a large bath by the position-momentum interaction such that

$$\hat{H}_{\mathrm{bath}} = \int_{-\infty}^{\infty} \hbar\omega\, \hat{b}^\dagger(\omega)\hat{b}(\omega)\,\mathrm{d}\omega \tag{3.15}$$

$$\hat{H}_{\mathrm{int}} = -i\hbar\int_0^{\infty} \kappa(\omega)\left[\hat{b}^\dagger(\omega) + \hat{b}(\omega)\right]\cdot\left[\hat{a}^\dagger - \hat{a}\right]\,\mathrm{d}\omega\,. \tag{3.16}$$

Assuming Markovian dynamics, a straightforward calculation yields the input-output equations after rotating-wave approximation. The input and output fields

$$\hat{a}_{\mathrm{in}}(t) = \frac{1}{\sqrt{2\pi}}\int_{-\infty}^{\infty} e^{-i\omega(t-t_i)}\hat{b}_i(\omega)\,\mathrm{d}\omega \tag{3.17}$$

$$\hat{a}_{\mathrm{out}}(t) = \frac{1}{\sqrt{2\pi}}\int_{-\infty}^{\infty} e^{-i\omega(t-t_f)}\hat{b}_f(\omega)\,\mathrm{d}\omega \tag{3.18}$$

are defined by the boundary value problem where $\hat{b}_i(\omega)$ [$\hat{b}_f(\omega)$] are the initial [final] state of the bath mode $\hat{b}(\omega)$ at initial time t_i [final time t_f]. The input-output relation (3.14) arises from the reflection condition of electromagnetic fields at the spatial boundary of the quantum system.

The commutation relations

$$[\hat{z}(t_1), \hat{a}_{\text{in}}(t_2)] = -\sqrt{\gamma_a}\theta(t_1 - t_2)[\hat{z}(t_1), \hat{a}(t_2)] \tag{3.19}$$
$$[\hat{z}(t_1), \hat{a}_{\text{out}}(t_2)] = +\sqrt{\gamma_a}\theta(t_2 - t_1)[\hat{z}(t_1), \hat{a}(t_2)] \tag{3.20}$$

with the step function

$$\theta(t_1 - t_2) = \begin{cases} 1 & \text{if } t_1 > t_2 \\ \frac{1}{2} & \text{if } t_1 = t_2 \\ 0 & \text{if } t_1 < t_2 \end{cases} \tag{3.21}$$

incorporate a causality relation: The system's evolution does not depend on input fields that will arrive in the future and does not influence output fields from the past.

Example: A driven damped harmonic oscillator

The equation of motion

$$\frac{\mathrm{d}}{\mathrm{d}t}\hat{a} = -\left(i\omega_0 + \frac{\gamma_a}{2}\right)\hat{a} - \sqrt{\gamma_a}\hat{a}_{\text{in}} \tag{3.22}$$

for the operator $\hat{a}$ of a harmonic oscillator with Hamiltonian $\hat{H} = \hbar\omega_0\hat{a}^\dagger\hat{a}$ that is driven by an input field can be Fourier transformed. Using the input-output relation Eq. (3.14),

$$\hat{a}_{\text{out}}(\omega) = \underbrace{\frac{i(\omega - \omega_0) + \frac{\gamma_a}{2}}{i(\omega - \omega_0) - \frac{\gamma_a}{2}}}_{=r(\omega)}\hat{a}_{\text{in}}(\omega)\,, \tag{3.23}$$

one obtains the frequency-dependent reflection coefficient $r(\omega)$.

The input-output equation of motion is a quantum Langevin equation. Expectation values of system operators can be found analytically in linear quantum systems [65, 66, 188], when the input field can be characterized sufficiently well by the moments $\langle \hat{a}_{\text{in}}^{\dagger m}\hat{a}_{\text{in}}^{n}\rangle$ that may appear in the set of equations of motion. In general, an analytic approach to nonlinear systems (like Josephson-photonics devices) yields a set of differential equations which does not close. The noise operators $\hat{a}_{\text{in/out}}$ contain the quantum noise properties of the interacting fields, making a numerical simulation practically unfeasible. Therefore, an alternative approach to analyze systems interacting with quantum fields uses cascaded quantum systems, where the first system generates the input field for the second system.

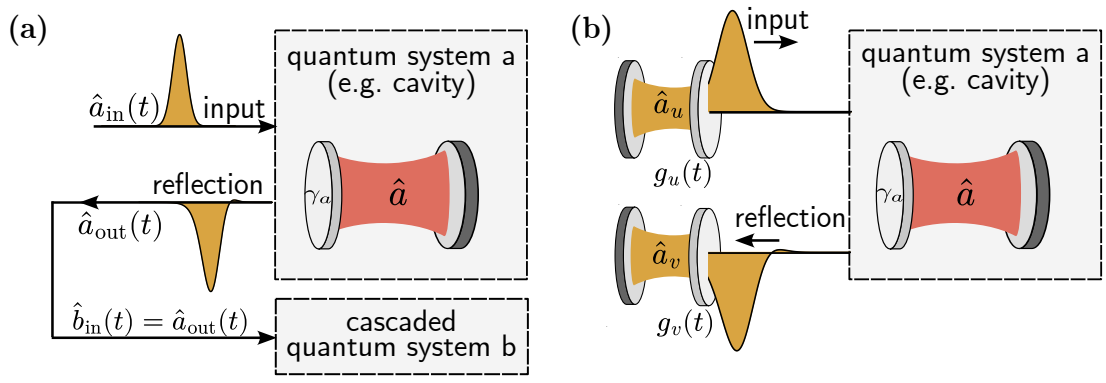

Figure 3.2: (a) Interaction of a system a with generic time-dependent quantum fields. For instance, the quantum system of interest could be a single-sided cavity (with one transmitting mirror in lighter gray), absorbing and reflecting an input field, which can be described by the input-output formalism, Eqs. (3.13) and (3.14). The output of a quantum system $\hat{a}_{\text{out}}$ can be used as input of another cascaded quantum system b. The cascaded master equation ensures unidirectional influence, where the dynamics of system b do not influence the dynamics of system a [see Eqs. (3.26), (3.27) and (3.28)]. In this way, an input $\hat{b}_{\text{in}}$ for a quantum system b can be modeled using a system a which emits $\hat{b}_{\text{in}} = \hat{a}_{\text{out}}$. (b) The Mølmer approach mathematically constructs an input pulse $\hat{a}_{\text{in}}$ with quantum state $\hat{\rho}_u$ in temporal pulse envelope $u(t)$ by auxiliary cavities with time-dependent loss rate $g_u(t)$ [see Eq. (3.31)]. Accordingly, another auxiliary cavity $\hat{a}_v$ with loss rate $g_v(t)$ [Eq. (3.32)] can model the output $\hat{a}_{\text{out}}$ of quantum system a into the specific mode $v(t)$. An easy example is given in Fig. 3.1(a,b) where a cavity with constant loss rate γ_a emits and perfectly absorbs an exponential temporal pulse. Cascading all quantum systems appropriately yields an efficient Lindblad description of the interaction of a quantum system with quantum fields.

3.2.2 Cascaded Quantum Systems

The fundamental concept of a cascaded system involves using the output of the first system to generate the input for the second system. Itinerant fields with tailored quantum properties are modeled as the output of a quantum system engineered to generate them. For example, sources that generate squeezed or antibunched light have been discussed in Secs. 1.4.1.2 and 1.5.1. Fig. 3.2(a) shows a cascaded quantum system composed of two subsystems characterized by annihilation operators $\hat{a}$ and $\hat{b}$.

For instance, we consider the example of two microwave cavities at zero temperature such that their joined but *uncoupled* dynamics can be described by the Lindblad master equation

$$\frac{\mathrm{d}\hat{\rho}}{\mathrm{d}t} = -\frac{i}{\hbar}[\hat{H}_a + \hat{H}_b, \hat{\rho}] + \sum_{\xi=a,b} \frac{1}{2}\left(2\hat{L}_\xi \hat{\rho} \hat{L}_\xi^\dagger - \hat{L}_\xi^\dagger \hat{L}_\xi \hat{\rho} - \hat{\rho}\hat{L}_\xi^\dagger \hat{L}_\xi\right) \tag{3.24}$$

$$\hat{L}_\xi = \sqrt{\gamma_\xi}\hat{\xi}\,. \tag{3.25}$$

When the output of the source (cavity $\hat{a}$) serves as the input of the second system, $\hat{a}_{\text{out}} = \hat{b}_{\text{in}}$, the two quantum systems must be coupled such that the dynamics of system $\hat{b}$ does not affect the time evolution $\hat{a}$.

Cascaded Master Equation (for two cavities with vacuum input into $\hat{a}$)

$$\frac{\mathrm{d}\hat{\rho}}{\mathrm{d}t} = -\frac{i}{\hbar}[\hat{H}_a + \hat{H}_b + \hat{H}_{\mathrm{int}}, \hat{\rho}] + \frac{1}{2}\left(2\hat{L}\hat{\rho}\hat{L}^\dagger - \hat{L}^\dagger\hat{L}\hat{\rho} - \rho\hat{L}^\dagger\hat{L}\right) \tag{3.26}$$

$$\hat{H}_{\mathrm{int}} = i\hbar\sqrt{\gamma_a\gamma_b}(\hat{a}^\dagger\hat{b} - \hat{a}\hat{b}^\dagger) \tag{3.27}$$

$$\hat{L} = \sqrt{\gamma_a}\hat{a} + \sqrt{\gamma_b}\hat{b} = \hat{L}_a + \hat{L}_b \tag{3.28}$$

The cascaded master equation models the unidirectional influence by a single joined Lindblad dissipator $\hat{L} = \hat{L}_a + \hat{L}_b$ and an interaction Hamiltonian term Eq. (3.27). In this way, the unidirectional influence $\hat{a} \to \hat{b}$ is reflected in the minus sign between $\hat{a}^\dagger\hat{b} - \hat{a}\hat{b}^\dagger$. The coherent (mutual) interaction introduced by $\hat{H}_{\mathrm{int}}$ is canceled by the modified dissipator $\hat{L}$. Although incorporating a quantum system modeling the source may considerably increase the Hilbert space dimensions, Eq. (3.26) retains a standard Lindblad form, which is easily implemented numerically.

3.2.3 Mølmer's Approach for Itinerant Photon Pulses

The Mølmer approach [see Fig. 3.2(b)] mathematically constructs an auxiliary harmonic oscillator as an artificial source that emits an arbitrary quantum pulse with temporal mode $u(t)$. A harmonic oscillator with constant single-photon loss rate, as in Sec. 3.1.3, emits an exponential pulse.

Interaction Hamiltonian and Loss Operator [for System in Fig. 3.2(b)]

$$\hat{H}_{\mathrm{int}} = \frac{i\hbar}{2}\left[\sqrt{\gamma_a}g_u\hat{a}_u^\dagger\hat{a} + \sqrt{\gamma_a}g_v^*\hat{a}^\dagger\hat{a}_v + g_ug_v^*\hat{a}_u^\dagger\hat{a}_v - \mathrm{h.c.}\right] \tag{3.29}$$

$$\hat{L} = \sqrt{\gamma_a}\hat{a} + g_u^*\hat{a}_u + g_v^*\hat{a}_v \tag{3.30}$$

To emit an arbitrary temporal pulse, the Mølmer approach employs auxiliary cavities with time-dependent loss rates. Specifically, a cavity with an artificial loss operator $\hat{L}_u = g_u^*(t)\hat{a}_u$ such that

$$g_u(t) = \frac{u^*(t)}{\sqrt{1 - \int_0^t |u(\tau)|^2\,\mathrm{d}\tau}} \tag{3.31}$$

emits the temporal mode $u(t)$ into its environment [189–193]. Perfect absorption of a mode $v(t)$ can be similarly modeled by an auxiliary cavity with the time-dependent loss function

$$g_v(t) = -\frac{v^*(t)}{\sqrt{\int_0^t |v(\tau)|^2\,\mathrm{d}\tau}}\,. \tag{3.32}$$

The method can be extended to model quantum systems that interact with multiple input and output modes [190].

3.3 Heterodyne Detection of a Cavity's Output

In experimental setups of Josephson-photonics devices, the microwave cavities leak microwave light into a transmission line. That signal is then amplified by a phase-preserving amplifier that introduces the noise mode $\hat{r}$. Subsequently, the quadratures of the output field are recorded with a classical device. If the gain of the amplifier is large, $G \gg 1$, the recorded signal

$$\hat{J}^{(a)}(t) = \sqrt{G}\hat{a}_{\text{out}}(t) + \sqrt{G-1}\hat{r}^\dagger \tag{3.33}$$

of cavity $\hat{a}$ behaves approximately classical. A quantum-limited amplifier would only add vacuum noise, resulting in classical white noise [194]. This experimental scenario can theoretically be modeled [195] using a heterodyne detection scheme from quantum optics [196], where the output is mixed with a beam splitter introducing vacuum noise, and subsequently recorded. Such a continuous measurement of the quadratures can be described by the stochastic Schrödinger equation.

3.3.1 The Stochastic Schrödinger Equation

The stochastic Schrödinger equation describes the continuous heterodyne quadrature measurement of the output of a quantum system. For simplicity, here we consider the heterodyne detection of the output of a single harmonic oscillator $\hat{a}$ that is coupled to a zero-temperature heat bath, such that the time evolution can be described by the Lindblad master equation

$$\frac{\mathrm{d}}{\mathrm{d}t}\hat{\rho} = -\frac{i}{\hbar}[\hat{H}, \hat{\rho}] + \frac{2\hat{L}_a\hat{\rho}\hat{L}_a^\dagger - \hat{L}_a^\dagger\hat{L}_a\hat{\rho} - \hat{\rho}\hat{L}_a^\dagger\hat{L}_a}{2} \tag{3.34}$$

with system Hamiltonian $\hat{H}$ and Lindblad operator $\hat{L}_a = \sqrt{\gamma_a}\hat{a}$.

The (unnormalized) stochastic Schrödinger equation [196, 197]

$$\mathrm{d}\,|\psi_k\rangle = \left[-\frac{i}{\hbar}\hat{H} - \frac{\hat{L}_a^\dagger\hat{L}_a}{2} + \hat{L}_a\left(J_k^{(a)}\right)^*\right]|\psi_k\rangle\ \mathrm{d}t \tag{3.35}$$

describes the time evolution of the quantum trajectory $|\psi_k\rangle$ that represents the quantum state of a single experimental realization. The equation of motion is a quantum diffusion equation that elegantly describes how the result of the noisy measurement

$$J_k^{(a)}(t) = \langle\psi_k|\,\hat{L}_a\,|\psi_k\rangle + \xi_k(t) \tag{3.36}$$

affects the time evolution of the quantum state. We note that this feedback is of pure quantum-informational nature, since in experiments circulators prevent back-reflection from the measurement apparatus (or the amplifier) to the Josephson-photonics device. Unlike a strong projective measurement, heterodyne detection only weakly modifies the time evolution of the quantum state. The stochastic white noise term, numerically modeled by the complex Wiener process

$$\xi_k(t) = \frac{\mathrm{d}Z_t}{\mathrm{d}t} = \frac{\mathrm{d}W_t^{(x)} + i\mathrm{d}W_t^{(p)}}{\sqrt{2}\mathrm{d}t} \tag{3.37}$$

with $\mathbb{E}[\mathrm{d}Z_t] = 0$ and $\mathbb{E}[\mathrm{d}Z_t^* \mathrm{d}Z_t] = \mathrm{d}t$, describes the measurement noise on the two quadratures. Thus, it is composed of two real independent Wiener increments $\mathrm{d}W_t^{(x)}$ and $\mathrm{d}W_t^{(x)}$ (with $\mathbb{E}[\mathrm{d}W_t^{(x/p)}] = 0$ and $\mathbb{E}[\mathrm{d}W_t^{(x/p)} \mathrm{d}W_t^{(x/p)}] = \mathrm{d}t$). In the limit of infinitely many recorded trajectories N_{traj}, the ensemble-average

$$\mathbb{E}\left[|\psi_k\rangle \langle\psi_k|\right] \to \hat{\rho} \quad (N_{\mathrm{traj}} \to \infty) \tag{3.38}$$

converges to the solution $\hat{\rho}$ of the Lindblad master equation.

3.3.2 Heterodyne Detection of a Single Microwave Cavity

As a specific example, we prepare the microwave cavity from Sec. 3.3.1 in the single-photon Fock state $|\psi(t=0)\rangle = |1\rangle$. A heterodyne detection scheme (as described above) measures the quadratures of the cavity that emits its photon.

A single experimental record $J_k^{(a)}(t)$ only gains limited information about the quantum system, but nevertheless affects the cavity's time evolution. At the few-photon level, the experimental record is dominated by noise [see Fig. 3.3(a)], hiding the information obtained about the quantum system. However, $J_k^{(a)}(t)$ can be integrated with a temporal mode envelope $u(t)$, resulting in a complex number α_k. When repeating the exact same measurement multiple times, a histogram of all α_k samples the Husimi-Q function of the quantum state of mode $u(t)$ [198, 199].

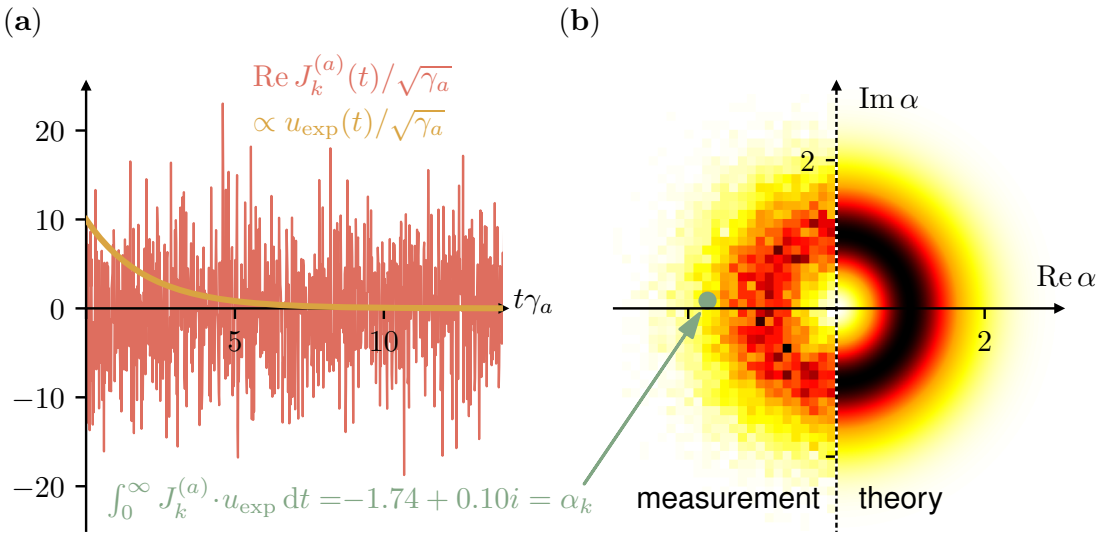

Figure 3.3: Heterodyne detection of the output of a microwave cavity. The resonator is initially prepared in Fock state $|\psi(t=0)\rangle = |1\rangle$ and emits the photon into a transmission line. A subsequent amplification with a quantum-limited amplifier introduces white noise. If the amplifier has large gain, a heterodyne detection scheme records a classical signal $J_k^{(a)}(t)$, composed of the (amplified) output field $\hat{a}_{\mathrm{out}}$ of the system hidden in noise. The recorded signal can be multiplied with the output mode of the system [in this case the exponential mode, c.f. Fig.3.1(a)] and integrated, resulting in a single number α_k.
(b) After repeating the same experiment multiple times, a histogram of all obtained values α_k samples the Husimi-Q function of the quantum state $|\psi(t=0)\rangle$ which is emitted in the exponential mode.
[Method: $4 \cdot 10^4$ trajectories for $J_k^{(a)}$ are sampled with the resolution $\mathrm{d}t = 0.015/\gamma_a$.]

In our specific example, the cavity $\hat{a}$ leaks its quantum state into an exponential mode $u = u_{\text{exp}}(t)$ (compare Eq. (3.12) of Sec. 3.1.3). Choosing this mode as the integration kernel, the repeated measurements sample the Husimi-Q function of the state $|\psi(t = 0)\rangle$, as shown in Fig. 3.3(b).

PART B

Results

4 Phase Stabilization of Josephson-Photonics Devices

Josephson-photonics devices, where a dc-voltage biased Josephson junction is connected in series to microwave cavities, can create resonator states that could be used in quantum technological applications, such as cat states for quantum computational tasks (see Sec. 1.4.2), or two-mode squeezed states for a quantum radar (compare Sec. 1.5.2). However, these applications crucially rely on a stable phase-space angle of the quantum states. Since Josephson-photonics devices are driven by a dc-voltage bias, they lack such a stable reference phase (c.f. Sec. 1.7). As a direct consequence, noise averages over the phase-space angle and phase-sensitive states are destroyed by noise and can no longer be directly observed.
One possible solution is to stabilize the phase-space angle by injecting a small ac signal with a stable phase to which the system is synchronized (see Sec. 2). Recently, injection locking was experimentally [59, 62, 200] as well as to some extent theoretically [201, 202] studied in multi-mode Josephson-photonics devices. Yet, an in-depth theory of a simpler model that explains in detail how the phase can be stabilized is still missing.

Pub. (*i*) (see Secs. 4.1.1) therefore studies in the classical regime how the phase of a Josephson-photonics device can be stabilized. To enable a correct description of Josephson-photonics devices as self-sustained oscillations, we will focus on adding an in-series resistance to the previously used theoretical model (presented in Sec. 1.3). We explicitly show how such self-sustained oscillations can be injection locked by an external signal and further study the case of mutual synchronization (without an external locking signal) between two devices that are capacitively coupled.
Furthermore, Sec. 4.1.2 extends the classical description by Adler (c.f. Sec. 2.2.2) for a circuit with an additional in-series resistor by replacing that resistor with an arbitrary impedance. To be precise, one knows that the noise entering the

system can be reduced by an in-series low-pass filter, i.e. a parallel R_0C_0-circuit. By modeling such a system, we find phase dynamics that are analogous to those of the RCSJ (resistively and capacitively shunted junction) model and that can, for instance, show hysteresis.
Pub. (*ii*) (see Sec. 4.2.1) translates the findings from the classical to the quantum regime, where we derive a detailed description of injection locking and synchronization in the presence of shot noise of the tunneling Cooper pairs.
The stabilization of the phase-space angle of single- and two-mode squeezed states, which are examples of states that exist solely in the quantum regime, is discussed in Pub. (*iii*) (compare Sec. 4.2.2), where we specifically explain how Josephson-photonics devices can be used for quantum technological applications.
Sec. 4.2.3 discusses injection locking of cat states. Although a quantum mechanical description of injection locking could be applied in a straightforward way, here we follow an instructive alternative theoretical approach for a regime which is dominated by classical noise, such that a full quantum description is less critical.
Finally, Sec. 4.2.4 presents an alternative to phase stabilization by injection locking and synchronization. By measuring only very few experimentally accessible expectation values, the resonator's quantum state without phase diffusion can be reconstructed by optimizing an ansatz for the undiffused quantum state. In this way, information about the phase-space angle can be restored, which mitigates the issue of the neutrally stable phase for certain use cases.

4.1 Phase Stabilization in the Classical Regime

We first focus on Josephson-photonics devices in the classical regime. Sec. 4.1.1 incorporates an in-series resistor into the theoretical model to correctly describe the physics of self-sustained oscillations with a neutrally stable phase-space angle. By deriving an effective Adler equation, we study how the phase can be stabilized by injection locking and mutual synchronization. Further, we discuss the effects of classical noise on the locking signatures. Here, we can also identify short periods in which the system is unsynchronized, the so-called phase slips.
Sec. 4.1.2 instead incorporates a general in-series impedance. We show how the Adler equation derived in Pub. (*i*) is then modified and consider the specific case, where the in-series impedance is a parallel R_0C_0-circuit. Such a low-pass filter can reduce the noise entering the system, but also introduces hysteretic effects known from the RCSJ model.

4.1.1 Publication (*i*): *Injection locking and synchronization in Josephson photonics devices*

4.1.1.1 Bibliographic Data and Author's Contribution

Title	Injection locking and synchronization in Josephson photonics devices
Authors	Lukas Danner, Ciprian Padurariu, Joachim Ankerhold, and Björn Kubala
Journal	Physical Review B
Volume	104
Number	054517
Year	2021
DOI	https://doi.org/10.1103/PhysRevB.104.054517
Copyright	©2021 American Physical Society [3]

The author is the first author of this publication. He performed analytics, implemented and executed numerical calculations and contributed to their interpretation. The author prepared the figures for the publication and contributed significantly to the preparation of the manuscript. The author is the main author.

4.1.1.2 Summary of Publication (*i*)

The publication *Injection locking and synchronization in Josephson photonics devices* develops an in-depth theory explaining how injection locking and synchronization can stabilize the resonator phase of Josephson-photonics devices against

[3] According to the copyright policies of APS, the usage of the complete article is kindly allowed: https://journals.aps.org/prl/copyrightFAQ.html

noise. Here, a single-mode Josephson-photonics setup is studied in the classical regime, which is optimally suited to fundamentally explain the phenomenon of synchronization. It serves as a role model to derive the Adler equation of the synchronization dynamics for similar devices [12, 48, 59, 62] and paves the way for a description of the quantum regime.

Josephson-photonics devices as self-sustained oscillators

Extending the description from Sec. 1.3.1, the theoretical model of a Josephson-photonics device includes a finite, but small in-series resistor R_0, which is present in real experiments, but was until now neglected in theoretical works. However, its role is crucial for understanding both phase diffusion by noise and injection locking and synchronization in such devices. To clarify the function of the in-series resistor, we first consider the case where the dc voltage is applied at resonance with the harmonic oscillator's eigenfrequency, $\omega_{\mathrm{dc}} \approx \omega_0$.
If $R_0 = 0$, the resonator's steady-state oscillation frequency is fixed to the applied dc voltage, $\omega_J = \omega_{\mathrm{dc}}$ (and to multiples of it due to the Josephson nonlinearity). The resulting oscillations are forced (see Fig. 2 of Pub. (i) and Sec. 2.1) with a fixed phase-space angle in the rotating frame. Therefore, this model does not describe the experimental reality of a free phase-space angle.
Instead, a finite in-series resistance $R_0 > 0$ introduces an additional phase

$$\varphi_{R_0}(t) \propto R_0 \int_0^t I_{\mathrm{CP}}(\tau)\,\mathrm{d}\tau \tag{4.1}$$

into the circuit, modeling a more realistic voltage source. The oscillation frequency of the resonator

$$\omega_J = \omega_{\mathrm{dc}} - \frac{2e}{\hbar} R_0 I_{\mathrm{dc}}[\varphi(t)] \tag{4.2}$$

then directly depends on the directed Cooper-pair current I_{dc}. Crucially, the dc current and the oscillator's position φ influence each other, giving rise to feedback between them. This dynamical interaction yields a free phase-space angle in the steady state. This system is therefore a self-sustained oscillator with a well-defined limit cycle with stable oscillation amplitude [Fig. 2(a) of Pub. (i)]. The neutrally stable phase-space angle is both susceptible to noise, but can also be entrained to phase-stable external oscillations.

Stabilization of the resonator's phase by injection locking

Pub. (i) focuses mainly on adding a small injection-locking signal to the dc voltage, $V(t) = V_{\mathrm{dc}} + V_{\mathrm{ac}} \cos(\Omega t + \phi_\epsilon)$. We specifically inject the signal at the fundamental resonance, $\Omega \approx \omega_0$ and assume a small locking amplitude $\epsilon = \frac{2e}{\hbar\Omega} V_{\mathrm{ac}} \ll \omega_{\mathrm{dc}}$. This locking signal influences the directed contribution $I_{\mathrm{dc}}(\epsilon)$ of the full Cooper-pair current

$$I_{\mathrm{CP}} = I_{\mathrm{crit}} \sin\left[\omega_{\mathrm{dc}} t - \varphi_{R_0} - \varphi + \epsilon \sin(\Omega t + \phi_\epsilon)\right] \tag{4.3}$$

and, consequently, also the oscillation frequency $\omega_J(\epsilon)$. When the applied locking signal is sufficiently large, $\omega_J(\epsilon)$ can be pulled towards the injected frequency to overcome a frequency mismatch $\nu_0 = \omega_J(\epsilon = 0) - \Omega$. As one main result, we find

that injection locking is only possible because of the system's finite impedance at small beating frequencies of orders of $\nu_0 \approx \gamma \ll \omega_0$. This impedance is introduced here (in the simplest possible way) by the in-series resistance R_0.

Reduced description of injection locking by Adler

The central result of Pub. (*i*) is the theoretical description of the locking dynamics by deriving a reduced Adler equation [c.f. Sec. 2.2.2 and Eq. (13) of Pub. (*i*)]. We first define the Adler phase

$$\psi = [\omega_J t + \theta(t)] - [\Omega t + \phi_\epsilon] \tag{4.4}$$

as the difference between the phase of the low-frequency contribution $\theta(t)$ of the Josephson phase φ_J and the phase of the locking drive. Then the oscillations of the system are synchronized to the external drive when the Adler phase becomes constant in time, $\dot{\psi} = 0$. Its equation of motion describes an overdamped phase particle ψ moving in a washboard potential

$$V(\psi) = \nu\,\psi + \frac{\epsilon}{2}\frac{2e}{\hbar} I_{\mathrm{crit}} R_0 \cos(\psi)\,, \tag{4.5}$$

where [when $\epsilon > \hbar|\nu|/(eI_{\mathrm{crit}}R_0)$] minima arise, in which the phase particle can then be trapped. The system is then synchronized to the injection drive.

Effects of noise

In a further step, we show that the synchronized state is stable by including voltage noise, which can push the phase particle out of its potential minimum. Without a locking signal, the potential is simply flat. The steady-state phase-space distribution (in a frame rotating with ω_J) of the self-sustained oscillator is averaged over all phase-space angles because of a broadened oscillation frequency [see Fig. 4(a, b) of Pub. (*i*)]. A locking drive of sufficient strength creates an attractive force $F \propto U'(\psi)$ for the phase particle to the potential minimum. Consequently, the oscillation frequency is sharpened [Fig. 4(a)], resulting in a steady-state phase-space distribution with a localized phase-space angle [Fig. 4(d)]. As expected, stronger noise can push ψ over the potential barrier leading to desynchronization. However, the phase particle can then be re-trapped in one of the next minima. A sudden dynamical change of ψ by (multiples of) 2π is called a phase slip. It corresponds to one or multiple full rotations of the phase-space angle around the limit cycle (in the rotating frame). In a Kramer's regime [203], phase slips are exponentially suppressed. Nevertheless, noise gives rise to a broadening of the transition between locked region and unlocked region [compare Fig. 5(c)], which is sharp in an Adler theory without noise (compare Fig. 2.5 of Sec. 2.2.3).

Injection locking of higher-order resonances

Since phase-stable quantum states, such as (two-mode) squeezed states, are highly relevant for quantum technological applications, we additionally study injection locking for higher-order resonance conditions $\omega_{\mathrm{dc}} \approx p\,\omega_0$ (where here $p \in \mathbb{N}$, also compare Secs. 1.4.1 and 1.5.2). Classically, a parametric resonance condition $\omega_{\mathrm{dc}} \approx 2\omega_0$ yields steady states with finite oscillation amplitude only when the system is driven above a threshold. Then, the steady state is two-fold degenerate

and exhibits solutions with the same stable amplitude but opposite phase-space angles. Of course, noise leads to an effective averaging of the neutrally stable phase and, as before, an injection locking signal can stabilize the phase-space angle [see Fig. 6(a)]. However, when the ac signal is injected with a frequency $\Omega \approx \omega_0$, it breaks the degeneracy and picks only one of the degenerate solutions. On the other hand, a parametric locking signal $\Omega \approx 2\omega_0 \approx \omega_{\mathrm{dc}}$ will preserve the degeneracy of the two degenerate solutions. Noise-induced phase slips then lead to a sudden change of the phase-space angle by only π. Here, the system switches between two degenerate stable solutions [Fig. 6(c)]. This is an important finding, which directly connects to Josephson-photonics devices in the quantum regime. When stabilizing the squeezing angle of a two-fold symmetric quantum state, it is crucial that the injected signal preserves the two-fold symmetry (compare Pub. (*iii*) in Sec. 4.2.2).

Mutual synchronization of two Josephson-photonics devices

Finally, Pub. (*i*) discusses mutual synchronization of two devices, which weakly interact when capacitively (or inductively) coupled. We show how such an interaction adjusts the oscillation frequency of both devices. The capacitive coupling cannot be tuned in situ in experiments, whereas the Josephson energy E_J of both devices can easily be adjusted using SQUIDs. In this way, the systems can be tuned into (and also out of) synchronized states [see Fig. 7 of Pub. (*i*)]. An extension of the single-mode theory yields a Kuramoto-like Adler equation for synchronization between two devices.

In summary, we have incorporated an in-series resistor into the theoretical model of a Josephson-photonics device, enabling the description of self-sustained oscillations of the resonator in the classical regime. Synchronization and injection locking can stabilize the phase-space angle of the resonator against noise. Pub. (*i*) lays the foundation for the development of a theory describing devices operated in the quantum regime, where a stable phase is crucial for quantum applications.

Injection locking and synchronization in Josephson photonics devices

Lukas Danner,[1,2,*] Ciprian Padurariu,[2,†] Joachim Ankerhold,[2,‡] and Björn Kubala[1,2,§]
[1]*Institute of Quantum Technologies, German Aerospace Center (DLR), Söflinger Straße 100, D-89077, Ulm, Germany*
[2]*Institute for Complex Quantum Systems and IQST, Ulm University, Albert-Einstein-Allee 11, D-89069 Ulm, Germany*

(Received 6 May 2021; revised 28 July 2021; accepted 10 August 2021; published 25 August 2021)

Injection locking can stabilize a source of radiation, leading to an efficient suppression of noise-induced spectral broadening and therefore, to a narrow spectrum. The technique is well established in laser physics, where a phenomenological description due to Adler is usually sufficient. Recently, locking experiments were performed in Josephson photonics devices, where microwave radiation is created by inelastic Cooper pair tunneling across a dc-biased Josephson junction connected in-series with a microwave resonator. An in-depth theory of locking for such devices, accounting for the Josephson nonlinearity and the specific engineered environments, is lacking. Here, we study injection locking in a typical Josephson photonics device where the environment consists of a single mode cavity, operated in the classical regime. We show that an in-series resistance, however small, is an important ingredient in describing self-sustained Josephson oscillations and enables the locking region. We derive a dynamical equation describing locking, similar to an Adler equation, from the specific circuit equations. The effect of noise on the locked Josephson phase is described in terms of phase slips in a modified washboard potential. For weak noise, the spectral broadening is reduced exponentially with the injection signal. When this signal is provided from a second Josephson device, the two devices synchronize. In the linearized limit, we recover the Kuramoto model of synchronized oscillators. The picture of classical phase slips established here suggests a natural extension towards a theory of locking in the quantum regime.

DOI: 10.1103/PhysRevB.104.054517

I. INTRODUCTION

A number of experiments have demonstrated injection locking in solid-state devices that generate microwave radiation, e.g., double quantum dot masers [1] and Josephson microwave amplifiers [2]. Recently, injection locking has also been observed in a Josephson photonics device dubbed the Josephson laser [3] refining earlier experiments employing a Cooper pair transistor [4]. Josephson photonics devices use inelastic Cooper pair tunneling across a Josephson junction to convert the energy from a constant voltage bias source into microwave radiation of corresponding frequency. By applying a small amplitude ac signal on top of the dc voltage bias, a small locked region was found in Ref. [3], where the spectrum of the emitted microwave radiation becomes an extremely sharp peak pinned to the frequency of the injected signal. Injection locking may prove a key enabling technology for Josephson photonics devices and, as we will show here, also allows us to study interesting synchronization phenomena when realized by coupling different devices.

The typical setup of Josephson photonics devices consists of a voltage-biased Josephson junction coupled in series to a microwave cavity. The cavity acts as an environment engineered to absorb the energy of the tunneling Cooper pair as microwave photons [5]. These devices have been developed as efficient sources of *quantum* microwaves by tailoring the properties of the cavity, or by deploying several cavities in series. In that manner, recent experiments have demonstrated bright single-photon sources [6,7] as well as sources of two-mode light with nonclassical correlations [8] and of entangled photons [9]. Theoretically, Josephson photonics devices have been proposed as platforms for nonlinear dynamics experiments that take advantage of the strong Josephson nonlinearity and can be operated both in the classical and in the quantum regimes [10–27] by designing low- or high-impedance resonators.

The scope of these varied applications can be significantly broadened by enhancing the phase stability of the emitted light against electronic noises, currently an outstanding challenge. While phase stability is a ubiquitous issue in microwave photonics of all types, Josephson photonics devices are particularly susceptible because the radiation is generated using a constant voltage source. This does not provide a reference phase and thus favors no particular value of the oscillation phase, i.e., in the language of nonlinear dynamics the phase is neutral.

Here, we will show that injection locking is an efficient method to achieve phase stability of Josephson photonics circuits. In this approach, an ac signal is injected directly into the circuit, with the purpose of phase locking the coupled Josephson and cavity oscillations. Furthermore, injection locking straightforwardly extends to a scenario where an ac signal stemming from one Josephson photonics circuit is used to lock another one so that the two devices synchronize. While exploring injection locking and synchronization as paradigmatic

*lukas.danner@uni-ulm.de
†ciprian.padurariu@uni-ulm.de
‡joachim.ankerhold@uni-ulm.de
§bjoern.kubala@uni-ulm.de

examples of nonlinear classical dynamics in a new system class is of interest in itself, Josephson photonics devices will allow future studies to extend such investigations to a regime where the dominant source of noise is due to quantum fluctuations. In particular, as we will later argue, injection locking in these devices could become a promising platform for studying quantum tunneling of the Josephson phase, a phenomenon analogous to the flux tunneling, or quantum phase slips [28], observed in thin superconducting wires [29–32].

The textbook theoretical description of injection locking is based on a phenomenological approach due to Adler [33]. Applied to a universal class of oscillators, termed self-sustained oscillators, the Adler equation describes their effective dynamics by a single equation for the (limit cycle) phase in the locked region and its vicinity [34]. Experimentally observed features in Ref. [3], such as frequency pulling and a scaling of the locking region's width with the amplitude of the injection signal, can successfully be described by such an approach. However, a derivation of the effective Adler equation starting from the fundamental underlying equations of motion, the Josephson circuit equations, has not been established. In consequence, the crucial parameter of the Adler model, the critical detuning that defines the locked region, has not been connected to the device properties, which in turn means that the optimal design of Josephson photonics devices for locking remains unknown.

In fact, the Josephson laser in Ref. [3] operated in a large dc-voltage bias regime, where microwaves are emitted at a down-converted frequency from a multimode cavity, and the resulting dynamics of the device is complicated and highly nonlinear. Recently, a theoretical description of the device dynamics was formulated [22], that describes the microwave emission using an approach based on a semiclassical system of coupled nonlinear differential equations. However, the model used could not capture the observed injection locking phenomena. The reason for this could not be clearly identified and to the best of our knowledge has remained an open challenge until now. The experiment Ref. [3] and the theory of Ref. [22] have been taken to imply that the highly nonlinear microwave emission generated in the Josephson laser and possibly the presence of a multimode cavity, may be a requirement for observing injection locking. As we show here, this interpretation turns out to be inaccurate, emphasizing the need for theoretical understanding of injection locking in Josephson photonics devices, particularly the theoretical description of the simplest Josephson photonics device that can be injection locked. Absent such a description, the best design, the circuit parameters, and the bounds on noises required to observe injection locking have not been systematically identified for Josephson photonics devices.

We find that adding a resistance in series with the conventional Josephson photonics device of a voltage-biased single-mode cavity is the important ingredient enabling injection locking. In fact, the in-series resistance realizes a model for an actual source, which is always somewhere in between the idealized voltage and current bias. If this resistance is small, as we will assume, the source is closer to an idealized voltage bias.

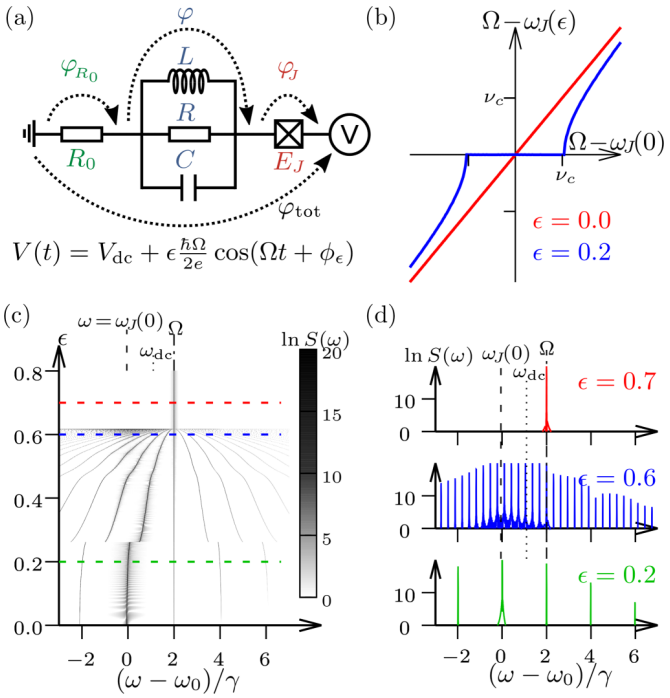

FIG. 1. Injection locking of Josephson oscillations. (a) Sketch of a Josephson photonics circuit with an in-series resistance and a single resonance (with frequency $\omega_0 = 1/\sqrt{LC}$ and width $\gamma = 1/RC$). (b) Typical Adler curve showing injection locking [$\omega_J(\epsilon) = \Omega$] as the Josephson frequency $\omega_J(\epsilon)$ is pulled towards the locking frequency Ω. Without a locking signal the Josephson frequency $\omega_J(0)$ is determined by the voltage bias, $\omega_{\rm dc} = 2eV/\hbar$, reduced by the voltage drop at the in-series resistance R_0 [$\omega_J(0) \approx \omega_0 + 2\gamma$; $\omega_{\rm dc} = \omega_0 + 2.3\gamma$]. Locking occurs for detunings, $\Omega - \omega_J(0)$, below a critical value $\nu_c(\epsilon) = \frac{e}{\hbar} I_c R_0 \epsilon$, see Sec. III. (c) Grayscale plot of emission spectrum $S(\omega, \epsilon)$ and (d) cuts for various locking signal amplitudes ϵ. In the locked state all emission occurs at the locking frequency Ω, whereas without a locking signal the cavity emits at the Josephson frequency given by the (reduced) dc bias, $\omega_J(0)$. The transition is marked by a characteristic fan structure. [Parameters values for $\omega_{\rm dc}, \omega_J(0)$ in (c) and (d) differ from (b) as indicated on the figure; other parameters: $Q = \omega_0/\gamma = 30$, $\frac{2e}{\hbar} I_c R/\omega_0 = \tilde{I}_c = 0.5$, $\frac{2e}{\hbar} I_c R_0 = v_{R_0} = \frac{4}{30}\omega_0$.]

Here, we study injection locking and synchronization in Josephson photonics devices in the classical regime. We show that injection locking can be achieved in the simplest Josephson photonics device, i.e., a device where the environment consists of an LC resonance, (a *single-mode* cavity), and a (small) in-series resistance R_0, see Fig. 1(a). We mainly focus on the case when the bias voltage is set close to this resonance, $2eV_{\rm dc}/\hbar = \omega_{\rm dc} \approx \omega_0 = 1/\sqrt{LC}$, and only briefly discuss the situation where the radiation is a result of parametric down conversion, when the bias is tuned near twice the value of the resonance frequency. For this model, we derive analytically the device-specific Adler-type equation starting from the Kirchhoff equations of the circuit. The Adler-equation allows us to explain all typical locking phenomena [see Figs. 1(b)–1(d)] resulting from the Kirchhoff equations of motion. Based on the Adler equation, we also provide bounds on the electric noises that can be stabilized, and suggestions for optimal device design.

TABLE I. Physical quantities that characterize the device.

Physical quantity	Parametrization	Unit
resonance frequency	ω_0	s^{-1}
resonance width	$\gamma = (RC)^{-1}$	s^{-1}
dc bias voltage	$\omega_{dc} = (2e/\hbar)V_{dc}$	s^{-1}
Josephson frequency	$\omega_J \neq \omega_{dc}$	s^{-1}
injection signal frequency	Ω	s^{-1}
scale of residual voltage at R_0	$v_{R_0} = (2e/\hbar)I_cR_0$	s^{-1}
Josephson driving strength	$\tilde{I}_c = (2e/\hbar)I_cR/\omega_0$	1
injection signal amplitude	$\epsilon = (2e/\hbar)V_{ac}/\Omega$	1

In Sec. II we will analyze the semiclassical nonlinear behavior of our model circuit based on the Kirchhoff equations and explain the concepts of forced versus self-sustained oscillations. In Sec. III we derive the analytical equation of Adler type that describes the injection locking region and the slow dynamics of the Josephson phase just outside the locked region. The effects of noise, the appearance of phase slips, and the reduction of the line width are presented in Sec. IV. Section V deals with locking at higher-order resonances, while in Sec. VI we turn to the synchronization of two capacitively coupled copies of the Josephson photonics device. Finally, Sec. VII presents our concluding remarks and an outlook on future work.

II. PRELIMINARIES

We study a Josephson photonics device modeled by the circuit in Fig. 1(a). The dynamics of the circuit is conveniently parametrized by the phase drop over the Josephson junction φ_J and the phase across the LC resonator φ. The classical equations of motion are the Kirchhoff equations of the circuit

$$\dot{\varphi}_J = \frac{2e}{\hbar}V(t) - \frac{2e}{\hbar}I_cR_0\sin(\varphi_J) - \dot{\varphi}; \tag{1a}$$

$$\ddot{\varphi} + \gamma\dot{\varphi} + \omega_0^2\varphi = \frac{2eI_cR}{\hbar\omega_0}\gamma\omega_0\sin\varphi_J. \tag{1b}$$

Here, $\omega_0 = 1/\sqrt{LC}$ is the resonance frequency and $\gamma = 1/RC$ is the resonance width. The parametrization of physical quantities characterizing the device used frequently throughout the paper is organized in Table I.

Before showing in Sec. III in detail how Eq. (1) allows the phase of the radiation emitted by the circuit to be stabilized by a locking signal, we want to gain some physical intuition, how the Josephson nonlinearity impacts the dynamics described by Eq. (1) within or outside of the locked regime.

While nonlinearity is generically known as a crucial ingredient for locking and synchronization phenomena, nonlinear effects have also been extensively studied (theoretically and experimentally) for Josephson photonics circuits, where $R_0 \equiv 0$ and locking phenomena are absent. In that case Eq. (1a) can be directly integrated [setting $\varphi_J(0) + \varphi(0) = 0$] and substituted in (1b) resulting in $\ddot{\varphi} + \gamma\dot{\varphi} + \omega_0^2\varphi = \tilde{I}_c\gamma\omega_0\sin[\frac{2e}{\hbar}\int_0^t dt'V(t') - \varphi]$, the standard equation of motion of (classical) Josephson photonics (cf. Refs. [12] and [17]) describing a *harmonic* LC resonator with an *unconventional nonlinear drive term*.

Considering a pure dc drive close to the fundamental resonance, $\omega_{dc} - \omega_0 \lesssim \gamma$, it is easy to see, that for small $\tilde{I}_c \ll 1$, the oscillation amplitude of $\varphi(t)$ remains small and the zeroth-order expansion of the Josephson nonlinearity in φ yields a linearly driven harmonic oscillator, that responds with an oscillation described by a complex amplitude $\tilde{\varphi}$ with $|\tilde{\varphi}| = |\tilde{I}_c\gamma/[2(\omega_{dc} - \omega_0) + i\gamma]|$.

For larger $\tilde{I}_c$ a rotating-wave approximation yields a time-independent equation for the oscillation amplitude at frequency ω_{dc} (higher harmonics of ω_{dc} are off resonant and can be neglected)

$$\tilde{\varphi} = \tilde{I}_c\frac{\gamma}{2(\omega_{dc} - \omega_0) + i\gamma}\left(J_0(|\tilde{\varphi}|)\frac{\tilde{\varphi}^*}{|\tilde{\varphi}|} - J_2(|\tilde{\varphi}|)\frac{\tilde{\varphi}}{|\tilde{\varphi}|}\right).$$

The Bessel functions of the first kind are manifestations of the highly nonlinear Josephson drive and can give rise to bifurcations and multistable states in this regime.

Adding a small ac signal to the voltage drive,

$$V(t) = V_{dc} + V_{ac}\cos(\Omega t + \phi_\epsilon), \tag{2}$$

leads to a simple superposition of responses with the two frequencies ω_{dc} and Ω, if R_0 is neglected.

In most of the following, to emphasize the simplest locking scheme, we restrict our study to locking of the linear regime of Josephson photonics, where $\tilde{I}_c \ll 1$. Despite the small amplitude of resonant oscillations in this regime, it is the presence of the in-series resistance R_0, which will lead to a different manifestation of Josephson nonlinearity and pave the path to locking and synchronization phenomena. To understand the nature of this distinct nonlinear effect, we have to consider how the presence of a finite resistance R_0 modifies the picture of the driven oscillator sketched above.

Origin of locking. For finite but small $R_0 \ll R$, and $\tilde{I}_c \ll 1$ so that φ remains small, Eq. (1a) can be iteratively integrated

$$\begin{aligned}\varphi_J(t) &= \int_0^t dt'\left\{\frac{2e}{\hbar}V(t') - v_{R_0}\sin[\varphi_J(t')]\right\} - \varphi(t)\\ &\approx \frac{2e}{\hbar}\int_0^t dt'V(t') - \varphi(t)\\ &\quad - v_{R_0}\int_0^t dt_1\sin\left[\frac{2e}{\hbar}\int_0^{t_1} dt_2V(t_2)\right]\end{aligned} \tag{3}$$

in a Born-like approximation up to leading order in the small quantities $\tilde{I}_c$ and (v_{R_0}/ω_0). (Note also that φ is small with $|\tilde{\varphi}| \propto \tilde{I}_c$.)

In addition to the dc and ac components of the voltage drive, the presence of R_0 gives rise to a low-frequency Fourier component $\tilde{\varphi}_J(\nu) = \mathcal{F}[\varphi_J(t)]_\nu$, at the frequency of beats $\nu = (\omega_{dc} - \Omega)$ caused by a slowly oscillating part of the Josephson current $I_J \sim \sin\varphi_J$. In fact, we find

$$\begin{aligned}|\tilde{\varphi}_J(\nu)| &= v_{R_0}\,\mathcal{F}\left[\int_0^t dt_1\sin\left(\frac{2e}{\hbar}\int_0^{t_1} dt_2V(t_2)\right)\right]_\nu\\ &= \frac{\epsilon}{2}\frac{v_{R_0}}{\nu},\end{aligned}$$

i.e., *the closer the frequencies of locking signal* Ω *and dc drive* $\omega_{\rm dc}$ *become, the slower the oscillations in* I_J*, and the larger the integrated effect in the* $\tilde{\varphi}_J(\nu)$ *oscillations.*

In consequence, even for small locking amplitude ϵ and small, but finite, υ_{R_0} the low-frequency oscillations in the Josephson phase $\tilde{\varphi}_J(\nu)$ can become so large that (despite $\tilde{I}_c \ll 1$) the nonlinearity of the driving term $\sim \sin\varphi_J$ in Eq. (1b) comes to bear. This nonlinearity of the slow response produces an increasing number of sidebands in the oscillator response $\tilde{\varphi}$ around the Josephson frequency, each sideband separated by ν, as seen in Fig. 1(d), until eventually the oscillations lock, with the response concentrated at frequency Ω, cf. the typical fan structure of Fig. 1(c).

While in Sec. III, we will properly derive the corresponding locked and unlocked solution, from the simple arguments above one can already estimate the locking range; namely by the onset of the new type of nonlinearity as $1 \stackrel{!}{=} |\tilde{\varphi}_J(\nu)| = (\epsilon/2)(\upsilon_{R_0}/\nu)$, which yields a locking region

$$|\nu| = |\Omega - \omega_{\rm dc}| \leqslant \nu_c = \tfrac{1}{2}\epsilon\upsilon_{R_0}. \tag{4}$$

Considering the crucial role any residual in-series resistance R_0 plays in establishing the nonlinear locking dynamics, it may seem surprising that it was mostly neglected in previous studies of Josephson photonics. This is justified by the observation that without an ac signal the residual resistance merely leads to a small and constant shift of the dc voltage with no significant consequence for the dynamics.[1] Only in combination with an additional injection signal, the residual resistance becomes a key parameter enabling low-frequency oscillations to access the nonlinear regime. The shift of the dc voltage, $I_{\rm dc}R_0$, becomes dependent on this nonlinear response $\varphi(t)$, so that the effective dc voltage seen by the junction and the resulting Josephson frequency is pulled and the Josephson oscillations can lock to the ac signal.

Forced and self-sustained oscillations. In the language of nonlinear dynamics, without R_0 the Josephson junction undergoes *forced oscillations*, where the Josephson frequency is directly fixed to the dc bias. The forced oscillations respond linearly to an injection signal. At finite R_0, the Josephson frequency becomes a dynamical quantity, different from the dc bias, which is determined by the equation

$$\omega_J = \omega_{\rm dc} - \frac{2e}{\hbar} I_{\rm dc}[\varphi\,;\varphi_J]R_0, \tag{5}$$

where the dc part of the Josephson current, $I_{\rm dc}$, depends on the solutions $\{\varphi(t), \varphi_J(t)\}$. In this case, the Josephson oscillations are *self-sustained oscillations* and can be locked.

These properties of a Josephson photonics device with an in-series resistance are demonstrated in Fig. 2. The cavity degree of freedom φ is driven to oscillations with $\omega_J < \omega_{\rm dc}$ according to (5). In the weak driving regime, $\tilde{I}_c \ll 1$, these are purely sinusoidal and correspond to a single point in Fig. 2(a)

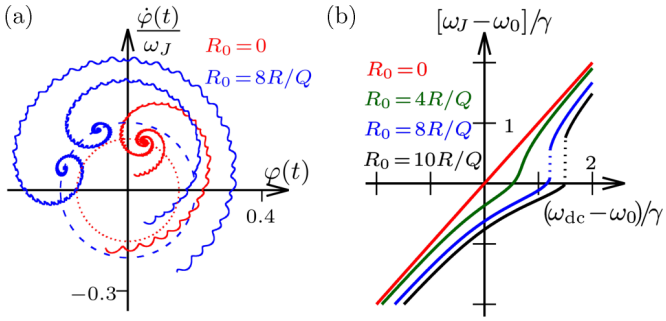

FIG. 2. Properties of Josephson oscillations without a locking signal. (a) Phase-space picture (in the frame rotating with ω_J) of the cavity dynamics showing trajectories (solid) relaxing towards limit cycles (dashed). Without in-series resistance a Josephson photonics circuit is forced into oscillations with a fixed, stable phase, so that all perturbations relax back to the same phase-space (fixed) point (red, dots: laboratory frame). The additional degree of freedom provided by an in-series resistance allows different perturbations to relax to different points along the limit cycle (blue). This freedom of the phase on the limit cycle makes a self-sustained oscillator susceptible to locking. Note that, in the reduced phase space of the cavity, trajectories may cross. (b) The oscillation frequency of the cavity, $\omega_J(0)$, is reduced from the dc bias, $\sim\omega_{\rm dc}$, by the (dc) voltage drop at the in-series resistance. For small R_0, this reduction is given by the Lorentzian resonance curve of Josephson photonics (red vs. green curve), whereas at larger R_0 an instability occurs [cf. the discontinuity in Fig. 1(c) at $\epsilon \approx 0.26$]. [Parameters: $\omega_{\rm dc} = \omega_0 + 1.5\gamma$, $0 \leqslant \omega_0 t \leqslant 450$ in (a); for other parameters see Fig. 1 and legends.]

in a frame rotating with ω_J. Depending on initial conditions different angles on a circular limit cycle are found in the long-time limit. Perturbations from this (nonequilibrium) steady state relax to a (possibly different) point on the limit cycle. These are all the typical features of a self-sustained oscillator, such as the van der Pol oscillator, with the slightly more complex relaxation dynamics here being caused by the extra degree of freedom φ_J. In contrast, without R_0, oscillations occur with $\omega_J \equiv \omega_{\rm dc}$ and a fixed phase angle (only depending on the choice of the rotating frame)[2] that corresponds to a single point on a cycle, stable against perturbations.

Figure 2(b) visualizes how the in-series resistance R_0 impacts the frequency of Josephson oscillations even in the absence of a locking signal. Without R_0 the Josephson frequency is given by the dc bias ($\omega_J = \omega_{\rm dc}$, red), whereas as described by Eq. (5) for finite R_0 it is reduced by the (average) voltage drop at the in-series resistance R_0 due to the dc part of the Josephson current $I_{\rm dc}$. For small R_0 (green) this reduction is simply given by the standard resonance curve of Josephson photonics, where $I_{\rm dc}$ (and the photon emission) peaks at the fundamental cavity resonance $\omega_{\rm dc} = \omega_0$ with a resonance width determined by the cavity decay rate γ. Increasing R_0 (blue, black) the resonance is shifted to larger $\omega_{\rm dc}$ compensating for the portion of the voltage dropping at R_0. For voltages above the resonance peak, i.e., at the flank

[1] It has been noted, however, that a model without R_0 and a strictly fixed dc bias would result in emission without spectral width, and the observed spectral linewidth, typically much sharper than the inverse cavity lifetime, has been associated with low-frequency fluctuations of the voltage at the junction

[2] Note that there is a subtlety in defining the phase of the rotating frame and there is also a valid approach which results in a limit cycle description for the $R_0 = 0$ case, but does not lead to locking.

of the resonance curve where $Y_J = (2e/\hbar)\partial I_{\rm dc}/\partial\omega_J < 0$, an instability develops, once $Y_J \leqslant -1/R_0$, so that the total device admittance vanishes. Formally, this follows by differentiating Eq. (5) with respect to ω_J, where $\partial\omega_{\rm dc}/\partial\omega_J = 0$ corresponds to the jumps in Fig. 2(b).

III. INJECTION LOCKING

In this section, we derive explicit equations describing the nonlinear behavior developing at small detuning $\nu \simeq \nu_c \ll \omega_J, \Omega$ and show that it results in frequency pulling and locking. In particular, we derive the equations governing the dynamics of the circuit at the slow frequency ν and show the similarity to the Adler equation, a universal equation describing injection locking in self-sustained oscillators.

Slow dynamics will describe how the circuit response shifts from oscillations at the natural frequency of the self-sustained oscillator ω_J to the frequency Ω of the locking signal. The definition of ω_J by Eq. (5) applies in the presence of a locking signal, so that $\omega_J = \omega_J(\epsilon)$ with $\omega_J(\epsilon) \equiv \Omega$ when the oscillations are locked.

In the limit of weak Josephson coupling $\tilde{I}_c \ll 1$ and small residual resistance $R_0 \ll R$, we can neglect the components of φ_J oscillating at multiples of the Josephson frequency. However, for a small frequency ν when phase locking develops, we must account for sidebands around ω_J at multiples of ν. We express these sidebands by slowly varying parameters in an ansatz for junction and cavity phases. Since locking primarily relies on the adaption of frequencies and phases, we can justifiably neglect a slow time dependence of oscillation amplitudes and write

$$\varphi_J(t) = \omega_J t + \theta_J(t) + a_J \sin[\omega_J t + \phi_J(t)] \tag{6}$$

to capture the driven dynamics of the junction phase consistent with our considerations above, cf. Eq. (3). For the cavity phase we similarly chose the ansatz,

$$\varphi(t) = a \sin[\omega_J t + \phi(t)], \tag{7}$$

which neglects the off-resonant response of the cavity phase, assuming a large quality factor, $Q \gg 1$, as is typical in Josephson photonics devices.

Time-scale separation. All unknown functions, $\theta_J(t)$, $\phi_J(t)$ and $\phi(t)$, are slowly varying in time, with $\dot{\theta}_J$, $\dot{\phi}_J$, $\dot{\phi} \simeq \nu \ll \omega_J$, while the fast frequencies are only slightly detuned from each other, $\omega_J \simeq \omega_{\rm dc} \simeq \omega_0$. We can thus use time-scale separation for the two time scales $\omega_J^{-1} \ll \nu^{-1}$ to obtain equations for the slowly varying functions. Inserting the ansatz in the circuit equations Eqs. (1a) and (1b), we can separate each resulting equation in a slow part and a part containing fast oscillations. The relation

$$\dot{\theta}_J = (\omega_{\rm dc} - \omega_J) - v_{R_0}\frac{a_J}{2}\sin(\phi_J - \theta_J), \tag{8}$$

follows from the low-frequency terms of Eq. (1a), while the corresponding result from Eq. (1b) yields an irrelevant offset of the ϕ oscillations.

Isolating terms with frequencies close to ω_J in Eq. (1a) and Eq. (1b), respectively, yields

$$\omega_J a_J \cos(\omega_J t + \phi_J) = \epsilon\Omega\cos(\Omega t + \phi_\epsilon) - v_{R_0}\sin(\omega_J t + \theta_J) - a\omega_J\cos(\omega_J t + \phi), \tag{9a}$$

$$\tilde{I}_c\omega_0\gamma\sin(\omega_J t + \theta_J) = a\,\{[\omega_0^2 - (\omega_J + \dot{\phi})^2]\sin(\omega_J t + \phi) + \gamma\omega_J\cos(\omega_J t + \phi)\}. \tag{9b}$$

Equations (9a) and (9b) can be rewritten in a frame rotating with frequency ω_J, where they are equivalent to the following set of complex equations,

$$a_J e^{i\phi_J} = \epsilon e^{i\phi_\epsilon} e^{i(\Omega-\omega_J)t} + i\frac{v_{R_0}}{\Omega}e^{i\theta_J} - a e^{i\phi}, \tag{10a}$$

$$a e^{i\phi} = \tilde{I}_c\frac{\gamma}{[2(\omega_0 - \omega_J - \dot{\phi}) + i\gamma]}e^{i\theta_J}. \tag{10b}$$

Equations (10a) and (10b), together with Eq. (8), form a set of five real-valued algebraic equations that can be solved for three unknown real-valued slowly varying functions θ_J, ϕ_J, and ϕ, and two real-valued parameters a_J and a.

Deriving an Adler equation. The injection locking phenomenon emerges by solving the above system of equations. However, the full analytical solution is cumbersome and fortunately, its behavior can be discussed quantitatively using a simplification commonly used in nonlinear sciences. The simplification arises when the system of equations is reduced to a single Adler-type equation, where a locking region can be directly identified. To derive the Adler-type equation analytically, we proceed by substituting Eq. (10b) into Eq. (10a), then taking the imaginary part of Eq. (10a) to obtain an expression for $a_J\sin(\phi_J - \theta_J)$. Finally, the latter expression can be substituted into Eq. (8) to arrive at

$$\dot{\theta}_J = (\omega_{\rm dc} - \omega_J) - \frac{v_{R_0}}{2}\left[\epsilon\sin[(\Omega - \omega_J)t - \theta_J + \phi_\epsilon] + \frac{v_{R_0}}{\Omega} + \tilde{I}_c\frac{\gamma^2}{4(\omega_0 - \omega_J - \dot{\phi})^2 + \gamma^2}\right]. \tag{11}$$

Equation (11) captures the dynamics of the circuit at the slow time scale ν^{-1}, describing the nonlinear response of the circuit to the injection signal. The analogy to the Adler equation becomes evident by defining the phase shift between slow components of the Josephson phase and the injection signal,

$$\psi(t) = \omega_J t + \theta_J - \Omega t - \phi_\epsilon. \tag{12}$$

In the phase-locked regime, where $\theta_J = $ const. and $\omega_J = \Omega$, the phase $\psi(t)$ becomes constant in time, $\dot{\psi} = 0$. Substituting the expression of ψ into Eq. (11) we arrive at

$$\dot{\psi} = \nu(\epsilon, \Omega) - v_{R_0}\frac{\epsilon}{2}\sin(\psi), \tag{13}$$

with the detuning $\nu(\epsilon, \Omega)$ defined as

$$\nu(\epsilon, \Omega) \equiv \nu_0(\Omega) + \Delta\nu(\epsilon, \Omega), \tag{14}$$

where ν_0 is the detuning between the injection frequency Ω and the Josephson frequency at $\epsilon = 0$, i.e., before the injection

signal is applied, and $\Delta\nu(\epsilon, \Omega)$ is the self-consistent change in the Josephson frequency, owing to the frequency dependence of the cavity response. These two terms have the following expressions:

$$\nu_0(\Omega) = \left(\omega_{\rm dc} - \frac{v_{R_0}}{\Omega}\frac{v_{R_0}}{2} - \frac{\tilde{I}_c}{2}\frac{\gamma^2}{4[\omega_0 - \omega_J(0)]^2 + \gamma^2}\, v_{R_0}\right) - \Omega. \tag{15}$$

$$\Delta\nu(\epsilon, \Omega) = \frac{\tilde{I}_c}{2}\left[\frac{\gamma^2}{4[\omega_0 - \omega_J(0)]^2 + \gamma^2} - \frac{\gamma^2}{4[\omega_0 - \omega_J(\epsilon, \Omega) - \dot{\phi}(\epsilon, \Omega)]^2 + \gamma^2}\right] v_{R_0}. \tag{16}$$

The detuning ν that depends on both the injection amplitude ϵ as well as frequency Ω, together with the prefactor of the sine term $(\epsilon/2)v_{R_0}$, reflect an Adler-type equation that is specific to Josephson photonics circuits. This is a central result of this paper.

Arnold tongues as locked regions. The Adler equation, Eq. (13), reveals the phase-locked region marked by solutions where $\dot{\psi}(t) = 0$. Such solutions exist for any fixed injection signal amplitude ϵ, as long as the injection frequency Ω is tuned such that $|\nu(\epsilon, \Omega)| < (\epsilon/2)v_{R_0}$. In that case, we find the time-independent solution ψ given by,

$$\psi = \arcsin\left(\frac{2\nu(\epsilon, \Omega)}{\epsilon v_{R_0}}\right) \pmod{2\pi}. \tag{17}$$

The edges of the phase-locked region are determined by the self-consistent equation,

$$|\nu(\epsilon, \Omega)| = \tfrac{1}{2}\epsilon v_{R_0}. \tag{18}$$

The resulting phase-locked region typically increases as a function of ϵ, creating a shape termed the Arnold tongue. In Fig. 3 we show such Arnold tongues, first in the case when the dc bias is chosen such that the Josephson frequency in the absence of injection signal is near the resonance of the cavity, $\omega_J(0) \approx \omega_0$, and second, in the case when the frequencies are far from the cavity resonance frequency.

Away from the resonance, in the frequency range where the electromagnetic environment of the junction is featureless, the term $\Delta\nu(\epsilon)$ is suppressed and can be neglected if $R \ll R_0$. In this limit, the cavity can be neglected and the circuit becomes equivalent to a resistively shunted Josephson junction (RSJ). For the RSJ model, Eq. (13) takes the canonical form of the Adler equation,

$$\dot{\psi} = \nu_0 - v_{R_0}\frac{\epsilon}{2}\sin(\psi). \tag{19}$$

For a sufficiently strong drive and small detuning ν_0, such that $\nu_0 \leqslant \nu_c$ with $\nu_c \equiv v_{R_0}(\epsilon/2)$, the Adler equation admits a time-independent solution $\psi_0 = \arcsin(\nu/\nu_c)$ that describes locked oscillations, $\dot{\varphi}_J = \Omega$, [see Fig. 1(b)] with relative phase ψ_0. For the RSJ model, the phase-locked region describes the well-known Shapiro step [35], occurring at $2e\langle V_J\rangle = \hbar\Omega$ between current plateaus in the I(V) curve. Linearization in the Josephson driving strength is of course not necessary in this far off-resonant regime, which has been extensively described in the past using a variety of theoretical methods in the context of the Josephson voltage standard [36], a mature field that we do not review here.

Alternatively to an oscillatory voltage, injection locking can also be achieved by injecting an ac current directly into the cavity of the Josephson device. The properties of locking are qualitatively similar to those described in this section. For completeness and due to the possible relevance for future experimental implementations, we have described in detail the derivation of the effective Adler equation for direct ac-current locking in the Supplemental Material [37].

Washboard potentials and locking signatures. It may be helpful to emphasize at this point the difference between two washboardlike potentials for the dynamics of different phase-like variables, which appear in the locking scenario. First, the washboard potential for the dynamics of the Josephson phase φ_J, obtained by Eq. (1a), describes a potential with a periodic part given by the Josephson coupling, and a tilt, which oscillates in time with an amplitude proportional to ϵ around an average value set by the dc voltage (with an additional term describing the coupling to the cavity variable).

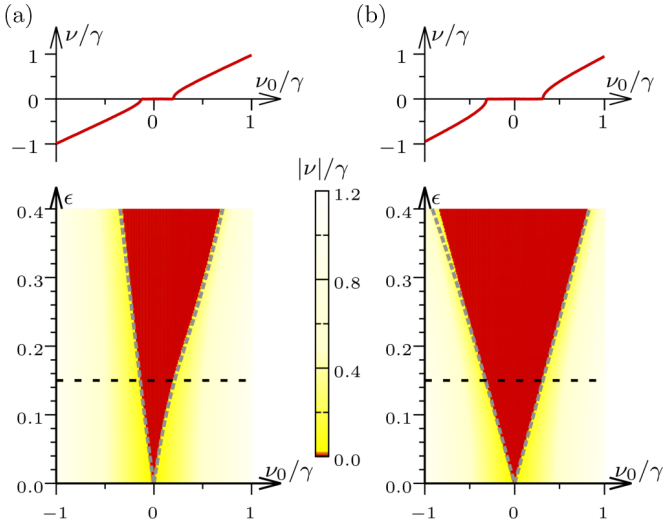

FIG. 3. Arnold tongues. In the locked region (red area in bottom panels and $\nu \equiv 0$ in top panels) the Josephson frequency, $\omega_J(\epsilon)$ becomes equal to the locking frequency, $\nu = \omega_J - \Omega \equiv 0$. The initial ($\epsilon = 0$) detuning, $\nu_0 = \omega_J(0) - \Omega$, is varied by changing the locking frequency Ω for a constant dc bias. (a) If the initial Josephson frequency is close to the cavity resonance [$\omega_J(0) \approx \omega_0 - \gamma/20$ found for $\omega_{\rm dc} = \omega_0 + 0.39\gamma$] the Arnold tongue is strongly deformed for $\epsilon \ll 1$, while (b) for off-resonant biasing [$\omega_J(0) \approx \omega_0 + 2\gamma$ found for $\omega_{\rm dc} = \omega_0 + 2.3\gamma$] the standard linear Arnold tongue shape is recovered. Black dashed lines indicate the position of the horizontal cuts shown in the top panels. Gray dashes are the analytical results for the locking boundaries based on the derived effective Adler equation, Eqs. (13)–(16). [The Josephson driving strength is (a) $\tilde{I}_c = 0.3$ and (b) $\tilde{I}_c = 0.5$. Other parameters are the same as in Fig. 1.]

Without ac drive and cavity, this is, of course, just the familiar RSJ potential for an overdamped junction describing, e.g., transitions between a running-voltage state and the trapped state. Second, the Adler-like potential, Eq. (13), also of washboard type, associated to the dynamics of the Adler variable ψ. This potential can essentially be related to the one for φ_J by a rotating-frame description (with rotation frequency Ω), where the tilt becomes static and is reduced to the detuning, and the periodic part stems from a combination of locking signal and Josephson coupling.

While the details of Eqs. (13)–(16) and the way locking affects the cavity emission are unique to the Josephson-photonics setup, many aspects of the dynamics in the tilted washboard potential are generic: The dynamics of a particle with negligible mass in a washboard potential $U(\psi) = \nu\psi + \nu_c \cos(\psi)$ depends on the relation between tilt and oscillation amplitude. The condition $\nu \leqslant \nu_c$ corresponds to the appearance of local minima in the potential that trap the relative phase ψ and stabilize it. Just outside the locking region, $\nu \gtrsim \nu_c$, $U(\psi)$ has the shape of a staircase. The phase particle advances slowly along the flat region of the staircase, then drops rapidly along the steep region, giving rise to periodic dynamics (for ψ modulo 2π). We define the distance from the locking region, $\delta = (\nu - \nu_c)/\nu_c$ and assume $\delta \ll 1$. The time spent by the phase particle on the flat region of the staircase is given by $T_s \sim (2\pi/\nu_c)(1/\sqrt{\delta})$ and diverges as the locking region is approached, $\delta \to 0$. The rapid drop along the steep region is relatively short, $(2\pi/\nu_c)$, and can be neglected in comparison to T_s close to the locking region. The slow rise during T_s followed by a rapid drop is well described by a sawtooth function. Its period is given by the slow time scale T_s and can be represented as a Fourier series in harmonics of $\tilde{\nu} \simeq (2\pi/T_s) \sim \nu_c\sqrt{\delta}$,

$$[\psi(t) - \psi(0)]_{(\mathrm{mod}\ 2\pi)} \sim \sqrt{\delta} \sum_{k=1}^{1/\sqrt{\delta}} (-1)^{k+1} \frac{\sin(k\tilde{\nu}t)}{k}, \quad (20)$$

valid close to the locking region, in the asymptotic limit $\delta \to 0$. The emergence of many, closely spaced harmonics $k\tilde{\nu}$ with $\tilde{\nu} \sim \sqrt{\delta}$ and $k = 1 \ldots 1/\sqrt{\delta}$ for $\delta \to 0$ in the dynamics of the rotating-frame variable ψ results in the fanlike spectrum of the cavity emission centered around ω_J observable in Figs. 1(c), 1(d) a telltale signature of the approach to the locking transition.

IV. EFFECTS OF NOISE

The hallmark of the injection locking phenomenon is that it stabilizes the phase of oscillations, ψ, against perturbations due to noise. To explicitly demonstrate and study this stabilization in numerical simulations stochastic noise forces are added to the equations governing the system's dynamics.

In recent Josephson photonics experiments the dominant source of noise were fluctuations $\Delta V(t)$ of the applied bias voltage, which were slow and of classical nature, and ascribed to thermal or external noises. Another unavoidable source of fluctuations is voltage noise created at the in-series resistance R_0 by the shot noise of the Josephson current across the tunnel junction. This quantum noise, stemming from the granular nature of charges, can only imperfectly be captured by a stochastic force term in a classical equation of motion, as we will briefly discuss further below.

Following the typical experimental situation, we include Gaussian colored noise as an addition to the voltage term in Eqs. (1). Before turning again to the effective Adler equation for analytical considerations and estimates, let us discuss the effects of adding noise to Eqs. (1), as observed in the full numerical solutions. Figure 4(a) reproduces the hallmark experimental signature of locking from such solutions: the emergence of an extremely sharp peak arising from the (thermally) broadened spectrum of the cavity emission as the system enters the locking region. The same physics is described by the phase-space distributions displayed in Figs. 4(b)–4(d). Without a locking signal, weak and slow fluctuations allow the quadratures of the cavity oscillation to diffuse around the complete limit cycle (with slight excursions in radial direction). A locking signal strongly restrains this diffusion and in the rotating-frame phase space both angle and radius are stabilized in the locked regime, see Fig. 4(d).

To understand and analyze the effects of noise observed in the results of the full numerical solutions of Eqs. (1) shown in Fig. 4, we can reconsider the derivation of the effective Adler equation, now in the presence of a fluctuating noise term. Reasoning that the high-frequency components of noise fluctuations are efficiently filtered and do not reach the device, as is typically the case in Josephson photonics experiments, which corresponds to assuming a correlation time of the colored noise larger than typical time scales of the dynamics, the time-scale separation used in the previous section will remain valid in the presence of noise. It is then easy to show that noise introduces in the circuit Adler equation a stochastic frequency detuning due to the variation of the dc bias, $\xi(t) = (2e/\hbar)\Delta V(t)$,

$$\dot{\psi} = \nu(\epsilon) - \nu_{R_0} \frac{\epsilon}{2} \sin(\psi) + \xi(t) = \frac{\partial U(\psi)}{\partial \psi} + \xi(t). \quad (21)$$

To the overdamped dynamics of the phase particle in the washboard potential $U(\psi) = \nu\psi + \nu_c \cos(\psi)$ tilted by the detuning ν and with a modulation amplitude increasing with the locking strength, there now contributes a fluctuating noise force, which can alternatively be seen as a fluctuation of the tilt.

In the absence of an injection signal, the potential is a flat tilted landscape, $U(\psi, \epsilon = 0) = \nu_0\psi$; the resultant uniform motion for Ψ with velocity ν_0 corresponds to cavity emission at ω_J. In a phase space rotating with the same frequency ω_J this motion is represented by a fixed point. Noise adds (free) diffusion to the motion of the phase particle, which yields the wide spectrum for the cavity emission shown by the blue line of Fig. 4(a) and the typical donut shape in the rotating phase space, Fig. 4(b). Adding the injection signal provides a series of minima to the potential, separated by 2π, which can reduce the effects of noise, restrict the diffusion, and decrease the average velocity. In a frame rotating with this average velocity [top panel of Fig. 4(c)] one nonetheless obtains diffusion exploring the whole limit cycle and a donut-shaped phase-space distribution. The modulation of this diffusion by the injection signal only becomes apparent in a frame rotating with Ω [bottom panel of Fig. 4(c)], where a modulated donut with more or less weight indicating potential minimum and maximum is

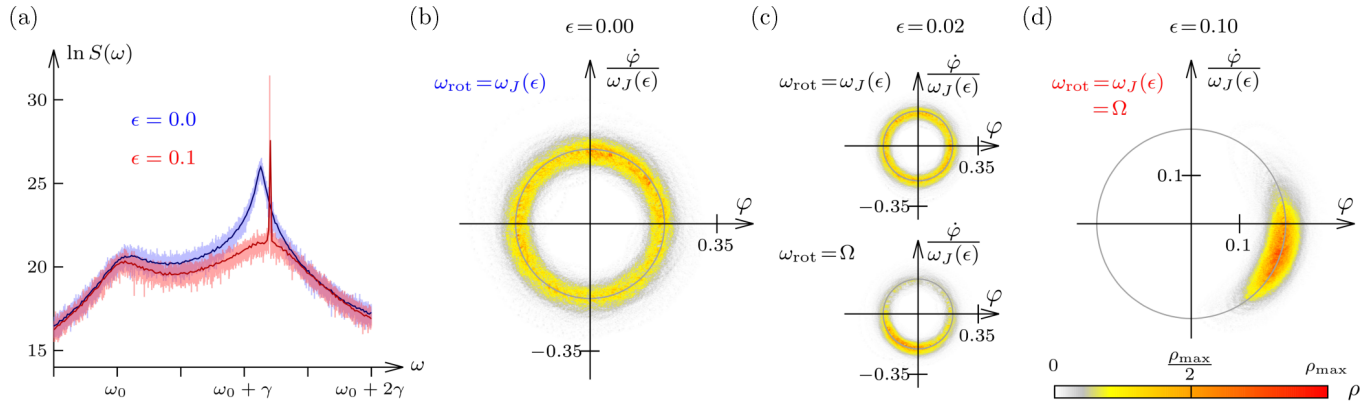

FIG. 4. Signatures of locking in classical dynamics with noise. (a) The hallmark signature of locking in the emission spectrum is the emergence of an extremely sharp peak (red) at the locking frequency Ω as compared to the unlocked (thermally) broadened emission (blue) around $\omega_J(0)$ [$\Omega = \omega_0 + 1.2\gamma; \omega_J(0) \approx \omega_0 + 1.13\gamma$, reduced from the dc bias, $\omega_{\rm dc} = \omega_0 + 1.5\gamma$ due to the in-series resistance]. The cavity resonance enhances thermal fluctuations around ω_0. [Light colors show the spectrum averaged over 10 long runs with $0 \leqslant \omega_0 t \leqslant 10^6$, which is further smoothened to a resolution $\delta\omega \approx \gamma/80$ to give the solid lines. Noise is modeled by an Ornstein-Uhlenbeck process with (zero-frequency) spectral noise density, $S_\xi = \gamma/30$, and correlation time $t_{\rm corr} = 2/\gamma$.] Phase-space distributions ρ are shown: (b) without a locking signal in a frame rotating with $\omega_J \neq \Omega$; (c) in the unlocked region for frames rotating with ω_J and with Ω; and (d) for the locked case rotating with $\omega_J = \Omega$. Diffusion around the limit cycle caused by the noise is modulated and eventually confined by increasing the locking signal. In the latter case, long-time phase correlations result in a pronounced reduction of the linewidth shown in (a). [For parameters not otherwise stated, see Fig. 1; (pseudo-)steady-state distributions are gained from a single run with $5 \times 10^5 \leqslant \omega_0 t \leqslant 10^6$.]

found. In the locked region, the distribution finally becomes strongly confined, see Fig. 4(d).

Starting from the known tilted washboard dynamics in the absence of noise, we see that adding even weak noise may have strong effects close to the onset of locking around the critical tilt ν_c. Just above the onset the average velocity of the phase particle $\omega_J - \Omega$ is approaching zero due to the slow creeping motion along the nearly flat part of the washboard. Clearly fluctuations of the tilt will cut this creeping motion short and strongly increase the average velocity, as is indeed seen in Fig. 5(c). The situation is very different deep inside the locking region, $|\nu/\nu_c| \ll 1$, where, if the spectral density of noise is smaller than the barrier height between consecutive minima, the dynamics of the locked phase particle can be qualitatively described as localized explorations of the local minimum (intrawell dynamics) combined with occasional escape events (interwell dynamics) where the phase crosses the barrier and is subsequently retrapped at the next potential minimum. These escape events are noise-assisted phase slips where the phase rapidly changes by 2π. Figures 5(a), 5(b) depicts the typical time dependence of $\psi(t)$ in the locked region and under the influence of colored noise generated by an Ornstein-Uhlenbeck process with a correlation time chosen as $2/\gamma$. The average rate of phase slips sets the average velocity $\omega_J - \Omega$, leading to deviations from the constant part of the locking curve in Fig. 5(c). The noisy dynamics of the Josephson phase particle ψ, described here on the basis of the Adler-like effective equation, is similar to known Shapiro-steps physics, where, however, there are no direct equivalents to the signatures in the cavity spectrum and the phase-space features.

In the emerging picture of locking in the presence of noise, the concept of injection locking can no longer be equivalent to $\dot\psi = 0$ and must be amended to account for the fact that the relative phase ψ between the injection signal and the oscillations in the Josephson device is no longer time independent.

Instead, the stabilization of the phase will be quantified by the rate of phase slips. For a simple quantitative estimate we turn to the Kramers regime of diffusion over a barrier for overdamped dynamics [38]. Neglecting correlations between consecutive slips and for a noise spectral density $S_\xi \equiv \int d\tau\ \xi(\tau)\xi(0)$ small compared to the barrier height, U_B, the rate of phase slips $\Gamma_{\rm ps}$ is exponentially suppressed,

$$\Gamma_{\rm ps}(U_B, S_\xi) \sim \exp\left(-\frac{U_B}{S_\xi}\right), \quad \text{for } U_B \gg S_\xi. \tag{22}$$

The barrier height has a maximum, when the detuning in the Adler equation vanishes $\nu(\epsilon) = 0$, and where locking is most stable against noise. Its maximal height can be estimated as $U_{B,\max} = \nu_c \simeq eI_cR_0\epsilon/\hbar$. This sets an upper limit for the noise intensity that can be overcome and stabilized by an injection signal with fixed amplitude ϵ,

$$S_\xi < (\epsilon/2)v_{R_0}. \tag{23}$$

The phase stabilization has important consequences for the spectral width of the radiation emitted by the Josephson photonics device. In absence of an injection signal, the spectral width $\delta\omega$ in the simplest linear scenario is directly set by the noise spectral density, $\delta\omega \simeq S_\xi$. By injection locking the device and tuning the injection frequency to the condition of maximum barrier height, $\nu(\epsilon) = 0$, the new spectral width will be given by the rate of phase slips, $\delta\omega \simeq \Gamma_{\rm ps}$. This will amount to an *exponential reduction of the spectral width*, yielding an extremely sharp spectral feature when the noise intensity falls well below the above threshold, as in Fig. 4(a).

Experimental requirements. The requirements to observe the exponential reduction of the spectral width can be

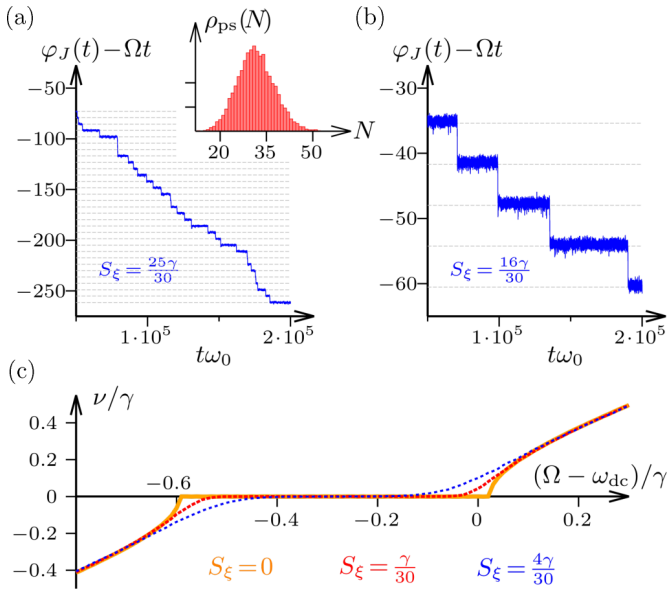

FIG. 5. Effect of noise on the dynamics of the junction phase. Noise induced diffusion allows the slow phase variable, $\varphi_J(t)-\Omega t$, to overcome the potential barrier in the tilted washboard potential described by Eq. (21) and slip by 2π from one potential minimum to the next. An increased noise strength [(a) as compared to (b)] results in a strongly (exponentially) enhanced rate of slips, $\Gamma_{\rm ps}$, see Eq. (22). In the simplest regime, slips follow a Poissonian distribution [see histogram of 10^4 traces in inset of (a)]. The slip rate, $\Gamma_{\rm ps}:=\frac{\langle N\rangle}{\Delta t}=\frac{\langle\langle N\rangle\rangle}{\Delta t}\approx\frac{30}{1.5\ 10^5}\omega_0$ determines the noise induced shift and linewidth of the spectral peak. [Parameters as in Fig. 2(a), $t_{\rm corr}=2/\gamma$]. (c) Bifurcations appearing in locking curves without noise are progressively washed out for increasing noise strength, and even deep in the locked region the average Josephson frequency differs from the locking frequency, $\omega_J(\epsilon)-\Omega\not\equiv 0$, due to (thermal) phase slips. [Parameters cf. Fig. 3(b) top].

estimated quantitatively based on typical realizations of the Josephson photonics device in experiments [5,7–9]. For a device with small Josephson coupling $\tilde{I}_c=2eI_cR/\hbar\omega_0=0.5$, as can be routinely realized, and a resonance quality factor $Z(\omega=\omega_0)/Z(\omega=0)\approx R/R_0\simeq 30$ (a low estimate), the barrier height that can be created with an injection signal of amplitude ϵ can be estimated to $U_{B,\max}\simeq(\epsilon/2)v_{R_0}=eI_cR_0\epsilon/\hbar\simeq(\epsilon/120)\omega_0$. Furthermore, the spectral width for such a device in absence of an injection signal is typically of the order $\delta\omega\simeq 10^{-3}\omega_0$, resulting in the same estimation for the noise spectral density $S_\xi\simeq 10^{-3}\omega_0$. Therefore, the requirement to observe the exponential suppression of noise $U_{B,\max}>S_\xi$ amounts to $\epsilon>0.12$. This places the amplitude of the injection signal reasonably well in the linear regime, see Fig. 3.

In the opposite limit, when the injection amplitude is weak, such that the noise satisfies $S_\xi>(\epsilon/2)v_{R_0}$, the stabilization is negligible [the evolution of the phase $\psi(t)$ in this case is shown in Fig. 5(a)]. While in this regime the phase is not stabilized and the spectrum remains broad, injection locking may have measurable consequences in other observables, such as in the statistics of the radiation emitted by the device. Interesting questions, such as the relation between the statistics of phase slips and the statistics of the emitted radiation, will be addressed elsewhere.

While the estimations above suggest that it may be optimal for locking to increase the resistor R_0, this step may become counterproductive if current fluctuations at R_0 become the dominant source of voltage noise. In that case, thermal noise can become negligible compared to the shot noise, as the Josephson photonics device is operated at low temperature. Therefore, quantum fluctuations due to Cooper pair tunneling become dominant.

Conjecturing that one may still arrive at an effective Adler-like dynamical equation, there are obvious ways in which quantum effects will modify the picture of the phase particle in the washboard potential $U(\psi)$. The pointlike phase particle will be replaced by a wave function, where the scale of (zero-point) quantum fluctuations is associated with a mass assigned to the phase particle, which emerges from the scale of (single Cooper pair) charging effects. Classical thermal diffusion over the barrier is superseded by tunneling across the barrier between consecutive minima of $U(\psi)$ under the influence of dissipation. One may anticipate a particularly interesting regime in this competition between dissipation and tunneling, where the quantum dynamics of the phase particle is described by a Bloch-type wave function in the time crystal defined by potential $U(\psi)$, in spite of dissipative effects.

Setting up a full model of quantum dynamics of locking in the shot-noise dominated regime to study the quantum statistical properties of the microwave radiation emitted from the Josephson photonics, as well as deriving and studying resulting effective Adler-like equations are intriguing avenues for further research. It will link our investigations to interesting recent studies of locking for various systems, where the quantum character of the oscillator becomes crucial [39–46]. A further direction is uncovering parallels and distinctions between two different types of (quantum) phase slips; the tunneling of the phase of a dynamical solution, such as the Josephson phase in the injection locked devices studied here, and flux tunneling in thin superconducting wires [31].

V. HIGHER-ORDER RESONANCES

Part of the attraction of Josephson photonics devices is the variety of resonances associated with multiphoton creation, which are easily addressable in such devices by a simple change of the dc-voltage bias. In addition to the fundamental resonance at $2eV_{\rm dc}\approx\hbar\omega_0$, there appear resonances at $2eV_{\rm dc}\approx p\hbar\omega_0$ ($p\in\mathbb{N}$), whenever the bias provides each Cooper pair crossing the junction with the energy to excite p photons in the mode ω_0. Such processes were observed already in the very first experiment [5] and also play a pivotal role for the Josephson laser [3] where, however, they mix with fundamental ($p=1$) resonances for higher modes $\omega_p=p\omega_0$ of the cavity. Equivalent processes in ac-driven Josephson devices [47] have very recently been observed for $p=3$ down conversion [48–50].

In the classical description these processes, which based on a quantum picture may be called p-photon creation processes, materialize as (higher-order) parametric resonances in the equations of motion. Setting $R_0\equiv 0$ and $\epsilon=0$ for the

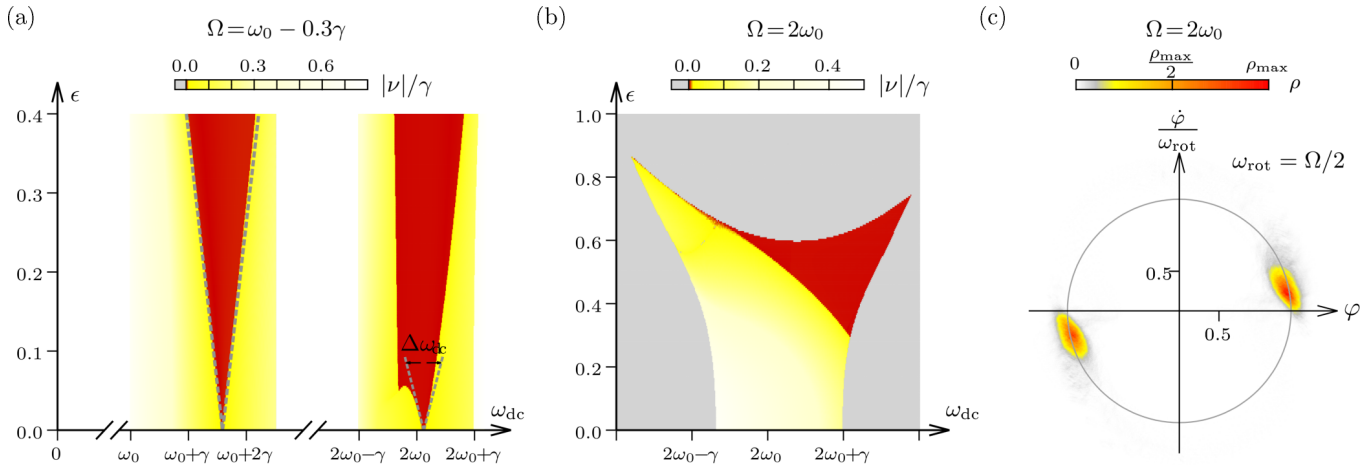

FIG. 6. (a) A locking signal with frequency $\Omega \approx \omega_0$ can lock a Josephson photonics system driven at different dc biases, $\omega_{\rm dc} \approx p\Omega$, where each tunneling Cooper pair creates p photons with frequency $\omega_{\rm dc}/p$. The strongly nonlinear driving regime above the threshold of the $(p = 2)$ parametric resonance, $\tilde{I}_c = 2.5 > 2 =: \tilde{I}_c^{\rm thr}$, modifies the shape of the Arnold tongues. [Dashed lines show analytical results based on an extended theory (nonperturbative in $\tilde{I}_c$, see main text) for both $p = 1$ and $p = 2$. Parameters are $v_{R_0} = \omega_0/6$ and other parameters as in Fig. 1]. (b) The down-converted oscillations with frequency $\sim\omega_0$ at the $(p = 2)$ parametric resonance can alternatively be locked by a signal oscillating at $\Omega \approx 2\omega_0$. The Arnold tongue [red, defined by $\nu(\epsilon) = [\omega_J(\epsilon) - \Omega]/2 \equiv 0$] appears at finite locking amplitude ϵ and crosses over into regions (gray), where directly driven oscillations at $\sim 2\omega_0$ prevail. (c) While a locking signal at $\Omega \approx \omega_0$ breaks the degeneracy of parametric oscillations, the degeneracy remains preserved for $\Omega = 2\omega_0$ as demonstrated by the phase-space distribution (in a frame rotating with $\Omega/2$) in the locked region ($\epsilon = 0.5$, $\omega_{\rm dc} = 2\omega_0 + \gamma$). Noise ($S_\xi = 16\gamma/30$, $t_{\rm corr} = 2/\gamma$) allows the system to slip between the two degenerate solutions, whose symmetry is not broken by the $\Omega = 2\omega_0$ locking signal.

moment, Eq. (1b), reduces to

$$\ddot{\varphi} + \gamma\dot{\varphi} + \omega_0^2\varphi = \tilde{I}_c\gamma\omega_0 \sin(\omega_{\rm dc}t - \varphi) \propto \frac{\varphi^{(p-1)}}{(p-1)!} \sin(\omega_{\rm dc}t + \text{const.}). \quad (24)$$

The conventional parametric resonance occurs at $\omega_{\rm dc} \approx 2\omega_0$, see Refs. [10–14,17,26] for details.

Important for our discussion below are two traits, which the conventional parametric $(p = 2)$ and all higher-order $(p > 2)$ resonances have in common: (i) Classically, there is a driving threshold above which a solution $\tilde{\varphi}(\omega = \omega_{\rm dc}/p) = 0$ becomes unstable and a parametric oscillation emerges. (ii) The parametric solution with period $T^{(p)} = \frac{2\pi}{\omega_{\rm dc}/p} = pT^{\rm drive}$ is p-fold degenerate, with the p solutions connected through time translation by an integer multiple of the period of the (effective) parametric drive $T^{\rm drive} := 2\pi/\omega_{\rm dc}$. This corresponds to a p-fold symmetry in phase space [with solutions $\tilde{\varphi}_k(\omega_{\rm dc}/p) = e^{i2\pi k/p}\,\tilde{\varphi}_{k=0}(\omega_{\rm dc}/p)$ with $k = 0 \ldots p-1$]. The p-fold symmetry has been described in the language of a spontaneous breaking of a discrete symmetry and termed phase-space time crystal [51–55].

The physics of phase locking at higher-order resonances is very rich and considerably more complex compared to the fundamental resonance; for one, due to the fact that the unlocked (classical) solution only exists in a nonlinear regime. Here, we do not want to discuss locking at higher-order resonances at the same level of detail as done for the fundamental resonance above. Instead, we only briefly present first results for $p = 2$. These are chosen to highlight a specific locking feature, newly arising for the $p > 1$ case, which is of both fundamental interest and practical relevance for possible applications (e.g., for stabilizing a squeezing axis). The locking signal aimed at stabilizing the phase and frequency of the oscillations at the (down-converted) slow frequency, $\omega_{\rm dc}/p$, can either *break, or preserve* the discrete p-fold time-translation symmetry. The symmetry will be broken by providing a signal at the slow frequency, $\Omega \sim \omega_{\rm dc}/p \simeq \omega_0$, but preserved by providing a signal at the fast frequency, $\Omega \simeq \omega_{\rm dc} \simeq p\omega_0$.

In the first case, the very same locking signal at $\Omega \simeq \omega_0$ can actually lock a Josephson photonics system driven at (two or even multiple) different dc biases; namely around the fundamental resonance, $\omega_{\rm dc} \simeq \omega_0$, but also around the higher-order resonances, $\omega_{\rm dc} \simeq p\omega_0$. This is demonstrated in Fig. 6(a), which shows the Arnold tongues of locked cavity oscillations with frequency Ω for fixed locking signal frequency $\Omega \simeq \omega_0$ and varying dc bias and locking amplitude. Shown are results from the numerical solutions of the full equations of motion, Eqs. (1), for a driving strength above the threshold of $(p = 2)$ parametric oscillations, compared to analytical results for the locking region's boundaries, based on Adler-like equations for slow variables. For the parametric case, we can make an ansatz analogous to Eqs. (6) and (7), and expand around the $\epsilon = 0$ solutions determined by nonlinear equations involving Bessel functions [11,12,17]. We find a locking region with width $\Delta\omega_{\rm dc}$ [as in Fig. 6(a)] that scales similarly to the fundamental resonance case as $\Delta\omega_{\rm dc} = A\epsilon v_{R_0}$ with a numerical prefactor $A \approx 1.41$ for the parameters of Fig. 6(a). [The numerical value of A depends on the nonlinear solutions of equations containing various Bessel functions in an involved manner, but we find $A \sim O(1)$ away from bifurcations of the equations.] Dashed lines in Fig. 6(a) also shows analytical results for the width of the Arnold tongue for $p = 1$ obtained by extending Eqs. (8)–(9b) for larger driving $\tilde{I}_c$ and expanding in ϵ the resulting Bessel-function expressions. For this case $p = 1$, the width of the Arnold tongue is given by $\Delta\omega_{\rm dc} = B\epsilon v_{R_0}$ where

$B \approx 0.626$ for the parameters of Fig. 6(a). Clearly, the mixing of down-converted and direct drive, and the nonlinearity of the $\epsilon = 0$ solution limits the validity of this ansatz more severely for $p \geqslant 2$ than for the $p = 1$ case, and capturing all features of Fig. 6(a) is beyond its scope.

For the second case, where the locking signal is provided at the fast frequency, $\Omega \approx \omega_{\rm dc} \approx 2\omega_0$, Fig. 6(b) reveals that a large locking amplitude is required even for optimal detuning, i.e., the Arnold tongue does not touch the $\epsilon = 0$ axis. Intuitively one may argue, that to lock oscillations at the slow frequency, $\Omega/p \sim \omega_0$, a locking signal provided at the fast frequency, $\Omega \sim \omega_{\rm dc} \sim p\omega_0$, has to be down converted, which only becomes effective above a certain threshold of signal strength ϵ. Moreover, however, there will be competition between direct locking of the cavity oscillations to a frequency Ω and the desired parametric locking to Ω/p. The extended Adler-like effective description of parametric locking that could explain the details of Fig. 6(b) remains a subject for further studies. What is known and strikingly demonstrated by Fig. 6(c) is the crucial coveted feature of parametric locking: the preservation of the p-fold phase-space symmetry. As can be seen directly from the equations of motion, if a solution, where the cavity is locked at the slow frequency, Ω/p, exists, it is degenerate and there exist p-equivalent solutions for the cavity oscillations shifted by an integer multiple of $2\pi/\Omega$ in time, or rotated by an integer multiple of $2\pi/p$ in phase space. In the phase-space distribution of Fig. 6(c) the twofold symmetry is clearly seen. In presence of noise as discussed in Sec. IV, the cavity oscillations will explore both possible degenerate solutions.

We expect that the scenario of the parametric locking that preserves symmetry will also be reproduced in a quantum description. This mechanism may be used, for instance, to reduce the diffusion of the orientation of the squeezing axis for degenerate or nondegenerate emission of quantum microwave radiation from dc-biased Josephson photonics devices without modifying other desired quantum emission properties. It may also considerably simplify experiments such as the recent confirmation of entanglement in Ref. [9] and enable new applications. Note, that a recent experiment on nondegenerate parametric oscillations [49] follows the diametrically opposite approach of applying a weak on-resonant tone as described above and consequently breaks the phase-space symmetry.

VI. SYNCHRONIZATION

The phenomenon of synchronization describes the mutual phase locking of weakly coupled self-sustained oscillators [34,56,57]. We envision a situation where two Josephson devices, each modeled by a circuit such as studied in the previous sections, are weakly coupled. Experimentally a capacitive, inductive or even resistive coupling can be easily realized and potentially tunable (or nonlinear) coupling scenarios could also be engineered by linking the two devices by a Josephson junction or more complex circuit.

The universal nature of synchronization implies that the resulting mutually locked dynamics are qualitatively similar for any of these type of couplings between the devices (even though variations may be envisioned for time-delayed or strongly nonlinear couplings). To provide an example of the dynamics, we have chosen to describe two Josephson circuits coupled by a mutual capacitance C_{12}, as depicted in Fig. 7, assumed small compared to the capacitance of the circuits $C_{12} \ll C^{(1)}, C^{(2)}$. We will demonstrate that the capacitive coupling leads to synchronization of the Josephson photonics devices. However, the formalism presented, as well as the qualitative aspects of our discussion, apply to any coupling mechanism.

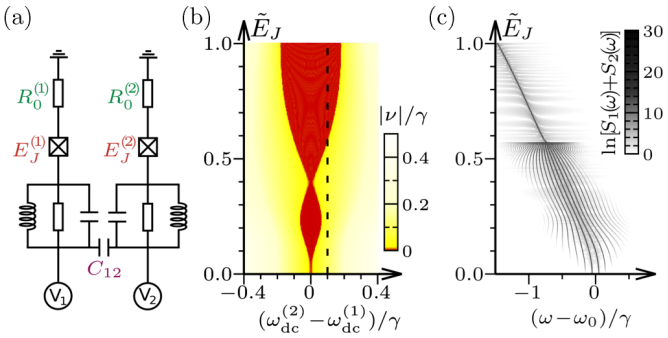

FIG. 7. Synchronization of Josephson oscillators. (a) Sketch of two lockable Josephson photonics circuits, which can synchronize if weakly coupled (e.g., by a capacitance). (b) Arnold tongue indicating the voltage detuning between the two circuits, where oscillations synchronize [red, $\nu(\epsilon) = (\omega_J^{(2)} - \omega_J^{(1)})/\gamma$], as the effective coupling increases with $\tilde{E}_J$. The coupling terms in the Adler-Kuramoto equations (29) scale with the critical detuning parameters (30), $\nu_c^{(\sigma)} \propto (\tilde{E}_J)^2$, explaining the shape of the tongue for weak coupling, while the change of Josephson frequencies with $\tilde{E}_J$ yields more complex behavior [such as multiple (de)synchronization transitions] at larger $\tilde{E}_J$. [results for identical cavities ($\tilde{E}_J^{(1)} = \tilde{E}_J^{(2)} = \tilde{E}_J$, etc.) with antisymmetric bias, $\omega_{\rm dc}^{(2/1)} = \omega_0 \pm (\omega_{\rm dc}^{(2)} - \omega_{\rm dc}^{(1)})$ and parameters as in Fig. 1; $\epsilon^{(\sigma)} = C_{12}/(C^{(\sigma)} + C_{12}) = 0.01$.] (c) (Sum) spectrum at bias $\omega_{dc}^{(2/1)} = \omega_0 \pm \gamma/20$ [dashed in (b)] showing frequency pulling and a fan of frequencies before both cavities synchronize to emit with a common single frequency for large $\tilde{E}_J$.

The system in Fig. 7 is governed by the following (Kirchhoff) equations of motion

$$\dot{\varphi}_J^{(\sigma)} = \omega_{\rm dc}^{(\sigma)} - v_{R_0}^{(\sigma)} \sin\left(\varphi_J^{(\sigma)}\right) - \dot{\varphi}^{(\sigma)} \tag{25a}$$

$$Z^{(\sigma)}\left[\varphi^{(\sigma)}\right] = \tilde{I}_c^{(\sigma)} \sin\left(\varphi_J^{(\sigma)}\right) + \frac{\epsilon^{(\sigma)}}{\omega_0^{(\sigma)}\gamma^{(\sigma)}} \ddot{\varphi}^{(\bar{\sigma})} \tag{25b}$$

where we have introduced superscripts $\sigma = 1, 2$ to label the two devices and $\bar{\sigma}$, defined as $\bar{\sigma} = 2$ if $\sigma = 1$, $\bar{\sigma} = 1$ if $\sigma = 2$.

The dimensionless response $Z^{(\sigma)}$ that describes the two cavities is defined by

$$Z^{(\sigma)}[\varphi^{(\sigma)}] = \frac{1}{\omega_0^{(\sigma)}\gamma^{(\sigma)}}\left[\ddot{\varphi}^{(\sigma)} + \gamma^{(\sigma)}\dot{\varphi}^{(\sigma)} + \left(\omega_0^{(\sigma)}\right)^2 \varphi^{(\sigma)}\right], \tag{26}$$

and further notation is summarized in Table II.

In close analogy to our calculations for locking in Sec. III we can now derive an effective equation for the slow dynamics describing how and in which parameter region the two systems synchronize. The synchronization region corresponds to a range of detuning values between the two dc voltages, $\omega_{\rm dc}^{(2)} - \omega_{\rm dc}^{(1)}$, where due to the coupling ϵ the frequency of Josephson oscillations will be identical in both circuits. To derive the

TABLE II. Physical quantities that characterize the two devices, $\sigma = 1, 2$.

Physical quantity	Parametrization	Unit
resonance frequencies	$\omega_0^{(\sigma)}$	s^{-1}
resonance widths	$\gamma^{(\sigma)} = (R^{(\sigma)}C^{(\sigma)})^{-1}$	s^{-1}
dc bias voltages	$\omega_{\rm dc}^{(\sigma)} = (2e/\hbar)V^{(\sigma)}$	s^{-1}
Josephson frequencies	$\omega_J^{(\sigma)} \neq \omega_{\rm dc}^{(\sigma)}$	s^{-1}
scale of residual voltages	$v_{R_0}^{(\sigma)} = (2e/\hbar)I_c^{(\sigma)}R_0^{(\sigma)}$	s^{-1}
Josephson driving strengths	$\tilde{I}_c^{(\sigma)} = (2e/\hbar)I_c^{(\sigma)}R^{(\sigma)}/\omega_0^{(\sigma)}$	1
coupling strengths	$\epsilon^{(\sigma)} = C_{12}/(C^{(\sigma)} + C_{12})$	1

Kuramoto-Adler equations, from which the boundaries of the synchronization region follow, we introduce slowly varying functions, as in Sec. III, for the Josephson and cavity phases,

$$\varphi_J^{(\sigma)} = \omega_J^{(\sigma)} + \theta_J^{(\sigma)}(t) + a^{(\sigma)} \sin\left[\omega_J^{(\sigma)} t + \phi_J^{(\sigma)}(t)\right], \quad (27)$$

$$\varphi^{(\sigma)} = b^{(\sigma)} \sin\left[\omega_J^{(\sigma)} t + \phi^{(\sigma)}(t)\right]. \quad (28)$$

The ansatz above is consistent with the limit of weak driving $\tilde{I}_c^{(\sigma)} \ll 1$ and small low-frequency impedance $R_0^{(\sigma)} \ll R^{(\sigma)}$. Assuming time-scale separation and further approximations (see Supplemental Material [37] for details) a system of coupled equations for the slowly varying functions can be derived, which finally reduces for weak capacitative coupling to the Kuramoto model

$$\dot{\theta}_J^{(1)} = \tilde{\nu}^{(1)} + \epsilon_1 \nu_c^{(1)} \sin[\nu_J t + \theta_J^{(2)} - \theta_J^{(1)} - \chi^{(1)} - \chi^{(2)}] \quad (29a)$$

$$\dot{\theta}_J^{(2)} = \tilde{\nu}^{(2)} - \epsilon_2 \nu_c^{(2)} \sin[\nu_J t + \theta_J^{(2)} - \theta_J^{(1)} + \chi^{(1)} + \chi^{(2)}]. \quad (29b)$$

Here, $\tilde{\nu}^{(\sigma)} \equiv \omega_J^{(\sigma)}(\epsilon = 0) - \omega_J^{(\sigma)}$ denotes the detuning between the Josephson frequency in absence of coupling, $\omega_J^{(\sigma)}(\epsilon = 0)$, i.e., at $C_{12} = 0$, and the Josephson frequency ω_J affected by mutual frequency pulling. The two critical detuning parameters ν_c^i are found to be

$$\nu_c^{(1)} = \frac{1}{2} v_{R_0}^{(1)} \frac{\omega_J^{(1)}}{\gamma^{(2)}} \frac{\tilde{I}_c^{(2)}}{|z^{(1)}||z^{(2)}|}, \quad (30a)$$

$$\nu_c^{(2)} = \frac{1}{2} v_{R_0}^{(2)} \frac{\omega_J^{(2)}}{\gamma^{(1)}} \frac{\tilde{I}_c^{(1)}}{|z^{(1)}||z^{(2)}|}. \quad (30b)$$

Both set of parameters depend on complex dimensionless impedances $z^{(\sigma)} \equiv |z^{(\sigma)}| e^{i\chi^{(\sigma)}} = (2\nu^{(\sigma)} + i\gamma^{(\sigma)})/\gamma^{(\sigma)}$, that are obtained from the Fourier transform of the responses $Z^{(\sigma)}$ evaluated at the detuning between the corresponding Josephson frequency and the resonance (see Supplemental Material [37]). This forms an implicit set of equations together with the definition of the Josephson frequency [based on averaging Eq. (25a)]

$$\omega_J^{(\sigma)} = \omega_{\rm dc}^{(\sigma)} - \frac{1}{2} \frac{\left(v_{R_0}^{(\sigma)}\right)^2}{\omega_0^{(\sigma)}} + \frac{1}{2} \frac{\tilde{I}_c^{(\sigma)}}{|z^{(\sigma)}|} v_{R_0}^{(\sigma)} \sin(\chi^{(\sigma)}). \quad (31)$$

Notably, the Josephson frequency without coupling $\omega_J^{(\sigma)}(\epsilon = 0)$ depends only on the parameters of the corresponding device $\sigma = 1, 2$.

Of particular interest in Eq. (29) is the appearance of the phases $\chi^{(\sigma)}$ of the oscillators' impedances. These reflect the indirect nature of the coupling of the synchronized Josephson-junction phases. Building on the notion that synchronization can be understood as one junction locking onto a signal provided by the other junction's oscillation, we can immediately discern from Fig. 7(a) that the locking signal is mediated by the cavities. The signal provided by the first Josephson junction's oscillation driving its cavity thus comes with an extra phase $\chi^{(1)}$ determined by that cavity's response function. That signal, in turn, drives the second circuit via an oscillating current, i.e., in a manner slightly different from the oscillating voltage drive considered in Secs. II and III. Considering the corresponding changes to the circuit equations (1) and the resulting Eqs. (8)–(9b), one notes that the cavity response enters again and brings an extra phase of $\chi^{(2)}$, thus explaining the phase shifts in Eq. (29). Also interesting to note considering Eq. (29) is the fact that the effective coupling can be amplified by a dimensionless factor, $\omega_J^{(\sigma)}/\gamma^{(\bar{\sigma})}$, similar to the quality factors of the cavities. Therefore, a significant coupling can be achieved between high quality factor Josephson devices despite a relatively low value of the mutual capacitance.

To emphasize the connection to an Adler-type equation, we define the relative phase of the Josephson oscillations $\psi \equiv \tilde{\varphi}_J^{(2)} - \tilde{\varphi}_J^{(1)} = \nu_J t + \theta_J^{(2)} - \theta_J^{(1)}$, where we introduced slow Josephson phases $\tilde{\varphi}_J^{(\sigma)} = \omega_J^{(\sigma)} t + \theta_J^{(\sigma)}$, obtained from the total Josephson phase, Eq. (27), by averaging over time scales of the order of $2\pi/\omega_J^{(\sigma)}$. With this definition, the condition of synchronization corresponds to $\dot{\psi} = 0$. The difference of the two Adler-Kuramoto equations yields an Adler-type equation for $\psi(t)$,

$$\dot{\psi} = \tilde{\nu}^{(2)} - \tilde{\nu}^{(1)} - \nu_{\rm eff} \sin(\psi + \chi_{\rm eff}), \quad (32)$$

with the effective critical detuning $\nu_{\rm eff}$ and effective phase offset $\chi_{\rm eff}$ given by

$$\nu_{\rm eff} = \sqrt{\left(\epsilon^{(1)}\nu_c^{(1)}\right)^2 + \left(\epsilon^{(2)}\nu_c^{(2)}\right)^2};$$
$$\chi_{\rm eff} = \arctan\left[\frac{\epsilon^{(2)}\nu_c^{(2)} - \epsilon^{(1)}\nu_c^{(1)}}{\epsilon^{(1)}\nu_c^{(1)} + \epsilon^{(2)}\nu_c^{(2)}} \tan\left(\chi^{(1)} + \chi^{(2)}\right)\right]. \quad (33)$$

Figure 7(b) illustrates the Arnold tongue described by the effective Adler equation, Eq. (32), where we ramp up the effective coupling by increasing the Josephson driving strengths, assumed equal for the two devices. The possibility to achieve synchronization by tuning the Josephson driving strength (using SQUIDs) may be experimentally more immediately feasible than direct control of the coupling capacitance. At low coupling, the synchronization window increases proportional to the square of the Josephson driving strength, $\nu_{\rm eff} \propto \tilde{I}_c^2$, consistent with the behavior predicted by Eq. (30). Remarkably, the synchronization window is not increasing monotonously with the Josephson driving strength, suggesting the experiment may exhibit sweet spots where synchronization is more efficient. Examining the analytical expressions, the behavior can be attributed to the dependence of the effective coupling on the dimensionless impedances z_1 and z_2 of the two coupled cavities. Due to frequency pulling, the detunings $\nu^{(\sigma)}$ may pass through their corresponding res-

onance ($\nu^{(\sigma)} = 0$) at different values of the Josephson driving strength, giving rise to a complicated dependence of the effective coupling.

VII. CONCLUSIONS

In this paper, we have studied injection locking and synchronization in Josephson photonics devices in the classical regime. We found that a residual resistance in series to the Josephson junction-cavity circuit is a crucial ingredient. If it is accounted for, a single-mode circuit weakly driven at its fundamental resonance undergoes self-sustained oscillations and therefore constitutes the simplest Josephson photonics device that can be injection locked and synchronized.

Based on the fundamental Kirchhoff circuit equations we derived an Adler-type equation describing locking to an additional ac voltage by a time-scale separation ansatz. The predicted scaling of the locking region with the device parameters will allow experimentalists to devise optimal circuit designs. Bounds on electrical noises against which the phase of cavity oscillations can be stabilized were derived and the noise dependence of the (strongly reduced) linewidth of the cavity emission were discussed.

At a parametric dc-voltage drive $\omega_{\rm dc} \approx 2\omega_0$, the down-converted oscillations can be locked with an ac signal being either at the parametric driving frequency, $\Omega \approx \omega_{\rm dc}$, or at the down-converted frequency, $\Omega \approx \omega_{\rm dc}/2$. These two scenarios correspond to breaking and preserving of the twofold time-translation symmetry of the cavity oscillations. In the latter case, noise allows for slips between the two degenerate solutions, yielding a phase-space distribution with two metastable solutions in the locked steady state. The phase stabilization of Josephson photonics devices by locking will boost their potential as sources of entangled and squeezed quantum microwaves.

Finally, we extended the model to study synchronization between two Josephson photonics devices. An analytical derivation of a Kuramoto-Adler-type equation again allows quantitative statements on the parameter dependence of synchronization regions, identified by characteristic emission spectra and easily mapped out by tuning the Josephson energy of the two devices.

While in this work the dynamics of the Josephson photonics circuits is governed by classical circuit equations and we studied stability against classical noise, the generic features of the locking and synchronization mechanism, in particular, the importance of an in-series resistance, are expected to carry over to a considerable extent to current experimental devices. These can be designed or tuned to operate in regimes where the dynamics are more or less strongly affected by quantum fluctuations, so that Josephson photonics devices may allow for a systematic study of locking and synchronization from the semiclassical to the deep quantum regime. A full theoretical quantum mechanical description including the residual resistance will be required to properly describe regimes where shot noise becomes more dominant than thermal voltage noise and to study such fascinating problems as quantum slips of the phase of the emitted light.

ACKNOWLEDGMENTS

We acknowledge fruitful discussions with Andrew Armour, Benjamin Huard, and Simon Dambach. The authors acknowledge funding through the DFG Grant No. AN336/13-1, the Carl Zeiss foundation, and the Center for Integrated Quantum Science and Technology (IQ^{ST}). The authors acknowledge support by the state of Baden-Württemberg through bwHPC and the German Research Foundation (DFG) through Grant No. INST 40/575-1 FUGG (JUSTUS 2 cluster).

[1] Y.-Y. Liu, J. Stehlik, C. Eichler, M. J. Gullans, J. M. Taylor, and J. R. Petta, Science **347**, 285 (2015).
[2] D. Marković, J. D. Pillet, E. Flurin, N. Roch, and B. Huard, Phys. Rev. Appl. **12**, 024034 (2019).
[3] M. C. Cassidy, A. Bruno, S. Rubbert, M. Irfan, J. Kammhuber, R. N. Schouten, A. R. Akhmerov, and L. P. Kouwenhoven, Science **355**, 939 (2017).
[4] F. Chen, J. Li, A. D. Armour, E. Brahimi, J. Stettenheim, A. J. Sirois, R. W. Simmonds, M. P. Blencowe, and A. J. Rimberg, Phys. Rev. B **90**, 020506(R) (2014).
[5] M. Hofheinz, F. Portier, Q. Baudouin, P. Joyez, D. Vion, P. Bertet, P. Roche, and D. Estève, Phys. Rev. Lett. **106**, 217005 (2011).
[6] A. Grimm, F. Blanchet, R. Albert, J. Leppäkangas, S. Jebari, D. Hazra, F. Gustavo, J.-L. Thomassin, E. Dupont-Ferrier, F. Portier, and M. Hofheinz, Phys. Rev. X **9**, 021016 (2019).
[7] C. Rolland, A. Peugeot, S. Dambach, M. Westig, B. Kubala, Y. Mukharsky, C. Altimiras, H. le Sueur, P. Joyez, D. Vion, P. Roche, D. Esteve, J. Ankerhold, and F. Portier, Phys. Rev. Lett. **122**, 186804 (2019).
[8] M. Westig, B. Kubala, O. Parlavecchio, Y. Mukharsky, C. Altimiras, P. Joyez, D. Vion, P. Roche, D. Esteve, M. Hofheinz, M. Trif, P. Simon, J. Ankerhold, and F. Portier, Phys. Rev. Lett. **119**, 137001 (2017).
[9] A. Peugeot, G. Ménard, S. Dambach, M. Westig, B. Kubala, Y. Mukharsky, C. Altimiras, P. Joyez, D. Vion, P. Roche, D. Esteve, P. Milman, J. Leppäkangas, G. Johansson, M. Hofheinz, J. Ankerhold, and F. Portier, Phys. Rev. X **11**, 031008 (2021).
[10] C. Padurariu, F. Hassler, and Y. V. Nazarov, Phys. Rev. B **86**, 054514 (2012).
[11] V. Gramich, B. Kubala, S. Rohrer, and J. Ankerhold, Phys. Rev. Lett. **111**, 247002 (2013).
[12] A. D. Armour, M. P. Blencowe, E. Brahimi, and A. J. Rimberg, Phys. Rev. Lett. **111**, 247001 (2013).
[13] J. Leppäkangas, G. Johansson, M. Marthaler, and M. Fogelström, Phys. Rev. Lett. **110**, 267004 (2013).
[14] B. Kubala, V. Gramich, and J. Ankerhold, Phys. Scr. **T165**, 014029 (2015).
[15] A. D. Armour, B. Kubala, and J. Ankerhold, Phys. Rev. B **91**, 184508 (2015).
[16] M. Trif and P. Simon, Phys. Rev. B **92**, 014503 (2015).
[17] S. Meister, M. Mecklenburg, V. Gramich, J. T. Stockburger, J. Ankerhold, and B. Kubala, Phys. Rev. B **92**, 174532 (2015).

[18] J.-R. Souquet and A. A. Clerk, Phys. Rev. A **93**, 060301(R) (2016).
[19] J. Leppäkangas, M. Fogelström, M. Marthaler, and G. Johansson, Phys. Rev. B **93**, 014506 (2016).
[20] A. D. Armour, B. Kubala, and J. Ankerhold, Phys. Rev. B **96**, 214509 (2017).
[21] H. Wang, M. P. Blencowe, A. D. Armour, and A. J. Rimberg, Phys. Rev. B **96**, 104503 (2017).
[22] S. H. Simon and N. R. Cooper, Phys. Rev. Lett. **121**, 027004 (2018).
[23] J. Leppäkangas, M. Marthaler, D. Hazra, S. Jebari, R. Albert, F. Blanchet, G. Johansson, and M. Hofheinz, Phys. Rev. A **97**, 013855 (2018).
[24] L. Arndt and F. Hassler, Phys. Rev. B **100**, 014505 (2019).
[25] W. T. Morley, A. Di Marco, M. Mantovani, P. Stadler, W. Belzig, G. Rastelli, and A. D. Armour, Phys. Rev. B **100**, 054515 (2019).
[26] B. Kubala, J. Ankerhold, and A. D. Armour, New J. Phys. **22**, 023010 (2020).
[27] B. Lang and A. D. Armour, New J. Phys. **23**, 033021 (2021).
[28] A. M. Hriscu and Y. V. Nazarov, Phys. Rev. Lett. **110**, 097002 (2013).
[29] A. Bezryadin, C. N. Lau, and M. Tinkham, Nature (London) **404**, 971 (2000).
[30] F. Altomare, A. M. Chang, M. R. Melloch, Y. Hong, and C. W. Tu, Phys. Rev. Lett. **97**, 017001 (2006).
[31] O. V. Astafiev, L. B. Ioffe, S. Kafanov, Y. A. Pashkin, K. Y. Arutyunov, D. Shahar, O. Cohen, and J. S. Tsai, Nature (London) **484**, 355 (2012).
[32] Y. Chen, Y.-H. Lin, S. D. Snyder, A. M. Goldman, and A. Kamenev, Nature Phys. **10**, 567 (2014).
[33] R. Adler, Proc. IRE **34**, 351 (1946).
[34] A. Pikovsky, M. G. Rosenblum, and J. Kurths, *Synchronization, A Universal Concept in Nonlinear Sciences* (Cambridge University Press, Cambridge, 2001).
[35] S. Shapiro, Phys. Rev. Lett. **11**, 80 (1963).
[36] C. A. Hamilton, Rev. Sci. Instrum. **71**, 3611 (2000).
[37] See Supplemental Material at http://link.aps.org/supplemental/10.1103/PhysRevB.104.054517 for details on locking by direct ac-current injection into the cavity, for the derivation of the effective Kuramoto equations, and for notes on the numerical calculations.
[38] H. A. Kramers, Physica **7**, 284 (1940).
[39] S. Walter, A. Nunnenkamp, and C. Bruder, Phys. Rev. Lett. **112**, 094102 (2014).
[40] N. Lörch, E. Amitai, A. Nunnenkamp, and C. Bruder, Phys. Rev. Lett. **117**, 073601 (2016).
[41] N. Lörch, S. E. Nigg, A. Nunnenkamp, R. P. Tiwari, and C. Bruder, Phys. Rev. Lett. **118**, 243602 (2017).
[42] A. Roulet and C. Bruder, Phys. Rev. Lett. **121**, 053601 (2018).
[43] E. Amitai, M. Koppenhöfer, N. Lörch, and C. Bruder, Phys. Rev. E **97**, 052203 (2018).
[44] M. Koppenhöfer and A. Roulet, Phys. Rev. A **99**, 043804 (2019).
[45] M. R. Jessop, W. Li, and A. D. Armour, Phys. Rev. Res. **2**, 013233 (2020).
[46] L. Ben Arosh, M. C. Cross, and R. Lifshitz, Phys. Rev. Res. **3**, 013130 (2021).
[47] W. Wustmann and V. Shumeiko, Low Temp. Phys. **45**, 848 (2019).
[48] I.-M. Svensson, A. Bengtsson, P. Krantz, J. Bylander, V. Shumeiko, and P. Delsing, Phys. Rev. B **96**, 174503 (2017).
[49] I.-M. Svensson, A. Bengtsson, J. Bylander, V. Shumeiko, and P. Delsing, Appl. Phys. Lett. **113**, 022602 (2018).
[50] C. W. Sandbo Chang, C. Sabín, P. Forn-Díaz, F. Quijandría, A. M. Vadiraj, I. Nsanzineza, G. Johansson, and C. M. Wilson, Phys. Rev. X **10**, 011011 (2020).
[51] L. Guo, M. Marthaler, and G. Schön, Phys. Rev. Lett. **111**, 205303 (2013).
[52] Y. Zhang, J. Gosner, S. M. Girvin, J. Ankerhold, and M. I. Dykman, Phys. Rev. A **96**, 052124 (2017).
[53] J. Gosner, B. Kubala, and J. Ankerhold, Phys. Rev. B **101**, 054501 (2020).
[54] P. Liang, M. Marthaler, and L. Guo, New J. Phys. **20**, 023043 (2018).
[55] F. Nathan, G. Refael, M. S. Rudner, and I. Martin, Phys. Rev. Res. **2**, 043411 (2020).
[56] Y. Kuramoto, Lect. Notes Phys. **30**, 420 (1975).
[57] J. A. Acebrón, L. L. Bonilla, C. J. Pérez Vicente, F. Ritort, and R. Spigler, Rev. Mod. Phys. **77**, 137 (2005).

Injection locking and synchronization in Josephson photonics devices

Lukas Danner,[1,2,*] Ciprian Padurariu,[2,†] Joachim Ankerhold,[2,‡] and Björn Kubala[1,2,§]

[1] *Institute of Quantum Technologies, German Aerospace Center (DLR), Söflinger Straße 100, D-89077, Ulm, Germany*
[2] *Institute for Complex Quantum Systems and IQST, Ulm University, Albert-Einstein-Allee 11, D-89069 Ulm, Germany*

(Dated: May 6, 2021)

SUPPLEMENTAL MATERIAL

In this supplemental material to our article we present further details on (*i.*) the theory of locking by direct ac-current injection into the cavity, deriving an effective Adler-equation similar to that presented in Sec. III; (*ii.*) the derivation of the effective Kuramoto equations that supplements the results presented in Sec. VI; and (*iii.*) notes on the numerical calculations, relevant to all sections.

LOCKING FROM DIRECT AC-CURRENT INJECTION

A similar locking scenario to the one described in the main text arises when directly injecting a locking signal into the cavity. Experimentally, this can be realized by feeding the cavity with an oscillating current through the transmission line. We now proceed to derive the locking equation for the circuit model of the Josephson photonics device shown in Fig. S.1.

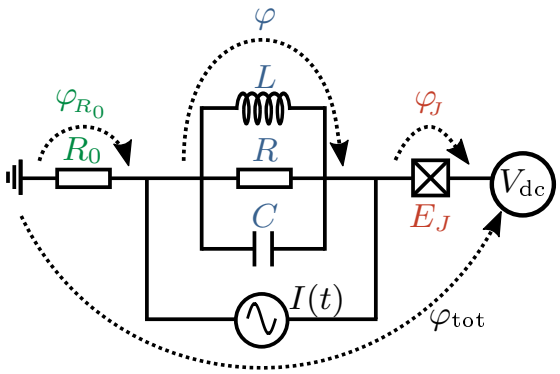

$$I(t) = \epsilon \tfrac{\hbar\Omega}{2eR}\cos(\Omega t + \phi_\epsilon), \quad \epsilon = \tfrac{2e}{\hbar\Omega} I_{\rm ac} R$$

FIG. S.1. (Color online.) Sketch of a dc-voltage biased Josephson photonics circuit with an in-series resistance and a single resonance (with frequency $\omega_0 = 1/\sqrt{LC}$ and width $\gamma = 1/RC$). A small ac-signal is injected by an external current source.

Analogously to the main text, the classical equations of motions are the Kirchhoff equations

$$\dot{\varphi}_J = \frac{2e}{\hbar} V_{\rm dc} - \frac{2e}{\hbar} I_c R_0 \sin(\varphi_J) - \dot{\varphi}; \tag{S.1a}$$

$$\ddot{\varphi} + \gamma\dot{\varphi} + \omega_0^2 \varphi = \frac{2eI_cR}{\hbar\omega_0}\gamma\omega_0 \sin\varphi_J - \frac{2e}{\hbar} I(t). \tag{S.1b}$$

Here we assume the device is dc-biased by a fixed voltage $V_{\rm dc}$. The injection locking signal is provided by the ac-current $I(t) = I_{\rm ac}\cos(\Omega t + \phi_\epsilon)$ with amplitude assumed small, $\epsilon = (2e/\hbar)(I_{\rm ac}R/\Omega) < 1$. For the other quantities, we use the same parametrization as in Table I. The locking equation of Adler-type is derived using the same time scale separation arguments as in the main text. We use a similar ansatz for the degrees of freedom $\varphi(t)$ and $\varphi_J(t)$ in

terms of slowly-varying quantities

$$\varphi_J(t) = \omega_J t + \theta_J(t) + a_J \sin[\omega_J t + \phi_J(t)]; \tag{S.2a}$$

$$\varphi(t) = a \sin[\omega_J t + \phi(t)]\,. \tag{S.2b}$$

The unknown functions, $\theta_J(t)$, $\phi_J(t)$ and $\phi(t)$, are slowly-varying in time, with $\dot{\theta}_J$, $\dot{\phi}_J$, $\dot{\phi} \simeq \nu \ll \omega_J$, while the 'fast' frequencies are only slightly detuned from each other, $\omega_J \simeq \omega_{\rm dc} \simeq \omega_0$.

Separating each equation of motion into slow and rapidly oscillating parts, we find the same equation for the slow component $\theta_J(t)$ as Eq. (8), namely

$$\dot{\theta}_J = \omega_{\rm dc} - \omega_J - v_{R_0} \frac{a_J}{2} \sin(\phi_J - \theta_J), \tag{S.3}$$

The components oscillating with frequencies close to ω_J are modified in this biasing condition compared to the main text,

$$-\omega_J a_J \cos(\omega_J t + \phi_J) = v_{R_0} \sin(\omega_J t + \theta_J) + a\omega_J \cos(\omega_J t + \phi), \tag{S.4a}$$

$$\tilde{I}_c \omega_0 \sin(\omega_J t + \theta_J) - \epsilon\Omega \cos(\Omega t + \phi_\epsilon) = a \left\{ \frac{1}{\gamma} \left[\omega_0^2 - \left(\omega_J + \dot{\phi} \right)^2 \right] \sin(\omega_J t + \phi) + \omega_J \cos(\omega_J t + \phi) \right\}. \tag{S.4b}$$

These equations are the counterparts of Eqs.(9a) and (9b) in the main text. A transformation of eqs. (S.4) to a frame rotating with ω_J yields

$$a_J e^{i\phi_J} = i \frac{v_{R_0}}{\Omega} e^{i\theta_J} - a e^{i\phi}, \tag{S.5a}$$

$$a e^{i\phi} = \frac{1}{z\,(\nu_j)} \left(\tilde{I}_c e^{i\theta_J} - i\epsilon e^{i\phi_\epsilon} e^{i(\Omega - \omega_J)t} \right), \tag{S.5b}$$

where we have defined the complex dimensionless impedance $z(\nu_j) \equiv |z| e^{i\chi} = (2\nu_j + i\gamma)/\gamma$, in analogy to Sec. VI, that here is always evaluated at the detuning $\nu_j \equiv \left(\omega_0 - \omega_J - \dot{\phi} \right)$ between the effective Josephson frequency and the resonance. Outside the locking region ν_j is a function of the injected signal through $\omega_J(\epsilon)$ and $\dot{\phi}(\epsilon, t)$ and imprints its dependence onto the dimensionless impedance, both on its absolute value $|z|(\epsilon)$ and its phase $\chi(\epsilon)$. In the locking region $\dot{\phi} = 0$ and $\omega_J = \Omega$, such that $\nu_j = \omega_0 - \Omega$ becomes independent of ϵ.

As in the main text, we find the locking equation by substituting Eq. (S.5b) into Eq. (S.5a) and taking the imaginary part to find an expression for $a_J \sin(\phi_J - \theta_J)$. The expression is then substituted into Eq. (S.3), yielding

$$\dot{\theta}_J = (\omega_{\rm dc} - \omega_J) - \frac{v_{R_0}}{2} \left[\epsilon \frac{1}{|z|} \sin\left[(\Omega - \omega_J)t - \theta_J + \phi_\epsilon - \chi + \frac{\pi}{2} \right] + \frac{v_{R_0}}{\Omega} + \frac{\tilde{I}_c}{|z|} \sin(\chi) \right]. \tag{S.6}$$

which is analogous to Eq.(11) in the main text.

Defining the Adler phase similarly to Eq. (12),

$$\psi(t) = \omega_J t + \theta_J - \Omega t - \phi_\epsilon - \frac{\pi}{2}, \tag{S.7}$$

we obtain the locking equation for a direct ac-current injection. Here too the locking equation has the form of a generalized Adler equation,

$$\dot{\psi} = \nu(\epsilon, \Omega) - \nu_c(\epsilon, \Omega)\, \frac{\epsilon}{2} \sin\left[\psi + \chi(\epsilon, \Omega) \right]. \tag{S.8}$$

The parameters are given by,

$$\nu(\epsilon, \Omega) = \left(\omega_{\rm dc} - \frac{v_{R_0}}{\Omega} \frac{v_{R_0}}{2} - \frac{\tilde{I}_c}{|z|(\epsilon, \Omega)} \frac{v_{R_0}}{2} \right) - \Omega. \tag{S.9a}$$

$$\nu_c(\epsilon, \Omega) = \frac{v_{R_0}}{|z|(\epsilon, \Omega)}, \quad |z|(\epsilon, \Omega) = \frac{1}{\gamma} \sqrt{4 \left[\omega_0 - \omega_J(\epsilon, \Omega) - \dot{\phi}(\epsilon, \Omega) \right]^2 + \gamma^2}. \tag{S.9b}$$

$$e^{i\chi(\epsilon,\Omega)} = \frac{z(\epsilon, \Omega)}{|z|(\epsilon, \Omega)} = \frac{2 \left[\omega_0 - \omega_J(\epsilon, \Omega) - \dot{\phi}(\epsilon, \Omega) \right] + i\gamma}{\sqrt{4 \left[\omega_0 - \omega_J(\epsilon, \Omega) - \dot{\phi}(\epsilon, \Omega) \right]^2 + \gamma^2}} \tag{S.9c}$$

Compared to Eq. (13), here not only the effective detuning $\nu(\epsilon, \Omega)$, but also the effective width of the locking region $\nu_c(\epsilon, \Omega)$ and the effective locked phase $\chi(\epsilon, \Omega)$ acquire dependence on the injection parameters Ω and ϵ through the dimensionless impedance $z(\nu_j)$.

DERIVATION OF THE EFFECTIVE KURAMOTO-TYPE EQUATIONS FOR SYNCHRONIZATION

The derivation of the Kuramoto-type equations for synchronization starts from the full circuit equations, Eq. (25), and the ansatz for the dominant oscillations, Eqs. (27) and (28) consistent with the limit of weak Josephson coupling $\tilde{I}_c^{(\sigma)} \ll 1$ and small low-frequency impedance $R_0^{(\sigma)}$, i.e. $v_{R_0}^{(\sigma)} \ll \omega_0^{(\sigma)}$. We further assume time scale separation $\dot{\theta}_J^{(\sigma)}, \dot{\phi}_J^{(\sigma)}, \dot{\phi}^{(\sigma)} \ll \omega_{\rm dc}^{(\sigma)}, \omega_0^{(\sigma)}, \omega_J^{(\sigma)}$, as well as $(\omega_{\rm dc}^{(\sigma)} - \omega_0^{(\sigma)}), \left(\omega_{\rm dc}^{(2)} - \omega_{\rm dc}^{(1)}\right) \ll \omega_{\rm dc}^{(\sigma)}, \omega_0^{(\sigma)}, \omega_J^{(\sigma)}$. The slowly-varying functions obey the following system of coupled equations

$$\dot{\theta}_J^{(1)} = \left(\omega_{\rm dc}^{(1)} - \omega_J^{(1)}\right) - v_{R_0}^{(1)} \frac{a^{(1)}}{2} \sin\left(\phi_J^{(1)} - \theta_J^{(1)}\right), \tag{S.10a}$$

$$\dot{\theta}_J^{(2)} = \left(\omega_{\rm dc}^{(2)} - \omega_J^{(2)}\right) - v_{R_0}^{(2)} \frac{a^{(2)}}{2} \sin\left(\phi_J^{(2)} - \theta_J^{(2)}\right), \tag{S.10b}$$

$$z^{(1)} b^{(1)} e^{i\phi^{(1)}} = \tilde{I}_c^{(1)} e^{i\theta_J^{(1)}} - \epsilon^{(1)} \frac{\omega_J^{(2)}}{\gamma^{(1)}} b^{(2)} e^{i\phi^{(2)}} e^{i\nu_J t}, \tag{S.10c}$$

$$z^{(2)} b^{(2)} e^{i\phi^{(2)}} = \tilde{I}_c^{(2)} e^{i\theta_J^{(2)}} - \epsilon^{(2)} \frac{\omega_J^{(1)}}{\gamma^{(2)}} b^{(1)} e^{i\phi^{(1)}} e^{-i\nu_J t}, \tag{S.10d}$$

$$a^{(1)} e^{i\phi_J^{(1)}} = i \frac{v_{R_0}^{(1)}}{\omega_0^{(1)}} e^{i\theta_J^{(1)}} - b^{(1)} e^{i\phi^{(1)}}, \tag{S.10e}$$

$$a^{(2)} e^{i\phi_J^{(2)}} = i \frac{v_{R_0}^{(2)}}{\omega_0^{(2)}} e^{i\theta_J^{(2)}} - b^{(2)} e^{i\phi^{(2)}}. \tag{S.10f}$$

where $\nu_J = \left(\omega_J^{(2)} - \omega_J^{(1)}\right)$ is the detuning between the Josephson oscillations of the two devices. We have also introduced the complex dimensionless impedance $z^{(\sigma)} = \left(2\nu^{(\sigma)} + i\gamma^{(\sigma)}\right)/\gamma^{(\sigma)}$, that is obtained from the Fourier transform $\tilde{Z}^{(\sigma)}(\omega)$ of the response $Z^{(\sigma)}$. The impedance $z^{(\sigma)} = \tilde{Z}^{(\sigma)}(\omega = \omega_0^{(\sigma)} - \nu^{(\sigma)})$ is evaluated at the detuning $\nu^{(\sigma)}$ given by $\nu^{(\sigma)} \equiv \left(\omega_0^{(\sigma)} - \omega_J^{(\sigma)} - \dot{\phi}^{(\sigma)}\right)$.

Eqs. (S.10c) and (S.10d) can be written as a matrix equation for the vector $v \equiv \left[b^{(1)} e^{i\phi^{(1)}}, b^{(2)} e^{i\phi^{(2)}}\right]^T$ containing the cavity oscillation amplitudes,

$$Mv = v_J, \quad \text{with} \quad M \equiv \begin{bmatrix} z^{(1)} & \epsilon^{(1)} \frac{\omega_J^{(2)}}{\gamma^{(1)}} e^{i\nu_J t} \\ \epsilon^{(2)} \frac{\omega_J^{(1)}}{\gamma^{(2)}} e^{-i\nu_J t} & z^{(2)} \end{bmatrix}, \quad \text{and} \quad v_J \equiv \left[\tilde{I}_c^{(1)} e^{i\theta_J^{(1)}}, \tilde{I}_c^{(2)} e^{i\theta_J^{(2)}}\right]^T.$$

The matrix M can be inverted analytically to obtain the following expressions for the cavity amplitudes

$$b^{(1)} e^{i\phi^{(1)}} = \frac{\tilde{I}_c^{(1)} e^{i\theta_J^{(1)}} z^{(2)} - \epsilon^{(1)} \left(\omega_J^{(2)}/\gamma^{(1)}\right) \tilde{I}_c^{(2)} e^{i\theta_J^{(2)}} e^{i\nu_J t}}{z^{(1)} z^{(2)} - \epsilon^{(1)} \epsilon^{(2)} \left(\omega_J^{(1)}/\gamma^{(1)}\right) \left(\omega_J^{(2)}/\gamma^{(2)}\right)}, \tag{S.11a}$$

$$b^{(2)} e^{i\phi^{(2)}} = \frac{\tilde{I}_c^{(2)} e^{i\theta_J^{(2)}} z^{(1)} - \epsilon^{(2)} \left(\omega_J^{(1)}/\gamma^{(2)}\right) \tilde{I}_c^{(1)} e^{i\theta_J^{(1)}} e^{-i\nu_J t}}{z^{(1)} z^{(2)} - \epsilon^{(1)} \epsilon^{(2)} \left(\omega_J^{(1)}/\gamma^{(1)}\right) \left(\omega_J^{(2)}/\gamma^{(2)}\right)}. \tag{S.11b}$$

The above expressions for the amplitudes of the two cavity oscillations can be inserted into the original set of coupled equations, specifically Eqns. (S.10e) and (S.10f), to obtain expressions for the relative phases $(\theta_J^{(\sigma)} - \phi_J^{(\sigma)})$, that can then be inserted back into Eqns. (S.10a) and (S.10b), in analogy to the procedure used in Sec. III. We arrive at the following two equations for the slow components of the Josephson phases,

$$\dot{\theta}_J^{(1)} = \left(\omega_{\rm dc}^{(1)} - \omega_J^{(1)}\right) - v_{R_0}^{(1)} \frac{1}{2} {\rm Im} \left\{ i \frac{v_{R_0}^{(1)}}{\omega_0^{(1)}} - \frac{\tilde{I}_c^{(1)} z^{(2)} - \epsilon^{(1)} \left(\omega_J^{(2)}/\gamma^{(1)}\right) \tilde{I}_c^{(2)} e^{i\nu_J t} e^{i\left(\theta_J^{(2)} - \theta_J^{(1)}\right)}}{z^{(1)} z^{(2)} - \epsilon^{(1)} \epsilon^{(2)} \left(\omega_J^{(1)}/\gamma^{(1)}\right) \left(\omega_J^{(2)}/\gamma^{(2)}\right)} \right\}, \tag{S.12a}$$

$$\dot{\theta}_J^{(2)} = \left(\omega_{\rm dc}^{(2)} - \omega_J^{(2)}\right) - v_{R_0}^{(2)} \omega_0^{(2)} \frac{1}{2} {\rm Im} \left\{ i \frac{v_{R_0}^{(2)}}{\omega_0^{(2)}} - \frac{\tilde{I}_c^{(2)} z^{(1)} - \epsilon^{(2)} \left(\omega_J^{(1)}/\gamma^{(2)}\right) \tilde{I}_c^{(1)} e^{-i\nu_J t} e^{i\left(\theta_J^{(1)} - \theta_J^{(2)}\right)}}{z^{(1)} z^{(2)} - \epsilon^{(1)} \epsilon^{(2)} \left(\omega_J^{(1)}/\gamma^{(1)}\right) \left(\omega_J^{(2)}/\gamma^{(2)}\right)} \right\}. \tag{S.12b}$$

The above equations give the non-linear evolution of the slow phases $\theta_J^{(\sigma)}$ as a function of the couplings $\epsilon^{(\sigma)}$. These equations reduce to the Kuramoto model in the limit $\epsilon^{(1)}\left(\omega_J^{(2)}/\gamma_{(1)}\right) \ll 1$ and $\epsilon^{(2)}\left(\omega_J^{(1)}/\gamma_{(2)}\right) \ll 1$, where after linearizing with respect to the couplings, the equations become

$$\dot{\theta}_J^{(1)} = \tilde{\nu}^{(1)} + \epsilon^{(1)}\ \frac{1}{2} v_{R_0}^{(1)} \frac{\omega_J^{(1)}}{\gamma^{(2)}} \frac{\tilde{I}_c^{(2)}}{|z_1||z_2|} \sin\left[\nu_J t + \theta_J^{(2)} - \theta_J^{(1)} - \chi_1 - \chi_2\right], \tag{S.13a}$$

$$\dot{\theta}_J^{(2)} = \tilde{\nu}^{(2)} - \epsilon^{(2)}\ \frac{1}{2} v_{R_0}^{(2)} \frac{\omega_J^{(2)}}{\gamma^{(1)}} \frac{\tilde{I}_c^{(1)}}{|z_1||z_2|} \sin\left[\nu_J t + \theta_J^{(2)} - \theta_J^{(1)} + \chi_1 + \chi_2\right]. \tag{S.13b}$$

with $\tilde{\nu}^{(\sigma)} \equiv \omega_J^{(\sigma)}(\epsilon = 0) - \omega_J^{(\sigma)}$ and $z^{(\sigma)} \equiv |z^{(\sigma)}|e^{\chi^{(\sigma)}}$. These equations are equivalent to Eq. (29) of the main text.

SOME NOTES ON NUMERICAL IMPLEMENTATION

For numerical results the coupled equations of motions, Eq. (1), were solved using a real-valued variable-coefficient ordinary differential equation (VODE) solver with a BDF method implemented in the Python library SciPy. Typically solutions were calculated for time intervals of $0 \leq t\omega_0 \leq 10^5$. Spectra were calculated using standard FFT routines from SciPy with a frequency resolution of $\delta\omega/\omega_0 \approx 8 \cdot 10^{-5}$ given by a time interval $2.5 \cdot 10^4 < t\omega_0 \leq 10^5$ after reaching the steady state. To regularize the spectra we used a Kaiser-Bessel window with a shape parametrized by $\alpha = 3$. The Josephson frequency was numerically computed by a time average of the solution for $\dot{\varphi}_J$ in a time interval $7.5 \cdot 10^4 \leq t\omega_0 \leq 10^5$.

Simulations including noise use a lower-order Euler-Maruyama algorithm to solve the full equations of motions with an included auxiliary equation creating colored noise by an Ornstein-Uhlenbeck process. Wiener increments are drawn from a Gaussian distribution with random seed by a NumPy random number generator. Here were used a rectangular window function to calculate spectra.

Phase space distributions were calculated in a rotating frame with 200 bins in both coordinate directions. We used a larger steady state interval $2.5 \cdot 10^5 \leq t\omega_0 \leq 10^6$ with $7.5 \cdot 10^7$ time steps ($2 \cdot 10^5 \leq t\omega_0 \leq 7.2 \cdot 10^5$ with $14 \cdot 10^7$ time steps for Fig. 6(c) respectively).

With these parameters plots can be easily created without extensive optimization to reduce numerical costs. Single runs on standard PCs, or two-parameters sweeps and multi-runs for noise averaging on a Baden-Württemberg Cluster JUSTUS2 require typical runtimes ranging from few minutes to a few days on ~ 100 cores.

4.1.2 Extension of the Classical Adler Equation

So far, Pub. (*i*) presented a realistic Josephson-photonics device in the classical regime by incorporating an in-series resistor R_0 [compare Fig. 4.1(a)]. As desired, the model then accurately captures autonomous self-sustained oscillations that can be injection locked and synchronized. The in-series resistor R_0 plays the dual role of both the problem and the solution for the stabilization of the neutrally stable phase-space angle:

- With an in-series resistor R_0, the system shows autonomous self-sustained oscillations with a neutrally stable phase-space angle that can be injection locked. In order to pull the oscillation frequency ω_J of the RLC-oscillator to the frequency of the injected signal, the circuit must be able to respond at low beating frequencies. The resistor introduces the simplest low-frequency impedance and thus enables the locking mechanism.

- The dc-voltage fluctuates due to the inevitable noise in experiments. A particularly important noise source is Johnson–Nyquist noise. Its strength can be found by integrating the noise power spectrum $\propto Z(f)$ up to the thermal cut-off frequency $f_T \sim \mathcal{O}(100\,\mathrm{GHz})$ set by the typical operating temperature $T \sim \mathcal{O}(10\,\mathrm{mK})$ in experiments [c.f. Fig. 4.1(b)]. The larger R_0, the more noise enters the system and disturbs the phase-space angle.

One potential solution that reduces the overall noise but maintains a low-frequency contribution is a low-pass filter. For instance, a parallel R_0C_0-circuit introduces

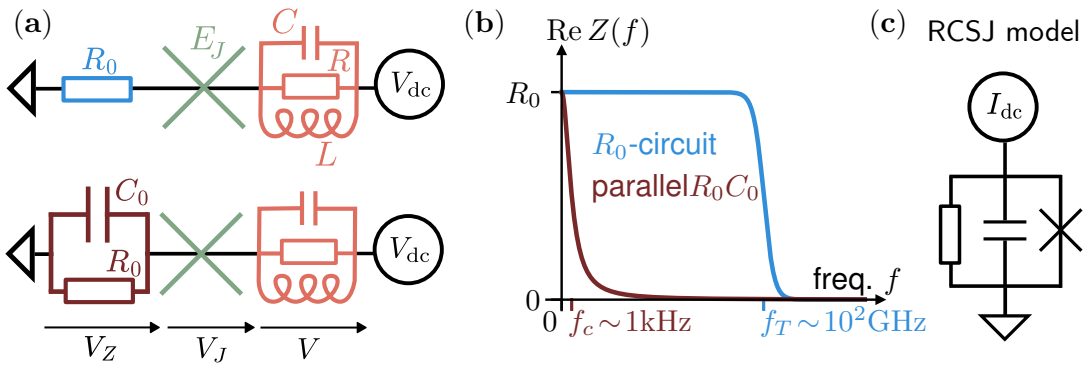

Figure 4.1: (a) Schematic electric circuits of Josephson-photonics devices with two possible choices of the in-series impedance. In the top circuit, Z is a resistor R_0 (studied in Sec. 4.1.1). In the bottom circuit, Z is a parallel R_0C_0-circuit functioning as a low-pass filter (also compare Sec. 4.1.2.3). (b) The strength of the noise that enters the device is found by integration involving the impedance. For $Z = R_0$, the contribution of a constant impedance enters up to the cut-off frequency f_T at typical experimental temperatures T (see main text), yielding a much larger noise than the fabrication of an R_0C_0-circuit with the cut-off frequency $f_c \propto 1/(R_0C_0) \ll f_T$. (c) An Adler-type description of injection locking in a Josephson-photonics device that incorporate an in-series R_0C_0-circuit can be reduced to the dynamics of a particle with mass in a tilted washboard potential. The description can be mapped to the dynamics of another well known electric circuit – namely the RCSJ model – where a resistively and capacitively shunted Josephson junction is driven by a dc current.

a small cut-off frequency $\omega_c = 1/(R_0 C_0)$ when the capacitance C_0 is sufficiently large [see Figs. 4.1(a,b)].

Here, we investigate how to stabilize the phase-space angle in the presence of a general in-series impedance $Z(\omega)$. In this way, we show how the dynamics of injection locking is modified when circuit elements other than a single in-series resistor R_0 are integrated. Therefore, we first derive an Adler equation for a Josephson-photonics device with a general in-series impedance $Z(\omega)$ when the circuit is injection locked by a small ac signal added to the dc-voltage drive,

$$V_{\mathrm{tot}}(t) = V_{\mathrm{dc}} + V_{\mathrm{ac}} \cos(\Omega t + \phi_\epsilon) \tag{4.6}$$

such that $V_{\mathrm{ac}} \ll V_{\mathrm{dc}}$.

The detailed derivation (Sec. 4.1.2.1) uses an ansatz for the phase variables appearing in the circuit equations of motion that makes it possible to separate fast (at the order of the oscillation frequency ω_J of the RLC-circuit) from slow (at orders of the detuning $\Omega - \omega_J$) circuit dynamics. Especially, the contribution of the interplay between the slow current and the impedance will yield a reduced and modified Adler-type description of injection locking (Sec. 4.1.2.2). We will find that the Adler phase

$$\psi = [\Omega t + \phi_\epsilon] - [\omega_J t + \theta_J(t)] \ , \tag{4.7}$$

i.e. the phase difference between the ac drive and the slow part the phase φ_J across the Josephson junction, will experience a potential with a linear slope and a contribution

$$\propto V_{\mathrm{ac}} [Z * I_{\mathrm{CP,slow}}](t)$$

given by the convolution between the impedance and the slow part of the current that creates potential minima where the system can be injection locked when $\dot{\psi} = 0$.

In Sec.4.1.2.3, we discuss the specific example of the in-series parallel $R_0 C_0$-circuit and show that the reduced dynamics of the Adler phase can then be described by a motion of a particle with mass $\propto C_0$ in a tilted washboard potential. The problem can be mapped to the dynamics found in the famous RCSJ model [204, 205] [compare Fig. 4.1(c)] .

4.1.2.1 Derivation of an Adler Equation for a General Impedance $Z(\omega)$

We consider a dc-voltage biased electric circuit, consisting of an RLC-oscillator connected in series with a Josephson junction and a general impedance $Z(\omega)$. In our derivations, we keep the variable definitions consistent with Pub. (i) (presented in Sec. 4.1.1), as summarized in Tab. 4.1.

General circuit equations

We first introduce the phase

$$\dot{\varphi}_Z = \frac{2e}{\hbar} V_Z(t) \tag{4.8}$$

Physical quantity	Parametrization
resonance frequency	$\omega_0 = 1/\sqrt{LC}$
resonance width	$\gamma = 1/(RC)$
in-series impedance	$Z(\omega)$
dc-voltage bias	$\omega_{\mathrm{dc}} = 2eV_{\mathrm{dc}}/\hbar$
Josephson frequency	$\omega_J \neq \omega_{\mathrm{dc}}, \omega_0$
dimensionless Josephson driving strength	$\tilde{I}_c = \frac{2e}{\hbar\omega_0} I_{\mathrm{crit}} R$
injection signal frequency	Ω
injection signal amplitude	$\epsilon = \frac{2e}{\hbar\Omega} V_{\mathrm{ac}} \ll \omega_{\mathrm{dc}}$

Table 4.1: Device characterization for the description of injection locking of a dc-voltage biased Josephson junction that is connected in series to an RLC-circuit and an impedance $Z(\omega)$.

as the integrated voltage across the impedance that is related to the Cooper-pair current in Fourier space[4] by

$$V_Z(\omega) = Z(\omega) \cdot I_{\mathrm{CP}}(\omega) = \frac{i\omega\hbar}{2e}\varphi_Z(\omega)\,. \tag{4.9}$$

Analogously to Sec. 1.3.1, a straightforward application of Kirchhoff's laws for the voltage and the current yields coupled circuit equations of motion

$$\ddot{\varphi} + \gamma\dot{\varphi} + \omega_0^2\varphi = \tilde{I}_c\gamma\omega_0 \cdot \sin\left[\varphi_J\right] \tag{4.10}$$

$$\dot{\varphi}_J = \frac{2e}{\hbar}V_{\mathrm{tot}}(t) - \dot{\varphi} - \dot{\varphi}_Z \tag{4.11}$$

$$\dot{\varphi_Z} = \frac{2e}{\hbar} \cdot [Z * I_{\mathrm{CP}}](t) = \frac{2e}{\hbar}\int_{-\infty}^{\infty} Z(\tau)\, I_{\mathrm{CP}}(t-\tau)\,\mathrm{d}\tau \tag{4.12}$$

between the impedance phase φ_Z, the cavity phase φ and the Josephson phase φ_J (all analogously defined as φ_Z). Crucially, the equations contain a convolution of $Z(\omega)$ with the Josephson current.

Ansatz for the phase variables

Without locking signal, the Josephson phase [Eq. (4.11)] is driven mainly by the frequency $\omega_J(\epsilon = 0) = \omega_{\mathrm{dc}} - 2eV_{Z,\mathrm{dc}}/\hbar$. The Josephson frequency ω_J is reduced compared to the directly applied dc voltage due to an additional dc-voltage drop across the impedance. A locking signal applied at a small frequency mismatch $\nu_0 = \Omega - \omega_J(\epsilon = 0)$ will eventually adjust the Josephson phase and pull the Josephson frequency $\omega_J(\epsilon)$ towards Ω (see Sec. 4.1.1). This slow response of the circuit to the locking signal can be captured by a slowly varying parameter θ_J in an ansatz for the Josephson phase

$$\varphi_J(t) = \omega_J t + \theta_J(t) + a_J \cdot \sin[\omega_J t + \phi_J(t)]\,. \tag{4.13}$$

[4]Here we define the Fourier transform of a function $f(t)$ as $\mathcal{F}_f(\omega) = f(w) = \int_{-\infty}^{\infty} f(t)e^{-i\omega t}\,\mathrm{d}t$

As described in Pub. (*i*), the circuit responds to the locking signal with multiple sidebands around ω_J, captured by a slow function $\phi_J(t)$. Since we consider only small Josephson driving $\tilde{I}_c \ll 1$, the ansatz justifiably neglects oscillations at multiples of ω_J that arise due to the coupled nonlinear equations of motion. With similar arguments, an ansatz for the oscillator and impedance phases [also compare Pub. (*i*)] is given by

$$\varphi(t) = a \cdot \sin[\omega_J t + \phi(t)] \tag{4.14}$$

$$\varphi_Z(t) = \theta_Z(t) + a_Z \sin[\omega_J t + \phi_Z(t)] \tag{4.15}$$

with constant parameters a, a_Z and slow functions $\phi(t)$, $\theta_Z(t)$ and $\phi_Z(t)$.

Slow and fast contributions of the Cooper-pair current and the impedance

The first step towards an Adler equation is to find an expression for the slow current. After substituting the ansatz into the Cooper-pair current,

$$I_{\mathrm{CP}} = I_{\mathrm{crit}} \sin(\varphi_J)\,, \tag{4.16}$$

we perform a Taylor expansion

$$\sin(\varphi_J) \approx \sin(\omega_J t + \theta_J) + \frac{a_J}{2} \sin(\phi_J - \theta_J) \tag{4.17}$$

that assumes small oscillation amplitudes a_J and self-consistently neglects oscillations at multiples of ω_J. Separating time scales, we identify one slow and one fast oscillatory contribution of the Cooper-pair current,

$$I_{\mathrm{CP,slow}}(t) \approx I_{\mathrm{crit}} \frac{a_J}{2} \sin(\phi_J - \theta_J) = I_{\mathrm{crit}} \frac{a_J}{2} \mathrm{Im}\left[e^{i(\phi_J - \theta_J)}\right] \tag{4.18}$$

$$I_{\mathrm{CP,fast}}(t) \approx I_{\mathrm{crit}} \sin(\omega_J t + \theta_J) = I_{\mathrm{crit}} \mathrm{Im}\left[e^{i(\omega_J t + \theta_J)}\right]\,. \tag{4.19}$$

Using the current-voltage relation of the impedance in Fourier space,

$$\dot{\varphi}_Z = \dot{\theta}_Z + a_Z(\omega_J + \dot{\phi}_Z)\cos[\omega_J t + \phi_Z] = \frac{2e}{2\pi\hbar} \int_{-\infty}^{\infty} e^{+i\omega t} Z(\omega) I_{\mathrm{CP}}(\omega)\, \mathrm{d}\omega\,, \tag{4.20}$$

we also identify slow and fast components of the voltage across the impedance,

$$\dot{\varphi}_{Z,\mathrm{slow}} = \dot{\theta}_Z = \frac{2e}{2\pi\hbar} \int_{-\infty}^{\infty} e^{+i\omega t} Z(\omega) I_{\mathrm{CP,slow}}(\omega)\, \mathrm{d}\omega \tag{4.21}$$

$$\dot{\varphi}_{Z,\mathrm{fast}} = a_Z(\omega_J + \dot{\phi}_Z)\cos[\omega_J t + \phi_Z] = \frac{2e}{2\pi\hbar} \int_{-\infty}^{\infty} e^{+i\omega t} Z(\omega) I_{\mathrm{CP,fast}}(\omega)\, \mathrm{d}\omega\,. \tag{4.22}$$

Time-scale separation of the equations of motion

Now, the ansatz and the approximation of the slow and fast current can be inserted into the remaining Eqs. (4.10) and (4.11). Both resulting equations

$$\begin{aligned} &a\left[\omega_0^2 - (\omega_J + \dot{\phi})^2\right] \sin(\omega_J t + \phi) + a\gamma(\omega_J + \dot{\phi}) \cos(\omega_J t + \phi) \\ &\approx \tilde{I}_c \gamma \omega_0 \cdot \left[\frac{a_J}{2} \sin(\phi_J - \theta_J) + \sin(\omega_J t + \theta_J)\right] \end{aligned} \tag{4.23}$$

and

$$\begin{aligned} &\omega_{\mathrm{dc}} + \epsilon\Omega \cos(\Omega t + \phi_\epsilon) - \dot{\theta}_Z - a_Z(\omega_J + \dot{\phi}_Z)\cos(\omega_J t + \phi_Z) - a(\omega_J + \dot{\phi})\cos(\omega_J t + \phi) \\ &= \omega_J + \dot{\theta}_J + a_J(\omega_J + \dot{\phi}_J)\cos(\omega_J t + \phi_J) \end{aligned} \tag{4.24}$$

can also be separated into fast and slow contributions:

- Fast oscillations around ω_J

  The two fast contributions oscillating around ω_J of Eqs. (4.23) and (4.24) can be written in the complex plane

$$ae^{i(\omega_J t+\phi)}\left[\omega_0^2+i\gamma(\omega_J+\dot{\phi})-(\omega_J+\dot{\phi})^2\right]=\tilde{I}_c\gamma\omega_0 e^{i(\omega_J t+\theta_J)} \tag{4.25}$$

$$a_J e^{i(\omega_J t+\phi_J)}(\omega_J+\dot{\phi}_J)=\epsilon\Omega e^{i(\Omega t+\phi_\epsilon)}-a(\omega_J+\dot{\phi})e^{i(\omega_J t+\phi)} - a_Z(\omega_J+\dot{\phi}_Z)e^{i(\omega_J t+\phi_Z)}\,. \tag{4.26}$$

  Moving to a rotating frame with ω_J, these two equations can be solved for

$$a_J e^{i(\phi_J-\theta_J)}=\epsilon\frac{\Omega}{\omega_J+\dot{\phi}_J}e^{i\psi(t)}-\tilde{I}_c\frac{\omega_J+\dot{\phi}}{\omega_J+\dot{\phi}_J}\frac{\gamma\omega_0}{\left[\omega_0^2+i\gamma(\omega_J+\dot{\phi})-(\omega_J+\dot{\phi})^2\right]} - a_Z\frac{\omega_J+\dot{\phi}_Z}{\omega_J+\dot{\phi}_J}e^{i(\phi_Z-\theta_J)}\,. \tag{4.27}$$

  The imaginary part of Eq. (4.27) yields a solution for the slow part $I_{\mathrm{CP,slow}}(t)\approx\frac{a_J}{2}\sin(\phi_J-\theta_J)$ of the current.

- Slow oscillations around frequency ν_0

  First, the slow part at low frequencies around the detuning of Eq. (4.23) describes a highly off-resonant response of the harmonic oscillator that has been neglected in the ansatz. Second, the slow contribution of Eq. (4.24),

$$\omega_{\mathrm{dc}}-\dot{\theta}_Z=\omega_J+\dot{\theta}_J \tag{4.28}$$

  can be used when taking the derivative of the Adler phase, $\psi=[\Omega t+\phi_\epsilon]-[\omega_J t+\theta_J(t)]$, c.f. Eq. (4.7). Finally, we obtain a **generalized Adler equation**

$$\dot{\psi}=\Omega-\omega_{\mathrm{dc}}+\dot{\theta}_Z \tag{4.29}$$

  that contains the slow contribution of the phase across the general in-series impedance.

4.1.2.2 The General Adler Equation for Josephson-Photonics Devices

After the separation of the equations of motion into slow and fast oscillating parts, we could derive a generalized Adler equation, Eq. (4.29), crucially containing a slow phase across the impedance

$$\dot{\theta}_Z=\dot{\varphi}_{Z,\mathrm{slow}}=\frac{2e}{2\pi\hbar}\int_{-\infty}^{\infty}e^{+i\omega t}Z(\omega)I_{\mathrm{CP,slow}}(\omega)\,\mathrm{d}\omega=\frac{2e}{\hbar}\left[Z*I_{\mathrm{CP,slow}}\right](t) \tag{4.21}$$

that depends on the convolution of $Z(\omega)$ with the slow part of the current

$$\frac{I_{\mathrm{CP,slow}}(t)}{I_{\mathrm{crit}}}\approx\frac{\epsilon}{2}\sin[\psi(t)]-\frac{\tilde{I}_c}{2}\frac{\omega_J+\dot{\phi}}{\omega_J+\dot{\phi}_J}\mathrm{Im}\left\{\frac{\gamma\omega_0}{\omega_0^2+i\gamma(\omega_J+\dot{\phi})-(\omega_J+\dot{\phi})^2}\right\} - \frac{a_Z}{2}\frac{\omega_J+\dot{\phi}_Z}{\omega_J+\dot{\phi}_J}\mathrm{Im}\left\{e^{i(\phi_Z-\theta_J)}\right\}\,. \tag{4.30}$$

General Adler Equation

$$\dot{\psi} = \nu_0 + \omega_0 \tilde{I}_c \frac{\epsilon}{2} \left[\frac{Z}{R} * \sin(\psi) \right] \tag{4.31}$$

Detuning $\nu_0 = \nu_1 + \nu_2 + \nu_3$ with

$$\nu_1 = \Omega - \omega_{\mathrm{dc}} \tag{4.32}$$

$$\nu_2 \approx -\omega_0 \frac{\tilde{I}_c^2}{2} \left[\frac{Z}{R} * \mathrm{Im} \left(\frac{\omega_J + \dot{\phi}}{\omega_J + \dot{\phi}_J} \frac{\gamma\omega_0}{\left[\omega_0^2 + i\gamma(\omega_J + \dot{\phi}) - (\omega_J + \dot{\phi})^2 \right]} \right) \right] \tag{4.33}$$

$$\nu_3 \approx -\omega_0 \frac{\tilde{I}_c}{2} \left[\frac{Z}{R} * \mathrm{Im} \left(a_Z \frac{\omega_J + \dot{\phi}_Z}{\omega_J + \dot{\phi}_J} e^{i(\phi_Z - \theta_J)} \right) \right] \tag{4.34}$$

Since the first part of the slow current is explicitly dependent on the locking strength, the generalized Adler equation is given by a convolution of the impedance with $\sin(\psi)$. The other two contributions are corrections to the detuning.

The complexity of the derivation and result arises because the impedance is kept general. To illustrate the findings more clearly, we now explicitly work out a more intuitively understandable example, where $Z(\omega)$ is a low-pass filter.

4.1.2.3 Adler Equation for a Josephson-Photonics Device with a Parallel R_0C_0-Circuit

In the specific case, where the RLC-circuit is connected in series with a Josephson junction and a parallel R_0C_0-circuit, as in Fig. 4.1(a), the circuit equations of motion (4.10), (4.11) and (4.12) reduce to

$$\ddot{\varphi} + \gamma\dot{\varphi} + \omega_0^2\varphi = \frac{2e}{\hbar} \frac{I_{\mathrm{crit}}}{C} \cdot \sin(\varphi_J) \tag{4.35}$$

$$\dot{\varphi}_J = \frac{2e}{\hbar} V_{\mathrm{tot}}(t) - \dot{\varphi} - \dot{\varphi}_Z \tag{4.36}$$

$$\ddot{\varphi}_Z + \omega_c\dot{\varphi}_Z = \frac{2e}{\hbar} \frac{I_{\mathrm{crit}}}{C_0} \sin(\varphi_J)\,. \tag{4.37}$$

The impedance of the parallel R_0C_0-circuit

$$Z(\omega) = \frac{R_0}{1 + i\omega/\omega_c} \tag{4.38}$$

[with $Z(\omega = 0) = R_0$] introduces an effective frequency cut-off in Fourier space at $\omega_c = 1/(R_0C_0)$.

The general Adler equation (4.31) can be Fourier transformed (formally writing the Fourier transform of $\sin[\psi(t)]$ as $\mathcal{F}_{\sin(\psi)}$) and divided by $Z(\omega)$. If the frequency-dependent parts of ν_0 ca be neglected, this yields

$$i\omega \frac{1 + i\omega/\omega_c}{R_0} \psi(\omega) = \frac{2\pi\,\nu_0 \cdot \delta(\omega)}{Z(\omega)} + \omega_0 \frac{\tilde{I}_c}{R} \frac{\epsilon}{2} \cdot \mathcal{F}_{\sin[\psi(t)]}(\omega)\,. \tag{4.39}$$

A subsequent back-transformation to time space will therefore introduce a first- and a second-order derivative into the Adler-type equation

$$\frac{\ddot{\psi}}{\omega_c} + \dot{\psi} = \nu_0 + \frac{\epsilon}{2}\omega_0 \tilde{I}_c \frac{Z(\omega = 0)}{R} \sin(\psi)\,. \tag{4.40}$$

Here, the Adler-type equation describes a particle with position ψ and effective finite mass $\propto 1/\omega_c$ (introduced by the low-pass filter) that moves in a tilted washboard potential. While the system's ability to respond at finite but small frequencies (in the order of the detuning between Ω and ω_J) enables frequency pulling and stabilization of the phase-space angle, a finite $Z(\omega = 0)$ builds a potential well for ψ and hence is crucial for locking to emerge.

Starting a detailed analysis, we first consider the limiting case of negligible mass, $\omega_c \to \infty$. The Adler-type equation then reduces to the case of an in-series resistor (with $Z(\omega) = R_0$) studied in Pub. (*i*), where the phase particle will perform an overdamped motion in the washboard potential

$$V_{\mathrm{WB}}(\psi) = -\nu_0 \psi + \nu_c \cos(\psi)\,. \tag{4.41}$$

Given a fixed locking amplitude, the critical detuning for the existence of injection locked solutions is then given by

$$\nu_c = \frac{\epsilon}{2}\omega_0 \tilde{I}_c \frac{R_0}{R}\,, \tag{4.42}$$

such that the system can be locked, $\dot{\psi} = 0$, when $\nu_0 < \nu_c$.
Considering now the case of a finite mass, the Adler equation is first rewritten in dimensionless units (with time $\tau = \nu_c t$) as

$$\frac{\nu_c}{\omega_c} \cdot \frac{d^2}{d\tau^2}\psi(\tau) + \frac{d}{d\tau}\psi(\tau) = \frac{\nu_0}{\nu_c} + \sin[\psi(\tau)]\,. \tag{4.43}$$

Due to the inertia of the massive Adler phase, its corresponding motion is no longer overdamped such that hysteresis can be observed (see Fig. 4.2) and bistable solutions can appear. In fact, many results are already known for this problem, as it maps onto the dynamics found in the RCSJ model. Here, we only give a brief discussion of the main results.

To gain insight into the hysteresis effect, we first consider the case where the locking signal is turned on with vanishing detuning $\nu_0 = 0$. The phase particle ψ is then at rest in the potential minimum (i.e. the system is injection locked). A slow increase in the detuning results in an effective tilt of the washboard potential with less pronounced minima (provided that $\nu_0 < \nu_c$). However, the phase particle will still remain at rest in its initial potential minimum [compare the blue point for $\nu_0 = 3\nu_c/5$ in Figs. 4.2(b,d)]. When tilting the potential beyond the critical point $\nu_0 = \nu_c$, the washboard potential no longer exhibits minima [compare the purple point in Figs. 4.2(b,e)]. Then the phase particle will be brought into an accelerating motion and eventually reaches a final mean velocity such that the system is no longer injection locked.

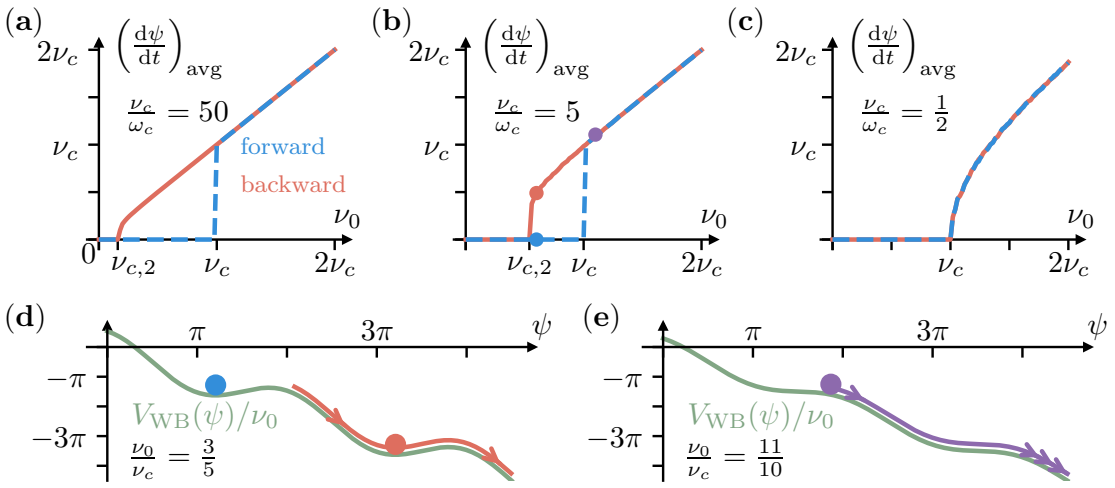

Figure 4.2: Injection Locking and hysteretic effects of Josephson-photonics devices with a low-pass filter, where we simulate the Adler equation (4.43). In the stationary state, the derivative of ψ is averaged over a long time interval $\Delta\tau$ to obtain an average steady-state velocity. (a-c) Resulting locking curves for different particle masses ν_c/ω_c show hysteresis (see forward and backward path) with regions of bistable solutions (also compare explanation below and in main text). (d) Washboard potential (green) for $\nu_0 = 3\nu_c/5$ from (b). Depending on the system's history, the steady-state motion of ψ either remains locked [blue point here and in (b)], because the potential tilt before was smaller and the system was at rest, or it moves with a finite average velocity [red motion here and red point in (b)], because the potential tilt was larger and the system had a finite average velocity. Due to inertia, the massive particle cannot be captured in a potential minimum. A second critical detuning $\nu_{c,2}$ emerges, where the Adler phase of the backward path becomes a constant in time, c.f. (a,b). (e) Washboard potential (green) for the forward path at the purple point of (b). Having tilted the potential from $\nu_0 = 0$ to $\nu_0 > \nu_c$, a previously locked phase particle will now start to slide down the potential and is accelerated until it reaches its steady-state velocity.
[Methods: We start for the forward path at $\nu_0 = 0$ with a state initially at the minimum position, $\psi_s(\tau = 0)$. After a first time evolution, $s = 1$, to a sufficiently large final time τ_f, the average velocity is calculated and the final state $\psi_s(\tau_f)$ is recorded. In a subsequent time evolution, $s + 1$, the state is prepared in $\psi_{s+1}(0) = \psi_s(\tau_f)$ and the potential is slightly tilted by $d\nu_0$. Analogously, the backward path is found by starting the first simulation at $\nu = 2\nu_c$ and subsequently decreasing ν_0.
Parameters: $d\nu_0 = \nu_c/50$, $\Delta\tau = \tau_f/2$, while $\tau_f = 2 \cdot 10^4$ for (a) and $\tau_f = 200$ in (b,c).]

Now, we consider large detunings $\nu_0 \gg \nu_c$ that are slowly reduced. When the detuning becomes sufficiently small, $\nu_0 < \nu_c$, the Adler potential develops minima. For the same detuning as before, $\nu_0 = 3\nu_c/5$, [compare the red point in Figs. 4.2(b,d)], the phase particle will continue to move because of its inertia arising from its finite mass. To stop massive particle from running, even deeper potential minima are needed. Of course, this hysteresis effect is more pronounced for larger masses ν_c/ω_c, whereas hysteresis is only marginally relevant when $\nu_c/\omega_c = 1/2$ [Fig. 4.2(c)].

While the analysis above is performed without noise, estimates for an upper bound of lockable noise can be made. Experimentally, the locking signal should be limited

to small signals, $\epsilon \ll 1$, to reduce the effect of the locking signal on the resonator's state. An upper bound for the experimentally used locking amplitude therefore fixes the critical detuning ν_c, for which a system (without noise) can still be injection locked. A larger capacitor C_0 will result in smaller cut-off frequencies ω_c that reduce the noise entering the circuit. However, small ω_c will yield stronger hysteresis effects that are reflected in a second critical detuning $\nu_{c,2}$ of the backward hysteresis path [compare Fig. 4.2(a, b)]. Therefore, noise fluctuations should remain smaller than $\nu_{c,2}$.

So far, a quantum mechanical description of injection locking in Josephson photonics has been developed and analyzed only for an in-series resistor R_0 (see Sec. 4.2). Analogous methods may be used in the future to show how circuits with general impedance, such as the low-pass filter that was analyzed here in a classical regime, behave in the quantum regime when injection locked. A first step towards a quantum description is to amend the quantum Lindblad description with a classical equation of motion for the Adler phase including classical noise, similar to the description of the locking of cat states from Sec. 4.2.3.2.

4.2 Phase Stabilization in the Quantum Regime

In the simplest case, the classical description of a Josephson-photonics device with an in-series resistor R_0 yields the physically correct description of self-sustained oscillations that can be injection locked. Thus, we incorporate the additional in-series resistor, which turned out to be crucial in the classical case, into the quantum model [Pub. (*ii*) in Sec. 4.2.1]. In the quantum regime, the effects of injection locking and synchronization can be investigated for states of light without a classical counterpart. For instance, injection locking also stabilizes the phase-space angle of squeezing ellipses [Pub. (*iii*) in Sec. 4.2.2] and cat states (see Sec. 4.2.3), which paves the way for the application of Josephson-photonics devices for quantum computing and other quantum technologies such as the quantum radar (c.f. Secs. 1.4.2 and 1.5.2). While Pubs. (*ii*) and (*iii*) focus on a regime that is dominated by the shot noise of the Cooper pairs, we discuss the stabilization of cat states in a regime dominated by classical noise. This serves as an instructive alternative that is more easily understandable than a full quantum mechanical treatment.
An alternative approach alleviating the need for phase stabilization by injection locking and synchronization is presented in Sec. 4.2.4. The issue of the neutrally stable phase-space angle can be partially mitigated when the steady state of the system without phase diffusion can be reconstructed. When measuring only a few experimentally accessible expectation values, the quantum steady state can be found by optimizing an ansatz. In this way, the theoretical quantum state can be recovered, and information about the phase can be restored.

4.2.1 Publication (*ii*): *Quantum synchronization in presence of shot noise*

4.2.1.1 Bibliographic Data and Author's Contribution

Title	Quantum synchronization in presence of shot noise
Authors	Florian Höhe, Lukas Danner, Ciprian Padurariu, Brecht I. C Donvil, Joachim Ankerhold, and Björn Kubala
Journal	New Journal of Physics
Volume	27
Number	023039
Year	2025
DOI	https://doi.org/10.1088/1367-2630/adb777
Copyright	

[5] https://creativecommons.org/licenses/by/4.0/

The author performed analytical calculations and contributed substantially to the interpretation of the results of this publication. The author contributed significantly to the preparation of the manuscript.

4.2.1.2 Summary of Publication (*ii*)

The publication *Quantum synchronization in presence of shot noise* studies injection locking and synchronization of Josephson-photonics devices that contain a single resonator and are driven at the fundamental resonance $\omega_{\mathrm{dc}} \approx \omega_0$. Here, we explicitly show how to incorporate the quantum effects of an in-series resistor R_0 into the theoretical model, which yields a description of Cooper-pair shot noise and enables injection locking and synchronization in the quantum regime.

Incorporating the in-series resistor into the quantum description

For devices operated in the classical regime (see Sec. 4.1.1), the inclusion of an in-series resistance R_0 in the theoretical model for a Josephson-photonics device will correctly describe self-sustained oscillations and enable phase-locking and synchronization. A brute-force microscopic description of the in-series resistor in the quantum regime would be cumbersome. Eqs. (1) and (2) of Pub. (*ii*) start with the description of the resistor's associated phase

$$\hat{\varphi}_{R_0} \propto R_0 \int_0^t \hat{I}_{\mathrm{CP}}\, \mathrm{d}\tau \tag{4.44}$$

as a quantum operator that depends on the Cooper-pair current. As a quantum operator, $\hat{\varphi}_{R_0}$ contains coherence effects between different numbers of tunneled Cooper pairs. If the resistance is much smaller than the quantum of resistance, $R_0 \ll R_Q$, coherence effects of tunneling Cooper pairs in the current operator are negligible. Then, $\hat{\varphi}_{R_0}$ can be approximated by

$$\varphi_{R_0} \propto R_0 \cdot 2e\, m(t)\,, \tag{4.45}$$

where $m(t)$ is a c-number describing how many Cooper pairs have tunneled across the junction after time t. In this approximation, φ_{R_0} becomes a stochastic time-dependent variable whose dynamics is governed by the Cooper-pair current.

Self-sustained oscillations with neutrally stable phase in the quantum regime

In previous works [25, 27, 28] (also compare Secs. 1.3.2 and 1.4.1), $\varphi_{R_0} = \eta$ was a simple constant phase shift in the steady state's Wigner function. Now, the time-dependent fluctuations of the tunneling processes give rise to shot noise. As an important consequence, shot noise will effectively average the phase of the resonator's quantum state resulting in a steady state of the microwave cavity that exhibits a rotationally symmetric Wigner distribution with a neutrally stable phase-space angle [Fig. 2(a) of Pub. (*ii*)]. Although the Wigner function of the self-sustained oscillator is averaged due to shot noise, many steady-state expectation values, such as the cavity occupation $\langle \hat{a}^\dagger \hat{a} \rangle_{\mathrm{st}}$ or the Cooper-pair current $\langle \hat{I}_{\mathrm{CP}} \rangle_{\mathrm{st}}$ are independent of φ_{R_0}. An energy conservation argument directly relates the Cooper-pair current to the photon emission rate from the microwave cavity in the steady state [25, 38]

$$\langle \hat{I}_{\mathrm{CP}} \rangle_{\mathrm{st}} = 2e\gamma \langle \hat{a}^\dagger \hat{a} \rangle_{\mathrm{st}}\,. \tag{4.46}$$

The long-time statistics of the Cooper-pair current in Josephson-photonics devices can be obtained by photon counting [38] when the energy conservation argument, Eq. (4.46), holds.

Injection locking of the Josephson-photonics device in the quantum regime

Analogously to the classical study of Sec. 4.1.1, we include a small ac voltage with amplitude ε and frequency $\Omega \approx \omega_{\mathrm{dc}}, \omega_0$ that is nearly resonant to the dc-driving frequency and to the fundamental resonance. It provides a stable reference phase to which the system can be injection locked. Since it is part of the voltage drive, the locking signal enters the (lab-frame) Hamiltonian and the Cooper-pair current. Within rotating-wave approximation, the locking signal enables additional resonant processes [see Eq. (3) of Pub. (*ii*)]. Most crucially, the contribution

$$\propto E_J^* \varepsilon : J_0(2\alpha_0 \sqrt{\hat{a}^\dagger \hat{a}}) : \tag{4.47}$$

describes the tunneling of a Cooper pair by emission of one excitation to the locking drive, which is renormalized by the presence of cavity excitations. Although this resonant process only yields a minor modification of the Hamiltonian (namely a constant energy shift that does not affect the dynamics) in the limit of small zero-point fluctuations, it adds a Shapiro-like constant term to the current operator. As main result, Pub. (*ii*) shows that the Cooper-pair current becomes dependent on the phase difference

$$\psi = (\Omega t + \varphi_{\mathrm{ac}}) - (\omega_{\mathrm{dc}} t - \varphi_{R_0}) \tag{4.48}$$

between the injected signal and the dc-driving phase of the microwave mode. As in the classical case [compare Pub. (*i*)], the Adler phase ψ elegantly describes injection locking in the quantum regime. Injection locked solutions with stabilized phase-space angle can thus exist when the Cooper-pair current adjusts φ_{R_0} such that the Adler phase ψ becomes constant in time.

Cooper-pair number resolved equation of motion

A dynamical equation of motion, which includes the feedback of the number of tunneled Cooper pairs into the time evolution of the cavity (and vice versa) can be derived by modifying a standard technique from quantum optics [66], which unravels the Lindblad master equation into quantum trajectories: n-resolved photon counting [206] uses a set of matrices ρ_n that describe the quantum state of a system conditioned on the number n of counted photons which have leaked. The quantum state of the system can be recovered by summing over all conditioned matrices,

$$\hat{\rho} = \sum_n \rho_n \,. \tag{4.49}$$

While without a locking signal, the statistics of the Cooper-pair current is directly linked to the rate of outgoing photons, a finite locking drive adds energy to the system. It breaks the correspondence that each tunneling Cooper pair creates one excitation in the resonator. Therefore, the energy conservation argument does not hold anymore and we cannot infer the number of tunneled Cooper pairs by counting

photons. A central result of Pub. (*ii*) is the derivation of an extended m-resolved master equation [for precise explanations, see Appendix B of Pub. (*ii*)] counting tunneling Cooper pairs. Our description includes both the effects of Cooper-pair shot noise and the locking drive. In this way, we properly describe the dynamics of phase diffusion and injection locking in the quantum regime.

Phase stabilization by injection locking

Without a locking signal, we obtain the behavior of a self-sustained oscillator subject to shot noise. Its oscillation frequency is broadened due to the shot noise, which is directly linked to a broad distribution of tunneling Cooper pairs in a given time interval [Fig. 1 of Pub. (*ii*)]. Consequently, the Wigner distribution of the steady state is phase averaged [Fig. 2(a)].
A locking drive, which is sufficiently large compared to the shot noise, can pull the oscillation frequency of the system to the locking frequency Ω. It directly affects the shot noise [c.f. Fig. 1 and Appendix B of Pub. (*ii*)] and results in a narrow distribution of tunneled Cooper pairs. Therefore, also the phase-space angle of the Wigner function of the resonator's steady state is stabilized [see Fig. 2(c)].

Reduced description of injection locking by Adler

Pub. (*ii*) continues to study the reduced dynamics of the Adler phase in the limit of a small in-series resistance, where the discrete steps in the quantum-stochastic variable become very small. Using mathematical methods of two-time perturbation theory [Appendix C of Pub. (*ii*)], we derive a Fokker-Planck equation for the phase distribution probability $P(t, \psi)$ [Eq. (7) of Pub. (*ii*)]. It describes the motion of ψ in an effective washboard potential [see Fig. 3(a)]. Stochastic trajectories of the corresponding Langevin equation [Fig. 3(b)] demonstrate synchronized solutions with long time periods of constant phase ψ, which are interrupted by short periods where the phase slips by 2π. We find a Kramer's rate for the escape process, which is exponentially suppressed for smaller shot noise and larger barrier heights of the washboard potential [compare also the classical study from Pub. (*i*)]. Such phase slips are visible in the statistics of the Cooper-pair current [compare Fig. 1(c)], which possesses side peaks at a distance of (multiples of) Δm (where Δm corresponds to a change of 2π in ψ) from the main peak. In the limit of negligible shot noise, the Fokker-Planck equation simplifies to the Adler equation derived in Pub. (*i*). This result beautifully connects injection locking in the classical realm with the quantum regime.

Mutual synchronization of two Josephson-photonics devices

Finally, we study mutual synchronization of two Josephson-photonics devices that are capacitively coupled. The reduced Fokker-Planck equation describes the dynamics of the sum and difference of the two phases. For uncoupled devices, the distribution of both phases [simulated by corresponding Langevin equations, see blue dots in Fig. 4(b)] is broadened due to the shot noise. Coupling them may result in a synchronized state, where the oscillation frequencies of both resonators are equal [Fig. 4(c)]. In the synchronized state, the probability distribution of the phase difference is located in the minimum of a washboard potential and, consequently, sharpened [red curve and dots in Fig. 4(b)].

In summary, we provided a quantum theory for Josephson-photonics devices to describe injection locking and quantum synchronization of self-sustained oscillations in presence of shot noise. We achieved that by including the quantum effects of an in-series resistor that models a realistic voltage source and enables the mechanisms of injection locking and synchronization. By deriving an m-resolved Master equation, we could extend the classical study of Pub. (i) to the quantum realm, which opens the possibility to stabilize the phase-space angle of true quantum states, like squeezed states or cat states, used in technological applications, which is discussed in detail in Secs. 4.2.2 and 4.2.3.

IOP Publishing New J. Phys. 27 (2025) 023039 https://doi.org/10.1088/1367-2630/adb777

New Journal of Physics
The open access journal at the forefront of physics

Deutsche Physikalische Gesellschaft DPG
IOP Institute of Physics

Published in partnership with: Deutsche Physikalische Gesellschaft and the Institute of Physics

OPEN ACCESS

RECEIVED
17 September 2024

REVISED
31 January 2025

ACCEPTED FOR PUBLICATION
18 February 2025

PUBLISHED
27 February 2025

PAPER

Quantum synchronization in presence of shot noise

Florian Höhe[1,*], **Lukas Danner**[1,2], **Ciprian Padurariu**[1], **Brecht I C Donvil**[1], **Joachim Ankerhold**[1] and **Björn Kubala**[1,2]

[1] Institute for Complex Quantum Systems and IQST, University of Ulm, 89069 Ulm, Germany
[2] German Aerospace Center (DLR), Institute of Quantum Technologies, 89081 Ulm, Germany
[*] Author to whom any correspondence should be addressed.

E-mail: florian.hoehe@uni-ulm.de

Keywords: superconducting circuits, Josephson photonics, quantum synchronization, full counting statistics, nonlinear quantum dynamics

Supplementary material for this article is available online

Abstract

Synchronization is a widespread phenomenon encountered in many natural and engineered systems with nonlinear classical dynamics. How synchronization concepts and mechanisms transfer to the quantum realm and whether features are universal or platform specific are timely questions of fundamental interest. They can be studied in superconducting electrical circuits which provide a well-established platform for nonlinear quantum dynamics. Here, we consider a Josephson-photonics device, where a dc-biased Josephson junction creates (non-classical) light in a microwave cavity. The combined quantum compound constitutes a self-sustained oscillator: a system susceptible to synchronization. This is due to the inherent effect of an in-series resistance, which realizes an autonomous feedback mechanism of the charge transport on the driving voltage. Accounting for the full counting statistics of transported charge not only yields phase diffusion, but allows us to describe phase locking to an ac-signal and the mutual synchronization of two such devices. Thereby one can observe phase stabilization leading to a sharp emission spectrum as well as unique charge transport statistics revealing shot noise induced phase slips. Two-time perturbation theory is used to obtain a reduced description of the oscillators phase dynamics in form of a Fokker–Planck equation in generalization of classical synchronization theories.

1. Introduction

Since Huygens's first study of pendulum clocks in 1665 [1] the nonlinear phenomenon of synchronization has extensively been studied in all fields of science [2–6]. It occurs in systems autonomously undergoing *self-sustained oscillations*, i.e. these are not powered by an external periodic drive, but are kept going by resupplying energy in an incoherent manner, such as by the gravity-driven weight in a pendulum clock or by a battery. In the absence of any periodic reference oscillation, self-sustained oscillations do not have any preferred phase which instead will be randomized by noise acting on the system. In the same manner, the phase will be strongly susceptible to regular external perturbations, so that even a weak injected signal can entrain one oscillator or a weak coupling can synchronize the motion of two such systems. While the oscillation spectrum of the free self-sustained oscillator is broad and centered around its natural frequency, it will be pulled towards the frequency of the injected signal and become very sharp when locked, explaining the technological relevance of locking and synchronization, e. g. in laser physics [7, 8].

Unsurprisingly, also quantum synchronization has attracted interest recently, both for systems whose classical counterparts show synchronization behavior with the paradigmatic example of the van der Pol oscillator [9–16], as well as for systems [17–25], such as small spins, or mechanisms [26–32] without classical analogue.

Superconducting electrical circuits incorporating Josephson junctions are an ideal platform to study, both, the fundamental physics of (circuit) quantum electrodynamics as well as the technological exploitation of nonlinear quantum dynamics. For instance, such circuits can oftentimes bridge all the way from the

semiclassical to the deep quantum regime. One manifestation of quantum effects is the appearance of shot noise: fluctuations of the electrical current associated with the granular nature of electrical charges, i.e. of electrons in a metal or (Cooper-)pairs of electrons in a superconductor. Synchronization physics in such devices is thus influenced by the quantum mechanical nature of the nonlinear oscillator and the quantum stochastic nature of the noise affecting its phase.

A perfect system to study such quantum synchronization in the presence of shot noise are Josephson-photonics devices, where Cooper pairs (CPs) tunneling across a dc-biased Josephson junction create photons in an in-series microwave cavity [33]. In such devices, the nonlinearity of the Josephson junction imprints a quantum nature on the microwave generation so that they can be employed to create entangled light [34], photon multiplets [35], or single-photons [36, 37]. Constituting versatile and bright quantum light sources they may become an important component for quantum technological applications [38, 39] in quantum communication, quantum information processing, and for sensing and imaging tasks, such as envisioned quantum radars [40]. While synchronization in (multi-mode) Josephson photonics has been observed in a semiclassical regime [41–43] and to some extent theoretically described [44–46], those devices are also particularly suited to study the deep quantum regimes of strong nonlinearity at the few-photon level [35, 37, 47], where such fundamental questions as quantum measures of synchronization [48–50] and synchronization of individual trajectories [26, 31] can be studied.

Here, we present a model for the quantum dynamics of a Josephson-photonics circuit biased by a realistic voltage source. We show that the system is driven into self-sustained oscillations and describe how it synchronizes to an external ac-signal or a second circuit. Such phase locking enables an immediate exploitation of these devices as sources of entanglement, thus dispensing with the elaborate scheme developed in [34] to characterize the entanglement of a two-mode squeezed state without phase stability, and opens the door to Wigner state tomography consequently broadening the potential technological impact of these devices. Moreover, this new platform for quantum synchronization allows studying fundamental limitations of phase stabilization in a regime, where the quantum shot noise of charge tunneling-events feeds back into the Hamiltonian and induces phase slips.

2. Quantum synchronization to an external signal

In a Josephson-photonics device CPs tunneling across a dc-biased Josephson junction create photonic excitations in a microwave cavity connected in series with the junction, see figure 1(a). The energy of CPs is converted into microwave radiation emitted from the leaky cavity with a frequency, $\omega_J \approx 2eV_{\rm dc}/\hbar = \omega_{\rm dc}$, when the dc-voltage is tuned close to a resonance frequency, $\omega_0 \approx \omega_J$, of the cavity. Placing a resistor R_0 in series with junction and cavity promotes a back-action of the CP tunneling on the voltage driving the tunneling process: the mean dc-current $\langle \hat{I}_{\rm CP}\rangle$ reduces the effective dc-voltage driving the junction, $\omega_J = 2e(V_{\rm dc} - R_0\langle \hat{I}_{\rm CP}\rangle)/\hbar$, while current shot noise is turned into voltage fluctuations assumed here to exceed thermal or other fluctuations of the voltage source. As we demonstrate in the following, the very same backaction mechanism can help to avert broadening, if a small ac-locking signal is added to the dc-voltage, $V(t) = V_{\rm dc} + V_{\rm ac}\cos[\Omega t + \varphi_{\rm ac}]$. Increasing the amplitude $\varepsilon = 2eV_{\rm ac}/(\hbar\Omega)$, the spectrum will first show an additional small δ-peak at Ω, while the broadened peak is pulled towards Ω, until eventually most light is emitted within a very sharp peak in sync with the external locking drive, see figure 1(b). How to model and simulate these fundamental features of nonlinear quantum dynamics – namely frequency pulling, phase locking, and the closely related synchronization to a second device, which takes the role of the external locking signal – is the central result of this work.

2.1. Josephson-photonics system with in-series resistor

A Josephson-photonics device is modeled by the Hamiltonian

$$H_S = \hbar\omega_0\hat{a}^\dagger\hat{a} - E_J\cos\left[\alpha_0\left(\hat{a}^\dagger + \hat{a}\right) + \frac{2e}{\hbar}\int_0^t V(\tau)\,{\rm d}\tau - \hat{\varphi}_{R_0}\right], \tag{1}$$

where $\hat{a}^\dagger$ and $\hat{a}$ denote creation and annihilation operators of the cavity with zero-point fluctuations $\alpha_0 = (2e^2\sqrt{L/C}/\hbar)^{1/2}$, E_J is the Josephson energy, and the argument of the cosine follows from Kirchhoff's sum rule. In contrast to ac-driven Josephson microwave devices, such as Josephson parametric amplifiers [38, 39], the nonlinear Josephson-photonics device is not driven by a periodic force, but by an incoherent power input from a battery. It thus emulates the textbook dynamical system susceptible to locking and synchronization, the pendulum clock driven by a weight. This aspect of Josephson-photonics devices is hidden in the standard description, when a perfect dc-voltage bias $V \equiv V_{\rm dc}$ without any resistance is assumed, i.e. $\hat{\varphi}_{R_0} = 0$, so that a periodic drive term $E_J\cos\left[2eV_{\rm dc}t/\hbar + \alpha_0(\hat{a}^\dagger + \hat{a})\right]$ results. The oftentimes

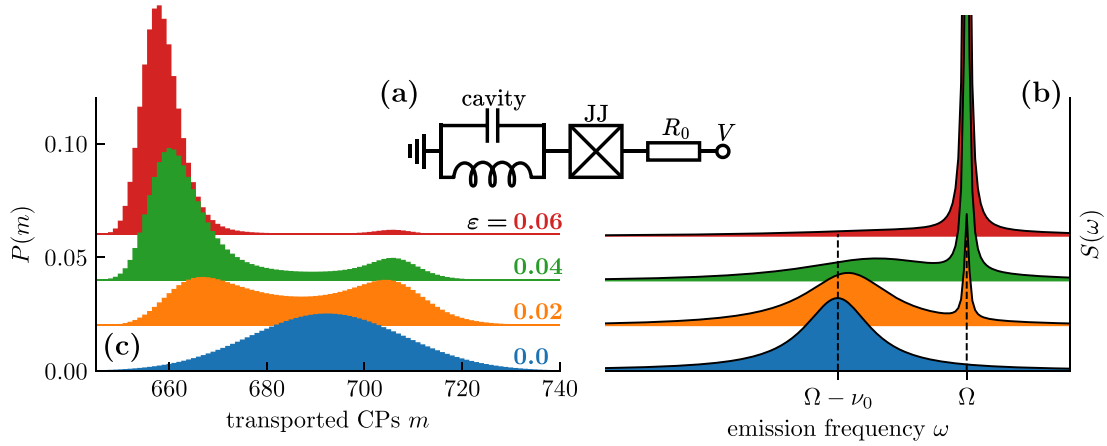

Figure 1. The microwave emission of a Josephson-photonics device (a), consisting of a Josephson junction in-series to a microwave cavity and a resistance R_0, can be locked by adding a small ac-signal (of strength ε and frequency Ω on top of a dc-voltage drive). (b) Emission spectra $S(\omega)$ are centered around a frequency ω_J determined by the voltage across the junction but broadened by phase fluctuations. Applying a locking signal [initially detuned by $\nu_0 = \Omega - \omega_J(\varepsilon = 0)$] pulls the emission frequency towards Ω, eventually resulting in a sharp emission peak at Ω [here artificially broadened by $\gamma/1000$ (FWHM)]. (c) The counting statistics of CPs transported within a time interval $T = 267/\gamma$ is directly linked to the statistics of voltage fluctuations and thus the spectral width. Increasing the locking strength narrows the CP distribution, while shot noise induces phase slips by $\Delta m = 1/r_0$. [Parameters: $E_J^*/(\hbar\gamma) = 20$, $\alpha_0 = 0.1$, $2eV_{\rm dc}/\hbar = \omega_0$, $\nu_0 = 1.25 r_0\gamma$, $r_0 = 1/50$.].

neglected fluctuations of the voltage [51] turn the system into a (lockable) self-sustained oscillator. These fluctuations arise from thermal or external sources, but crucially contain an unavoidable contribution from the shot noise of the current through the junction. We describe this by considering a resistance in-series with a perfect voltage source, as visualized in figure 1(a). The integrated voltage fluctuations due to shot noise on this resistance yield the phase,

$$\hat{\varphi}_{R_0} = (2e/\hbar)\int_0^t \hat{V}_{R_0}\mathrm{d}\tau = (2e/\hbar)\,R_0\int_0^t \hat{I}_{\rm CP}\mathrm{d}\tau\,, \tag{2}$$

appearing in (1).

In general, the current in (2) is a full quantum operator and so is the integral for the phase, which being proportional to the number of CPs m transferred across the junction in the elapsed time interval incorporates the effects of coherences between different charge transfer numbers. In a model without in-series resistance these coherences are limited by the typical number of photons in the cavity and a resistance will introduce additional decoherence. Instead of retaining the full quantum character of $\hat{\varphi}_{R_0}$ and a full microscopic model of the resistance in the Hamiltonian, we can effectively model the resistor phase by treating the number m of transferred CPs as a stochastic variable with statistics described by the full counting statistics of the coherent CP tunneling process. Such a modeling of the driving phase in the Hamiltonian (1) by an m-dependent c-number, $\varphi_{R_0} = 2\pi\, r_0 m$, where $r_0 = R_0/R_Q$ is the in-series resistance in units of the superconducting resistance quantum $R_Q = h/(4e^2)$, is valid for small r_0, where any residual coherences between charge states would correspond to minute changes of the driving phase. Using the m-dependent Hamiltonian (1) within a quantum master equation for the state of the system, which is conditioned on the number of tunneled CPs, resembles a feedback-based locking scheme, where the in-series resistance realizes an inherent autonomous adaptation of the driving phase to a measurement outcome.

The model outlined here comprises two essential components that extend beyond the standard description of Josephson photonic devices used in previous works. First, a small ac-voltage signal is added on top of the usual dc-bias and we need to derive the rotating-wave Hamiltonian of the system incorporating both these voltages. Second, the in-series resistance turns the system into a self-sustained oscillator and we require an equation governing the time-evolution of the system that accurately reflects the dynamics of the m-dependent parameter φ_{R_0}. These two extensions are covered in sections 2.2 and 2.3, respectively. Together, this will provide a complete model that can be simulated numerically or simplified through approximations to a reduced description of the phase.

2.2. Hamiltonian: inclusion of a small ac-voltage signal

Technically, we first move to a frame rotating with the frequency Ω of the ac-signal (introducing a detuning $\Delta = \delta_{\rm dc} + \delta_{\rm ac} = (\omega_0 - \omega_{\rm dc}) + (\omega_{\rm dc} - \Omega)$) while neglecting fast oscillating terms in a rotating wave

approximation (RWA). The resulting Hamiltonian (cf appendix A), $H_{\mathrm{RWA}} = \hbar\Delta a^\dagger a + h + h^\dagger$, with

$$h^\dagger(m) = \frac{E_J^*\alpha_0}{2} e^{i\psi} :ia^\dagger \frac{J_1\left(2\sqrt{\alpha_0^2 a^\dagger a}\right)}{\sqrt{\alpha_0^2 a^\dagger a}}: + \varepsilon \frac{E_J^*}{4} e^{i\psi} : a^{\dagger 2} \frac{J_2\left(2\sqrt{\alpha_0^2 a^\dagger a}\right)}{a^\dagger a} + J_0\left(2\sqrt{\alpha_0^2 a^\dagger a}\right) :$$
$$\approx \frac{E_J^*\alpha_0}{2} e^{i\psi}\, ia^\dagger + \varepsilon \frac{E_J^*}{4} e^{i\psi}\left[\frac{\alpha_0^2 a^{\dagger 2}}{2} + \left(1 - \alpha_0^2 a^\dagger a\right)\right], \tag{3}$$

depends on the phase-difference

$$\psi(t, m) = \Omega t + \varphi_{\mathrm{ac}} - (\omega_{\mathrm{dc}} t - 2\pi r_0 m) \tag{4}$$

between the ac-signal and the cavity oscillation. Here, the Josephson energy is renormalized, $E_J^* = E_J e^{-\alpha_0^2/2}$, and colons signal normal-ordering of the operators. The second line, valid for small zero-point fluctuations and weak driving, so that all Bessel functions may be expanded, allows easy interpretation of the various terms: the first term describes direct driving of the cavity by the dc-bias, where each tunneling CP creates a photon; the second term, $\propto a^{\dagger 2} \cdot E_J \cdot \varepsilon$, accounts for the generation of two photons by one CP and one ac-drive excitation; and the last term represents one CP tunneling and emitting an excitation into the drive renormalized by the presence of cavity photons (see also appendix A). The various CP transfer processes come with different leading powers of the zero-point fluctuations, α_0, and accordingly for small α_0 the first term of (3) is dominant (and the approximation leading to the second line is valid). In consequence, if ψ were to be a fixed external parameter, the photonic state of the cavity would have a trivial dependence on ψ, which essentially rotates the state space, with only minor corrections stemming from the second term. Without a locking signal, $\varepsilon = 0$, the photonic state also determines the current, which is independent of the value of ψ, as seen by invoking energy conservation and the photon loss rate, $\propto \gamma\langle a^\dagger a\rangle$ [47], or by evaluating the explicitly ψ-dependent current operator, $\hat{I}_{\mathrm{CP}} = -i2e(h^\dagger - h)/\hbar$, acting on the trivially ψ-dependent cavity state. The fact, that the current describes changes of the number of transferred CPs m and thus of ψ, then leads to a driving phase that drifts and diffuses and to the self-sustained oscillator dynamics described above, cf figure 2 (a).

Turning on an oscillating locking signal, $\varepsilon > 0$, breaks the phase symmetry of such an oscillator and is generically expected to eventually lead to a state locked to specific constant values of $\psi \mod 2\pi$. Here, the locking mechanism can be ascribed to the third CP transfer process discussed above, $\propto \varepsilon E_J \cdot (1 - \alpha_0^2 a^\dagger a)$, which - while irrelevant in the Hamiltonian (3) as an energetic shift in the $\alpha_0 \to 0$ limit - yields a Shapiro-like term in the current operator and results in a ψ dependence of the expectation value of the current. In particular, the ψ-dependence of the CP transfer and thus of m in (4) can lead to locked solutions, where $\mathrm{d}\psi/\mathrm{d}t = 0$ for specific values of $\psi \mod 2\pi$.

2.3. Time-evolution: adding a feedback-mechanism

The locking mechanism relies on the feedback of the number of transferred CPs into the phase ψ appearing in the Hamiltonian (3). We can capture this physics by a slight modification of the number-resolved master equation technique [52], which is routinely used for the counting of *incoherent* processes, such as photon emission or other rate processes appearing as Lindblad terms in the time-evolution. To generalize to the counting of *coherent* CP transport processes, the density matrix, $\rho(t) = \sum_m \rho_m(t)$ (m are half-integers), is divided into components according to the number of tunneled CPs m having crossed the Josephson junction after a time t. As explained in appendix B the half-integer indexing accounts for the coherent nature of the transfer process. The components are then coupled by CP tunneling amplitudes

$$\dot{\rho}_m = \mathcal{L}_0\rho_m - \frac{i}{\hbar}[h^\dagger(m - 1/2)\,\rho_{m-1/2} + h(m + 1/2)\,\rho_{m+1/2}$$
$$- \rho_{m+1/2}h^\dagger(m + 1/2) - \rho_{m-1/2}h(m - 1/2)]. \tag{5}$$

The contribution from $\mathcal{L}_0$ which includes photon loss $\gamma\mathcal{D}[a]\rho = \gamma(a\rho a^\dagger - \{a^\dagger a, \rho\}/2)$ with rate γ

$$\mathcal{L}_0\rho_m = -i\left[\Delta a^\dagger a, \rho_m\right] + \gamma\mathcal{D}[a]\,\rho_m, \tag{6}$$

does not correspond to CP tunneling-events. Different components $\rho_{m\pm1/2}$ appear in a manner completely analogous to how counting fields are added with different signs to coherent forward and backward tunneling terms [53, 54].

Since the m-dependence of $h(m)$ is periodic, there exists a natural compactification, when we chose (without loss of generality) $M = 1/r_0 \in \mathbb{N}$ and set $\rho_M = \rho_0$. This enables numerical simulations up to such a long time, that a very large number of CPs has been transported.

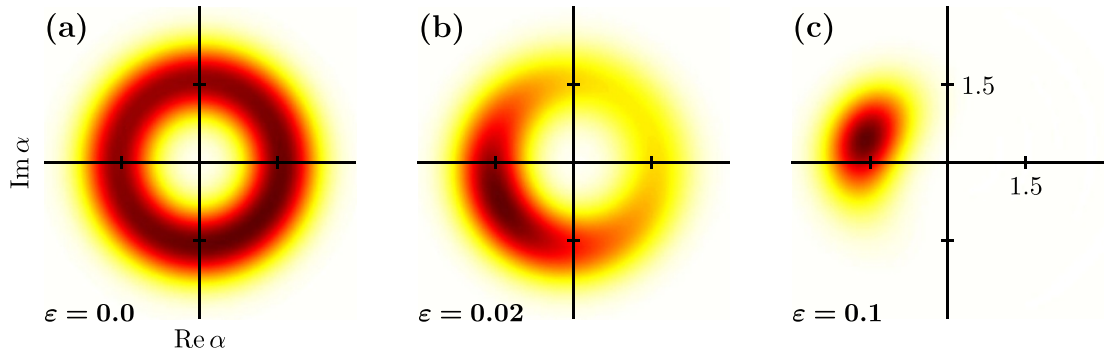

Figure 2. Wigner phase-space distributions of the cavity in the steady-state in a reference frame rotating with Ω. (a) Without locking signal the shot noise diffuses the oscillator's phase which becomes completely undefined. (c) The injection of a small ac-signal reduces the phase uncertainty, yielding a state with a sharply refocused phase in the locked regime. (b) In the intermediate regime shot noise and locking signal compete resulting in a state with partially diffused phase. [Parameters: $E_J^*/(\hbar\gamma) = 20$, $\alpha_0 = 0.1$, $2eV_{\rm dc}/\hbar = \omega_0$, $\nu_0 = 1.25 r_0\gamma$, $r_0 = 1/50$. Wigner functions are normalized to their maxima.].

With this method (and the quantum regression theorem) the steady-state spectra of figure 1(b) discussed above were found. These can be compared to the counting statistics of CPs, $P(m) = {\rm tr}\rho_m$ after a finite time T, shown in figure 1(c). When the ac-signal is absent, the distribution of counted CPs is broad, conforming with a broad emission spectrum of the cavity. An increase of the strength of the external locking signal reduces the width in the statistics of counted CPs, pulls the frequency emission towards the locking frequency, and eventually results in a sharp photon emission spectrum and a sharpened probability distribution $P(m)$. In the long-time limit the peak of the locked distribution (red in figure 1(c)) will not become wider, but the distribution will develop many sidepeaks, see appendix B, which as we will show in the next section, are associated with slips of the phase variable by 2π.

3. Phase diffusion and its constraint by locking

The impact of the in-series resistance and resulting voltage fluctuations, and the effects of the locking signal can also be studied in a phase-space picture of the cavity dynamics. In figure 2, quantum master-equation results for the steady-state Wigner distribution are shown for different amplitudes of an injected ac-signal. The dc-voltage fixed close to resonance drives the cavity quickly into a (near coherent) state with finite amplitude. However, due to the lack of a reference phase, the imperfect dc-voltage drive across the junction disperses the neutrally stable phase of this state on the limit cycle (figure 2(a)). The resulting steady state of the system is diagonal (and hence identical in the lab and the rotating frame) and all information about the driving phase is lost. The unstable phase-space angle is mirrored by the noise-induced broadening of the emission spectrum, cf blue spectrum in figure 1(b). Turning on and progressively increasing the amplitude of the ac-voltage, the completely dephased steady-state distribution contracts and locks the state to a certain position on the limit cycle (figures 2(b) and (c)). Concomitantly the variance of the phase-space angle is reduced and a sharpened peak emerges in the emission spectrum (cf figure 1(b)). In the lab frame the state rotates with the frequency of this emission peak. Notably, in phase-space the effects of synchronization emerge completely smoothly with increasing strength ε, while the spectral pulling shows remnants of the classical criticality, see figures 1(b) and 3(c) below.

We will understand and quantify the observed dynamics of the phase-space angle by linking it to the notion of constrained diffusion. For that purpose, we again turn to the phase difference ψ between the phase of the locking signal and the phase which drives the cavity (4). The synchronized state will then be characterized by the phase difference ψ becoming constant in time (modulo 2π), as the cavity emits photons with frequencies centered sharply about the injection frequency Ω.

4. Reduced dynamics of the phase

The question that now arises is, whether a reduced equation for the dynamics of the phase variable ψ can be derived in the quantum domain, thus generalizing the Adler-theory of classical synchronization dynamics [2, 45, 55]. Indeed, the quantum master equation (5) can be rewritten as an equation for a density $\rho'(t,\psi)$ by first treating m as continuous and transforming to a moving frame as shown in appendix C. Crucially, the explicit time dependence of the Hamiltonian (3) is removed by the latter step. Assuming a time scale separation between the (fast) adaptation of the cavity state to the phase of its driving term and the slow

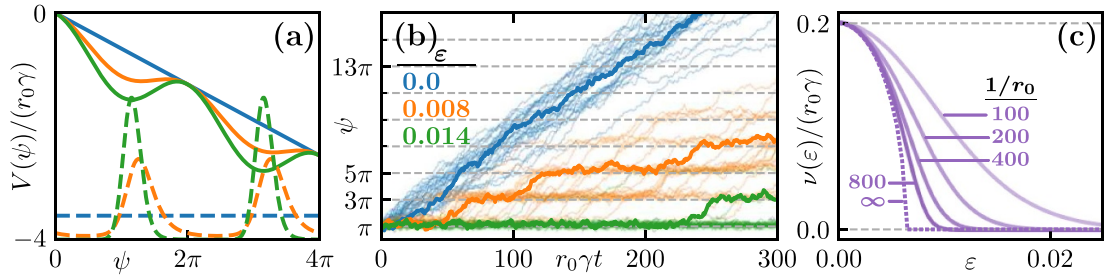

Figure 3. Dynamics of the reduced phase in a tilted washboard potential. (a) The injection of a sufficiently strong ac-signal creates a potential with minima in which periodic steady-state distributions (dashed) are found. (b) Individual trajectories of a phase particle in the potentials of (a). Long intervals of constant phase in the synchronized state (green) are interrupted by phase slips of 2π, which proliferate (orange) and overlap (blue) in the unsynchronized regime. (c) The steady-states of (a) yield the rate $\nu(\varepsilon) = \langle\dot{\psi}\rangle$ of these slips. For smaller resistance the locking transition becomes more pronounced until for $1/r_0 \to \infty$ the criticality of classical synchronization is recovered. [Parameters: $E_J^*/(\hbar\gamma) = 10$, $\alpha_0 = 0.1$, $2eV_{\rm dc}/\hbar = \omega_0$, $\nu_0 = 0.2 r_0\gamma$, $r_0 = 1/300$.].

dynamics of the phase ψ, two-time perturbation theory can provide a Fokker–Planck equation for the dynamics on slow time scales $r_0 t$ ($r_0 \ll 1$) of the phase distribution probability [56, 57]

$$\frac{\partial}{\partial t}P(t,\psi) = -\frac{\partial}{\partial\psi}\left[j(\psi)\,P(t,\psi)\right] + \frac{\partial^2}{\partial\psi^2}\left[D(\psi)\,P(t,\psi)\right]. \tag{7}$$

The drift coefficient, in the first order of r_0, is given by $j(\psi) = 2\pi r_0\langle\hat{I}_{\rm CP}/(2e)\rangle - \delta_{\rm ac}$ as derived in appendix C. In second order one obtains a correction for the drift and a diffusion term which are calculated via the pseudo-inverse of the system's Liouvillian. Without locking signal we find free diffusion of the phase with diffusion constant, $D = (2\pi r_0)^2 S_{\rm CP}/2$, determined by the zero-frequency CP shot noise power $S_{\rm CP}$. Injecting the ac-signal creates a potential $V(\psi) = -\int j(\psi)\,{\rm d}\psi$ for the phase, which develops local minima for sufficient locking strength, restricting diffusion and stabilizing the phase, see figure 3(a). For small α_0 the potential simplifies to a Shapiro-like tilted washboard $V(\psi) = \nu_c\cos\psi - \nu_0\psi$ with $\nu_c = \pi r_0\varepsilon E_J^*/\hbar$. The diffusion D remains roughly constant in this regime.

The dynamics of a phase particle in this potential is obtained via the Langevin equation corresponding to (7), see figure 3(b). Deep in the synchronized state (green), plateaus of nearly constant phase appear, interrupted by rare slips of the phase by 2π. Here, the dynamics may be approximated as an escape process which yields for $\alpha_0 \ll 1$ a Kramer's rate $\nu_K = \sqrt{\nu_c^2 - \nu_0^2}\exp\{-\Delta V/[(2\pi r_0)^2 S_{\rm CP}/2]\}$ with $\Delta V = 2\sqrt{\nu_c^2 - \nu_0^2} + 2\nu_0\arcsin(\nu_0/\nu_c) - \pi\nu_0$ [58]. Reducing the strength of the locking drive (orange) accordingly increases the number of slips until the synchronized plateaus are completely absent (blue). How well a system is synchronized, can be quantified by the rate of such slips. From the steady-state distributions for the phase ψ, dashed in figure 3(a), we obtain the rate of phase slips, i.e. the mean flow $\langle\dot{\psi}\rangle = \int P(\psi)j(\psi){\rm d}\psi$ in figure 3(c). For large R_0, the dependence of the phase-slip rate on the locking strength in figure 3(c) shows a shot noise induced broadening of the locking transition while in the limit $R_Q/R_0 \to \infty$ shot noise becomes negligible. Then, the Fokker–Planck equation simplifies to the well-known Adler-equation describing the locking dynamics of a classical phase variable, $\dot{\psi} = \nu_0 + \nu_c\sin(\psi)$ [45].

5. Synchronization of two quantum microwave cavities

Instead of the synchronization of a single nonlinearly driven microwave cavity to an external locking signal investigated above, one can also consider the mutual synchronization of several devices [2, 59]. Dispensing with the need of a phase-stable ac-signal, the prospect of mutual synchronization of a potentially large number of devices promises a source of correlated high-intensity emission. The Hamiltonian,

$$H = H_a + H_b + \epsilon\left(a^\dagger b + a b^\dagger\right), \tag{8}$$

where

$$H_\xi = \hbar\omega_0\xi^\dagger\xi - E_J\cos\left[\alpha_0\left(\xi^\dagger + \xi\right) + \omega_{{\rm dc},\xi}t - 2\pi r_0 m_\xi\right] \tag{9}$$

describes a scenario (see figure 4(a)), where each device $\xi = a, b$ is biased by a dc-voltage $V_\xi = \hbar\omega_{{\rm dc},\xi}/(2e)$ applied across a resistance R_0, and the coupling term stems from a small coupling capacitor and a rotating wave approximation. We assume identical devices except for differing dc-voltage drives. As before each

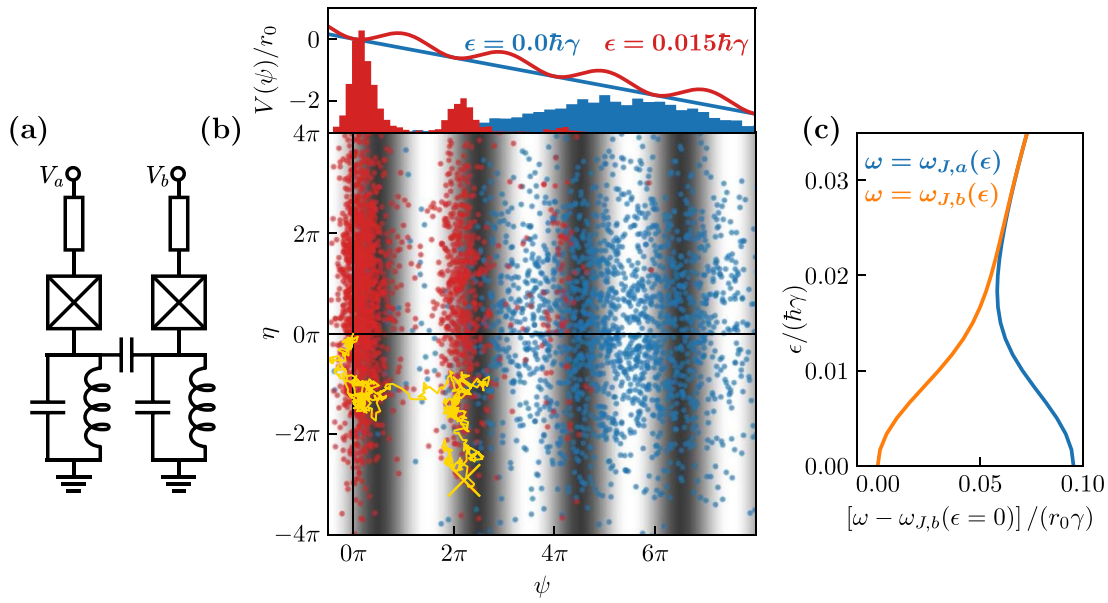

Figure 4. Statistics $P(\eta.\psi)$ of the phase-sum and -difference of two Josephson-photonics systems (a). (b) The background color indicates the force on the phase-particle in positive (white) and negative (black) ψ-direction respectively which yields the red potential shown in the panel above. The simulation shows the endpoints of individual trajectories, initially starting at $\eta = \psi = 0$, after a time $T = 170/(r_0\gamma)$ (one full trajectory is highlighted in yellow with cross at the endpoint). When the oscillators are uncoupled (blue), the phase diffuses freely in both directions. In the synchronized state (red), the phase diffuses freely along η, while the potential restricts diffusion in ψ, resulting in the emergence of two sidebands that indicate phase slips of 2π. Synchronization can be quantified by the maximum of the phase difference in phase-space $S = 2\pi \max P(\phi)$ [28], e.g. $S(\epsilon = 0.015\hbar\gamma) = 0.78$. (c) Pulling curve of the effective driving frequencies ω_J coinciding with the respective main emission peaks. [Parameters: $E_J^*/(\hbar\gamma) = 8$, $\alpha_0 = 0.1$, $2eV_a/\hbar = \omega_0$, $2e(V_a - V_b)/\hbar = 0.1 r_0\gamma$, $r_0 = 1/300$, 2000 trajectories.].

device is a self-sustained oscillator subjected to phase-diffusion on its own limit cycle. However, when two oscillators synchronize with each other, their relative phase becomes constant and stable against noise. Instead of using the driving phases of each individual oscillator as phase variables, it is therefore useful to introduce sum and difference variables

$$\eta = -2\pi\, r_0\, [(m_a + m_b) - \langle m_a + m_b \rangle_{\epsilon=0}] \tag{10}$$

$$\psi = (\omega_{\mathrm{dc},a} - \omega_{\mathrm{dc},b})\, t - 2\pi\, r_0\, (m_a - m_b)\,, \tag{11}$$

so that $\langle \eta \rangle_{\epsilon=0} = 0$ and $\langle \psi \rangle_{\epsilon=0}$ drifts with the effective detuning in the uncoupled case.

We again derive a 2d-Fokker–Planck equation for $P(\eta, \psi)$ by using time-scale separation, see appendix D. When the systems are uncoupled, the phase particle described by its 2d-position $\vec{x} = (\eta, \psi)$ diffuses freely, as illustrated by the statistics in figure 4. If the initially detuned oscillators are coupled ($\epsilon > 0$) one device will provide a reference frequency $\omega_{J,a}$ for the second device, which pulls the emission frequency of the second cavity $\omega_{J,b}$ towards that reference frequency, and vice versa. In the initially flat potential $V(\eta, \psi)$, minima form along the ψ direction and in the synchronized state both cavities will emit photons about the same frequency, such that $\langle \dot{\psi} \rangle \approx 0$. Hence, the statistics of the phase difference ψ becomes sharp. However, shot noise permits the phase difference to slip by 2π. Notably, the resulting strong correlation between the cavities is not associated with concomitant entanglement.

6. Context and conclusion

We compare our work to other concepts of quantum synchronization presented in the literature. One possible approach involves examining systems, that inherently exhibit distinctly quantum mechanical behavior. These include systems without classical analog like spins [60], nonlinear systems that yield negative Wigner densities [61], or systems where quantum mechanical uncertainty plays a role [48]. While our model provides a quantum description where large zero-point fluctuations quantitatively influence the synchronization behavior, its primary quantum feature is the granularity of charges which yields shot noise in the phase of the drive. This contrasts with other schemes for quantum self-sustained oscillators, where the incoherent drive is realized by a Lindblad operator with negative damping rate (van der Pol model).

Furthermore, in our approach, the Josephson photonics device achieves synchronization in a steady-state, in contrast to quantum systems that synchronize during their transient evolution [62, 63].

Instead of focusing on the quantum properties of the oscillators themselves, one can also investigate how the synchronization mechanism and the type of coupling influence synchronization dynamics in the quantum regime. Examples are measurement-induced synchronization [31], nonreciprocal couplings [64], or nonlinearly driven time crystals [65]. These differ from our work, where we consider only linear drive and coupling.

Regarding mutual synchronization there are works that directly relate synchronization to quantum correlations [66, 67] or focus on the complete equalization of the quantum states of two systems [68]. Our scenario differs from both concepts, since we focus on the regime where a description of φ_{R_0} as a c-number is sufficient: quantum correlations or entanglement are not crucial for the synchronization mechanism and the two systems only adapt their oscillation frequencies rather than their full quantum states.

To conclude, this paper introduces dc-driven Josephson-photonics devices as a new platform to study quantum synchronization in the presence of shot noise and the thereby induced phase-slip dynamics. Mechanism and modeling of quantum synchronization dynamics in such devices differ from heretofore investigated systems and do not map to the paradigmatic case of a van der Pol oscillator. Nonetheless, the system can be reduced to its phase dynamics governed by a Fokker–Planck equation with a generalized Adler potential. Implementing synchronization in Josephson-photonics devices is of technological interest due their versatility as a source of quantum microwave light, but also promises fundamental insights in a deep quantum regime, where the nature of phase slips and the potential coexistence and interplay of charge and phase tunneling [69] can be studied.

Data availability statement

The data cannot be made publicly available upon publication because they are not available in a format that is sufficiently accessible or reusable by other researchers. The data that support the findings of this study are available upon reasonable request from the authors.

Acknowledgments

We thank Andrew Armour, Julien Basset, Jérôme Estève, Benjamin Huard, and Ambroise Peugeot for fruitful discussions and acknowledge the support of the DFG through AN336/17-1 and AN336/18-1 and the BMBF through QSens (project QComp).

Appendix A. Hamiltonian in rotating wave approximation

The Hamiltonian of the dc-biased Josephson-photonics device with in-series resistance R_0 and an applied voltage $V = V_{\rm dc} + V_{\rm ac}\cos(\phi_{\rm ac})$ (where $\phi_{\rm ac} = \Omega t + \varphi_{\rm ac}$ is the phase of the ac-signal) can be derived from Kirchhoff's laws as

$$H = \hbar\omega_0 a^\dagger a - E_J \cos\left[\omega_{\rm dc} t - \varphi_{R_0} + \alpha_0\left(a^\dagger + a\right) + \varepsilon\sin\left(\phi_{\rm ac}\right)\right], \tag{A.1}$$

where $\phi_a = \omega_{\rm dc} t - \varphi_{R_0}$ (with $\omega_{\rm dc} = 2eV_{\rm dc}/\hbar$) is the driving phase of the cavity, and $\varepsilon = 2eV_{\rm ac}/(\hbar\Omega)$ is the amplitude of the ac-signal assumed to be small. We move to a reference frame rotating at $\omega_{\rm rf} \approx \omega_{\rm dc}$ with the unitary operator $U = \mathrm{e}^{\mathrm{i}\phi_{\rm rf} a^\dagger a}$, where $\phi_{\rm rf} = \omega_{\rm rf} t + \phi_0$. The Hamiltonian is then transformed as $H_{\rm rf} = UHU^\dagger + i\hbar\dot{U}U$. Linearizing the expression in the strength of the ac-signal ε, we find $H_{\rm rf} = H_0 + h + h^\dagger$ with $H_0 = \hbar(\omega_0 - \omega_{\rm rf})a^\dagger a$ and

$$h = -\frac{E_J \mathrm{e}^{-\alpha_0^2/2}}{2}\left\{\left[1 + i\varepsilon\sin\left(\phi_{\rm ac}\right)\right]\mathrm{e}^{\mathrm{i}\phi_a}\cdot\,\mathrm{e}^{\mathrm{i}\alpha_0 a^\dagger\cdot\exp(i\phi_{\rm rf})}\cdot\,\mathrm{e}^{-\mathrm{i}\alpha_0 a\cdot\exp(-i\phi_{\rm rf})}\right\}, \tag{A.2}$$

where the Josephson energy is renormalized, $E_J^* = E_J \mathrm{e}^{-\alpha_0^2/2}$. Finally, we perform a rotating wave approximation, keeping slowly oscillating terms only, resulting in

$$\begin{aligned} h \approx & -\frac{E_J^*\alpha_0}{2} i\mathrm{e}^{-\mathrm{i}[\phi_{\rm rf} - \phi_a]} : a\frac{J_1\left(2\sqrt{\alpha_0^2 a^\dagger a}\right)}{\sqrt{\alpha_0^2 a^\dagger a}} : \\ & + \varepsilon\frac{E_J^*\alpha_0^2}{8}\mathrm{e}^{-\mathrm{i}[2\phi_{\rm rf} - \phi_{\rm ac} - \phi_a]} : a^2\frac{2\cdot J_2\left(2\sqrt{\alpha_0^2 a^\dagger a}\right)}{\sqrt{\alpha_0^2 a^\dagger a}^2} + \varepsilon\frac{E_J^*}{4}\mathrm{e}^{-\mathrm{i}[\phi_{\rm ac} - \phi_a]} J_0\left(2\alpha\sqrt{a^\dagger a}\right) :, \end{aligned} \tag{A.3}$$

where each infinite series of powers of the annihilation and creation operators was written compactly as normally-ordered Bessel-functions. After defining the Adler phase ψ as the phase difference between ac-driving phase and the phase of the cavity $\psi = \phi_{\rm ac} - \phi_a$ and choosing the rotating frame such that $\phi_{\rm rf} = \phi_{\rm ac}$, we find the Hamiltonian (3) from the main text.

Appendix B. Coherent Cooper pair (CP) counting

The tunneling of CPs, the process we want to count, appears as part of the coherent time-evolution of the system, i.e. in the Hamiltonian dynamics contribution to the quantum master equation for the density matrix. This contrasts with counting emitted photons or any other incoherent process where there is a single, clear procedure to count: by introducing a counting field in a prefactor $\mathrm{e}^{\mathrm{i}\chi}$ of the photon jump operator of the Lindblad Master equation to get a generating function from the χ-dependence of the density matrix [53, 70], or fully equivalently by working in the corresponding Fourier domain by 'number-resolving' the density matrix into components corresponding to a certain number of emitted photons, whose dynamic equations are coupled by photon jumps [52].

Counting is more subtle for coherent processes. In fact, there are various schemes of introducing a counting field to the Hamiltonian part of the dynamics, which have been linked to different (virtual) measurement devices and protocols [71]. Here, we start by attaching $e^{\pm i\chi/2}$ prefactors to all terms in the Hamiltonian corresponding to the forward/backward transfer of a CP. That Hamiltonian acts from the left side on the density matrix in the coherent part of the time-evolution corresponding to the forward branch of a Keldysh contour [53], while acting from the right and residing on the backward branch, $\chi \to -\bar{\chi}$ is used. For Josephson-photonics setups where each CP transfer goes along with the creation of a cavity photon (i.e. purely dc-driven biasing without an ac-component) this method (with $\bar{\chi} \equiv \chi$) has been shown [54] to yield a coherent counting statistics identical to the incoherent photon emission statistics in the long-time limit.

To capture the effect of transferred charges on the voltage drop at the in-series resistance, namely by the driving phase's dependence on the number of charges, $\varphi_{R_0} = 2\pi r_0$, one has to go from χ-space to number space. The number-resolved quantum master equation (5) introduced in the main text corresponds to Fourier-transforming with respect to the sum variable, $\chi + \bar{\chi}$ while summing over the different numbers of transferred charges on both Keldysh branches, so that both, density matrices diagonal in the Keldysh counts (dubbed 'classical' in [72]) and off-diagonal ones contribute to the ρ_m, $2m \in \mathbb{Z}$. The average of transfers on upper and lower branch determines the fed-back charge affecting the driving phase. The off-diagonal contributions have been associated via a picture of interfering paths with negativities making $P(m) = \mathrm{tr}\rho_m$ a quasiprobability at short times which, however, do not matter due to the time-scale separation. It can easily be confirmed, that without the feedback mechanism, i.e. taking $r_0 \to 0$, the unresolved quantum master equation is found by re-summing and that the Fokker–Planck equation derived from the generalized number-resolved quantum master equation (5) yields the expected current-noise.

The *frequency-dependent current noise*

$$S_{\rm CP}(\omega) = 2\mathrm{Re}\int_0^\infty \mathrm{d}\tau \langle \delta I(t+\tau)\, \delta I(t)\rangle \mathrm{e}^{\mathrm{i}\omega\tau} \tag{B.1}$$

in the steady-state ($t \to \infty$) with $\delta I = I_{\rm CP} - \langle I_{\rm CP}\rangle$ is calculated from the full dynamical equations (3) and (5) shown in figure B1(a). Without locking the noise is the same as for the idealized case of a fixed driving phase. Due to the nonlinearity of the Josephson-photonics system the transport is slightly sub-Poissonian [73] and the noise shows (fast) features on the scale of γ in this regime. As the ac-locking signal is switched on, the slow phase dynamics changes from free diffusion to the drift and diffusion in a periodic potential and the current-correlations show signatures of this motion as sidepeaks at a frequency $|\omega| \lesssim |\nu_0|$ (yellow), which merge and develop into a dip as the phase gets trapped in the potential's minima. The feedback of the transferred charges on the driving phase correlates current fluctuations over very long times and correspondingly suppresses the zero-frequency noise down to a value connected to the total rate of phase slips. On time scales faster than the phase dynamics, the current fluctuations remain nearly unaffected.

The zero-frequency noise is of course linked to the second cumulant of the CP counting statistics. The long-time limit of $P(m)$ shown in figure 1(c) of the main text can be more easily calculated from the reduced phase dynamics, so that $P(\psi)$ (with $\psi \in \mathbb{R}$) gained from a histogram of 2000 Langevin trajectories is shown here in figure B1(b). Without locking the full counting statistics spreads out via free phase diffusion corresponding to (near-)Poissonian CP transport events as $\langle\langle \psi \rangle\rangle \propto \langle\langle m\rangle\rangle \propto Dt$, while in the locked regime ψ is distributed in peaks around the minima of the potential and spreads very slowly between these peaks by phase-slip processes.

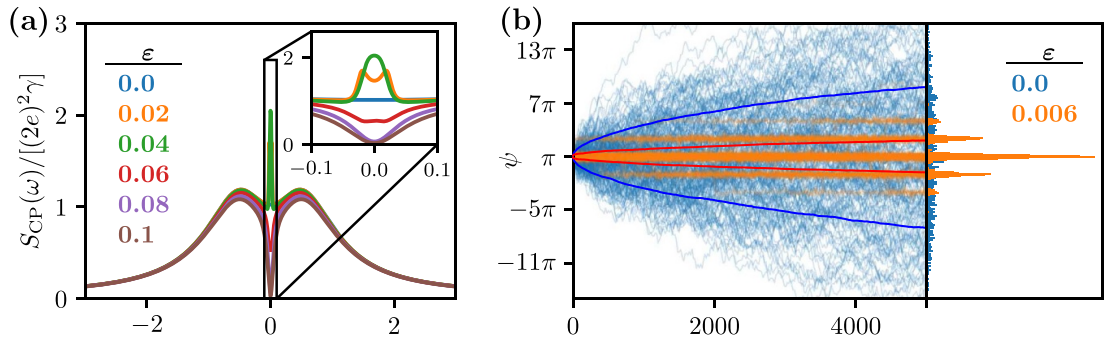

Figure B1. (a) The noise of the Cooper-pair current in a single Josephson-photonics device is analyzed for various locking amplitudes ε. At low frequencies, an injection signal initially adds noise for strengths insufficient to achieve locking, but as the system locks for larger ε, the zero-frequency noise becomes almost entirely suppressed. [Parameters see figure 1.] (b) The long-time full counting statistic of CP transport is calculated from the distribution of the phase $\psi \in \mathbb{R}$ gained from simulating 2000 trajectories. The standard deviation $\Delta\psi$ shows the $\propto \sqrt{t}$ behavior typical for diffusive processes, where the free diffusion (blue) is replaced by a much slower phase-slip process in the (weakly) locked case. [Parameters: $E_J^*/(\hbar\gamma) = 10$, $\alpha_0 = 0.1$, $2eV_{\mathrm{dc}}/\hbar = \omega_0$, $\nu_0 = 0$, $r_0 = 1/300$.].

Appendix C. Derivation of the reduced equation for the phase

Starting from the full dynamical equations we first write (5) in terms of the phase $\varphi_{R_0} = 2\pi r_0 m$ instead of the number m of transferred CP and treat φ_{R_0} as a continuous quantity $\rho_m(t) \to \rho(t, \varphi_{R_0} = 2\pi r_0 m)$. We want to express φ_{R_0} in terms of a phase ψ in a moving reference frame, which is defined by the transformation, cf (4),

$$\varphi_{R_0}(t,\psi) = \psi + \omega_{\mathrm{dc}} t - (\Omega t + \varphi_{\mathrm{ac}}). \tag{C.1}$$

Accordingly, the density matrix becomes a new function of t and ψ

$$\rho'(t,\psi) = \rho(t, \varphi_{R_0}(t,\psi)) \tag{C.2}$$

with the time derivative

$$\frac{\partial \rho'}{\partial t}(t,\psi) = \frac{\mathrm{d}\rho}{\mathrm{d}t}(t,\varphi_{R_0}(t,\psi)) = \frac{\partial \rho}{\partial t}(t,\varphi_{R_0}(t,\psi)) + \frac{\partial \rho}{\partial \varphi_{R_0}}(t,\varphi_{R_0}(t,\psi))\frac{\partial \varphi_{R_0}}{\partial t}(t,\psi). \tag{C.3}$$

Introducing the evolution generator $\Lambda(\psi)$ this yields

$$\begin{aligned}\frac{\partial \rho'}{\partial t}(t,\psi) = \Lambda\rho'(\psi) = \delta_{\mathrm{ac}}\frac{\partial \rho'}{\partial \psi}(t,\psi) + \mathcal{L}_0\rho'(\psi) - \frac{i}{\hbar}[h^\dagger(\psi - \pi r_0)\rho'(\psi - \pi r_0) \\ + h(\psi + \pi r_0)\rho'(\psi + \pi r_0) - \rho'(\psi + \pi r_0)h^\dagger(\psi + \pi r_0) - \rho'(\psi - \pi r_0)h(\psi - \pi r_0)]\end{aligned} \tag{C.4}$$

Note that the Hamiltonian $h(\psi) = h(t, \varphi_{R_0}(t,\psi))$ does not have an explicit time dependence, see (3).

We perform two time-scale perturbation theory (or homogenization) [74, 75] to derive an effective Fokker-Plank equation for the phase ψ. For that purpose it is assumed that the oscillator dynamics takes place on a much faster time scale than the phase dynamics. We explicitly introduce a fast time scale t and a slow time scale $\tau = r_0 t$ and the dependence of the state on these times $\rho'(t,\psi) = \rho(t,\tau,\psi)$. Then, the derivative of the density matrix becomes

$$\begin{aligned}\partial_t \rho'(t,\psi) = \frac{\mathrm{d}}{\mathrm{d}t}\rho(t,\tau,\psi) = \partial_t\rho(t,\tau,\psi) + (\partial_t\tau)\,\partial_\tau\rho(t,\tau,\psi) \\ = \partial_t\rho(t,\tau,\psi) + r_0\partial_\tau\rho(t,\tau,\psi).\end{aligned} \tag{C.5}$$

Furthermore, we assume that the fast oscillator dynamics have already relaxed and we study the evolution of the state $\rho(\tau,\psi) = \lim_{t\to\infty}\rho(t,\tau,\psi)$, so that (C.4) becomes

$$r_0\partial_\tau\rho(\tau,\psi) = \Lambda\rho(\tau,\psi) \tag{C.6}$$

In a next step, we expand $\rho(\tau,\psi) = \sum_{l=0}^{\infty} r_0^l \rho^{(l)}$ and $\Lambda\rho = \mathcal{L}\rho + r_0\partial_\psi(\Lambda^{(1)}\rho) + \frac{1}{2}r_0^2\partial_\psi^2(\Lambda^{(2)}\rho) + \mathcal{O}(r_0^3)$ in orders of r_0. Taking $\rho(\psi \pm \pi r_0) = \rho \pm \pi r_0\partial_\psi\rho + \mathcal{O}(r_0^2)$ and $h(\psi \pm \pi r_0) = h \pm \pi r_0\partial_\psi\rho + \mathcal{O}(r_0^2)$ results in the zeroth-order Liouvillian $\mathcal{L}\rho = -\frac{i}{\hbar}[h + h^\dagger, \rho] + \mathcal{L}_0\rho$ and for the next order $\Lambda^{(1)} = \delta_{\mathrm{ac}}/r_0 - 2\pi\mathcal{I}_{\mathrm{CP}}/(2e)$ with the symmetrized current operator $\mathcal{I}_{\mathrm{CP}}\rho = \frac{1}{2}(I_{\mathrm{CP}}\rho + \rho I_{\mathrm{CP}})$.

We proceed by solving (C.6) order by order. In *zeroth order* of r_0 we obtain

$$0 = \mathcal{L}(\psi)\,\rho^{(0)}(\tau,\psi) \tag{C.7}$$

which determines $\rho^{(0)}(\tau,\psi) = P^{(0)}(\tau,\psi)\rho_{\mathrm{eq}}(\psi)$ up to a factor which we interpret as a probability density $P^{(0)}(\tau,\psi)$ for a certain ψ at time τ. To find it, we consider the *first order* of $\rho(\tau,\psi)$ in r_0

$$\partial_\tau \rho^{(0)}(\tau,\psi) = \mathcal{L}(\psi)\,\rho^{(1)}(\tau,\psi) + \partial_\psi\left\{\left[\delta_{\mathrm{ac}}/r_0 - 2\pi\mathcal{I}_{\mathrm{CP}}(\psi)/(2e)\right]\rho^{(0)}(\tau,\psi)\right\}. \tag{C.8}$$

Taking the trace yields the desired equation of motion

$$\partial_\tau P^{(0)}(\tau,\psi) = \partial_\psi\left[\left\langle\delta_{\mathrm{ac}}/r_0 - 2\pi\mathcal{I}_{\mathrm{CP}}(\psi)/(2e)\right\rangle_{\rho_{\mathrm{eq}}(\psi)} P^{(0)}(\tau,\psi)\right] \tag{C.9}$$

which describes a drift of ψ. The *second order* (see supplemental material) in r_0 provides a correction for the drift and a diffusion term.

Then the equation of motion can be written as the Fokker–Planck equation in (7) with drift

$$j(\psi) = 2\pi r_0\langle\mathcal{I}_{\mathrm{CP}}/(2e)\rangle_{\rho_{\mathrm{eq}}(\psi)} - \delta_{\mathrm{ac}} + r_0^2\langle(\partial_\psi 2\pi\mathcal{I}_{\mathrm{CP}}/(2e)\,\mathcal{R})\,(\delta_{\mathrm{ac}}/r_0 - 2\pi\mathcal{I}_{\mathrm{CP}}/(2e))\rangle_{\rho_{\mathrm{eq}}(\psi)} \tag{C.10}$$

and diffusion

$$D(\psi) = -(2\pi r_0)^2\,\langle\mathcal{I}_{\mathrm{CP}}/(2e)\,\mathcal{R}\mathcal{I}_{\mathrm{CP}}/(2e)\rangle_{\rho_{\mathrm{eq}}(\psi)} \tag{C.11}$$

where $\mathcal{R}$ is the pseudo-inverse of $\mathcal{L}$. The r_0^2 contribution in the drift term may be neglected for small r_0.

Appendix D. Note on mutual synchronization

Two Josephson-photonics devices can be coupled, e. g. , inductively or capacitively, where we here choose to analyze a capacitive coupling. Since charge and phase are conjugate variables associated with momentum and position of the cavities, a capacitive coupling will lead to a interaction term of the form $\hat{Q}_a\hat{Q}_b \propto (a^\dagger - a)(b^\dagger - b)$ in the Hamiltonian. A sufficiently small capacitor will lead in RWA to the Hamiltonian given in the main text. We further note that a coupling capacitor modifies the eigenfrequencies of the cavities.

As in the case of locking to an ac-signal, a Fokker–Planck equation can also be derived for the synchronization of two devices. Similar to the case of injection locking, one introduces new phase variables φ_a' and φ_b' which are given by $\varphi_a' = -(\eta+\psi)/2$ and $\varphi_b = -(\eta-\psi)/2$. Calculations analogous to appendix C yield a Fokker–Planck equation for the probability density $P(t,\varphi_a,\varphi_b)$

$$\frac{\partial}{\partial t}P = \left\{-\frac{\partial}{\partial\varphi_a'}j_a - \frac{\partial}{\partial\varphi_b'}j_b + \frac{\partial^2}{\partial\varphi_a'^2}D_{aa} + 2\frac{\partial^2}{\partial\varphi_a'\partial\varphi_b'}D_{ab} + \frac{\partial^2}{\partial\varphi_b'^2}D_{bb}\right\}P \tag{D.1}$$

with drift and diffusion coefficients given in the supplemental material.

ORCID iDs

Florian Höhe https://orcid.org/0009-0008-4503-2539
Lukas Danner https://orcid.org/0000-0002-2222-2486
Ciprian Padurariu https://orcid.org/0000-0001-9568-2080
Brecht I C Donvil https://orcid.org/0000-0002-3952-6283
Joachim Ankerhold https://orcid.org/0000-0002-6510-659X
Björn Kubala https://orcid.org/0000-0001-6685-0233

References

[1] Huygens C 1897 *Oeuvres Complètes de Christiaan Huygens* vol 1 ed M Nijhoff and L Haye (Publiées par la Société hollandaise des sciences) (available at: www.biodiversitylibrary.org/bibliography/21031) pp 1888–950
[2] Pikovsky A, Rosenblum M G and Kurths J 2001 *Synchronization, A universal Concept in Nonlinear Sciences* (Cambridge University Press)
[3] Strogatz S H 2000 *Nonlinear Dynamics and Chaos: With Applications to Physics, Biology, Chemistry and Engineering* (Westview Press)
[4] Kuramoto Y 2003 *Chemical Oscillations, Waves and Turbulence* (*Dover Books on Chemistry Series*) (Dover Publications)
[5] Strogatz S H and Stewart I 1993 Coupled oscillators and biological synchronization *Sci. Am.* **269** 102–9
[6] Glass L 2001 Synchronization and rhythmic processes in physiology *Nature* **410** 277–84
[7] Buczek C J, Freiberg R J and Skolnick M L 1973 Laser injection locking *Proc. IEEE* **61** 1411–31
[8] van Tartwijk G H M and Agrawal G P 1998 Laser instabilities: a modern perspective *Prog. Quantum Electron.* **22** 43–122

[9] Walter S, Nunnenkamp A and Bruder C 2014 Quantum synchronization of a driven self-sustained oscillator *Phys. Rev. Lett.* **112** 094102
[10] Amitai E, Lörch N, Nunnenkamp A, Walter S and Bruder C 2017 Synchronization of an optomechanical system to an external drive *Phys. Rev.* A **95** 053858
[11] Walter S, Nunnenkamp A and Bruder C 2015 Quantum synchronization of two van der pol oscillators *Ann. Phys., Lpz.* **527** 131–8
[12] Lee T E and Sadeghpour H R 2013 Quantum synchronization of quantum van der pol oscillators with trapped ions *Phys. Rev. Lett.* **111** 234101
[13] Weiss T, Walter S and Marquardt F 2017 Quantum-coherent phase oscillations in synchronization *Phys. Rev.* A **95** 041802(R)
[14] Lee T E, Chan C-K and Wang S 2014 Entanglement tongue and quantum synchronization of disordered oscillators *Phys. Rev.* E **89** 022913
[15] Dutta S and Cooper N R 2019 Critical response of a quantum van der pol oscillator *Phys. Rev. Lett.* **123** 250401
[16] Arosh L B, Cross M C and Lifshitz R 2021 Quantum limit cycles and the Rayleigh and van der pol oscillators *Phys. Rev. Res.* **3** 013130
[17] Roulet A and Bruder C 2018 Synchronizing the smallest possible system *Phys. Rev. Lett.* **121** 053601
[18] Parra-López Alvaro and Bergli J 2020 Synchronization in two-level quantum systems *Phys. Rev.* A **101** 062104
[19] Koppenhöfer M, Bruder C and Roulet A 2020 Quantum synchronization on the ibm q system *Phys. Rev. Res.* **2** 023026
[20] Roulet A and Bruder C 2018 Quantum synchronization and entanglement generation *Phys. Rev. Lett.* **121** 063601
[21] Jaseem N, Hajdušek M, Vedral V, Fazio R, Kwek L-C and Vinjanampathy S 2020 Quantum synchronization in nanoscale heat engines *Phys. Rev.* E **101** 020201(R)
[22] Hush M R, Li W, Genway S, Lesanovsky I and Armour A D 2015 Spin correlations as a probe of quantum synchronization in trapped-ion phonon lasers *Phys. Rev.* A **91** 061401(R)
[23] Warsi Laskar A W, Adhikary P, Mondal S, Katiyar P, Vinjanampathy S and Ghosh S 2020 Observation of quantum phase synchronization in spin-1 atoms *Phys. Rev. Lett.* **125** 013601
[24] Krithika V R, Solanki P, Vinjanampathy S and Mahesh T S 2022 Observation of quantum phase synchronization in a nuclear-spin system *Phys. Rev.* A **105** 062206
[25] Zhang L, Wang Z, Wang Y, Zhang J, Wu Z, Jie J and Lu Y 2023 Quantum synchronization of a single trapped-ion qubit *Phys. Rev. Res.* **5** 033209
[26] Es'haqi-Sani N, Manzano G, Zambrini R and Fazio R 2020 Synchronization along quantum trajectories *Phys. Rev. Res.* **2** 023101
[27] Sonar S, Hajdušek M, Mukherjee M, Fazio R, Vedral V, Vinjanampathy S and Kwek L-C 2018 Squeezing enhances quantum synchronization *Phys. Rev. Lett.* **120** 163601
[28] Lörch N, Nigg S E, Nunnenkamp A, Tiwari R P and Bruder C 2017 Quantum synchronization blockade: energy quantization hinders synchronization of identical oscillators *Phys. Rev. Lett.* **118** 243602
[29] Nigg S E 2018 Observing quantum synchronization blockade in circuit quantum electrodynamics *Phys. Rev.* A **97** 013811
[30] Shen Y, Yi Soh H, Fan W and Kwek L-C 2023 Enhancing quantum synchronization through homodyne measurement, noise and squeezing *Phys. Rev.* E **108** 024204
[31] Schmolke F and Lutz E 2024 Measurement-induced quantum synchronization and multiplexing *Phys. Rev. Lett.* **132** 010402
[32] Kehrer T, Nadolny T and Bruder C 2024 Quantum synchronization through the interference blockade (arXiv:2405.05182)
[33] Hofheinz M, Portier F, Baudouin Q, Joyez P, Vion D, Bertet P, Roche P and Estève D 2011 Bright side of the coulomb blockade *Phys. Rev. Lett.* **106** 217005
[34] Peugeot A *et al* 2021 Generating two continuous entangled microwave beams using a dc-biased Josephson junction *Phys. Rev.* X **11** 031008
[35] Ménard G C *et al* 2022 Emission of photon multiplets by a dc-biased superconducting circuit *Phys. Rev.* X **12** 021006
[36] Grimm A *et al* 2019 Bright on-demand source of antibunched microwave photons based on inelastic cooper pair tunneling *Phys. Rev.* X **9** 021016
[37] Rolland C *et al* 2019 Antibunched photons emitted by a dc-biased Josephson junction *Phys. Rev. Lett.* **122** 186804
[38] Casariego M *et al* 2023 Propagating quantum microwaves: towards applications in communication and sensing *Quantum Sci. Technol.* **8** 023001
[39] Gu X, Frisk Kockum A, Miranowicz A, Liu Y-xi and Nori F 2017 Microwave photonics with superconducting quantum circuits *Phys. Rep.* **718** 1–102
[40] Sandbo Chang C W, Vadiraj A M, Bourassa J, Balaji B and Wilson C M 2019 Quantum-enhanced noise radar *Appl. Phys. Lett.* **114** 112601
[41] Cassidy M C, Bruno A, Rubbert S, Irfan M, Kammhuber J, Schouten R N, Akhmerov A R and Kouwenhoven L P 2017 Demonstration of an ac Josephson junction laser *Science* **355** 939–42
[42] Chen F, Li J, Armour A D, Brahimi E, Stettenheim J, Sirois A J, Simmonds R W, Blencowe M P and Rimberg A J 2014 Realization of a single-cooper-pair Josephson laser *Phys. Rev.* B **90** 020506(R)
[43] Yan C, Hassel J, Vesterinen V, Zhang J, Ikonen J, Grönberg L, Goetz J and Möttönen M 2021 A low-noise on-chip coherent microwave source *Nat. Electron.* **4** 885–92
[44] Simon S H and Cooper N R 2018 Theory of the Josephson junction laser *Phys. Rev. Lett.* **121** 027004
[45] Danner L, Padurariu C, Ankerhold J and Kubala B 2021 Injection locking and synchronization in Josephson photonics devices *Phys. Rev.* B **104** 054517
[46] Lang B, Morley G F and Armour A D 2023 Discrete time translation symmetry breaking in a Josephson junction laser *Phys. Rev.* B **107** 144509
[47] Gramich V, Kubala B, Rohrer S and Ankerhold J 2013 From Coulomb-blockade to nonlinear quantum dynamics in a superconducting circuit with a resonator *Phys. Rev. Lett.* **111** 247002
[48] Mari A, Farace A, Didier N, Giovannetti V and Fazio R 2013 Measures of quantum synchronization in continuous variable systems *Phys. Rev. Lett.* **111** 103605
[49] Ameri V, Eghbali-Arani M, Mari A, Farace A, Kheirandish F, Giovannetti V and Fazio R 2015 Mutual information as an order parameter for quantum synchronization *Phys. Rev.* A **91** 012301
[50] Shen Y, Yi Soh H, Kwek L-C and Fan W 2023 Fisher information as general metrics of quantum synchronization *Entropy* **25** 1116
[51] Wang H, Blencowe M P, Armour A D and Rimberg A J 2017 Quantum dynamics of a Josephson junction driven cavity mode system in the presence of voltage bias noise *Phys. Rev.* B **96** 104503
[52] Xu C and Vavilov M G 2013 Full counting statistics of photons emitted by a double quantum dot *Phys. Rev.* B **88** 195307
[53] Novotny T 2013 Full counting statistics of electronic transport through interacting nanosystems *J. Comput. Electron.* **12** 375–87

[54] Kubala B, Ankerhold J and Armour A D 2020 Electronic and photonic counting statistics as probes of non-equilibrium quantum dynamics *New J. Phys.* **22** 023010
[55] Adler R 1946 A study of locking phenomena in oscillators *Proc. IRE* **34** 351–7
[56] Pavliotis G A and Stuart A M 2008 *Multiscale Methods: Averaging and Homogennization* 1st Edition (Springer)
[57] Bender C M and Orszag S A 1978 *Advanced Mathematical Methods for Scientists and Engineers I* (Springer)
[58] Risken H 1996 *The Fokker-Planck equation* (Springer)
[59] Kuramoto Y 1975 *International Symposium on Mathematical Problems in Theoretical Physics* (*Lecture Notes in Physics*) vol 30 p 420
[60] Reimann P, Vorndamme P and Schnack J 2023 Nonequilibration, synchronization and time crystals in isotropic Heisenberg models *Phys. Rev. Res.* **5** 043040
[61] Lörch N, Amitai E, Nunnenkamp A and Bruder C 2016 Genuine quantum signatures in synchronization of anharmonic self-oscillators *Phys. Rev. Lett.* **117** 073601
[62] Luca Giorgi G, Cabot A and Zambrini R 2019 Transient synchronization in open quantum systems *Advances in Open Systems and Fundamental Tests of Quantum Mechanics: Proc. 684 (Bad Honnef, Germany, 2–5 December 2018) (WE-Heraeus-Seminar)* (Springer) pp 73–89
[63] Siwiak-Jaszek S, Le T P and Olaya-Castro A 2020 Synchronization phase as an indicator of persistent quantum correlations between subsystems *Phys. Rev.* A **102** 032414
[64] Nadolny T, Bruder C and Brunelli M 2025 Nonreciprocal synchronization of active quantum spins *Phys. Rev.* X **15** 011010
[65] Cabot A, Luca Giorgi G and Zambrini R 2024 Nonequilibrium transition between dissipative time crystals *PRX Quantum* **5** 030325
[66] Luca Giorgi G, Galve F, Manzano G, Colet P and Zambrini R 2012 Quantum correlations and mutual synchronization *Phys. Rev.* A **85** 052101
[67] Li W, Zhang W, Li C and Song H 2017 Properties and relative measure for quantifying quantum synchronization *Phys. Rev.* E **96** 012211
[68] Czartowski J, Müller R, Życzkowski K and Braun D 2021 Perfect quantum-state synchronization *Phys. Rev.* A **104** 012410
[69] Hriscu A M and Nazarov Y V 2013 Quantum synchronization of conjugated variables in a superconducting device leads to the fundamental resistance quantization *Phys. Rev. Lett.* **110** 097002
[70] Bagrets D A and Nazarov Y V 2003 Full counting statistics of charge transfer in coulomb blockade systems *Phys. Rev.* B **67** 085316
[71] Graf G M and Lesovik G B 2010 Time ordering and counting statistics *J. Stat. Phys.* **138** 333–50
[72] Hofer P P and Clerk A A 2016 Negative full counting statistics arise from interference effects *Phys. Rev. Lett.* **116** 013603
[73] Armour A D, Kubala B and Ankerhold J 2017 Noise switching at a dynamical critical point in a cavity-conductor hybrid *Phys. Rev.* B **96** 214509
[74] Pavliotis G A and Stuart A 2008 *Multiscale Methods: Averaging and Homogenization* (*Texts in Applied Mathematics*) (Springer)
[75] Donvil B, Muratore-Ginanneschi P and Pekola J P 2019 Hybrid master equation for calorimetric measurements *Phys. Rev.* A **99** 042127

Supplemental Material to Quantum Synchronization in Presence of Shot Noise

Florian Höhe[1,*], Lukas Danner[1,2], Ciprian Padurariu[1], Brecht I. C Donvil[1], Joachim Ankerhold[1], and Björn Kubala[1,2]

[1]Institute for Complex Quantum Systems and IQST, University of Ulm, 89069 Ulm, Germany

[2]German Aerospace Center (DLR), Institute of Quantum Technologies, 89081 Ulm, Germany

[*]Author to whom any correspondence should be addressed.

E-mail: florian.hoehe@uni-ulm.de

In the supplemental material we complete the derivation of the equation for the reduced phase of Appendix C. Furthermore, we give details on Kramer's escape rate which approximates the phase dynamics and we present the reduced equation for the phases of two synchronized Josephson-photonics devices.

1. Second order correction to the Fokker-Planck equation

First we note, that by taking the trace of the first order equation

$$\partial_\tau |\rho^{(0)}(\tau,\psi)\rangle\rangle = \mathcal{L}(\psi)|\rho^{(1)}(\tau,\psi)\rangle\rangle + \partial_\psi \left[\Lambda^{(1)}(\psi)|\rho^{(0)}(\tau,\psi)\rangle\rangle\right]. \tag{1}$$

we did not extract its full information. To do so, let $\mathcal{R}$ be the pseudoinverse (Moore–Penrose inverse) of $\mathcal{L}$ i.e. $\mathcal{R} = (\mathcal{L}+\mathcal{P})^{-1} - \mathcal{P}$ and with $\mathcal{P} = |\rho_{\mathrm{eq}}\rangle\rangle\langle\langle 1|$

$$\mathcal{L}\mathcal{R} = \mathcal{R}\mathcal{L} = \mathcal{Q} \tag{2}$$

applies, where $\mathcal{Q} = 1 - \mathcal{P}$. Then multiplying with $\mathcal{R}$ from left yields

$$0 = \mathcal{R}\mathcal{L}|\rho^{(1)}\rangle\rangle + \mathcal{R}\partial_\psi\left(\Lambda^{(1)}|\rho^{(0)}\rangle\rangle\right) \tag{3}$$

and equivalently

$$\mathcal{Q}|\rho^{(1)}\rangle\rangle = -\mathcal{R}\partial_\psi\left(\Lambda^{(1)}|\rho^{(0)}\rangle\rangle\right). \tag{4}$$

The second order equation reads

$$\partial_\tau|\rho^{(1)}\rangle\rangle = \mathcal{L}|\rho^{(2)}\rangle\rangle + \partial_\psi\left(\Lambda^{(1)}|\rho^{(1)}\rangle\rangle\right) + \frac{1}{2}\partial_\psi^2\left(\Lambda^{(2)}|\rho^{(0)}\rangle\rangle\right). \tag{5}$$

From the the expansion of Λ in r_0 we find

$$\Lambda^{(2)}\rho = -i\pi^2 r_0^2[h^\dagger + h, \rho]. \tag{6}$$

Taking the trace, using $\mathcal{Q}+\mathcal{P}=1$, and inserting (4) gives

$$\begin{aligned}\partial_\tau P^{(1)} = \;& \partial_\psi\langle\langle 1|\partial_\psi\left(\Lambda^{(1)}\mathcal{R}\right)\Lambda^{(1)}|\rho^{(0)}\rangle\rangle + \partial_\psi\left(\langle\langle 1|\Lambda^{(1)}|\rho_{\mathrm{eq}}\rangle\rangle P^{(1)}\right)\\ &+\frac{1}{2}\partial_\psi^2\langle\langle 1|\Lambda^{(2)}|\rho^{(0)}\rangle\rangle - \partial_\psi^2\langle\langle 1|\Lambda^{(1)}\mathcal{R}\partial_\psi\Lambda^{(1)}|\rho^{(0)}\rangle\rangle\end{aligned} \tag{7}$$

where we made use of $A\partial_x(B) = \partial_x(AB) - \partial_x(A)B$. As $\Lambda^{(2)}$ is a commutator with ρ its expectation value vanishes. Finally we approximate $P \approx P^{(0)} + P^{(1)}$. We expect the $P^{(1)}$ contribution to the other terms will come in the next order of r_0 and already add it. With that we obtain the Fokker-Planck equation

$$\partial_\tau P(\tau,\psi) = -\partial_\psi \left[(j^{(0)}(\psi) + j^{(1)}(\psi)) P(\tau,\psi) \right] + \partial_\psi^2 \left[D(\psi) P(\tau,\psi) \right] \tag{8}$$

with

$$j^{(0)}(\psi) = -\langle\langle 1|\Lambda^{(1)}|\rho_{\mathrm{eq}}\rangle\rangle \tag{9}$$

$$j^{(1)}(\psi) = -\langle\langle 1|\partial_\psi \left(\Lambda^{(1)}\mathcal{R}\right)\Lambda^{(1)}|\rho_{\mathrm{eq}}\rangle\rangle \tag{10}$$

$$D(\psi) = -\langle\langle 1|\Lambda^{(1)}\mathcal{R}\Lambda^{(1)}|\rho_{\mathrm{eq}}\rangle\rangle. \tag{11}$$

and we define $j(\psi) = j^{(0)}(\psi) + j^{(1)}(\psi)$. We show the different contributions to the drift, (9) and (10), and the diffusion term (11) in figure 1.

As described in the main text, the potential is determined by the drift term, $V(\psi) = -\int j(\psi)\,\mathrm{d}\psi$, which in turn is gained from the expectation value of the dc-current I_{CP} in the steady state of $\mathcal{L}(\psi)$. In the limit of small zero-point fluctuations, the Hamiltonian and the current operator can be approximated, only including bilinear operator terms,

$$H_{\mathrm{RWA}} = \left[\hbar\Delta - \varepsilon E_J^* \frac{\alpha_0^2}{2}\cos(\psi)\right] a^\dagger a + \frac{E_J^*}{2}\left(ie^{i\psi}\alpha_0 a^\dagger + e^{i\psi}\varepsilon\frac{\alpha_0^2}{4}a^{\dagger 2} + h.c.\right) \tag{12}$$

$$\frac{I_{\mathrm{CP}}}{2e} = \varepsilon\frac{E_J^*}{2\hbar}\sin(\psi)\left(1 - \alpha_0^2 a^\dagger a\right) + \frac{E_J^*}{2\hbar}\left(e^{i\psi}\alpha_0 a^\dagger - ie^{i\psi}\varepsilon\frac{\alpha_0^2}{4}a^{\dagger 2} + h.c.\right) \tag{13}$$

For this bilinear problem we can find a closed set of coupled equations for expectation values in the steady state

$$\left[\frac{\hbar\gamma}{2} + i\left(\hbar\Delta - \frac{E_J^*}{2}\varepsilon\alpha_0^2\cos\psi\right)\right]\langle a\rangle + i\frac{E_J^*}{4}\alpha_0^2\varepsilon e^{i\psi}\langle a^\dagger\rangle = \frac{E_J^*}{2}e^{i\psi} \tag{14}$$

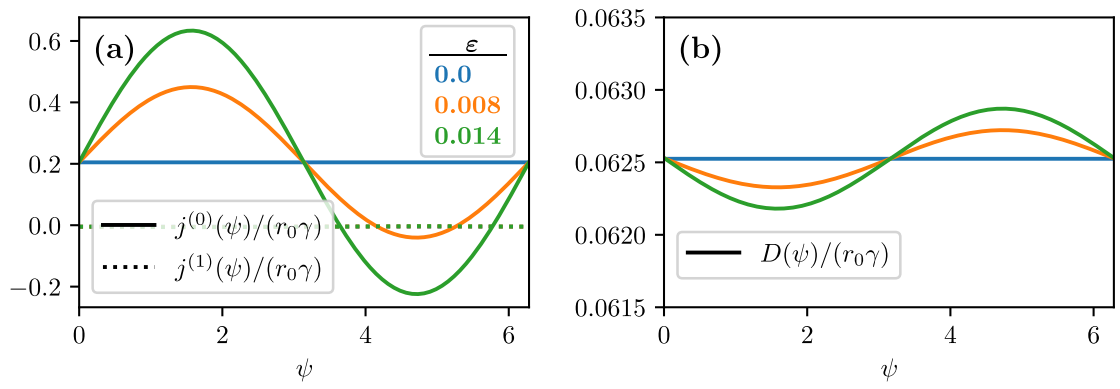

Figure 1. Drift and diffusion coefficients for injection locking. (a) The drift coefficient shows a strong phase dependence for $\varepsilon > 0$ while the diffusion coefficients (b) only show a weak dependence. [Parameters see figure 3 in the main text.]

$$\left[\hbar\gamma + 2i\left(\hbar\Delta - \frac{E_J^*}{2}\varepsilon\alpha_0^2\cos\psi\right)\right]\langle a^2\rangle - E_J^*\alpha_0 e^{i\psi}\langle a\rangle + i\frac{E_J^*}{2}\alpha_0^2\varepsilon e^{i\psi}\langle a^\dagger a\rangle = -i\frac{E_J^*}{4}\alpha_0^2\varepsilon e^{i\psi} \quad (15)$$

$$\hbar\gamma\langle a^\dagger a\rangle - \frac{E_J^*}{2}\alpha_0\left(e^{i\psi}\langle a^\dagger\rangle + e^{-i\psi}\langle a\rangle\right) + \frac{E_J^*}{4}\alpha_0^2\varepsilon\left(ie^{i\psi}\langle a^{\dagger 2}\rangle - ie^{-i\psi}\langle a^2\rangle\right) = 0\,. \quad (16)$$

In linear order of ε, we find

$$\langle a\rangle \approx \frac{E_J^*\alpha_0}{\hbar\gamma}e^{i\psi} + \frac{i}{2}\varepsilon\left(\frac{E_J^*\alpha_0}{\hbar\gamma}\right)^2\alpha_0 e^{2i\psi} \quad (17)$$

$$\langle a^2\rangle \approx \left(\frac{E_J^*\alpha_0}{\hbar\gamma}\right)^2 e^{2i\psi} - \frac{i}{4}\varepsilon\alpha_0\frac{E_J^*\alpha_0}{\hbar\gamma} \quad (18)$$

$$\langle a^\dagger a\rangle \approx \left(\frac{E_J^*\alpha_0}{\hbar\gamma}\right)^2 - \varepsilon\alpha_0\left(\frac{E_J^*\alpha_0}{\hbar\gamma}\right)^3 \quad (19)$$

Thus, the steady state current is

$$\frac{\langle I_{\mathrm{CP}}\rangle}{2e\gamma}(\psi) \approx \frac{E_J^*}{\hbar\gamma}\frac{\varepsilon}{2}\sin(\psi) + \alpha_0^2\left(\frac{E_J^*}{\hbar\gamma}\right)^2. \quad (20)$$

For this limiting scenario we thus have explicitly found an analytical expression for the ψ-dependence of the current. In addition to the conventional (ψ-independent) Josephson photonics contribution, the ac-signal causes a Shapiro-like term, which leads to locking.

2. Kramer's escape rate

In angular frequencies Kramer's escape rate r_K is given by [1]

$$\nu_K = 2\pi r_K = \sqrt{V''(\psi_{\min})|V''(\psi_{\max})|}\exp\left[-(V(\psi_{\max}) - V(\psi_{\min}))/D\right]\,, \quad (21)$$

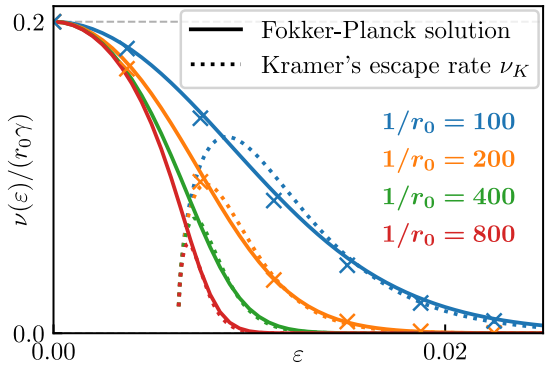

Figure 2. Comparison of two-time perturbation theory and Kramer's escape rate with the numerical solution of the master equation. The smaller the resistance r_0, the better the Fokker-Planck solution fits the numerical result (crosses). Kramer's escape rate (dotted) is calculated with a diffusion constant extracted from the two-timing result and only matches the Fokker-Planck solution for a clearly pronounced minimum. [Parameters: $E_J^*/(\hbar\gamma) = 10$, $\alpha_0 = 0.1$, $2eV_{\mathrm{dc}}/\hbar = \omega_0$, $\nu_0 = 0.2r_0\gamma$.]

where we use that for small r_0 the coefficient $D(\psi)$ is only weakly ψ-dependent $D(\psi) \approx \text{const.} = D$, cf. figure 1(b). For a sinusoidal potential

$$V(\psi) = \nu_c \cos\psi - \nu_0 \psi \tag{22}$$

we find

$$\psi_{\min} = \pi + \arcsin\frac{\nu_0}{\nu_c} \qquad \text{and} \qquad \psi_{\max} = 3\pi - \arcsin\frac{\nu_0}{\nu_c} \tag{23}$$

and with that the rate given in the main text. This is a good approximation for tilted potentials with pronounced minima (ε large enough to be well locked), as shown in figure 2 of the main text.

3. Derivation of the reduced equation for mutual synchronization

The reduced equation for the phases of two coupled Josephson-photonics devices is derived in a similar way as in the case for injection locking of a single device. First, the Hamiltonian (8) in the main text is transformed to a frame rotating with the same frequency ω_r for a and b via the unitary transformation $U = e^{i\omega_r t(a^\dagger a + b^\dagger b)}$ such that

$$\omega_{\mathrm{dc},a} = \omega_r + \delta_a \qquad \text{and} \qquad \omega_{\mathrm{dc},b} = \omega_r + \delta_b \tag{24}$$

to obtain

$$\begin{aligned} H = {} & \hbar(\omega_a - \omega_{\mathrm{dc},a} + \delta_a)a^\dagger a + \hbar(\omega_a - \omega_{\mathrm{dc},a} + \delta_a)a^\dagger a \\ & + (h_a^\dagger + h_a) + (h_b^\dagger + h_b) + \epsilon(a^\dagger b + a b^\dagger) \end{aligned} \tag{25}$$

with

$$h_a^\dagger = i\frac{E_J^*}{2} : e^{-i(\delta_a - \varphi_a)} a^\dagger \frac{J_1(2\alpha_0\sqrt{a^\dagger a})}{\sqrt{a^\dagger a}} : \tag{26}$$

and analogous for b. Note that the coupling term remains time-independent.

We again utilize Cooper-pair counting as in (5) of the main text, but count CPs transferred across the resistors in system a and b separately. Hence, the dynamics of the density matrix ρ_{m_a,m_b} is governed by

$$\begin{aligned} \dot\rho_{m_a,m_b} = {} & \mathcal{L}_0 \rho_{m_a,m_b} \\ & - \frac{i}{\hbar}[h_a^\dagger(m_a - 1/2, m_b)\rho_{m_a - 1/2, m_b} + h_a(m_a + 1/2, m_b)\rho_{m_a + 1/2, m_b}] + h.c. \\ & - \frac{i}{\hbar}[h_b^\dagger(m_a, m_b - 1/2)\rho_{m_a, m_b - 1/2} + h_b(m_a, m_b + 1/2)\rho_{m_a, m_b + 1/2}] + h.c.\,. \end{aligned} \tag{27}$$

Again, we treat $\varphi_a = 2\pi r_0 m_a$ and $\varphi_b = 2\pi r_0 m_b$ as continuous and transform to a moving reference frame

$$\varphi_a' = \varphi_a - \delta_a t \qquad \text{and} \qquad \varphi_b' = \varphi_b - \delta_b t. \tag{28}$$

Hereby, the Hamiltonian becomes time-independent. We choose δ_a and δ_b such that they are of the order of $r_0\gamma$. After expanding in r_0 and solving the resulting equation order by order, we end up with a two-dimensional Fokker-Planck equation

$$\frac{\partial}{\partial t}P = \left\{ -\frac{\partial}{\partial \varphi_a'} j_a - \frac{\partial}{\partial \varphi_b'} j_b + \frac{\partial^2}{\partial \varphi_a'^2} D_{aa} + 2\frac{\partial^2}{\partial \varphi_a' \partial \varphi_b'} D_{ab} + \frac{\partial^2}{\partial \varphi_b'^2} D_{bb} \right\} P \tag{29}$$

with drift and diffusion coefficients

$$j_a^{(0)}(\varphi'_a, \varphi'_b) = -\langle\langle 1|\Lambda_a|\rho_{\rm eq}\rangle\rangle \tag{30}$$

$$j_b^{(0)}(\varphi'_a, \varphi'_b) = -\langle\langle 1|\Lambda_b|\rho_{\rm eq}\rangle\rangle \tag{31}$$

$$j_a^{(1)}(\varphi'_a, \varphi'_b) = -\langle\langle 1|\partial_{\varphi'_a}\left(\Lambda_a\mathcal{R}\right)\Lambda_a|\rho_{\rm eq}\rangle\rangle - \langle\langle 1|\partial_{\varphi'_b}\left(\Lambda_a\mathcal{R}\right)\Lambda_b|\rho_{\rm eq}\rangle\rangle \tag{32}$$

$$j_b^{(1)}(\varphi'_a, \varphi'_b) = -\langle\langle 1|\partial_{\varphi'_a}\left(\Lambda_b\mathcal{R}\right)\Lambda_a|\rho_{\rm eq}\rangle\rangle - \langle\langle 1|\partial_{\varphi'_b}\left(\Lambda_b\mathcal{R}\right)\Lambda_b|\rho_{\rm eq}\rangle\rangle \tag{33}$$

$$D_{aa}(\varphi'_a, \varphi'_b) = -\langle\langle 1|\Lambda_a\mathcal{R}\Lambda_a|\rho_{\rm eq}\rangle\rangle \tag{34}$$

$$D_{ab}(\varphi'_a, \varphi'_b) = -\langle\langle 1|\Lambda_a\mathcal{R}\Lambda_b|\rho_{\rm eq}\rangle\rangle - \langle\langle 1|\Lambda_b\mathcal{R}\Lambda_a|\rho_{\rm eq}\rangle\rangle \tag{35}$$

$$D_{bb}(\varphi'_a, \varphi'_b) = -\langle\langle 1|\Lambda_b\mathcal{R}\Lambda_b|\rho_{\rm eq}\rangle\rangle\ , \tag{36}$$

where

$$\Lambda_a = -2\pi r_0\mathcal{I}_{{\rm CP},a}/(2e) + \delta_a \tag{37}$$

$$\Lambda_b = -2\pi r_0\tilde{R}_0\mathcal{I}_{{\rm CP},b}/(2e) + \delta_b. \tag{38}$$

Here, $\mathcal{I}_{{\rm CP},a}$ and $\mathcal{I}_{{\rm CP},b}$ are the current operators for system a and b respectively. As before $\mathcal{R}$ is the pseudo-inverse of the Liouvillian $\mathcal{L} = -\frac{i}{\hbar}[H,\rho] + \gamma\mathcal{D}[a]\rho + \gamma\mathcal{D}[b]\rho$. A transformation to sum and difference variables $\eta = -(\varphi'_a + \varphi'_b)$ and $\psi = -(\varphi'_a - \varphi'_b)$ is useful as the drift and diffusion coefficients are independent of η.

References

[1] Hannes Risken. *The Fokker-Planck equation.* Springer, 1996.

4.2.2 Publication (*iii*): *Quantum microwaves: Stabilizing squeezed light by phase locking*

4.2.2.1 Bibliographic Data and Author's Contribution

Title	Quantum microwaves: Stabilizing squeezed light by phase locking
Authors	Lukas Danner, Florian Höhe, Ciprian Padurariu, Joachim Ankerhold, and Björn Kubala
Journal	Physical Review B
Volume	111
Number	184519
Year	2025
DOI	https://doi.org/10.1103/PhysRevB.111.184519

The author is a shared first author of this publication. He carried out analytical calculations and contributed substantially to the interpretation of the results of this publication. The author created one of the figures and assumed the primary role in the preparation of the manuscript.

4.2.2.2 Summary of Publication (*iii*)

The publication *Quantum microwaves: Stabilizing squeezed light by phase locking* applies the theory of injection locking in Josephson-photonics devices, which was derived in Pub. (*ii*), to single- and two-mode squeezed states. We investigate various scenarios of injection locking in presence of shot noise and highlight differences in the locking features compared to coherent states.
Here, we specifically consider two different Josephson-photonics platforms: First, we focus on devices with a single microwave resonator that are driven at the parametric resonance $\omega_{\mathrm{dc}} \approx 2\omega_a$. They produce single-mode squeezed states (c.f. Sec. 1.4.1), where one quadrature is squeezed below vacuum level. Second, devices with two cavities, which are driven such that each tunneling Cooper pair effectively creates one photon in each microwave resonator, $\omega_{\mathrm{dc}} \approx \omega_a + \omega_b$, give rise to two-mode squeezed states, where the squeezing is found in the mixed reduced phase-space (see Sec. 1.5.2). Crucially, the technological application of these devices relies on a stable direction of the squeezing angle.

[6] https://creativecommons.org/licenses/by/4.0/

Phase diffusion of squeezed states

Like in Pubs. (*i*) and (*ii*), we include an in-series resistor R_0, which leads to a time-dependent phase $\varphi_{R_0} \propto R_0 \int_0^t I_{\mathrm{CP}}\,\mathrm{d}\tau$. In this way, we capture the stochastic nature and the shot noise of the tunneling Cooper pairs. While for $R_0 = 0$, a constant phase φ_{R_0} defines the angle of the squeezing ellipses [c.f. Fig. 1(b) and Eq. (3) of Pub. (*iii*)], shot noise (for $R_0 > 0$) leads to a φ_{R_0} that increases in time, which effectively averages the squeezing angle. This results in rotationally symmetric or squared-shaped steady-state Wigner functions (c.f. Fig. 1.13 of Sec. 1.7), such that squeezing is hidden from direct observation. Then, all quadratures are anti-squeezed with variances above the vacuum limit [Fig. 1(c) and Fig. 3(a)].

Injection locking of squeezed quantum states

In the same manner as before, injection locking can stabilize the phase in Josephson-photonics devices. However, here we additionally require that the $Z^{k=2}$-symmetry in phase-space is preserved by locking. In the classical analysis, the phase-space symmetry of the two stable solutions, which emerged for a drive above the parametric threshold, could be preserved when the locking signal was also applied at the parametric resonance, $\Omega \approx \omega_{\mathrm{dc}} \approx 2\omega_0$ [c.f. Fig. 5(c) of Pub. (*i*) in Sec. 4.1.1]. In the quantum regime, squeezing ellipses exist when the system is driven below the parametric threshold. Also, here, the locking signal must preserve the two-fold symmetry of the squeezing ellipses in phase space, $\Omega \approx \omega_{\mathrm{dc}}$. Most importantly, we find that the locking drive effectively adds a Shapiro-like contribution to the Hamiltonian and the Cooper-pair current [see Eqs. (4) and (5)] which is mainly responsible for the locking mechanism. Similarly to Pub. (*ii*), the dc current becomes dependent on the Adler phase

$$\psi = (\Omega t + \varphi_{\mathrm{ac}}) - (\omega_{\mathrm{dc}} t - \varphi_{R_0}) \tag{4.50}$$

and yields a potential that effectively locks the system.

Hallmark signatures of injection locking of squeezed states

While the locking mechanism itself is similar to Pubs. (*i*) and (*ii*), squeezed states show inherently different locking signatures than coherent states. In contrast to driving at the fundamental resonance, only the sum of the frequencies of the excitations created by a single Cooper pair tunneling process is fixed, $\omega_{\mathrm{dc}} = \omega_1 + \omega_2$. Hence, the emission spectrum (in Fourier space) of a single-mode squeezed cavity is broad (even without voltage fluctuations). Injection locking only results in a marginal (re)sharpening of the spectrum, which therefore cannot serve as a hallmark signature in single-mode squeezed states. Instead, we can choose the two-time phase correlation function

$$G^{(\phi)}(t+\tau, t) = \langle \hat{a}^{\dagger 2}(t+\tau)\hat{a}^2(t)\rangle \tag{4.51}$$

as an experimentally observable quantity. In the stationary state and for long time differences ($\tau \to \infty$), the two-time correlation function factorizes, such that, without phase diffusion $G^{(\phi)} \to G^{(\phi)}_{\infty} = |\langle \hat{a}^2\rangle|^2$. Without a locking signal, the phase-space angle of the squeezed state diffuses due to noise, and phase correlations are lost, $G^{(\phi)}_{\infty} = 0$ (with diffusion). In turn, an injection locked and phase stabilized microwave resonator exhibits a finite $G^{(\phi)}_{\infty}$. Consequently, the Fourier

transform $S_\phi(\omega)$ of the phase correlation function is sharpened at $\omega \approx \Omega$ when the squeezed state is injection locked [see Fig. 2].

Influence of zero-point fluctuations on injection locking

The start of Pub. (*iii*) focused mainly on a parameter regime for zero-point fluctuations, where a bilinear expansion of Hamiltonian and Cooper-pair current is sufficient. Summarizing the specifics of injection locking for single-mode squeezing, we have found that the locking signal has introduced two resonant Hamiltonian processes [c.f. Appendix A.1 of Pub. (*iii*)]:

- $\propto E_J^* \epsilon J_0(2\alpha_0\sqrt{\hat{a}^\dagger\hat{a}}) \approx E_J^*\epsilon(1-\alpha_0^2\hat{a}^\dagger\hat{a})$
  A tunneling Cooper pair creates an excitation in the locking signal without changing the number of photons in the cavity. Within bilinear approximation, this contribution adds a Shapiro-like term to the Cooper-pair current and just a detuning term to the Hamiltonian.

- $\propto E_J^*\epsilon\hat{a}^{\dagger 4} J_4(2\alpha_0\sqrt{\hat{a}^\dagger\hat{a}}) + \text{h.c.}$
  A tunneling Cooper pair and a locking-signal photon create four excitations in the cavity. Within bilinear approximation, this term can be neglected.

Furthermore, the model of a (single-mode) parametric amplifier diverges at the threshold $E_J^*\alpha_0^2 \to \hbar\gamma_a$ (compare Sec. 1.4.1.2).

Now, we highlight how zero-point fluctuations of the cavity strongly modify the locking mechanism. To do so, we move to a parameter regime of a strongly nonlinear drive. When a Josephson-photonics setup is driven beyond the parametric threshold, the squeezing ellipse splits into two parts with same finite amplitude but opposite phase. In contrast to the bilinear case, where the Bessel function J_0 could be approximated [compare also Fig. 4(a)], its full nonlinear contribution to the current,

$$\langle : J_0(2\alpha_0^2\sqrt{\hat{a}^\dagger\hat{a}}) : \rangle = \sum_m \rho_{mm} \frac{L_m^{(0)}(\alpha_0^2)}{L_m^{(0)}(0)} \tag{4.52}$$

now strongly affects the height of the barrier of the locking potential. Most strikingly, zero-point fluctuations can be fabricated such that the expectation value in Eq. (4.52) is zero: extrema in the locking potential then vanish and the system cannot be injection locked [see Fig. 4(b)]. (Due to other resonant contributions in the Hamiltonian and current that are proportional to the Bessel function J_4, the value for α_0 at which the potential vanishes is slightly below the root of the J_0-function). Even larger values for α_0 lead to a sign flip of the above expectation value in Eq. (4.52) and thus of the potential. Consequently, the quantum state is injection locked [see Fig. 4(c)] to a phase-space angle shifted by π.

Symmetry-breaking injection locking of single-mode squeezed states

Finally, Pub. (*iii*) discusses injection locking of a single-mode squeezed state by a direct microwave drive (instead of an ac voltage) with a frequency $\Omega \approx \omega_a$. Since the microwave drive does not appear as a term inside the Josephson-energy contribution, many nonlinear effects induced by the junction as well as the Shapiro-like

locking term are now absent. First, we find that such a drive can injection lock the device. However, we stress that such a direct driving signal is resonant with the resonator's eigenfrequency. It is not a parametric drive and unavoidably destroys the $Z^{k=2}$ symmetry of the steady-state Wigner function.
For small amplitudes of the microwave drive, the steady-state squeezing ellipse remains close to the phase-space origin. Then, locking results only in a weak breaking of the $Z^{k=2}$-symmetry. By a variable transformation, we find that the center of the injection-locked squeezing ellipse is just shifted to some value $\alpha = |\alpha|e^{i\phi_\alpha}$. To be precise [c.f. Fig. 5 and App. A.3], the squeezing ellipse performs a circular motion with a given radius around a new central point (different from the origin) when the Adler phase ψ is varied. Also, here, the feedback of the Cooper-pair current effectively creates a force $\propto \dot{\psi}$, which pulls the phase particle into the minimum of the locking potential. By a geometric construction [as in Fig. 5(a)], we find the position and orientation of the injection locked squeezing ellipse.

In summary, we have theoretically demonstrated injection locking and phase stabilization of the squeezing angle in Josephson-photonics devices for squeezed quantum states in the presence of shot noise. First, we have shown how to preserve the $Z^{k=2}$-symmetry of the squeezing ellipses. Secondly, a symmetry-breaking direct microwave drive leads to injection locked squeezed states that are centered around a shifted phase-space origin. The experimentally accessible two-time phase correlation function serves as a hallmark signature of phase stabilization. Specific values of zero-point fluctuations can impair the locking mechanism. We note that this scheme can immediately be applied to any other quantum state with a neutrally stable phase, such as cat states. Our techniques enable the usage of Josephson-photonics devices as suitable on-chip sources for quantum microwaves that only require minute ac power.

Quantum microwaves: Stabilizing squeezed light by phase locking

Lukas Danner,[1,2,*,†] Florian Höhe,[2,*,‡] Ciprian Padurariu,[2] Joachim Ankerhold,[2] and Björn Kubala[1,2]
[1]*German Aerospace Center (DLR), Institute of Quantum Technologies, 89081 Ulm, Germany*
[2]*Institute for Complex Quantum Systems and IQST, University of Ulm, 89069 Ulm, Germany*

(Received 5 February 2025; revised 9 May 2025; accepted 13 May 2025; published 30 May 2025)

Bright sources of quantum microwave light are an important building block for various quantum technological applications. Josephson junctions coupled to microwave cavities are a particularly versatile and simple source for microwaves with quantum characteristics, such as different types of squeezing. Due to the inherent nonlinearity of the system, a pure dc-voltage bias can lead to the emission of correlated pairs of photons into a stripline resonator. However, a drawback of this method is that it suffers from bias voltage noise, which disturbs the phase of the junction and consequently destroys the coherence of the photons, severely limiting its applications. Here we describe how adding a small ac reference signal either to the dc bias or directly into the cavity can stabilize the system and counteract the sensitivity to noise. We first consider the injection locking of a single-mode device before turning to the more technologically relevant locking of two-mode squeezed states, where phase locking preserves the entanglement between photons. Finally, we describe locking by directly injecting a microwave into the cavity, which breaks the symmetry of the squeezing ellipse. In all cases, locking can mitigate the effects of voltage noise and enable the use of squeezed states in quantum technological applications.

DOI: 10.1103/PhysRevB.111.184519

I. INTRODUCTION

Squeezed states of light are an important resource for various quantum technological applications. Most prominently in metrology, they can be used for quantum enhanced precision measurements [1,2], realized, for instance, with visible light in optomechanical gravitational wave detection, where they allow beating the shot-noise limit [3]. In the microwave regime, propagating squeezed microwaves is an indispensable ingredient of emerging quantum communication and quantum sensing technologies [4]: protocols for quantum teleportation [5–7] and for quantum key distribution [8,9] have been realized in cryogenic environments, while open-air extensions are investigated. Quantum enhanced interferometry can beat the standard quantum limit [10] and quantum illumination [11–13] can offer a quantum advantage for imaging and radar applications under certain conditions [14–18]. Less explored is the use of sources of squeezed states in quantum information technologies, where they could find use for autonomous remote entanglement stabilization [19].

The eponymous characteristic of squeezed light is that fluctuations are reduced beyond the vacuum level for one generalized quadrature with respectively enhanced fluctuations in the other. Clearly, this distinguishes one distinct fixed direction in a (rotating-frame) phase space. A source, which keeps this direction stable, is thus crucial. While in ac-driven sources, such as various types of Josephson parametric amplifiers [20–26], the distinguished phase-space direction is simply determined by the phase of the ac-drive, dc-driven devices lack such a reference and consequently suffer from phase diffusion. Here, we investigate how stabilization can nonetheless be achieved by locking onto a weak oscillating reference signal.

We do this for a specific recently developed platform [27–31] for creating squeezed microwave light [32–37] by a dc-biased Josephson junction connected in series to microwave resonators. One appeal of such Josephson-photonics devices is the versatility of these sources, as a variety of different interesting quantum states [38–40] can be created by a simple change of the dc bias. However, being dc biased, they exhibit a phase instability directly linked to fluctuations of the voltage dropping across the junctions, as $\varphi \sim \int dt\, \delta V(t)$ [41].

A model of these devices and their phase diffusion caused by shot noise of the Josephson current and an investigation of locking at the fundamental resonance, where each tunneling Cooper pair creates one photonic excitation, has been presented elsewhere [42]. Here, we expand this description to the locking of squeezed states, encountered when each Cooper pair creates two photons. Besides being of immediate technological relevance, the locking of squeezed states shows strikingly different features. In contrast to a standard locking scenario, the phase stabilization of a squeezed state relies on the injection of a signal at twice the frequency of the emitted radiation, which we want to lock. The way in which the radiation spectrum is modified by locking will thus obviously differ from the conventional case, where locking frequency and frequency to be locked (nearly) coincide [43].

*These two authors contributed equally to this paper.
†Contact author: lukas.danner@dlr.de
‡Contact author: florian.hoehe@uni-ulm.de

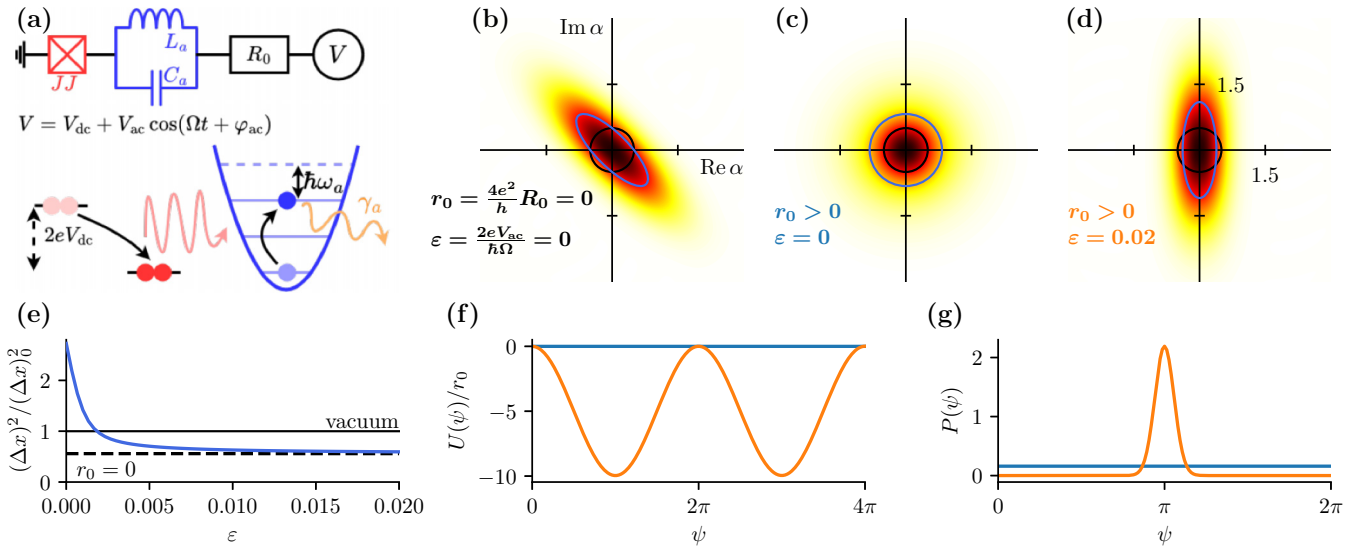

FIG. 1. Single-mode squeezing. (a) Circuit model of a Josephson-photonics device, where an *LC* resonator (with eigenfrequency ω_a and single-photon loss rate γ_a is connected in series with a Josephson junction). The circuit is resonantly dc biased, $2eV_{dc} \approx 2\omega_a$, such that each tunneling Cooper pair creates two photons in the resonator. (b) An idealized device with a fluctuationless dc bias will reach a steady state which is squeezed [blue ellipse and dashed line in (e)] below vacuum level [black circle and gray line in (e)]. The ellipse angle is constant in the frame rotating with $2eV_{dc}/(2\hbar)$ and set by the driving phase. (c) Voltage fluctuations through Cooper-pair shot noise, modeled by a small in-series resistance R_0 lead to diffusion of the driving phase, effectively resulting in the loss of squeezing and the $\mathbb{Z}^{k=2}$ symmetry. The ideal picture can be recovered (d) by adding an ac-locking signal with frequency $\Omega \approx 2eV_{dc}/\hbar$ of sufficient amplitude ε [blue curve in (e)]. The locking signal effectively creates a potential $U(\psi)$ for the driving phase with minima (f), in which it can be trapped. A competition between the force $\dot{\psi} = -U'(\psi)$ and noise yields (g) a steady-state probability distribution $P(\psi)$ centered around the potential minimum as the (steady-state) solution of Eq. (B8) from Appendix B 1. Parameters: $E_J^* = 80\hbar\gamma_a$, $\alpha_0 = 0.1$, $\delta_{dc} = 0$, $r_0 = 1/500$. The ellipse's minor and major axes indicate standard deviations of dimensionless phase space quadratures in the displayed state, whereas the black circle's radius indicates the same for the vacuum state.]

This generic feature of locking of squeezed states has, to our knowledge, not been investigated before. We will first consider Josephson-photonics devices operating in a regime, where they approximately realize generic single-mode and two-mode squeezing Hamiltonians, and study the locking of the corresponding squeezed states by an injected ac-voltage signal before considering the peculiar strong quantum nonlinearities these devices can also exhibit and their influence on locking. Finally, we will briefly consider the symmetry-breaking case of injecting a near-resonant microwave signal directly into the cavity, which resembles experiments performed in ac-driven systems [44,45].

II. DC-GENERATED SINGLE-MODE SQUEEZING

The Josephson-photonics platform we consider here for creating microwaves with a nonclassical nature, such as various squeezed states, consists of a dc-voltage biased Josephson junction connected in series to an LC-stripline resonator and a resistance R_0; see Fig. 1(a).

The system is described by a Hamiltonian

$$\hat{H} = \hbar\omega_a\hat{a}^\dagger\hat{a} - E_J\cos[\omega_{dc}t - \varphi_{R_0} + \alpha_0(\hat{a}^\dagger + \hat{a})], \quad (1)$$

amended by a Lindblad operator $\hat{L}_0 = \sqrt{\gamma_a}\hat{a}$ [30,31]. The resonator hosts a single mode of frequency ω_a with an (external) quality factor ω_a/γ_a and a phase variable, $\alpha_0(\hat{a}^\dagger + \hat{a})$, with zero-point fluctuations $\alpha_0 = (2e^2\sqrt{L/C}/\hbar)^{1/2}$. Besides the resonator's energy, the Hamiltonian contains a Josephson term, where the phase across the junction, appearing as the argument of the cosine, is found by Kirchhoff's rule, adding up the phases across elements to find the phase, $\omega_{dc}t = \int dt\, 2eV_{dc}/\hbar$, associated with the bias voltage. Crucially, the model includes the integrated voltage dropping across the (small) resistance R_0 if a current I_{CP} flows,

$$\frac{\hbar}{2e}\varphi_{R_0}(t) = R_0\int_0^t d\tau\, I_{CP}(\tau) = R_0 2e\, m_{CP}(t), \quad (2)$$

which is connected to the number of Cooper pairs m_{CP} that have crossed the junction. A dc current across the junction arises as Cooper pairs tunnel across the biased junction and lose energy by creating photonic excitations in the resonator, from which they eventually leak out via a transmission line. Clearly, we may expect various resonances when tuning the dc voltage such that $\omega_{dc} \approx k\omega_a (k \in \mathbb{N})$ and k photons are created. Considering $k = 2$, we find that for small detuning $\delta_{dc} = \omega_a - \omega_{dc}/2 \ll \omega_a$ and in the limit of small zero-point fluctuations, $\alpha_0 \ll 1$, see Appendix A 1, the effective Hamiltonian in the rotating frame [defined by $\hat{U}(t) = e^{i\hat{a}^\dagger\hat{a}\omega_{dc}t/2}$] takes in rotating wave approximation (RWA) the form

$$\hat{H}_{RWA} \approx \hbar\delta_{dc}\hat{a}^\dagger\hat{a} + \frac{E_J^*\alpha_0^2}{4}\cdot(e^{i\varphi_{R_0}}\hat{a}^{\dagger 2} + e^{-i\varphi_{R_0}}\hat{a}^2) \quad (3)$$

of a squeezing Hamiltonian with φ_{R_0} appearing as the phase of the squeezing parameter. Without resistance, $R_0 = 0 = \varphi_{R_0}$, one finds, indeed, a squeezed state, see Fig. 1(b) for

the steady-state Wigner function, where the $Z^{k=2}$ symmetry in phase-space reflects the symmetry of the Hamiltonian. Whereas the state has a trivial dependence on φ_{R_0} (i.e., the squeezing angle is $\varphi_{R_0}/2 - \pi/4$), many observables such as occupation $\hat{n} = \hat{a}^\dagger\hat{a}$ and current $\hat{I}_{\rm CP}$ have such symmetry that their expectation values are independent of φ_{R_0}. The degree of squeezing increases with the renormalized Josephson energy $E_J^* = E_J \cdot e^{-\alpha_0^2/2}$ and the maximum suppression of one quadrature fluctuation below the vacuum fluctuations, the so-called of 3dB limit, is approached for $\alpha_0 \ll 1$ when driving at threshold $E_J^*\alpha_0^2 \to \hbar\gamma_a$ [31] [A divergence, which appears for $\alpha_0 \to 0$, respectively, for the Hamiltonian (3), in photon number and antisqueezed quadrature fluctuations is regularized for finite α_0 by higher-order correction terms neglected in Eq. (3) but kept in Fig. 1.].

A. Phase diffusion and locking

Including now a finite resistance, $R_0 \neq 0$, phase φ_{R_0} no longer remains fixed to zero, but increases over time with each Cooper pair tunneling across the junction. In fact, there will be a mean growth determined by the mean Cooper-pair current and fluctuations caused by its shot noise. The consequent diffusion of phase φ_{R_0} leads to an effective averaging over all squeezing angles as the phase variance grows beyond 2π and the steady state under phase diffusion is rotationally symmetric [cf. Fig. 1(c)]. No squeezing is observable and, in fact, fluctuations in any direction are larger than vacuum fluctuations. To stabilize the squeezing ellipse, we add a small ac voltage, $V(t) = V_{\rm dc} + V_{\rm ac}\cos(\Omega t + \varphi_{\rm ac})$, as a locking signal which breaks rotational symmetry but does not break the $\mathbb{Z}^{k=2}$ symmetry, which is the case for $\Omega \approx 2\omega_a \approx \omega_{\rm dc}$. As expected, a sufficiently strong locking signal restores the undiffused phase-space squeezing ellipse as a stationary state of the system in the frame rotating with $\Omega/2$, see Fig. 1(d), and recovers nearly the full subvacuum noise squeezing of the $R_0 = 0$ case, see Fig. 1(e).

For the simulations of phase diffusion and locking as shown in Figs. 1(c) and 1(d), and for an understanding of the locking mechanism, we have to employ a model that goes beyond simple Lindbladian dynamics with the Hamiltonians (3) and (A3) with a fixed phase φ_{R_0}, but account for the feedback of the stochastic Cooper pair current on that phase, as described by Eq. (2). Such a model, relying on an extension of the number-resolved master equation technique [46] to the counting of the number $m_{\rm CP}$ of Cooper pairs transported in a *coherent* tunneling process, has been established in Ref. [42] for a Josephson-photonics device operated at a voltage bias, where each Cooper pair excites a single photon and the oscillator is driven into a coherent state for small zero-point fluctuations. Locking is then achieved by including the ac voltage in the Hamiltonian (1), $\omega_{\rm dc}t \to \int_0^t d\tau\, V(\tau)$, which in the frame rotating with $\Omega/2$ can be approximated (see Appendix A 1) in lowest order of zero-point fluctuations and locking strength $\varepsilon = 2eV_{\rm ac}/\hbar\Omega$ to

$$\hat{H} \approx \hbar\delta\hat{a}^\dagger\hat{a} + \frac{E_J^*\alpha_0^2}{4}\cdot(e^{+i\psi}\hat{a}^{\dagger 2} + e^{-i\psi}\hat{a}^2). \tag{4}$$

Here, the detuning $\delta = (\delta_{\rm dc} + \delta_{\rm ac}) - \varepsilon\frac{E_J^*\alpha_0^2}{2\hbar}\cos\psi$, where $2\delta_{\rm ac} = \omega_{\rm dc} - \Omega$ is the difference between the frequencies of the ac and dc drives. The detuning δ also depends on the phase difference $\psi = (\Omega t + \varphi_{\rm ac}) - (\omega_{\rm dc}t - \varphi_{R_0})$ between the ac-driving phase and the dc-driving phase. This term stems from tunneling processes, which do not change the occupation of the cavity: the absorption of an ac-drive photon drives a Cooper pair tunneling against the dc bias or, in the reverse process, a Cooper pair tunnels with the bias and emits a photon into the drive. These processes, which are proportional to εE_J, are renormalized by the presence of the cavity and the concomitant (virtual) emission and reabsorption of cavity photons. While the term in the Hamiltonian, which is the lowest-order expansion of a normal ordered Bessel-function $J_0(2\alpha_0\sqrt{\hat{a}^\dagger\hat{a}})$, cf. Eq. (A4) in Appendix A 1, reflects the minor (back-action) effect of this tunneling processes on the cavity, the same processes will also contribute to the current

$$\frac{\hat{I}_{CP}}{2e} \approx \frac{E_J^*\epsilon}{2\hbar}\sin(\psi)\big(1 - \alpha_0^2\hat{a}^\dagger\hat{a}\big) + i\frac{E_J^*\alpha_0^2}{4\hbar}(e^{-i\psi}\hat{a}^2 - e^{+i\psi}\hat{a}^{\dagger 2}). \tag{5}$$

The second term with photon pair creation and annihilation operators is the conventional Josephson-photonics current for a pure dc bias, which results in a ψ-independent current for $\varepsilon = 0$. The first term is the extra contribution added by the ac signal and hence proportional to ε. That current arises as the difference of the aforementioned forward and backward processes and consequently yields the sine term, which now also includes an $\mathcal{O}(\alpha_0^0) = \mathcal{O}(1)$ term without virtual cavity photons that is irrelevant in the Hamiltonian. It is this Shapiro-like term [47] which can lock the system. As $\dot{\psi} = -2\delta_{\rm ac} + \dot{\varphi}_{R_0}$ and $\dot{\varphi}_{R_0} \propto I_{\rm CP}(\psi)$ instead of ψ being a fixed parameter, its dynamic is governed by a stochastic differential equation. Average drift and fluctuations of ψ depend on mean and fluctuations of the Cooper pair current, which itself depends on ψ. The resulting reduced dynamics can be understood as diffusive (overdamped) motion in a potential [48,49], whose form can be formally derived via two-time perturbation theory, see Refs. [42,50,51] and Appendix B.

Without locking drive, the current is independent of ψ, so we get diffusion on a potential $U(\psi) \propto \psi$ with a slope related to the detuning, including an average voltage drop at R_0. The phase ψ will therefore explore its full parameter space, leading to the rotationally symmetric Wigner density of Fig. 1(c) without squeezing. With locking drive, the expectation value of the current oscillates with ψ around a mean value, eventually allowing for the creation of maxima and minima in the Adler-type potential [52], $U(\psi) = 2\delta_{\rm ac}\psi - 2eR_0/\hbar\int\langle\hat{I}_{\rm CP}(\psi)\rangle d\psi$, see Fig. 1(f). The phase particle can become trapped in one of the minima and the phase is constant but for small variations. As demonstrated in Fig. 1(d), this restores the undiffused squeezing ellipse of Fig. 1(b) with some minute additional broadening due to the remaining fluctuations of ψ.

While diffused and deeply locked states are clearly distinguishable, phase-space properties are typically not the observables most suited to clearly indicate a locking transition. This can be seen in the very smooth crossover of the quadrature with increasing the locking strength in Fig. 1(d) and can be understood from the dynamics in the locking

potential: Values of ψ, where the slope is reduced (increased), will be more (less) likely than the average, well before the emergence of local minima at larger locking signal ε.

B. Correlation functions

For the locking of a conventional (not squeezed) oscillator, an experimentally readily observable hallmark of a locked state is the sharpening of the resonators noise-broadened emission spectrum [29,43]. However, squeezing is different: as each tunneling Cooper pair creates two photons and distributes its energy between the two, only the sum of the photon frequency is fixed by $\omega_1 + \omega_2 = \omega_{\rm dc}$, while each individual photon frequency and thus the spectrum is lifetime broadened even without voltage fluctuations. These will only add insubstantially to the broadening (for typical experimental parameters) and locking can at best curtail this small extra broadening, see inset Fig. 2(b). The closest analog to the locking-induced spectral sharpening is found in a different experimentally accessible observable that can reveal phase-phase correlations:

$$G^{(\phi)}(t+\tau, t) = \langle \hat{a}^{\dagger 2}(t+\tau)\hat{a}^2(t)\rangle. \tag{6}$$

In a recent Josephson-photonics experiment, such observables were used as entanglement witnesses for two-mode squeezed radiation, cf. [33], and Sec. III below. On very short timescales ($\gamma_a\tau \lesssim 1$), the observable $G^{(\phi)}(\tau)$ reflects the bunching of photons due to the pair creation process and the relaxation dynamics of such excitations [53], similar to the conventional second-order correlation function [54]. For times much longer than all internal cavity relaxation and excitation dynamics, the correlation function factorizes, $G^{(\phi)}(\tau) \to \langle (a^\dagger)^2(t+\tau)\rangle\langle a^2(t)\rangle$, and only the phases of the two terms remain correlated. Without fluctuations and locking signal, these phases strictly oscillate with the applied dc voltage, $G^{(\phi)}(t+\tau, t) \to |\langle \hat{a}^2\rangle_{\rm st}|^2 \exp[-i\omega_{\rm dc}(t+\tau-t)]$, and $G^{(\phi)}(\tau)$ becomes constant in the corresponding rotating frame in the long-time limit. Phase diffusion is thus directly reflected in the long-time-decay of $G^{(\phi)}(\tau)$ shown in the blue line of Fig. 2(a). In our model, shot noise yields an exponential decay of phase-phase correlations on the scale $D\tau \sim 1$, where the free diffusion parameter $D(\psi) \approx D = 0.164 r_0\gamma_a$ can be calculated via two-time perturbation theory [42,50,51] and Appendix B, and a Lorentzian spectral broadening in Fourier space. In the frame rotating with the locking signal Ω, the decay is overlaid by an oscillation with the detuning $\nu_0 = \langle\dot{\psi}\rangle_{\varepsilon=0}$ of the broad unlocked peak from Ω. Note that in recent experiments [33,40], quasistatic classical fluctuations instead yielded Gaussian shapes in time and frequency. Adding a sufficiently strong locking signal, however, will constrain phase diffusion in the minima of the potential and preserve some phase-phase correlations, such that $G_{\phi,\infty}$ remains nonzero, leading to a delta-peaked spectrum (green line in Fig. 2), while the remaining broad part in the Fourier spectrum and the corresponding partial decay is caused by diffusion within one minimum.

Before revisiting the single-mode case to investigate few-photon nonlinearities and symmetry-breaking locking by a directly injected ac signal at a different frequency in Secs. IV and V below, we now turn to the case where each Cooper pair creates photons in two different modes.

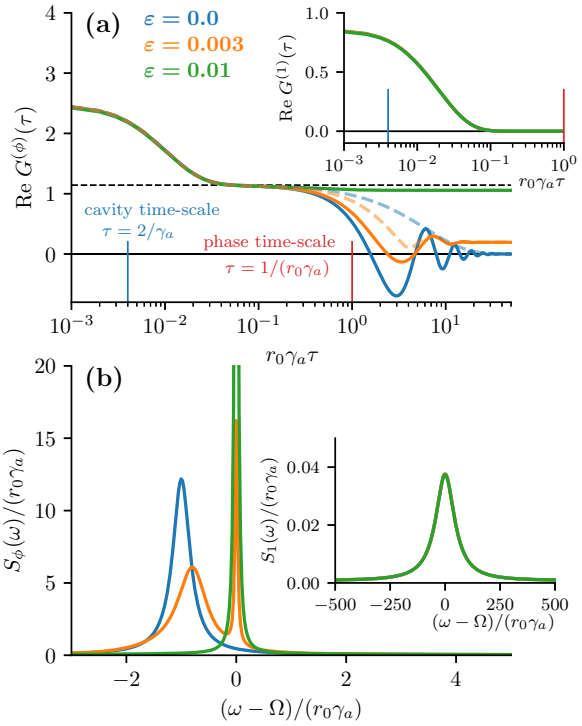

FIG. 2. First-order correlation functions $G^{(1)}(\tau) = \langle \hat{a}^\dagger(t+\tau)\hat{a}(t)\rangle$ (insets) and unconventional second-order correlation functions $G^{(\phi)}$ in the time domain (a) and the corresponding Fourier transforms, the frequency dependent spectra, $S_1(\omega)$ and $S_\phi(\omega)$ (b). The conventional spectrum [inset of (b)] of squeezed light is broadened by the cavity decay rate for weak driving but becomes substantially sharpened when driven closer to the squeezing divergence as in (b). In time domain, it decays toward $|\langle\hat{a}\rangle|^2 = 0$ for times larger than the timescale of the cavity dynamics irrespective of the much slower dynamics of the cavity phase. The (unconventional) second-order correlation function $G^{(\phi)}$ instead shows cavity and phase dynamics timescales (a). After an initial partial decay to $|\langle\hat{a}^2\rangle_{r_0=0}|^2$ (dashed line) on cavity timescales, which is independent of the ac-signal strength, the phase diffusion determines the further behavior. Injection locking is indicated by nonzero correlations $G^{(\phi)}$ in the long-time limit $\tau \to \infty$. In frequency domain (b), locking is reflected by the emergence of a dominant spectrally sharp contribution at Ω. Width and position of the broad peak reflect the corresponding time evolution on the timescales of the slow phase dynamics and yield direct insight into the phase-phase correlations of the diffusive motion in the potential, cf. Fig. 1(f). [Parameters: $E_J^* = 80\hbar\gamma_a$, $\alpha_0 = 0.1$, $\delta_{\rm dc} = 0$, $\nu_0 = r_0\gamma_a$, $r_0 = 1/500$. Delta peaks are artificially broadened by $r_0\gamma_a/20$ (FWHM).]

III. TWO-MODE SQUEEZING

Biasing at a resonance, $2eV_{\rm dc} = \hbar(\omega_a + \omega_b)$, a Josephson-photonics device can create two-mode squeezed states [32,33,36,37]. The two modes can be realized within a single resonator or in two cavities connected in series by the junction, which allows for an easy separation of the emission from

the cavities into two distinct microwave strip lines. A bright and simple quantum source of two-mode squeezed microwave light is of high technological relevance, as it enables applications such as (continuous variable) quantum teleportation [5,6] and quantum illumination protocols proposed as a potential quantum radar [13–17], and many more as explained in the Introduction.

Transforming the two-mode generalization of the Hamiltonian, Eq. (1),

$$\hat{H} = \hbar\omega_a \hat{a}^\dagger \hat{a} + \hbar\omega_b \hat{b}^\dagger \hat{b} - E_J \cos[\omega_{\rm dc} t + \alpha_0(\hat{a}^\dagger + \hat{a}) + \beta_0(\hat{b}^\dagger + \hat{b}) - \varphi_{R_0}], \quad (7)$$

to a frame rotating with frequency Ω, we obtain the RWA Hamiltonian

$$\hat{H}_{\rm RWA} = \hbar\delta \frac{\hat{a}^\dagger \hat{a} + \hat{b}^\dagger \hat{b}}{2} + \frac{E_J^* \alpha_0 \beta_0}{2}(e^{i\psi}\hat{a}^\dagger \hat{b}^\dagger + e^{-i\psi}\hat{a}\hat{b}), \quad (8)$$

where the detuning is $\delta = \omega_a + \omega_b - \Omega = \delta_{\rm dc} + \delta_{\rm ac}$ and $E_J^* = E_J e^{-(\alpha_0^2+\beta_0^2)/2}$. Detunings $\delta_{\rm dc} = \omega_a + \omega_b - \omega_{\rm dc}$ and $\delta_{\rm ac} = \omega_{\rm dc} - \Omega$ are defined analogously to the single-mode case, as is the phase drop across an in-series resistor, φ_{R_0}, and its relation to the Cooper pair current.

Again, in Eq. (8) we only kept those terms of lowest order in the zero-point fluctuations α_0, β_0 relevant for the squeezing and locking physics (see, e.g., Refs. [36,37] and Appendix A 2 for the full Hamiltonian used also for all numerical results below).

Adding a weak ac-locking signal with a frequency Ω close to $\omega_{\rm dc}$ again adds a detuning term to the Hamiltonian

$$\hat{H} = \hat{H}_{\rm RWA} - \varepsilon \frac{E_J^*}{2} \cos\psi \cdot (\alpha_0^2 \hat{a}^\dagger \hat{a} + \beta_0^2 \hat{b}^\dagger \hat{b}). \quad (9)$$

For two-mode squeezing, the applied voltage determines the phase of the common bilinear drive term, $a^\dagger b^\dagger$, corresponding to a sum of phase-space angles for the a and b cavities. Including the resistance and the locking signal, it will be this combined phase which acquires a stochastic dynamics in an effective potential $U(\psi)$, which will diffuse and eventually can be locked. For the Wigner function, $W(X_a, P_a, X_b, P_b)$, expressed in the dimensionless phase space variables ($X_a = \mathrm{Re}\,\alpha$, $P_a = \mathrm{Im}\,\alpha$) and ($X_b, P_b$) of the cavities, this means that the features of an undiffused two-mode squeezed state [20,55], which are destroyed by voltage fluctuations, see Fig. 3(a), can be restored when locking the system to a sufficiently strong ac signal, see dashed lines in Figs. 3(e) and 3(f). Figure 3(d) shows the rotationally symmetric, thermal Wigner distribution of the reduced density matrices for cavity a (and similar for b), and the squeezing ellipses in a combined phase-space of a and b quadratures are shown in Figs. 3(b) and 3(c). The two-mode squeezing drive of the Hamiltonian (8) creates entanglement between the two modes, see dashed line in Fig. 3(f), which, however, is lost due to voltage fluctuations (solid gray line). Increasing the amplitude of the locking signal restores the entanglement measured by the logarithmic negativity, although remaining diffusion around the locking minimum of $U(\psi)$ will lead to some degradation. The proposed locking mechanism thus overcomes a crucial impediment for employing a quantum source lacking phase stability, an inherent drawback of dc-driven devices, for quantum information transfer and processing technologies.

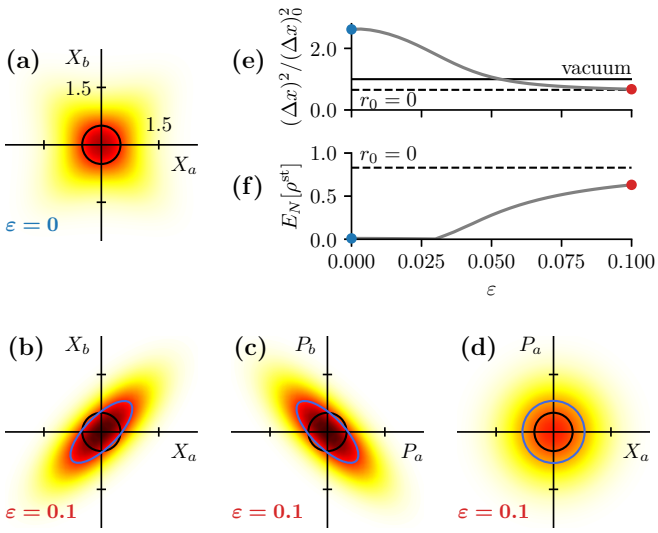

FIG. 3. Phase locking of two-mode squeezed light. (a) Mixed phase space without locking. (b), (c) In mixed phase spaces (X_a, X_b) and (P_a, P_b), the injected ac signal restores the phase coherence of the squeezing ellipse. (d) Still, the coherence vanishes in the reduced phase space of each cavity. (e) The width Δx of the squeezing ellipse decreases below zero-point fluctuations of the vacuum, remaining ultimately limited to 3 dB. (f) Entanglement of photons characterized by the logarithmic negativity E_N is restored. [Parameters: $E_J^* = 80\hbar\gamma_a$, $\alpha_0 = \beta_0 = 0.1$, $\delta_{\rm dc} = 0$, $\nu_0 = 0$, $r_0 = 1/700$, $\gamma_a = \gamma_b$. Rotating frame angles for a and b are chosen, so maximal squeezing appears in the $X_a - X_b$ and $P_a - P_b$ reduced phase spaces.]

IV. BEYOND THE SQUEEZING LIMIT

So far, we have considered the locking of one- and two-mode squeezed states created by a Josephson-photonics device operated in the bilinear regime of the approximated Hamiltonian (4) and (8). These are approximations of more complex normal-ordered Bessel-function terms, e.g., $\hat{a}^2 \to :2\hat{a}^2 J_2(2\alpha_0\sqrt{\hat{n}})/(\alpha_0\sqrt{\hat{n}})^2:$, which are valid if the arguments of the Bessel function $2\alpha_0\sqrt{\hat{n}} \ll 1$, where higher Fock states $|n\rangle$ become relevant, when the effective driving strength $E_J^*\alpha_0^2$ ($E_J^*\alpha_0\beta_0$ for two modes) is increased. Turning now, therefore, to the regime of strongly nonlinear driving of the single-mode device, in particular, to larger zero-point fluctuations α_0, so nonlinearities are becoming pertinent on the few-photon level, the Josephson-photonics dynamics and the locking features change substantially. We first briefly recapitulate the well-studied [40,56–58] effects on the system without resistance and locking signal: In the Hamiltonian, the squeezing terms are amended by higher-order nonlinear corrections terms diagonal in the number basis, which can conveniently be expressed as a series expansion of the normal-ordered Bessel function or as transition matrix elements involving Laguerre polynomials, $\langle n+2|H|n\rangle \propto L_n^{(2)}(\alpha_0^2)$ (see Appendix A 4). For the pure squeezing Hamiltonian (4), the occupation and major axis of the squeezing ellipse diverge for $E_J^*\alpha_0^2/(\hbar\gamma_a) \to 1$. For $\alpha_0 \ll 1$, the nonlinearities of the full Hamiltonian limit this growth and, as the effective driving increases across the

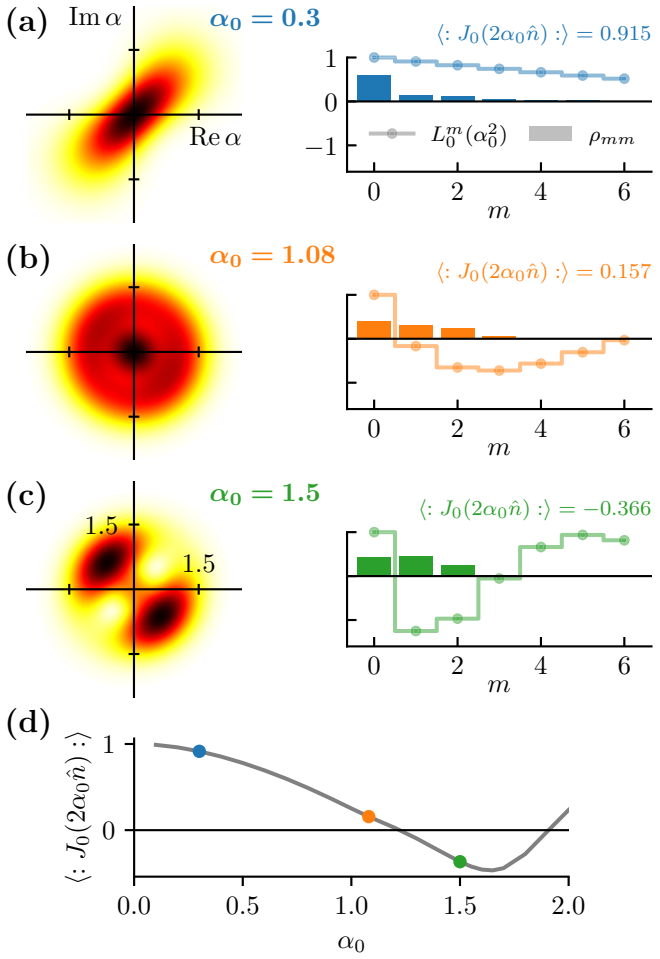

FIG. 4. Beyond the squeezing limit of weak driving and low zero point fluctuations α_0, a nontrivial dependence of the locked Wigner distributions is found upon increasing α_0 is found. This is mainly due to a renormalization of the Shapiro-like effective locking term by Bessel functions $J_0(2\alpha_0\hat{n})$ describing virtual emission and absorption of cavity photons. (a) For moderate zero point fluctuations, the matrix elements of the normal-ordered Bessel functions $L_0^m \sim 1$ for all occupied states and the (slightly deformed) squeezing ellipse is well locked. Increasing α_0, a region without locking potential (b), and (c) an eventual reversal of the potential resulting in a state locked perpendicular to the original orientation is found. The vanishing of the locking potential in (b) does not exactly coincide with the zero of $\langle J_0 \rangle$ due to higher-order correction terms. [Parameters: $\langle \hat{n} \rangle = 1$, $\delta_{\rm dc} = 0$, $r_0 = 1/1000$, $\varepsilon = 0.01$.]

erstwhile divergence, the squeezing ellipse splits into two parts which eventually branch out along a circle [40,58]. Larger α_0 leads to a smoothened crossover and stronger deformations of the ellipsoid, cf. Figs. 4(a) and 4(c).

Adding the ac locking signal to the dc bias, the Hamiltonian, Eq. (4), and the current, Eq. (5), are furthermore modified in similar fashion: Most crucially, the Bessel function J_0 appears in the $\cos\psi$ term in the Hamiltonian and the corresponding $\sin\psi$ term of the current, which describe, as explained above, the renormalization effects of the exchange of photons with the cavity on the $E_J\varepsilon$ processes of ac-assisted Cooper pair tunneling. In addition to this, modification of the term solely responsible for the locking at $\alpha_0 \ll 1$, there appears an additional locking-enabling term $\propto E_J\varepsilon\alpha_0^4\hat{a}^4 +$ H.c. creating higher-order squeezing. To illustrate how the renormalization terms can dramatically modify the locking features, we consider in Fig. 4 three different values of zero point fluctuations and chose corresponding driving strengths, so the average cavity occupation $\langle \hat{n} \rangle = 1.0$. Increasing the zero point fluctuations, we find a transition from locked to unlocked and back to locked with the squeezing axis rotated by $\pi/2$. While this reflects the behavior of the Bessel function $J_0(x)$ moving through its first zero at $x \sim 2\alpha_0\langle \hat{n} \rangle$, for the squeezed state and even more so for the strongly nonlinear squeezing for $\alpha_0 \sim 1$ instead of the mean occupation $\langle \hat{n} \rangle$, the occupation distribution $P(n) = \langle n|\hat{\rho}|n \rangle$ has to be considered, see bars in Fig. 4. Weighting these occupations with the matrix elements $\langle n|e^{i\alpha_0(\hat{a}^\dagger + \hat{a})}|n \rangle$ corresponding to J_0 yields the effective strength and sign of the main locking term, see lines and numerical values in Fig. 4. The newly appearing higher-order squeezing term also contributes and shifts the delocking transition to a slightly smaller α_0 value.

Staying with the single-mode case but reverting to smaller α_0 and the squeezing approximation, we now turn to locking by injecting a microwave directly into the cavity instead of feeding it via the bias line as above.

V. SYMMETRY BREAKING LOCKING

Instead of adding a small ac voltage to the dc bias, locking can also be achieved by coupling an ac oscillation directly to the resonator cavity, e.g., by sending a microwave signal into the strip lines typically used as the output port of the Josephson-photonics device. In general, there are different coupling scenarios, such as inductive or capacitive, corresponding to $\hat{x}_{\rm in} \cdot \hat{x}_a$ or $\hat{p}_{\rm in} \cdot \hat{p}_a$ schemes. Ultimately, any weak bilinear coupling can be described by a linear driving term $\hat{a}_{\rm in} \cdot \hat{a}^\dagger +$ H.c. $\to \alpha_{\rm in} \cdot \hat{a}^\dagger +$ H.c. after rotating-wave approximation and assuming a classical (coherent) drive [59]. As the ac term no longer appears within the cos term of the Josephson-photonics Hamiltonian, higher powers of the oscillations and frequency mixing effects, which appeared above when feeding the ac signal via the bias, are absent now. As a consequence, the ac-locking signal is to be sent with a frequency $\Omega \approx \omega_a \approx \omega_{\rm dc}/2$ close to the cavity emission frequency we want to lock. That locking signal will, however, break the discrete time-translational invariance of the dc drive at the $k = 2$ parametric resonance, $\omega_{\rm dc} \approx k\omega_a$ and the corresponding $\mathbb{Z}^{k=2}$ phase-space symmetry of the squeezing Hamiltonian. Nonetheless, one may aim for a locking signal amplitude small enough, so this symmetry breaking is weak and a largely undisturbed squeezing ellipse with stable phase is restored.

A. Hamiltonian and current

Starting from the purely dc-driven ($\omega_{\rm dc} = 2eV_{\rm dc}/\hbar$) Josephson-photonics Hamiltonian (1) with an additional drive term $\hat{H}_\mu = \varepsilon_\mu \cos(\Omega t + \phi_\mu)(\hat{a} + \hat{a}^\dagger)$ describing a direct microwave injection into the cavity, as in Secs. II and III, we can again consider the limit of small zero-point fluctuations, so the

rotating wave Hamiltonian

$$\hat{H}_{\mathrm{RWA}} \approx \hbar\delta\hat{a}^\dagger\hat{a} + \left[\frac{E_J^*\alpha_0^2}{4}e^{i\psi}\hat{a}^{\dagger 2} + \frac{\varepsilon_\mu}{2}e^{i\phi_\mu}\hat{a}^\dagger + \mathrm{H.c.}\right] \quad (10)$$

results. The approximate Hamiltonian combines the squeezing term, $\propto E_J^*\alpha_0^2\hat{a}^2 + \mathrm{H.c.}$, of the dc drive with a linear term, $\propto \varepsilon_\mu\hat{a} + \mathrm{H.c.}$, from the direct ac drive. Crucially, there are no Shapiro-like terms of $\propto \varepsilon_\mu^2 E_J^*$ form, where dc- and ac-drive exchange excitations and the dominant nonlinear corrections to the approximate Hamiltonian (10) will be the familiar Bessel-functions modifying the squeezing. Similar fundamental differences are found in the expression for the Cooper pair current, which is within rotating-wave approximation found as

$$\frac{\hat{I}_{\mathrm{CP}}}{2e} \approx \frac{E_J^*\alpha_0^2}{\hbar}\frac{1}{4}\left(ie^{-i\psi}\hat{a}^2 - ie^{+i\psi}\hat{a}^{\dagger 2}\right). \quad (11)$$

As in the Hamiltonian, there are no Shapiro-like terms and only the dc-driven squeezing terms of the Hamiltonian appear, as only those terms involve Cooper pair tunneling. Since it is the feedback of this Cooper pair current on the phase ψ of the dc-driving terms which yields locking, not only the dynamics of the cavity state governed by the modified Hamiltonian (10) but also the locking mechanism determined by the current is fundamentally different from the afore-studied scenarios.

B. Breaking the phase-space symmetry

Still, we can proceed in the same manner as above, by first investigating the steady state of the cavity for a fixed ψ, which will then yield the current from which, in turn, the locking potential $U(\psi)$ follows. The first step is, hence, an interesting though simple quantum optics problem of finding the steady state of a damped cavity driven in parallel by a squeezing term, resulting on its own in a squeezing ellipse centered around the origin, and a linear term, which by itself yields a displaced vacuum state. Pursuing the most elegant way to understand how these two driving terms coordinate their emission into a common mode, we remove the linear drive by a shift of the cavity operators, $\hat{a}^{(\dagger)} \to \alpha^{(*)} + \hat{b}^{(\dagger)}$, with a properly chosen α. Clearly, the strength of the squeezing term remains unchanged, so the squeezing ellipse found in the absence of a linear term is merely displaced to a new position α, which depends on the strength and phase of the ac drive, but the ellipse is neither shifted nor rotated, nor is its form changed by the addition of that drive. For the linear term of the Hamiltonian, we obtain, cf. Eq. (A14):

$$\hat{b}^\dagger\left(\frac{\varepsilon_\mu}{2}e^{i\phi_\mu} - i\hbar\frac{\alpha}{2}(\gamma_a + 2i\delta) + \alpha^*\frac{E_J^*\alpha_0^2}{2}e^{i\psi}\right) + \mathrm{H.c.} \quad (12)$$

Finding the proper value of the shift α for which all linear contributions—from performing the transformation in the linear and squeezing terms of the Hamiltonian and in the Lindbladian—cancel, can be mapped to a trigonometric exercise visualized in Fig. 5, where we consider the resonant case, $\delta = 0$, for simplicity and set the phase of the ac drive to zero, $\phi_\mu = 0$. As shown in Appendix A 3, the solutions for $\alpha = |\alpha|e^{i\phi_\alpha}$ describe a circle in the complex plane as ψ is varied. Distinct dependencies of phase ϕ_α, see Fig. 5(b), and amplitude $|\alpha|$ of the shift on ψ are found for squeezing far below and close to the squeezing divergence $E_J^*\alpha_0^2/(\hbar\gamma_a) \to 1$ (the divergence will, of course, again be regularized by higher-order terms in α_0). These can be visually understood as resulting from the circle in Fig. 5(a) remaining far from or approaching the center of the complex plane, but may also easily be investigated analytically (see Appendix A 3).

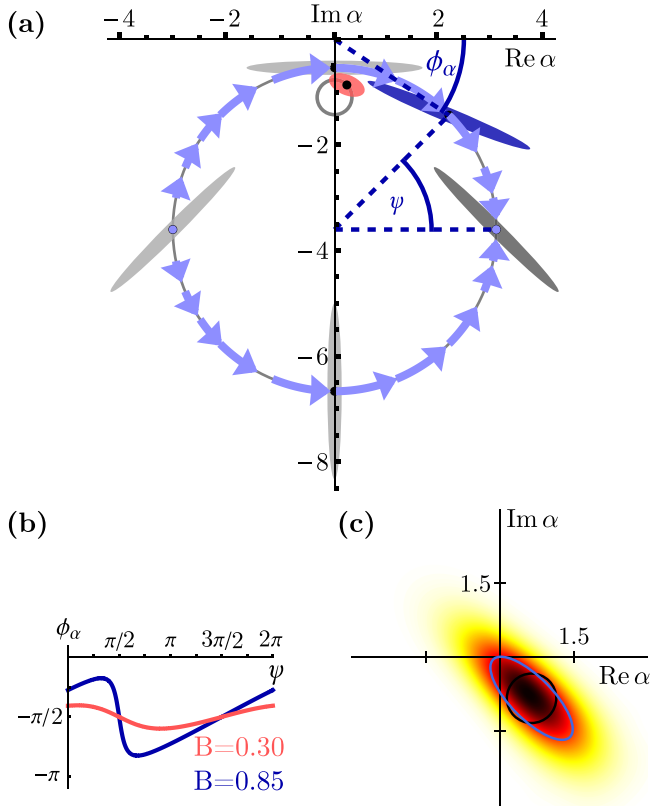

FIG. 5. (a) Sketch of steady-state solutions of a bilinear Hamiltonian with effective squeezing strength $B = E_J^*\alpha_0^2/(\hbar\gamma_a)$ as the phase ψ of the squeezing is varied. The centers of the squeezing ellipses, described by the solutions for $\alpha = |\alpha|e^{i\phi_\alpha}$, are found on a shifted circle. The amount of the shift and the radius of the circle depend on the strengths of the microwave signal and of the squeezing drive [compare Eq. (A17)]. The major ellipse axis rotates with $\psi/2 - \pi/4$. For the large circle shown in blue, the strength and direction of the force $\dot{\psi}$ on the squeezing ellipse caused by the current feedback on ψ are indicated by blue arrows, resulting in the example in a locked solution at $\psi = 0$ [since $\omega_{\mathrm{dc}} = 2\omega_a + \frac{2e}{\hbar}R_0\langle\hat{I}_{\mathrm{CP}}(\psi = 0)\rangle_{\rho(\psi=0)}$ is chosen]. (b) Solutions with a squeezing drive far below the divergence, $B = 0.3 \ll 1$ [cf. the red ellipse on the small circle in (a)], have their phase shift ϕ_α undergoing small near-sinusoidal oscillations around $-\pi/2$, while solutions close to the divergence point with $B = 0.85 \approx 1$ [solutions on the large circle in (a)] have a strong sawtoothlike feature. (c) Wigner density of a squeezed state locked by a symmetry breaking, directly injected ac signal. Shift and rotation are explained by the sketch in (a), while the squeezing below vacuum level (black circle) is indicated by the blue ellipse. [Parameters for (a) and (b): $\epsilon_\mu = \hbar\gamma_a$, $\phi_\mu = 0$, $\Omega = \omega_a$. Parameters for (c): $E_J^* = 80\hbar\gamma_a$, $\alpha_0 = 0.1$, $\varepsilon_\mu = 0.3\hbar\gamma_a$, $r_0 = 1/2000$.]

Having gained a thorough understanding of the quantum optical interplay of linear and squeezing drive and the resulting stationary state $\rho(\psi)$ for a fixed phase ψ of the dc-drive

term,[1] we can now calculate the corresponding Cooper pair current (11), which, while having no obvious counterpart in the generic quantum optics problem, is relevant to the phase dynamics of our problem. Somewhat surprisingly, much of the richness of different regimes and nontrivial behavior of $\alpha(\psi)$ is lost in the current $\langle \hat{I}_{\mathrm{CP}}(\psi)\rangle_{\rho(\psi)}$, which shows simple sinusoidal oscillations scaling with ε_μ^2 around an average. From Fig. 5(a), one can easily guess that (for $\delta = 0 = \phi_\mu$) the current is maximal when the shift of the squeezing ellipse is along its major axis as occurs at the south pole of the circle and minimal on the north pole when it is perpendicular. As the current directly determines the change of ψ, we can easily sketch flow lines on the circle in Fig. 5(a), indicating the stable fixed point where locking will occur. In Fig. 5(c), we show locked solutions of the dynamical simulation governed by the full Hamiltonian (A11) without the $\alpha_0 \ll 1$ approximation, which conforms with the analytical calculation.

VI. CONCLUSION AND OUTLOOK

Squeezed states of light can be created in a microwave cavity by dc biasing a Josephson junction connected in series to it. When applying a dc voltage at the parametric resonance of a single cavity, $2eV_{\mathrm{dc}} \approx 2\hbar\omega_a$, the Josephson junction's nonlinearity will create pairs of photons in that cavity, while in a two-mode setup a resonant bias with $2eV_{\mathrm{dc}} \approx \hbar(\omega_a + \omega_b)$ yields two-mode squeezed states. The squeezed states are reflected in steady-state distributions showing a $\mathbb{Z}^{k=2}$ symmetry in the respective phase space, with a well-defined squeezing angle and a nonzero steady-state expectation value $\langle \hat{a}^2\rangle_{\mathrm{st}}$. Since dc biasing lacks a reference phase, this simple way of creating squeezed light, however, suffers from a phase instability stemming from the voltage noise present in any realistic experimental setup. Here, we first have included a small in-series resistance R_0 in the theory modeling the circuit, which allows us to efficiently simulate the effect of shot noise of Cooper pairs tunneling through the junction. This captures how noise hides many (otherwise experimentally observable) properties of squeezing by effectively averaging over the neutrally stable squeezing angle, resulting in rotationally symmetric phase-space distribution. Second, we have applied injection locking to restore the ideally expected phase-space distributions: two methods of injection locking are possible, either by adding a small ac-voltage signal to the dc drive or by directly injecting a microwave into the cavity. Both methods create an effective sinusoidal potential for the phase-space angle $U(\psi)$, which can be trapped in one of the potential's minima and is thus protected against noise.

For locking via an ac bias, we find that ac-assisted Cooper pair tunneling stabilizes the current in a Shapiro-like manner. The $\mathbb{Z}^{k=2}$ symmetry of the system is protected in this case if the applied signal is also at the parametric resonance, $\hbar\Omega \approx 2eV_{\mathrm{dc}}$. In contrast to the case where the system is biased at the single-photon resonance, where an observable hallmark of locking is the resharpening of the noise-broadened emission spectrum of the cavity, for squeezing even the ideal spectrum is broadened. An experimentally accessible observable of the stabilization of squeezing is the incomplete decay of the phase-phase correlation function $G^{(\phi)}$ to a finite, nonzero expectation value $|\langle \hat{a}^2\rangle_{\mathrm{st}}|^2$. Large zero-point fluctuations of the cavity can drastically change the strength and sign of the created potential. Then, the stabilization of the current by ac-assisted Cooper pair tunneling is strongly modified by the presence of the cavity, which allows an exchange of photons and additionally adds a higher-order squeezing term.

Injection locking through a direct microwave drive, in contrast, will not have Shapiro-like terms. Although breaking the $\mathbb{Z}^{k=2}$ symmetry, the method may be experimentally attractive, as symmetry breaking can be kept small or completely removed by an additional phase-space shift. We conclude that the proposed locking mechanism works with both methods of injection, thus overcoming a crucial impediment for employing dc-driven Josephson-photonics devices, a quantum source lacking phase stability, for quantum information transfer and processing technologies.

Beyond their immediate impact, our results allow more generic conclusions: The model and method applied here for the locking of various squeezed states can immediately be applied to any other phase-sensitive quantum state, which can be created in Josephson-photonics devices by accessing different resonances by the dc bias: e.g., for Schrödinger cat states obtainable at a difference resonance of a two-mode setup [60]. The classical locking theory [61] has very recently been applied to such a scenario [60]. Based on the insights gained here, conclusions on the specifics of the locking mechanism, its efficiency, and parameter dependence can be drawn directly from deriving the RWA Hamiltonian for the respective injection scheme and resonance. Based on our classical investigations [61] and results of Ref. [42] for near coherent states at the fundamental resonance, it is also expected that several Josephson-photonics devices creating squeezed states can mutually synchronize their emission in a completely analogous way in which they lock onto an external ac signal—exemplifying the close relation between the respective universal phenomenological Adler and Kuramoto models [43,52,62,63]. Notably, this would dispense with the need for any external ac generator and allow extremely compact setups. Finally, this paper may give an impulse to investigate feedback locking of a quantum state for other setups lacking an ac drive in completely different platforms, e.g., for optical frequencies.

One more reason why making dc-driven quantum microwaves sources fit for application is so important is their perfect suitability as an on-chip component of a larger integrated device. Proposals for an on-chip coherent source [64] and very recently of a microwave comb [65] emphasize compactness and energy efficiency of such an approach. While overcoming cooling power and refrigerator size restrictions may be immediate advantages, there is also a growing interest in the resource efficiency of quantum information processing devices in general, both for practical and fundamental reasons [66–69]. Requiring only minute ac power for locking or none for synchronization, this paper shows that integrated on-chip sources cannot only yield coherent classical microwave

[1]Notably, it is this interplay alone which leads to locking-type phenomena in recent experiments [24,45] on two-mode devices operated beyond the parametric threshold, which are ac driven and, hence, do not exhibit dynamics of the driving phase and the feedback mechanism discussed here.

radiation but also squeezed states or other phase-sensitive quantum states.

ACKNOWLEDGMENTS

We thank A. Armour, M. Hofheinz, B. Huard, A. Peugeot, T. Aissaoui, and A. Murani for fruitful discussions and acknowledge the support of the Deutsche Forschungsgemeinschaft (DFG, German Research Foundation) through AN336/17-1 and AN336/18-1 and the Bundesministerium für Bildung und Forschung (BMBF) through QSolid.

DATA AVAILABILITY

The data that support the findings of this paper are not publicly available. The data are available from the contact authors upon reasonable request.

APPENDIX A: HAMILTONIANS AND COOPER-PAIR CURRENTS IN ROTATING-WAVE APPROXIMATION

In this Appendix, we provide the derivation for the rotating-wave Hamiltonians and Cooper pair currents for all cases studied in the main text.

1. Single mode: Symmetry-preserving locking

The circuit from Fig. 1, consisting of a single-mode cavity connected in series with a Josephson junction and a resistor R_0, where a voltage bias $V(t) = V_{\rm dc} + V_{\rm ac}\cos(\phi_{ac})$ with $\phi_{ac} = \Omega t + \varphi_{\rm ac}$ is applied, can be described by the Hamiltonian

$$\hat{H}_J = \hbar\omega_a \hat{a}^\dagger\hat{a} - E_J \cos[\varphi_{\rm tot} + \alpha_0(\hat{a}^\dagger + \hat{a}) - \varphi_{R_0}]. \tag{A1}$$

Here, we have defined the total driving phase $\varphi_{\rm tot}(t) = \omega_{\rm dc}t + \varepsilon\sin(\phi_{\rm ac})$ with $\varepsilon = 2eV_{\rm ac}/(\hbar\Omega)$ and $\omega_{\rm dc} = 2eV_{\rm dc}/\hbar$. We assume that the dc voltage is applied at the two-photon resonance $\omega_{\rm dc} \approx 2\omega_a$ and that the frequency of the locking signal is applied at $\Omega \approx \omega_{\rm dc}$. We move to a rotating reference frame defined by the unitary transformation

$$\hat{U}_a = \exp[i\phi_{\rm rot,a}\hat{a}^\dagger\hat{a}] = \exp[i(\omega_{\rm rot,a}t + \phi_a)\hat{a}^\dagger\hat{a}] \tag{A2}$$

and linearize in the locking strength ε. Then, we perform a rotating wave approximation (keeping only slowly oscillating terms), which yields

$$\hat{H}_{\rm RWA} = \hbar(\omega_a - \omega_{\rm rot,a})\hat{a}^\dagger\hat{a} + E_J^*(\hat{h} + \hat{h}^\dagger), \tag{A3}$$

with

$$\begin{aligned}\hat{h}^\dagger = {}& \frac{\alpha_0^2}{4} e^{i[2\phi_{\rm rot,a} - (\omega_{\rm dc}t - \varphi_{R_0})]} : \hat{a}^{\dagger 2} \frac{J_2(2\alpha_0^2\sqrt{\hat{a}^\dagger\hat{a}})\cdot 2}{(\alpha_0\sqrt{\hat{a}^\dagger\hat{a}})^2} : \\ & + \frac{\varepsilon}{4} e^{i[\phi_{\rm ac} - (\omega_{\rm dc}t - \varphi_{R_0})]} : J_0(2\alpha_0\sqrt{\hat{a}^\dagger\hat{a}}) : \\ & - \frac{\varepsilon}{4}\frac{\alpha_0^4}{4!} e^{i[4\phi_{\rm rot,a} - \phi_{\rm ac} - (\omega_{\rm dc}t - \varphi_{R_0})]} : \hat{a}^{\dagger 4} \frac{J_4(2\alpha_0^2\sqrt{\hat{a}^\dagger\hat{a}})\cdot 4!}{(\alpha_0\sqrt{\hat{a}^\dagger\hat{a}})^4} : .\end{aligned} \tag{A4}$$

Here, $E_J^* = E_J \cdot e^{-\alpha_0^2/2}$ is the renormalized Josephson energy and the colons signal normal ordering of operators. Since the Cooper-pair current is defined as

$$\hat{I}_J = I_{\rm crit}\sin[\varphi_{\rm tot} + \alpha_0(\hat{a}^\dagger + \hat{a}) - \varphi_{R_0}] \tag{A5}$$

with the critical current $I_{\rm crit} = 2eE_J/\hbar$, the dc component in rotating wave approximation is

$$\hat{I}_{\rm CP} = \frac{2e}{\hbar} E_J^*(i\hat{h} - i\hat{h}^\dagger). \tag{A6}$$

For small arguments of the Bessel function, we approximate them up to order α_0^2. Then in Eq. (A4), the fraction in the first line can be approximated to **1**, in the second line $J_0(2\alpha_0\sqrt{\hat{a}^\dagger\hat{a}}) \approx \mathbf{1} - \alpha_0^2\hat{a}^\dagger\hat{a}$, and the third line can be neglected as it does not contain terms lower than α_0^4. Choosing $\omega_{{\rm rot},a} = \omega_{\rm dc}$ for $\varepsilon = 0$ yields the Hamiltonian (3) in the main text.

2. Two modes: Symmetry-preserving locking

We now consider two cavities connected in series with a Josephson junction and an additional resistor R_0. We assume that the cavities are non-degenerate $|\omega_a - \omega_b| \gg \gamma_{a/b}$. The circuit is dc biased at the two-mode resonance $\omega_{\rm dc} \approx \omega_a + \omega_b$ and a locking signal with $\Omega \approx \omega_{dc}$ is applied. Starting from the laboratory-frame Hamiltonian

$$\begin{aligned}\hat{H} = {}& \hbar\omega_a\hat{a}^\dagger\hat{a} + \hbar\omega_b\hat{b}^\dagger\hat{b} - E_J\cos[\varphi_{\rm tot} + \alpha_0(\hat{a}^\dagger + \hat{a}) \\ & + \beta_0(\hat{b}^\dagger + \hat{b}) - \varphi_{R_0}],\end{aligned} \tag{A7}$$

we again move to a rotating frame with $\hat{U} = \hat{U}_a \otimes \hat{U}_b$ (with $\omega_{\rm rot,a} + \omega_{\rm rot,b} = \omega_{\rm rot,tot}$ such that $\omega_{{\rm rot,a/b}} \approx \omega_{a/b}$). Then, only the sum of the (single-space) rotating frame frequencies is fixed and we choose $\delta = \omega_a - \omega_{\rm rot,a} = \omega_b - \omega_{\rm rot,b}$. We define

$$\begin{aligned}\hat{h}^\dagger = {}& \frac{\alpha_0\beta_0}{2} e^{i[\phi_{\rm rot,a} + \phi_{\rm rot,b} - (\omega_{\rm dc}t - \varphi_{R_0})]} : \hat{a}^\dagger\hat{b}^\dagger \frac{J_1(2\alpha_0\sqrt{\hat{a}^\dagger\hat{a}})}{\alpha_0\sqrt{\hat{a}^\dagger\hat{a}}} \frac{J_1(2\beta_0\sqrt{\hat{b}^\dagger\hat{b}})}{\beta_0\sqrt{\hat{b}^\dagger\hat{b}}} : \\ & + \frac{\varepsilon}{4} e^{i[\phi_{ac} - (\omega_{\rm dc}t - \varphi_{R_0})]} : J_0(2\alpha_0\sqrt{\hat{a}^\dagger\hat{a}}) J_0(2\beta_0\sqrt{\hat{b}^\dagger\hat{b}}) : \\ & - \frac{\varepsilon}{4}\frac{\alpha_0^2\beta_0^2}{4} e^{i[2\phi_{\rm rot,a} + 2\phi_{\rm rot,b} - \phi_{ac} - (\omega_{\rm dc}t - \varphi_{R_0})]} : \hat{a}^{\dagger 2}\hat{b}^{\dagger 2} \frac{J_2(2\alpha_0\sqrt{\hat{a}^\dagger\hat{a}})\cdot 2}{(\alpha_0\sqrt{\hat{a}^\dagger\hat{a}})^2} \frac{J_2(2\beta_0\sqrt{\hat{b}^\dagger\hat{b}})\cdot 2}{(\beta_0\sqrt{\hat{b}^\dagger\hat{b}})^2} :\end{aligned} \tag{A8}$$

and then find in rotating wave approximation

$$\hat{H}_{\rm RWA} = \hbar\delta\frac{\hat{a}^\dagger\hat{a} + \hat{b}^\dagger\hat{b}}{2} + E_J^*(\hat{h} + \hat{h}^\dagger), \tag{A9}$$

$$\hat{I}_{\rm CP} = \frac{2e}{\hbar} E_J^*(i\hat{h} - i\hat{h}^\dagger), \tag{A10}$$

where now $E_J^* = E_J e^{-(\alpha_0^2+\beta_0^2)/2}$. Keeping only maximally quadratic powers of zero-point fluctuations, we can neglect the fractions of Bessel functions in the first term and the complete last term of (A8), while approximating $:J_0(2\alpha_0\sqrt{\hat{a}^\dagger\hat{a}})J_0(2\beta_0\sqrt{\hat{b}^\dagger\hat{b}}):\approx \mathbf{1}-\alpha_0^2\hat{a}^\dagger\hat{a}-\beta_0^2\hat{b}^\dagger\hat{b}$.

3. Single mode: Symmetry-breaking locking

We consider a single mode biased at the two-photon resonance $\omega_{\rm dc}\approx 2\omega_a$ of a dc-biased Josephson photonics circuit, similar to Fig. 1 in the main text. Now, however, the locking signal is not applied by an ac voltage but is directly injected as a microwave locking signal with an additional drive term $\hat{H}_\mu = \varepsilon_\mu\cos(\Omega t+\phi_\mu)\cdot(\hat{a}^\dagger+\hat{a})$ with effective strength ε_μ and frequency $\Omega\approx\omega_a$ into the cavity. The constant phase ϕ_μ is determined by the coupling of the injected microwave signal. With an analogous rotating-frame transformation with $\omega_{\rm rot,a}=\Omega$ and rotating wave approximation as in Appendix A 1, we find

$$\hat{H}_{\rm RWA} = \hbar(\omega_a-\Omega)+\left[E_J^*\hat{h}^\dagger+\frac{\varepsilon_\mu}{2}e^{i\phi_\mu}\hat{a}^\dagger+\text{H.c.}\right], \quad \text{(A11)}$$

with

$$\hat{h}^\dagger = \frac{\alpha_0^2}{4}e^{i[2\phi_{\rm rot,a}-(\omega_{\rm dc}t-\varphi_{R_0})]}:\hat{a}^{\dagger 2}\frac{J_2(2\alpha_0^2\sqrt{\hat{a}^\dagger\hat{a}})\cdot 2}{(\alpha_0\sqrt{\hat{a}^\dagger\hat{a}})^2}:. \quad \text{(A12)}$$

We can apply an operator transformation $\hat{a}=\alpha\mathbf{1}+\hat{b}$, which is effectively a constant shift of the phase space. If the cavity is coherently driven and damped ($E_J=0$), its steady state will be a coherent state (which is a displaced vacuum state) with steady-state amplitude $\langle a\rangle_{\rm st}$. An operator transformation with $\alpha=\langle\hat{a}\rangle_{\rm st}$ effectively shifts the center of the phase-space to $\langle\hat{a}\rangle_{\rm st}$. Under this transformation, mode $\hat{b}$ is undriven and damped, yielding a vacuum state as a steady state.

In the limit of small Bessel function argument, the Hamiltonian can be approximated to

$$\hat{H}_{\rm RWA}\approx\hbar\delta\hat{a}^\dagger\hat{a}+\left[\frac{E_J^*\alpha_0^2}{4}e^{i\psi}\hat{a}^{\dagger 2}+\frac{\varepsilon_\mu}{2}e^{i\phi_\mu}\hat{a}^\dagger+\text{H.c.}\right], \quad \text{(A13)}$$

where $\delta=\omega_a-\Omega$ and $\psi=2\phi_{\rm rot,a}-(\omega_{\rm dc}t-\varphi_{R_0})$. This bilinear system consists of a Hamiltonian with a squeezing drive and coherent drive, amended by a Lindblad operator $\hat{L}_0=\sqrt{\gamma_a}\hat{a}$. It can be solved analytically for constant ψ. If the same operator transformation is applied, the system is analogously described by a Hamiltonian

$$\begin{aligned}\hat{H}_{\rm RWA}\approx{}&\hbar\delta\hat{b}^\dagger\hat{b}+\frac{E_J^*\alpha_0^2}{4}(e^{-i\psi}\hat{b}^2+e^{+i\psi}\hat{b}^{\dagger 2})\\&+\left[\hat{b}^\dagger\left(\frac{\varepsilon_\mu}{2}e^{i\phi_\mu}-i\hbar\frac{\alpha}{2}(\gamma_a+2i\delta)\right.\right.\\&\left.\left.+\alpha^*\frac{E_J^*\alpha_0^2}{2}e^{i\psi}\right)+\text{H.c.}\right]\end{aligned} \quad \text{(A14)}$$

and a Lindblad operator $\hat{L}_b=\sqrt{\gamma_a}\hat{b}$. The linear drive term vanishes if

$$\varepsilon_\mu e^{i\phi_\mu} = i\hbar\gamma_a\alpha\frac{\gamma_a+2i\delta}{\gamma_a}-\alpha^*E_J^*\alpha_0^2e^{i\psi}. \quad \text{(A15)}$$

Again, the condition is fulfilled for the steady-state solution, $\alpha=\langle\hat{a}\rangle_{\rm st}$. Then, mode $\hat{b}$ behaves like a squeezed damped single mode and the Cooper-pair current can be described by

$$\hat{I}_{\rm CP}\approx\frac{2e}{\hbar}\frac{E_J^*\alpha_0^2}{4}ie^{-i\psi}(\hat{b}^2+\alpha^2\mathbf{1})+\text{H.c}. \quad \text{(A16)}$$

If, e.g.. $\delta=0$, we find

$$\alpha = r_{\rm c}e^{i(\phi_\mu-\pi/2)}+r_{\rm ell}e^{i(\psi-\phi_\mu)}. \quad \text{(A17)}$$

Varying ψ, the squeezing ellipse of mode $\hat{b}$ performs a circular motion $e^{i(\psi-\phi_\mu)}$ with radius

$$r_{\rm ell} = \frac{\frac{\varepsilon_\mu}{\hbar\gamma_a}}{1-\left(\frac{E_J^*\alpha_0^2}{\hbar\gamma_a}\right)^2}\frac{E_J^*\alpha_0^2}{\hbar\gamma_a} \quad \text{(A18)}$$

about a new center shifted by the amount

$$r_{\rm c} = \frac{\frac{\varepsilon_\mu}{\hbar\gamma_a}}{1-\left(\frac{E_J^*\alpha_0^2}{\hbar\gamma_a}\right)^2}. \quad \text{(A19)}$$

The orientation of the ellipse (direction of the major axis) is $\phi_{\rm ell}=\psi/2-\pi/4$.

4. Matrix elements of normal-ordered Bessel functions

Using the series expansion of Bessel functions and the properties of the creation and annihilation operators, we find for $k,n\in\mathbf{N}_0$ the only nonzero matrix elements

$$\langle n+k|:\hat{a}^{\dagger k}\cdot\frac{J_k(2\alpha_0\sqrt{\hat{a}^\dagger\hat{a}})\cdot k!}{(\alpha_0\sqrt{\hat{a}^\dagger\hat{a}})^k}:|n\rangle = \sqrt{\frac{(n+k)!}{n!}}\cdot\frac{L_n^{(k)}(\alpha_0^2)}{L_n^{(k)}(0)}. \quad \text{(A20)}$$

An applied dc voltage with $\omega_{\rm dc}\approx 2\omega_a$ then, e.g., drives the two-photon transition, where in the Hamiltonian matrix elements $\langle n+2|\hat{H}|n\rangle$ the nonlinear effect of the zero-point fluctuations is expressed by Laguerre polynomials $L_n^{(2)}(\alpha_0^2)$.

APPENDIX B: TWO-TIME PERTURBATION THEORY

In Ref. [42], two-time perturbation theory was utilized to obtain an equation of motion for the reduced dynamics of the phase ψ. Here we want to extend this approach to calculate the full quantum state of the system and to obtain two-time correlation functions.

1. Reduced dynamics of the phase

As the dynamics of the cavity and the phase ψ takes place on two separate timescales given by γ_a and $r_0\gamma_a$, we explicitly introduce the fast time t and the slow time $\tau=r_0t$. In the limit $t\to\infty$ where fast oscillator dynamics have already relaxed, the time evolution of the system is given by

$$r_0\partial_\tau|\rho(\tau,\psi)\rangle\rangle = \Lambda(\psi)|\rho(\tau,\psi)\rangle\rangle, \quad \text{(B1)}$$

with the generator of the time evolution $\Lambda(\psi)=\mathcal{L}+r_0\partial_\psi\Lambda^{(1)}+\mathcal{O}(r_0^2)$, where $\mathcal{L}$ is the Liouvillian of the system and $\Lambda^{(1)}=\delta_{\rm ac}/r_0-2\pi\hat{I}_{\rm CP}/(2e)$. By expanding $|\rho(\tau,\psi)\rangle\rangle=\sum_{l=0}^\infty r_0^l\hat{\rho}^{(l)}$, we can solve (B1) order by order in r_0. Accordingly, we define $P(\tau,\psi)=\sum_{l=0}^\infty r_0^lP^{(l)}(\tau,\psi)=$

$\sum_{l=0}^{\infty} r_0^l \operatorname{tr} \hat{\rho}^{(l)}(\tau, \psi)$. In *zeroth order*, we find

$$0 = \mathcal{L}(\psi)|\rho^{(0)}(\tau, \psi)\rangle\rangle, \tag{B2}$$

which determines $\hat{\rho}^{(0)}(\tau, \psi) = P^{(0)}(\tau, \psi)\hat{\rho}_{\mathrm{eq}}(\psi)$ up to the unknown factor $P^{(0)}(\tau, \psi)$ with $\operatorname{tr} \hat{\rho}_{\mathrm{eq}}(\psi) = 1$.

To find $P^{(0)}(\tau, \psi)$, we consider the *first order* equation

$$\begin{aligned}\partial_\tau |\rho^{(0)}(\tau, \psi)\rangle\rangle &= \mathcal{L}(\psi)|\rho^{(1)}(\tau, \psi)\rangle\rangle \\ &\quad + r_0 \partial_\psi [\Lambda^{(1)}(\psi)|\rho^{(0)}(\tau, \psi)\rangle\rangle].\end{aligned} \tag{B3}$$

Taking the trace, i.e., multiplying $\langle\langle 1|$ from the left, we find the desired equation of motion

$$\partial_\tau P^{(0)}(\tau, \psi) = r_0 \partial_\psi [\langle\langle 1|\Lambda^{(1)}(\psi)|\rho_{\mathrm{eq}}(\psi)\rangle\rangle P^{(0)}(\tau, \psi)]. \tag{B4}$$

We note that we did not extract the full information of (B3) by taking its trace. To do so, we define $\mathcal{R}$ as the pseudoinverse of $\mathcal{L}$, i.e., $\mathcal{R} = (\mathcal{L} + \mathcal{R})^{-1} - \mathcal{P}$ with $\mathcal{P} = |\rho_{\mathrm{eq}}\rangle\rangle\langle\langle 1|$, whereby

$$\mathcal{L}\mathcal{R} = \mathcal{R}\mathcal{L} = \mathcal{Q} \tag{B5}$$

with $\mathcal{Q} = \mathbf{1} - \mathcal{P}$ applies. Then, multiplying (B3) with $\mathcal{R}$ from the left yields

$$0 = \mathcal{R}\mathcal{L}|\rho^{(1)}\rangle\rangle + r_0 \mathcal{R}\partial_\psi(\Lambda^{(1)}|\rho^{(0)}\rangle\rangle) \tag{B6}$$

and, equivalently,

$$\mathcal{Q}|\rho^{(1)}\rangle\rangle = -r_0 \mathcal{R}\partial_\psi(\Lambda^{(1)}|\rho^{(0)}\rangle\rangle), \tag{B7}$$

which we will need for the full reconstruction of the quantum state.

As shown in Ref. [42], the *second order* of (B1) yields a Fokker-Planck equation for $P(\psi) \approx P^{(0)}(\tau, \psi) + r_0 P^{(1)}(\tau, \psi)$,

$$\partial_\tau P(\tau, \psi) = -\partial_\psi [j(\psi)P(\tau, \psi)] + \partial_\psi^2 [D(\psi)P(\tau, \psi)], \tag{B8}$$

with

$$j^{(0)}(\psi) = -r_0 \langle\langle 1|\Lambda^{(1)}|\rho_{\mathrm{eq}}\rangle\rangle, \tag{B9a}$$

$$j^{(1)}(\psi) = -r_0 \langle\langle 1|\partial_\psi(\Lambda^{(1)}\mathcal{R})\Lambda^{(1)}|\rho_{\mathrm{eq}}\rangle\rangle, \tag{B9b}$$

$$D(\psi) = -r_0^2 \langle\langle 1|\Lambda^{(1)}\mathcal{R}\Lambda^{(1)}|\rho_{\mathrm{eq}}\rangle\rangle, \tag{B9c}$$

containing shot noise of the Cooper pair current [70].

2. Reconstruction of the state

Now we want to go one step further and find the full density matrix $\hat{\rho}(\tau) = \int_0^{2\pi} \mathrm{d}\psi\, \hat{\rho}(\tau, \psi)$. In zeroth order, we have

$$|\rho^{(0)}(\tau, \psi)\rangle\rangle = P^{(0)}(\tau, \psi)|\rho_{\mathrm{eq}}(\psi)\rangle\rangle \tag{B10}$$

in the first order:

$$\begin{aligned}|\rho^{(1)}(\tau, \psi)\rangle\rangle &= (\mathcal{P}(\psi) + \mathcal{Q}(\psi))|\rho^{(1)}(\tau, \psi)\rangle\rangle \\ &= |\rho_{\mathrm{eq}}(\psi)\rangle\rangle\langle\langle 1|\rho^{(1)}(\tau, \psi)\rangle\rangle \\ &\quad + \mathcal{Q}(\psi)|\rho^{(1)}(\tau, \psi)\rangle\rangle \\ &= P^{(1)}(\tau, \psi)|\rho_{\mathrm{eq}}(\psi)\rangle\rangle - r_0 \mathcal{R}(\psi) \\ &\quad \times \partial_\psi(\Lambda^{(1)}(\psi)|\rho^{(0)}(\tau, \psi)\rangle\rangle).\end{aligned} \tag{B11}$$

Summing up both orders, we obtain

$$\begin{aligned}|\rho(\tau, \psi)\rangle\rangle &\approx |\rho^{(0)}(\tau, \psi)\rangle\rangle + r_0|\rho^{(1)}(\tau, \psi)\rangle\rangle \\ &= P(\tau, \psi)|\rho_{\mathrm{eq}}(\psi)\rangle\rangle \\ &\quad - r_0 \mathcal{R}(\psi)\partial_\psi(\Lambda^{(1)}(\psi)P(\tau, \psi)|\rho_{\mathrm{eq}}(\psi)\rangle\rangle).\end{aligned} \tag{B12}$$

3. Fast timescale dynamics and two-time correlation functions

In zeroth order of r_0, the fast timescale dynamics is given by

$$\partial_t |\rho_{\mathrm{eq}}(t, \psi)\rangle\rangle = \Lambda^{(0)}(\psi)|\rho_{\mathrm{eq}}(t, \psi)\rangle\rangle, \tag{B13}$$

which yields the full density matrix of the system

$$\hat{\rho}(t, \psi) = P(\tau, \psi)\hat{\rho}_{\mathrm{eq}}(t, \psi), \tag{B14}$$

where $P(\tau, \psi)$ is evolved via the Fokker-Planck equation (B8).

To calculate two-time correlation functions, we make use of the quantum regression theorem

$$\langle \hat{B}(t_2)\hat{A}(t_1)\rangle = \int_0^{2\pi} \mathrm{d}\psi \operatorname{tr}\{\hat{B}[\hat{A}\hat{\rho}(t_1, \psi)]_{t_2}\}. \tag{B15}$$

To evolve the matrix $\hat{A}\rho(t_1, \psi)$ to t_2, we first normalize it,

$$\hat{\rho}'(t_1, \psi) = \frac{\hat{A}\hat{\rho}(t_1, \psi)}{\operatorname{tr}[\hat{A}\hat{\rho}(t_1, \psi)]}, \tag{B16}$$

and define

$$P'(t_1, \psi) = \operatorname{tr}[\hat{A}\hat{\rho}(t_1, \psi)], \tag{B17}$$

which is not real, in general. Then we evolve P' with the Fokker-Planck equation and ρ' according to (B13) and get

$$\langle \hat{B}(t_2)\hat{A}(t_1)\rangle = \int_0^{2\pi} \mathrm{d}\psi \operatorname{tr}[\hat{B}P'(t_2, \psi)\hat{\rho}'(t_2, \psi)]. \tag{B18}$$

The time evolution of P' is a diffusion process in the complex plane.

[1] M. Xiao, L.-A. Wu, and H. J. Kimble, Precision measurement beyond the shot-noise limit, Phys. Rev. Lett. **59**, 278 (1987).

[2] P. Grangier, R. E. Slusher, B. Yurke, and A. LaPorta, Squeezed-light–enhanced polarization interferometer, Phys. Rev. Lett. **59**, 2153 (1987).

[3] L. Barsotti, J. Harms, and R. Schnabel, Squeezed vacuum states of light for gravitational wave detectors, Rep. Prog. Phys. **82**, 016905 (2019).

[4] M. Casariego, E. Z. Cruzeiro, S. Gherardini, T. Gonzalez-Raya, R. André, G. Frazão, G. Catto, M. Möttönen, D. Datta, K. Viisanen, J. Govenius, M. Prunnila, K. Tuominen, M. Reichert, M. Renger, K. G. Fedorov, F. Deppe, H. van der Vliet, A. J. Matthews, Y. Fernández *et al.*, Propagating quantum microwaves: towards applications in communication and sensing, Quantum Sci. Technol. **8**, 023001 (2023).

[5] R. Di Candia, K. Fedorov, L. Zhong, S. Felicetti, E. Menzel, M. Sanz, F. Deppe, A. Marx, R. Gross, and E. Solano, Quantum teleportation of propagating quantum microwaves, EPJ Quantum Technol. **2**, 25 (2015).

[6] K. G. Fedorov, M. Renger, S. Pogorzalek, R. Di Candia, Q. Chen, Y. Nojiri, K. Inomata, Y. Nakamura, M. Partanen, A. Marx *et al.*, Experimental quantum teleportation of propagating microwaves, Sci. Adv. **7**, eabk0891 (2021).

[7] T. Gonzalez-Raya, M. Casariego, F. Fesquet, M. Renger, V. Salari, M. Möttönen, Y. Omar, F. Deppe, K. G. Fedorov, and M. Sanz, Open-air microwave entanglement distribution for quantum teleportation, Phys. Rev. Appl. **18**, 044002 (2022).

[8] F. Fesquet, F. Kronowetter, M. Renger, W. K. Yam, S. Gandorfer, K. Inomata, Y. Nakamura, A. Marx, R. Gross, and K. G. Fedorov, Demonstration of microwave single-shot quantum key distribution, Nat. Commun. **15**, 7544 (2024).

[9] F. Fesquet, F. Kronowetter, M. Renger, Q. Chen, K. Honasoge, O. Gargiulo, Y. Nojiri, A. Marx, F. Deppe, R. Gross *et al.*, Perspectives of microwave quantum key distribution in the open air, Phys. Rev. A **108**, 032607 (2023).

[10] F. Kronowetter, F. Fesquet, M. Renger, K. Honasoge, Y. Nojiri, K. Inomata, Y. Nakamura, A. Marx, R. Gross, and K. G. Fedorov, Quantum microwave parametric interferometer, Phys. Rev. Appl. **20**, 024049 (2023).

[11] S. Lloyd, Enhanced sensitivity of photodetection via quantum illumination, Science **321**, 1463 (2008).

[12] S.-H. Tan, B. I. Erkmen, V. Giovannetti, S. Guha, S. Lloyd, L. Maccone, S. Pirandola, and J. H. Shapiro, Quantum illumination with gaussian states, Phys. Rev. Lett. **101**, 253601 (2008).

[13] A. Karsa, A. Fletcher, G. Spedalieri, and S. Pirandola, Quantum illumination and quantum radar: A brief overview, Rep. Prog. Phys. **87**, 094001 (2024).

[14] R. Assouly, R. Dassonneville, T. Peronnin, A. Bienfait, and B. Huard, Quantum advantage in microwave quantum radar, Nat. Phys. **19**, 1418 (2023).

[15] C. W. S. Chang, A. M. Vadiraj, J. Bourassa, B. Balaji, and C. M. Wilson, Quantum-enhanced noise radar, Appl. Phys. Lett. **114**, 112601 (2019).

[16] N. Messaoudi, C. S. Chang, A. Vadiraj, C. Wilson, J. Bourassa, and B. Balaji, Practical advantage in microwave quantum illumination, in *2020 IEEE Radar Conference (RadarConf20), Florence, Italy* (IEEE, Piscataway, NJ, 2020), pp. 1–5.

[17] S. Barzanjeh, S. Pirandola, D. Vitali, and J. M. Fink, Microwave quantum illumination using a digital receiver, Sci. Adv. **6**, eabb0451 (2020).

[18] F. Bischeltsrieder, M. Würth, J. Russer, M. Peichl, and W. Utschick, Engineering constraints and application regimes of quantum radar, IEEE Trans. Radar Syst. **2**, 197 (2024).

[19] N. Didier, J. Guillaud, S. Shankar, and M. Mirrahimi, Remote entanglement stabilization and concentration by quantum reservoir engineering, Phys. Rev. A **98**, 012329 (2018).

[20] C. Eichler, D. Bozyigit, C. Lang, M. Baur, L. Steffen, J. M. Fink, S. Filipp, and A. Wallraff, Observation of two-mode squeezing in the microwave frequency domain, Phys. Rev. Lett. **107**, 113601 (2011).

[21] N. Bergeal, F. Schackert, L. Frunzio, and M. H. Devoret, Two-mode correlation of microwave quantum noise generated by parametric down-conversion, Phys. Rev. Lett. **108**, 123902 (2012).

[22] E. Flurin, N. Roch, F. Mallet, M. H. Devoret, and B. Huard, Generating entangled microwave radiation over two transmission lines, Phys. Rev. Lett. **109**, 183901 (2012).

[23] L. Zhong, E. P. Menzel, R. Di Candia, P. Eder, M. Ihmig, A. Baust, M. Haeberlein, E. Hoffmann, K. Inomata, T. Yamamoto *et al.*, Squeezing with a flux-driven Josephson parametric amplifier, New J. Phys. **15**, 125013 (2013).

[24] I.-M. Svensson, A. Bengtsson, J. Bylander, V. Shumeiko, and P. Delsing, Period multiplication in a parametrically driven superconducting resonator, Appl. Phys. Lett. **113**, 022602 (2018).

[25] X. Gu, A. F. Kockum, A. Miranowicz, Y.-x. Liu, and F. Nori, Microwave photonics with superconducting quantum circuits, Phys. Rep. **718–719**, 1 (2017).

[26] W. Wustmann and V. Shumeiko, Parametric effects in circuit quantum electrodynamics, Low Temp. Phys. **45**, 848 (2019).

[27] M. Hofheinz, F. Portier, Q. Baudouin, P. Joyez, D. Vion, P. Bertet, P. Roche, and D. Estève, Bright side of the Coulomb blockade, Phys. Rev. Lett. **106**, 217005 (2011).

[28] F. Chen, J. Li, A. D. Armour, E. Brahimi, J. Stettenheim, A. J. Sirois, R. W. Simmonds, M. P. Blencowe, and A. J. Rimberg, Realization of a single-Cooper-pair Josephson laser, Phys. Rev. B **90**, 020506(R) (2014).

[29] M. C. Cassidy, A. Bruno, S. Rubbert, M. Irfan, J. Kammhuber, R. N. Schouten, A. R. Akhmerov, and L. P. Kouwenhoven, Demonstration of an ac Josephson junction laser, Science **355**, 939 (2017).

[30] V. Gramich, B. Kubala, S. Rohrer, and J. Ankerhold, From Coulomb-blockade to nonlinear quantum dynamics in a superconducting circuit with a resonator, Phys. Rev. Lett. **111**, 247002 (2013).

[31] A. D. Armour, M. P. Blencowe, E. Brahimi, and A. J. Rimberg, Universal quantum fluctuations of a cavity mode driven by a Josephson junction, Phys. Rev. Lett. **111**, 247001 (2013).

[32] M. Westig, B. Kubala, O. Parlavecchio, Y. Mukharsky, C. Altimiras, P. Joyez, D. Vion, P. Roche, D. Esteve, M. Hofheinz, M. Trif, P. Simon, J. Ankerhold, and F. Portier, Emission of nonclassical radiation by inelastic Cooper pair tunneling, Phys. Rev. Lett. **119**, 137001 (2017).

[33] A. Peugeot, G. Ménard, S. Dambach, M. Westig, B. Kubala, Y. Mukharsky, C. Altimiras, P. Joyez, D. Vion, P. Roche *et al.*, Generating two continuous entangled microwave beams using a dc-biased Josephson junction, Phys. Rev. X **11**, 031008 (2021).

[34] C. Padurariu, F. Hassler, and Y. V. Nazarov, Statistics of radiation at Josephson parametric resonance, Phys. Rev. B **86**, 054514 (2012).

[35] J. Leppäkangas, G. Johansson, M. Marthaler, and M. Fogelström, Nonclassical photon pair production in a voltage-biasedJosephson junction, Phys. Rev. Lett. **110**, 267004 (2013).

[36] A. D. Armour, B. Kubala, and J. Ankerhold, Josephson photonics with a two-mode superconducting circuit, Phys. Rev. B **91**, 184508 (2015).

[37] M. Trif and P. Simon, Photon cross-correlations emitted by a Josephson junction in two microwave cavities, Phys. Rev. B **92**, 014503 (2015).

[38] C. Rolland, A. Peugeot, S. Dambach, M. Westig, B. Kubala, Y. Mukharsky, C. Altimiras, H. le Sueur, P. Joyez, D. Vion, P. Roche, D. Esteve, J. Ankerhold, and F. Portier, Antibunched photons emitted by a dc-biased Josephson junction, Phys. Rev. Lett. **122**, 186804 (2019).

[39] A. Grimm, F. Blanchet, R. Albert, J. Leppäkangas, S. Jebari, D. Hazra, F. Gustavo, J.-L. Thomassin, E. Dupont-Ferrier, F. Portier, and M. Hofheinz, Bright on-demand source of anti-bunched microwave photons based on inelastic Cooper pair tunneling, Phys. Rev. X **9**, 021016 (2019).

[40] G. C. Ménard, A. Peugeot, C. Padurariu, C. Rolland, B. Kubala, Y. Mukharsky, Z. Iftikhar, C. Altimiras, P. Roche, H. le Sueur, P. Joyez, D. Vion, D. Esteve, J. Ankerhold, and F. Portier, Emission of photon multiplets by a dc-biased superconducting circuit, Phys. Rev. X **12**, 021006 (2022).

[41] H. Wang, M. P. Blencowe, A. D. Armour, and A. J. Rimberg, Quantum dynamics of aJosephson junction driven cavity mode system in the presence of voltage bias noise, Phys. Rev. B **96**, 104503 (2017).

[42] F. Höhe, L. Danner, C. Padurariu, B. I. C. Donvil, J. Ankerhold, and B. Kubala, Quantum synchronization in presence of shot noise, New J. Phys. **27**, 023039 (2025).

[43] A. Pikovsky, M. Rosenblum, and J. Kurths, *Synchronization: A Universal Concept in Nonlinear Sciences*, Cambridge Nonlinear Science Series (Cambridge University Press, New York, 2001).

[44] A. Bengtsson, P. Krantz, M. Simoen, I.-M. Svensson, B. Schneider, V. Shumeiko, P. Delsing, and J. Bylander, Nondegenerate parametric oscillations in a tunable superconducting resonator, Phys. Rev. B **97**, 144502 (2018).

[45] D. Marković, J.-D. Pillet, E. Flurin, N. Roch, and B. Huard, Injection locking and parametric locking in a superconducting circuit, Phys. Rev. Appl. **12**, 024034 (2019).

[46] C. Xu and M. G. Vavilov, Full counting statistics of photons emitted by a double quantum dot, Phys. Rev. B **88**, 195307 (2013).

[47] S. Shapiro, Josephson currents in superconducting tunneling: The effect of microwaves and other observations, Phys. Rev. Lett. **11**, 80 (1963).

[48] H. A. Kramers, Brownian motion in a field of force and the diffusion model of chemical reactions, Physica **7**, 284 (1940).

[49] H. Risken, *The Fokker-Planck equation* (Springer, Berlin, 1996).

[50] B. Donvil, P. Muratore-Ginanneschi, J. P. Pekola, and K. Schwieger, Model for calorimetric measurements in an open quantum system, Phys. Rev. A **97**, 052107 (2018).

[51] G. Pavliotis and A. Stuart, *Multiscale Methods: Averaging and Homogenization*, Texts in Applied Mathematics (Springer, New York, 2008).

[52] R. Adler, A study of locking phenomena in oscillators, Proc. IRE **34**, 351 (1946).

[53] S. Dambach, B. Kubala, V. Gramich, and J. Ankerhold, Time-resolved statistics of nonclassical light in Josephson photonics, Phys. Rev. B **92**, 054508 (2015).

[54] C. W. Gardiner and P. Zoller, *Quantum Noise. A Handbook of Markovian and Non-Markovian Quantum Stochastic Methods with Applications to Quantum Optics*, Springer Series in Synergetics (Springer-Verlag, Berlin, 2000), Vol. 2.

[55] K. G. Fedorov, S. Pogorzalek, U. Las Heras, M. Sanz, P. Yard, P. Eder, M. Fischer, J. Goetz, E. Xie, K. Inomata *et al.*, Finite-time quantum entanglement in propagating squeezed microwaves, Sci. Rep. **8**, 6416 (2018).

[56] B. Kubala, V. Gramich, and J. Ankerhold, Non-classical light from superconducting resonators coupled to voltage-biased Josephson junctions, Phys. Scr. **T165**, 014029 (2015).

[57] B. Kubala, J. Ankerhold, and A. D. Armour, Electronic and photonic counting statistics as probes of non-equilibrium quantum dynamics, New J. Phys. **22**, 023010 (2020).

[58] B. Lang and A. D. Armour, Multi-photon resonances in Josephson junction-cavity circuits, New J. Phys. **23**, 033021 (2021).

[59] A. Blais, A. L. Grimsmo, S. M. Girvin, and A. Wallraff, Circuit quantum electrodynamics, Rev. Mod. Phys. **93**, 025005 (2021).

[60] T. Aissaoui, A. Murani, R. Lescanne, and A. Sarlette, A cat qubit stabilization scheme using a voltage biased Josephson junction, arXiv:2411.08132.

[61] L. Danner, C. Padurariu, J. Ankerhold, and B. Kubala, Injection locking and synchronization in Josephson photonics devices, Phys. Rev. B **104**, 054517 (2021).

[62] Y. Kuramoto, International symposium on mathematical problems in theoretical physics, Lect. Notes Phys. **39**, 420 (1975).

[63] J. A. Acebrón, L. L. Bonilla, C. J. Pérez Vicente, F. Ritort, and R. Spigler, The Kuramoto model: A simple paradigm for synchronization phenomena, Rev. Mod. Phys. **77**, 137 (2005).

[64] C. Yan, J. Hassel, V. Vesterinen, J. Zhang, J. Ikonen, L. Grönberg, J. Goetz, and M. Möttönen, A low-noise on-chip coherent microwave source, Nat. Electron. **4**, 885 (2021).

[65] C.-G. Wang, W. Xu, C. Li, L. Shi, J. Jiang, T. Guo, W.-C. Yue, T. Li, P. Zhang, Y.-Y. Lyu *et al.*, Integrated and dc-powered superconducting microcomb, Nat. Commun. **15**, 4009 (2024).

[66] D. Jaschke and S. Montangero, Is quantum computing green? An estimate for an energy-efficiency quantum advantage, Quantum Sci. Technol. **8**, 025001 (2023).

[67] M. Fellous-Asiani, J. H. Chai, Y. Thonnart, H. K. Ng, R. S. Whitney, and A. Auffèves, Optimizing resource efficiencies for scalable full-stack quantum computers, PRX Quantum **4**, 040319 (2023).

[68] T. Śmierzchalski, Z. Mzaouali, S. Deffner, and B. Gardas, Efficiency optimization in quantum computing: Balancing thermodynamics and computational performance, Sci. Rep. **14**, 4555 (2024).

[69] J. Ikonen, J. Salmilehto, and M. Möttönen, Energy-efficient quantum computing, npj Quantum Inf. **3**, 17 (2017).

[70] A. D. Armour, B. Kubala, and J. Ankerhold, Noise switching at a dynamical critical point in a cavity-conductor hybrid, Phys. Rev. B **96**, 214509 (2017).

4.2.3 Phase Stabilization of Cat States

The platform of Josephson photonics can be used to create cat states in a microwave resonator $\hat{c}$, the cat mode, that can be used as basis states of a qubit for quantum computation (see Sec. 1.4.2). Like squeezed states (Sec. 4.2.2), their usability in quantum technological applications strongly relies on a stable reference phase.

Briefly reviewing the results derived in Sec. 1.4.2, cat states can be created by the resonance condition $2eV_{\mathrm{dc}} \approx 2\omega_c - \omega_b$ and a direct coherent microwave drive (with amplitude E_{mw} and frequency $\omega_{mw} = \omega_b - \delta_{mw}$) of a buffer mode $\hat{b}$. Then, within RWA, the system can be described by the Hamiltonian

$$\begin{aligned}\hat{H}_{\mathrm{cat}} =& \hbar\delta_{mw}\hat{b}^\dagger\hat{b} + \hbar\frac{\delta_{\mathrm{dc}}+\delta_{mw}}{2}\hat{c}^\dagger\hat{c} + E_{mw}(e^{-i\phi_{mw}}\hat{b}^\dagger + e^{i\phi_{mw}}\hat{b}) \\ &+ \frac{E_J^*\beta_0\kappa_0^2}{4} : (ie^{-i\eta}\hat{b}^\dagger\hat{c}^2 - ie^{i\eta}\hat{b}\hat{c}^{\dagger 2})\frac{J_1(2\beta_0\sqrt{\hat{b}^\dagger\hat{b}})}{\beta_0\sqrt{\hat{b}^\dagger\hat{b}}}\frac{J_2(2\kappa_0\sqrt{\hat{c}^\dagger\hat{c}})\cdot 2}{\kappa_0^2\sqrt{\hat{c}^\dagger\hat{c}}^2} : .\end{aligned} \tag{1.53}$$

Fluctuations of the dc voltage will destroy the possibility to directly observe cat states in Josephson-photonics devices. As we have described in Sec. 1.7, the effect of quasistatic Gaussian noise can be modeled either by a slowly varying time-dependent phase $\eta \to \eta(t)$ or alternatively by quasistatic averaging of the steady state over Gaussian-distributed detunings δ_{dc}. While the theoretical Wigner function of a cat state $W_{\mathrm{ref}}^{(\pm)}(\kappa)$ created by a Josephson-photonics device possesses two coherent-state peaks at finite amplitude and coherence fringes, the experimentally observable state $W_{\mathrm{avg}}^{(\pm)}(\kappa)$ is phase averaged by noise and hence radially symmetric (see Fig. 4.3).

So far, an injection locking mechanism for cat states has only been explicitly described classically [12, 48] and is built on the derivations shown in Sec. 4.1.1. However, a full quantum mechanical description in a shot-noise dominated regime is straightforward when following the methods shown in Secs. 4.2.1 and 4.2.2.

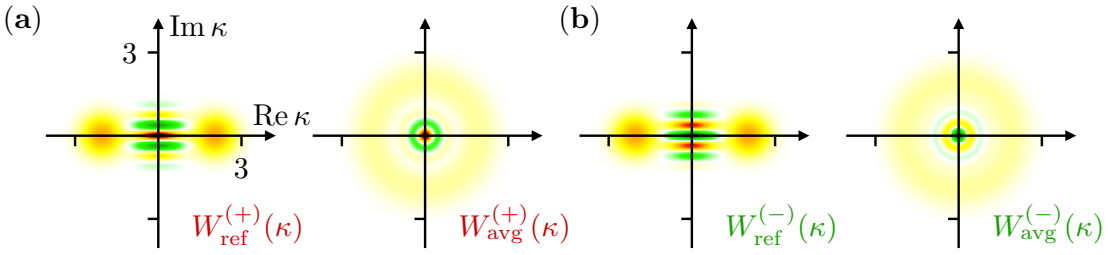

Figure 4.3: Effect of quasistatic Gaussian noise on cat states (a) for the positive cat state and (b) the negative cat state. In both cases, noise will hide the clear signatures, i.e. the coherent-state contributions (peaks at a finite amplitude) and the coherence fringes, from direct observation. The resulting state is diagonal where all phase information and the coherence fringes are hidden.
[Parameters: $2\kappa_0 = \beta_0 = 0.3$, $E_J^*\beta_0\kappa_0^2 = E_{mw} = \hbar\gamma_b/2$, averaging by sampling δ_{dc} that are Gaussian distributed around $\delta_{\mathrm{dc}} = 0$ with standard deviation $\sigma_{\delta_{\mathrm{dc}}} = \gamma_b/10$. (See Fig. 1.5 for color scale of Wigner functions.)]

Here, we present an alternative approach (Secs. 4.2.3.1 and 4.2.3.2) that relies on a classical noise model and is appropriate in regimes where Johnson-Nyquist noise dominates. Then, a full quantum treatment is less critical. This method thus provides an efficient and intuitive way to describe noise sources distinct from Cooper-pair shot noise.

First, we will include the locking drive in the relevant quantum operators (compare Sec. 4.2.3.1). Even without a full simulation, the form of the locking potential can then be derived such that a steady-state solution of a Fokker-Planck equation enables an estimation of the quality of the locked state, measured by the fidelity between the locked state and the theoretical reference state. As a second step, we include a description of classical noise in our quantum system (see Sec. 4.2.3.2). We specifically show that injection locking can stabilize the cat state against classical white noise. A strong injected signal itself introduces small parasitic terms and may destroy the cat state. This fact sets an upper bound for the noise strength such that the system stays reasonably phase-stable.

4.2.3.1 Modifications of the Hamiltonian and Current by a Locking Signal

To analyze injection locking of cat states in Josephson-photonics devices, the circuit model incorporates an additional in-series resistor R_0 [c.f. Fig. 4.1(a) from Sec. 4.1.2.3) to show self-sustained oscillations. In contrast to Secs. 4.2.1 and 4.2.2, the phase across the additional resistor, φ_{R_0}, is now assumed to behave like a classical quantity. As a second step, we include the additional ac locking signal with amplitude $\epsilon = 2eV_{\mathrm{ac}}/(\hbar\Omega)$ at a frequency close to the dc bias $\Omega = \omega_{\mathrm{dc}} + \delta_L$ (with small detuning $\delta_L \ll \omega_b, \omega_c$). First, both ingredients, the resistor phase and the locking signal, are included in the (lab-frame) Hamiltonian

$$\hat{H}_J = E_J^*(\hat{h}^\dagger + \hat{h}) \tag{4.53}$$

and in the Cooper-pair current

$$\hat{I}_{\mathrm{CP}} = \frac{2e}{\hbar} E_J^*(i\hat{h}^\dagger - i\hat{h}) \tag{4.54}$$

with $E_J^* = E_J e^{-(\beta_0^2+\kappa_0^2)/2}$ and

$$\hat{h}^\dagger = -\frac{1}{2} e^{i\epsilon\sin(\Omega t+\phi_\epsilon)} e^{i\left(\omega_{\mathrm{dc}}t-\varphi_{R_0}\right)} e^{i\beta_0\hat{b}^\dagger} e^{i\beta_0\hat{b}} e^{i\kappa_0\hat{c}^\dagger} e^{i\kappa_0\hat{c}}\,. \tag{4.55}$$

As a second step, we aim to find a Hamiltonian in rotating-wave approximation using the resonance condition of the dc-voltage bias $\omega_{\mathrm{dc}} \approx 2\omega_c - \omega_b$. In contrast to Sec. 1.4.2, where a single resonant process generating cat states could be isolated, now multiple resonances are met because of the presence of the locking signal.

Box 4.1: Rotating-Wave Approximation of Eq. (4.55) for Small ϵ

Rotating-Wave Hamiltonian and Current

$$\hat{H}^{\text{cat}}_{\text{RWA}} = \hbar\delta_{mw}\hat{b}^\dagger\hat{b} + \hbar\frac{\delta_{\text{dc}} + \delta_{mw} - \delta_l}{2}\hat{c}^\dagger\hat{c} + E_J^*(\hat{h}^\dagger_{\text{RWA}} + \hat{h}_{\text{RWA}}) + E_{mw}(e^{-i\phi_{mw}}\hat{b}^\dagger + e^{i\phi_{mw}}\hat{b}) \tag{4.56}$$

$$\hat{I}_{\text{dc}} = \frac{2e}{\hbar}E_J^*(i\hat{h}^\dagger_{\text{RWA}} - i\hat{h}_{\text{RWA}}) \tag{4.57}$$

with

$$\begin{aligned}\hat{h}^\dagger_{\text{RWA}} =& \frac{\beta_0\kappa_0^2}{4}ie^{-i\psi} : \hat{b}^\dagger\hat{c}^2\frac{J_1\left(2\beta_0\sqrt{\hat{b}^\dagger\hat{b}}\right)}{\beta_0\sqrt{\hat{b}^\dagger\hat{b}}}\frac{J_2\left(2\kappa_0\sqrt{\hat{c}^\dagger\hat{c}}\right)\cdot 2}{\kappa_0^2\hat{c}^\dagger\hat{c}} : \\ &+ \frac{\epsilon}{4}\frac{\beta_0^2\kappa_0^4}{2!\cdot 4!}e^{-i\psi} : \hat{b}^{\dagger 2}\hat{c}^4\frac{J_2\left(2\beta_0\sqrt{\hat{b}^\dagger\hat{b}}\right)\cdot 2}{\beta_0^2\hat{b}^\dagger\hat{b}}\frac{J_4\left(2\kappa_0\sqrt{\hat{c}^\dagger\hat{c}}\right)\cdot 4!}{\kappa_0^4(\hat{c}^\dagger\hat{c})^2} : \\ &+ \frac{\epsilon}{4}e^{-i\psi} : J_0\left(2\beta_0\sqrt{\hat{b}^\dagger\hat{b}}\right)J_0\left(2\kappa_0\sqrt{\hat{c}^\dagger\hat{c}}\right) :\end{aligned} \tag{4.58}$$

ren. Josephson energy	$E_J^*\beta_0\kappa_0^2$	microwave energy	E_{mw}
microwave frequency	$\omega_{mw} = \omega_b - \delta_{mw}$	locking frequency	$\Omega = \omega_{\text{dc}} + \delta_l$
dc voltage	$\omega_{\text{dc}} = 2\omega_c - \omega_b - \delta_{\text{dc}}$	locking amplitude	$\epsilon = \frac{2e}{\hbar\Omega}V_{\text{ac}}$
Adler phase	$\psi(\mathbf{t}) = (\mathbf{\Omega t} + \phi_\epsilon) - (\omega_{\text{dc}}\mathbf{t} - \varphi_{\mathbf{R_0}})$		

definition and action of unitary transformation
$\hat{U} = \hat{U}_b \otimes \hat{U}_c$

$\hat{U}_\xi = e^{i\phi_{\xi,\text{rot}}\hat{\xi}^\dagger\hat{\xi}}$ with $\phi_{\xi,\text{rot}}(t) = \omega_{\xi,\text{rot}}t + \phi_{\xi,0}$ for $\xi = b, c$

$\Rightarrow$

$\hat{O}$	$\hat{\xi}$	$\hat{\xi}^\dagger\hat{\xi}$	$e^{i\hat{\xi}}$
$\hat{U}_\xi\,\hat{O}\,\hat{U}_\xi^\dagger$	$\hat{\xi}\,e^{-i\phi_{\xi,\text{rot}}}$	$\hat{\xi}^\dagger\hat{\xi}$	$e^{i\hat{\xi}\exp[-i\phi_{\xi,\text{rot}}]}$

rotating-frame transformation $\hat{h}^\dagger_{\text{rot}} = \hat{U}\hat{h}^\dagger\hat{U}^\dagger$
fix the rotating frames such that $2\omega_{c,\text{rot}} - \omega_{b,\text{rot}} = \Omega = \omega_{\text{dc}} + \delta_l$
$\Rightarrow$ effectively obtain additional phase factors

linearize $\hat{h}^\dagger_{\text{rot}} \approx \hat{h}^\dagger_1 + \hat{h}^\dagger_2 + \hat{h}^\dagger_3$ **for** $\epsilon \ll 1$
$\hat{h}^\dagger_0 = \sum_{k_b,l_b=0}^\infty \sum_{k_c,l_c=0}^\infty e^{i(l_b-k_b)\phi_{b,\text{rot}}}e^{i(l_c-k_c)\phi_{c,\text{rot}}}\frac{(i\beta_0)^{k_b+l_b}}{k_b!\,l_b!}\frac{(i\kappa_0)^{k_c+l_c}}{k_c!\,l_c!}\hat{b}^{\dagger l_b}\hat{b}^{k_b}\hat{c}^{\dagger l_c}\hat{c}^{k_c}$

single contributions	pick resonant terms	
$\hat{h}^\dagger_1 = -\frac{1}{2}e^{i\left(\omega_{\text{dc}}t - \varphi_{R_0}\right)}\hat{h}_0$	$l_b = k_b + 1$	$k_c = l_c + 2$
$\hat{h}^\dagger_2 = -\frac{\epsilon}{4}e^{i\left[(\Omega t+\phi_\epsilon) + \left(\omega_{\text{dc}}t - \varphi_{R_0}\right)\right]}\hat{h}_0$	$l_b = k_b + 2$	$k_c = l_c + 4$
$\hat{h}^\dagger_3 = +\frac{\epsilon}{4}e^{-i\left[(\Omega t+\phi_\epsilon) - \left(\omega_{\text{dc}}t - \varphi_{R_0}\right)\right]}\hat{h}_0$	$l_b = k_b$	$k_c = l_c$

rewrite infinite series in closed form using Bessel functions

Restricting ourselves to small locking amplitudes $\epsilon \ll 1$, we find within RWA (derivation and results in Box 4.1) three resonant processes:

(1) Process $\propto E_J^* \hat{b}\hat{c}^{\dagger 2} + \text{h.c.}$
This process generates cat states and does not involve the locking signal (see the description in Sec. 1.4.2). Each tunneling Cooper pair effectively creates two cat-mode photons by annihilating one buffer excitation.

(2) Process $\propto E_J^* \epsilon \hat{b}^{\dagger 2}\hat{c}^4 + \text{h.c.}$
One tunneling Cooper pair and one locking-signal excitation provide the energy for the creation of four cat-mode photons by annihilating two buffer photons. It is a higher-order process that is similar to process (1) and does not introduce harmful parasitic terms.

(3) Process $\propto E_J^* \epsilon : J_0\left(2\beta_0\sqrt{\hat{b}^\dagger\hat{b}}\right) J_0\left(2\kappa_0\sqrt{\hat{c}^\dagger\hat{c}}\right) : + \text{h.c.}$
Since $\omega_{\text{dc}} \approx \Omega$, a tunneling Cooper pair can also create an excitation of the locking signal. This process is amended by the creation and annihilation of multiple virtual resonator photons, and does not change the total number of photons in the resonators. The first contributions of the Bessel functions contain trivial detuning terms and, in second order, a parasitic cross-Kerr term (c.f. Sec. 1.4.2.3)

$$\propto E_J^* \epsilon\, \beta_0^2 \kappa_0^2 \cdot \hat{b}^\dagger\hat{b}\, \hat{c}^\dagger\hat{c}\,, \tag{4.59}$$

which can be kept small by adjusting zero-point fluctuations and the locking signal.

The precise dynamics strongly depends on the mutual interaction between the resistor phase φ_{R_0}, which is related to the noise entering the device, and the density matrix of the system (see Sec. 4.2.3.2). However, even without a full dynamical analysis, the effect of the locking signal can be estimated. To do this, we start from a reduced description of injection locking by the Adler phase (see, e.g., Sec. 2.2.2)

$$\psi(t) = (\Omega t + \phi_\epsilon) - (\omega_{\text{dc}} t - \varphi_{R_0})\ , \tag{4.60}$$

which yields an overdamped motion of ψ in an effetive potential. In the absence of noise, the system is perfectly injection locked and phase stabilized when $\dot{\psi} = 0$. External perturbations then lead to diffusion of ψ in the potential that should remain confined to obtain a reasonably stable phase-space angle.
Using the classical current-voltage relation for resistors (while still neglecting Johnson-Nyquist noise), the potential can be written as the integral over the directed Cooper-pair current

$$V_{\text{WB}}(\psi) = -\delta_l \psi - \frac{2e}{\hbar} R_0 \int \langle \hat{I}_{\text{dc}} \rangle(\psi)\, \mathrm{d}\psi\,. \tag{4.61}$$

For the moment, we assume ψ as a constant variable and find the steady state of the system that is dynamically described by the Lindblad master equation

$$\frac{\mathrm{d}\hat{\rho}}{\mathrm{d}t} = -\frac{i}{\hbar}[\hat{H}^{\text{cat}}_{\text{RWA}}, \hat{\rho}] + \frac{\gamma_b}{2}\left(2\hat{b}\hat{\rho}\hat{b}^\dagger - \hat{b}^\dagger\hat{b}\hat{\rho} - \hat{\rho}\hat{b}^\dagger\hat{b}\right)\ , \tag{4.62}$$

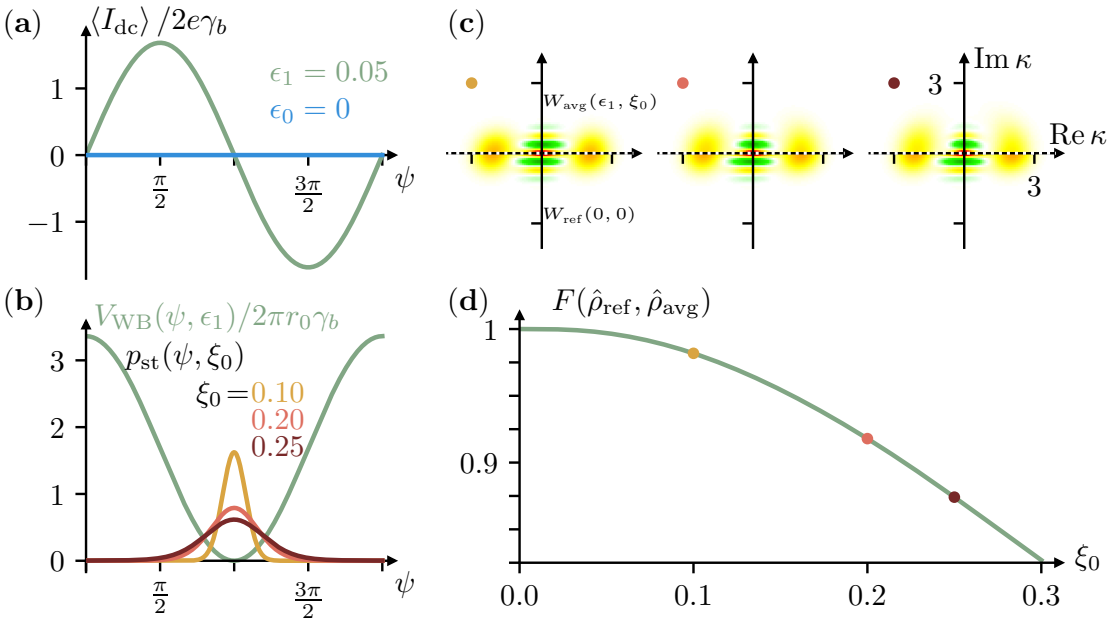

Figure 4.4: (a) Steady-state expectation value of the dc Cooper-pair current of the Lindblad equation of motion, Eq. (4.62). Here, the Adler phase $\psi = \varphi_{R_0}$ is assumed a constant in time. Without locking signal, the current is independent of ψ. A locking signal mainly introduces the Shapiro-step like contribution from Eq. (4.63) and the steady-state current becomes ψ-dependent. (b) The locking potential for the overdamped phase particle ψ is found by integrating the dc Cooper-pair current, c.f. Eq. (4.61). The phase-space angle of the cat states is stabilized when $\dot{\psi} = 0$ is the potential minimum. Fluctuations due to classical Johnson-Nyquist noise with strength ξ_0 lead to a broadened steady-state Fokker-Planck distribution [see Eq. (4.65)]. (c) Averaging the obtained steady-state density matrices from (a) with $p_{\mathrm{ss}}(\psi, \xi_0)$ gives an estimate for the quality of phase stabilization of the cat states. The plots of the Wigner densities show a comparison between the averaged state above and the reference state (where $\xi_0 = 0$ and $\epsilon_1 = 1/20$) below the axis $\mathrm{Re}\,\kappa$. (d) Fidelities between the reference state and the averaged states as a measure of the quality of phase stabilization given a fixed locking signal ϵ_1. To protect the phase-space angle against larger noise sufficiently well, a stronger locking signal is needed.
[Parameters: $2\kappa_0 = \beta_0 = 0.3$, $E_J^*\beta_0\kappa_0^2 = E_{mw} = \hbar\gamma_b/2$, $\phi_\epsilon = 0$, $r_0 = R_0/R_Q$ with $R_Q = h/(2e)^2$, $\delta_l = 0$ (as well as all other detunings). (See Fig. 1.5 for color scale of Wigner functions.)]

where we neglect the single-photon loss with rate γ_c of the high-Q cat mode. Calculating the steady-state expectation value of the current $\langle\hat{I}_{\mathrm{dc}}\rangle(\psi)$ [compare Fig. 4.4(a)] yields a potential for the Adler phase [see Fig. 4.4(b)].
Without locking drive, $\epsilon = 0$, expectation values like $\langle\hat{b}\hat{c}^{\dagger 2}\rangle$ have such a symmetry that the steady-state dc current is independent of ψ. As a direct consequence, the potential is vanishing (for $\delta_l = 0$) and does not exhibit minima. Perturbations due to external noise lead to a free diffusion of ψ in the flat potential, resulting in a neutrally stable phase-space angle of the cat state.
A finite locking amplitude breaks the symmetry for the expectation values by introducing additional terms in the Hamiltonian and the dc current, c.f. Eqs. (4.56) to (4.58). Specifically, the last term of Eq. (4.58) yields a large Shapiro-step like

contribution to the current

$$I_3 = \frac{2e}{\hbar} E_J^* \frac{\epsilon}{2} \sin(\psi) \ \langle : J_0\left(2\beta_0\sqrt{\hat{b}^\dagger \hat{b}}\right) J_0\left(2\kappa_0\sqrt{\hat{c}^\dagger \hat{c}}\right) : \rangle \tag{4.63}$$

which becomes a sinusoidal function of ψ. Consequently, the potential has minima in which the phase particle can be trapped.

The diffusion of a particle in a potential $V_{\mathrm{WB}}(\psi)$ due to Johnson-Nyquist noise with (dimensionless) strength ξ_0^2 can be described by the Fokker-Planck equation [207]

$$\frac{\partial}{\partial t} p(\psi, t) = \frac{\partial}{\partial \psi} \left[V'_{\mathrm{WB}}(\psi) p(\psi, t)\right] + \frac{\gamma_b \xi_0^2}{2} \frac{\partial^2}{\partial \psi^2} p(\psi, t)\,. \tag{4.64}$$

The stationary distribution

$$p_{\mathrm{st}}(\psi, \xi_0) \propto \exp\left[-\frac{2V(\psi)}{\gamma_b \xi_0^2}\right] \tag{4.65}$$

yields an estimation of the Adler phase's confinement due to perturbations by thermal noise, c.f. Fig.4.4(b). From the simulations assuming a variable ψ that is constant in time (compare above), we obtain stationary cat states $\hat{\rho}_{\mathrm{ss}}(\psi)$ whose orientation in phase space is determined by ψ. Therefore, we can estimate the stationary phase-averaged quantum state

$$\hat{\rho}_{\mathrm{avg}} = \int_0^{2\pi} p_{\mathrm{st}}(\psi, \xi_0) \hat{\rho}_{\mathrm{ss}}(\psi)\, \mathrm{d}\psi \tag{4.66}$$

when the system is subject to noise by averaging the stationary states $\hat{\rho}_{\mathrm{ss}}(\psi)$ with the stationary solution of the Fokker-Planck equation.

One possible measure for the quality of phase stabilization is the fidelity [72]

$$F(\hat{\rho}_{\mathrm{ref}}, \hat{\rho}_{\mathrm{avg}}) = \mathrm{tr}\sqrt{\sqrt{\hat{\rho}_{\mathrm{ref}}}\hat{\rho}_{\mathrm{avg}}\sqrt{\hat{\rho}_{\mathrm{ref}}}} \tag{4.67}$$

between the reference state $\hat{\rho}_{\mathrm{ref}} = \hat{\rho}_{\mathrm{ss}}(\psi = \pi)$ and the averaged quantum state (see Fig. 4.4(d). Stronger noise will result in an imperfect stabilization of the phase-space angle, as it can be seen by comparing the three averaged Wigner functions for different noise strengths in Fig. 4.4(c).

In this preliminary analysis, we completely separated the dynamics of the phase and of the quantum state. As a next step, we derive and analyze a system of equations of motion that captures the interplay between the quantum system and the resistor phase in a regime where φ_{R_0} behaves classically.

4.2.3.2 Modeling Classical Noise Influencing Quantum Systems

Crucially, the time derivative of the Adler phase depends on the voltage $\propto \dot{\varphi}_{R_0}$ across the resistor R_0. Pubs. (i) and (ii) have treated φ_{R_0} quantum mechanically and have incorporated fluctuations of the Cooper-pair current into a Lindblad master equation. Here, we want to present an instructive alternative in a regime where noise at the resistor behaves classically and a full quantum description is not necessary.

The Langevin equation

$$\mathrm{d}\varphi_{R_0} = \frac{2e}{\hbar} R_0 \langle \hat{I}_{\mathrm{dc}} \rangle \, \mathrm{d}t + \sqrt{\gamma_b}\xi_0 \mathrm{d}W_t \tag{4.68}$$

separates the deterministic change of the resistor phase (i.e. the classical current-voltage relation) from random white-noise fluctuations with strength ξ_0 (modeled by Wiener increments).

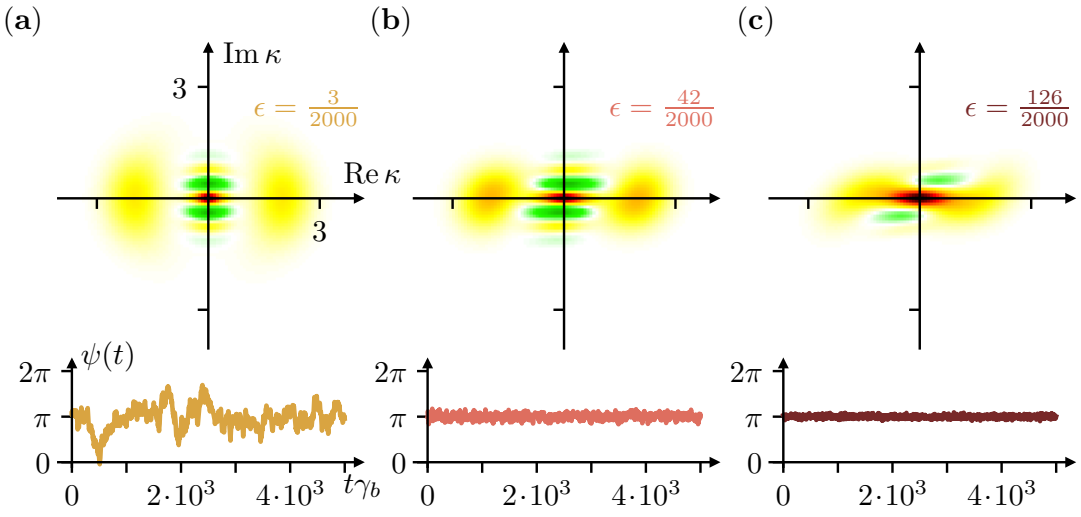

Figure 4.5: (top) Time-averaged quantum states and (bottom) dynamics of the Adler phase for different amplitudes of the locking signal and fixed noise strength $\xi_0 = 1/10$. The time $t = 0$ denotes some time in the steady state, long after the locking signal was turned on. (a) Given a fixed noise, a weak locking signal can partially stabilize the phase-space angle. The fluctuations in the Adler phase have a quite large variance, but ψ prefers to stay close to the minimum. For longer simulation times, phase slips (compare Sec. 2.2.3) could possibly be observed, where ψ changes by 2π and moves into the next (Adler-) potential minimum. (b) A sufficiently strong locking signal can confine the phase in the potential minimum, in which it weakly fluctuates due to external noise. The phase-space angle of the cat state is also stabilized reasonably well. (c) Due to additional resonant terms, a locking signal with too strong amplitude can inhibit the generation of a cat state, although the Adler phase shows even better confinement to its potential minimum.
[Methods: The quantum state is averaged over a time interval $\Delta t_{\mathrm{avg}}\gamma_b = 7.5 \cdot 10^3$. Simulations solve the time evolution of the Wiener process with a small step width and feed a running average (with averaging time $\delta t_{\mathrm{RA}}\gamma_b = 2$) for noise fluctuations into the equations of motion.
Parameters: $\kappa_0 = 2\beta_0 = 0.15$, $r_0 = 2/250$, $E_J^*\beta_0\kappa_0^2 = E_{mw} = \hbar\gamma_b/2$. (See Fig. 1.5 for color scale of Wigner functions.)]

We obtain the set of equations

$$\mathrm{d}\hat{\rho}_\psi = \left(-\frac{i}{\hbar}[\hat{H}^{\mathrm{cat}}_{\mathrm{RWA}}(\psi), \hat{\rho}_\psi] + \frac{\gamma_b}{2}\left(2\hat{b}\hat{\rho}_\psi\hat{b}^\dagger - \hat{b}^\dagger\hat{b}\hat{\rho}_\psi - \hat{\rho}_\psi\hat{b}^\dagger\hat{b}\right)\right) \mathrm{d}t \tag{4.69}$$

$$\mathrm{d}\psi = \left(\delta_l + 2\pi r_0 \frac{\langle \hat{I}_{\mathrm{dc}}(\psi)\rangle_{\hat{\rho}_\psi}}{2e} \right) \mathrm{d}t + \sqrt{\gamma_b}\xi_0 \,\mathrm{d}W_t \,, \tag{4.70}$$

where $r_0 = R_0/R_Q$ with the quantum of resistance $R_Q = h/(2e)^2$. The stochastic time evolution of the Adler phase feeds back into the Lindblad equation for the quantum state of the resonators. On the other hand, their dynamical time evolution influences the Adler phase by taking the expectation value of the Cooper-pair current in the quantum state $\hat{\rho}_\psi(t)$. In this way, the system can dynamically adapt to the locking drive.

Fig. 4.5 shows the results of a time evolution of the set of equations above for different locking amplitudes ϵ while fixing the strength of the noise ξ_0. A locking amplitude that is weak compared to the noise strength [see Fig. 4.5(a)] cannot completely stabilize the phase-space angle of the cat state. Some information about the phase could still be preserved. The partial stabilization is reflected in a phase ψ that shows quite large steady-state fluctuations. A stronger locking signal [see Fig. 4.5(b)] leads to a better phase stabilization, such that ψ is well confined in its minimum with minor fluctuations. An even stronger locking signal leads to stronger phase confinement, such that the phase-space angle should be even more stabilized. However, the locking drive adds parasitic terms to the Hamiltonian that do not contribute to the generation of a cat state. When the Hamiltonian contributions due to the locking signal become too large [see Fig. 4.5(c)], the cat state is destroyed.

The quality of an injection-locked state strongly depends on the relation between the amplitude of the applied locking signal ϵ and the noise strength ξ_0. The fidelity tongue of Fig. 4.6(a) investigates in detail the distance between an injection-locked quantum state that is subject to noise and the theoretical reference state (without noise and $\epsilon = 0$). Given an experimentally observed noise strength, we can thus provide clear guidelines for the required strength of the locking signal that stabilizes the system without destroying the cat state. The lines of constant fidelity visually support the identification of a parameter regime, in which locking protects the cat state against noise.
Assuming a fixed experimentally measured noise strength $\xi_0 = 1/10$ (see horizontal cuts in the fidelity tongue), the application of a sufficiently large locking signal leads to near-perfect fidelities [blue curve in Fig. 4.6(b)], such that two coherent-state peaks and interference fringes of the cat state are clearly visible [middle plot of Fig. 4.6(c)]. If the locking signal is too weak, the coherent-state peaks are blurred and fringes are partially lost [first plot of Fig. 4.6(c)].
We clearly find that the crucial factor for phase-stabilized cat states is the noise strength. With growing noise, a larger locking amplitude would be needed to stabilize the phase of the quantum state. However, for a noise strength of $\xi_0 = 0.3$, the fidelity reaches a plateau well below $F = 1$ [compare the green curve in Fig. 4.6(b)] before it decreases for larger ϵ. Although a large locking signal stabilizes the phase-space angle of the quantum state, it destroys the cat state. While the phase-locked

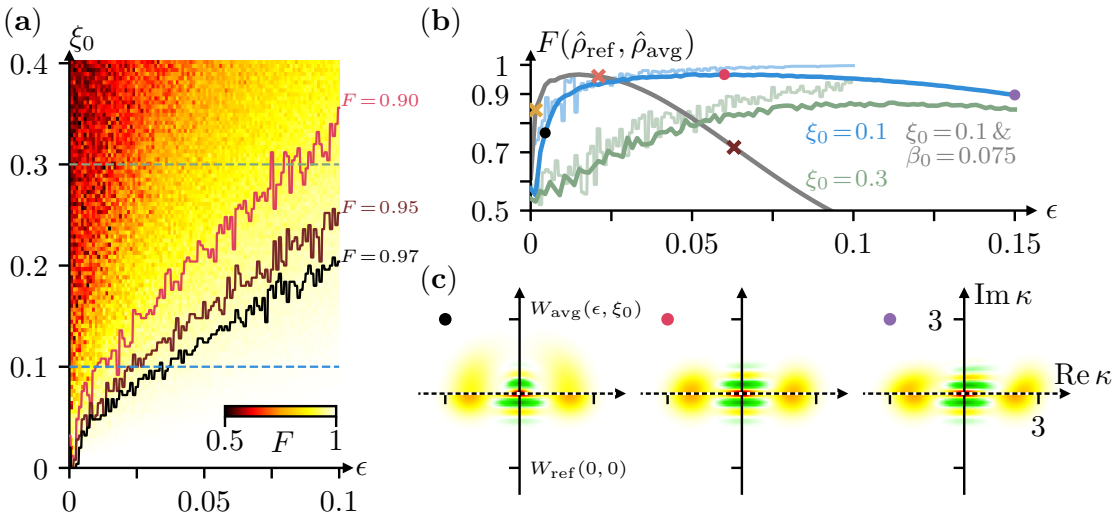

Figure 4.6: (a) The fidelity tongue (similar to the Adler tongue, see Sec. 2.2), as a function of the locking signal and the noise strength, is a measure of the distance between the reference cat state (without noise/locking signal) and the averaged injection-locked quantum state that is subject to noise. Lines of constant fidelity are visual guides for the quality of the stabilization of cat states. (Due to a rather short steady-state averaging time $\Delta t_{\rm avg}\gamma_b = 5 \cdot 10^3$ in simulations, the tongue is not completely averaged over noise realizations, but yields a sufficient estimation.) (b) Fidelity as a function of the locking signal, given a fixed noise strength. Transparent lines are cuts of the fidelity tongue, marked by two horizontal cuts in (a). Solid lines use a larger averaging time $\Delta t_{\rm avg}\gamma_b = 7.5 \cdot 10^3$ for a more precise resolution. Keeping $E_J^*\beta_0\kappa_0^2 = E_{mw} = \hbar\gamma_b/2$ fixed, smaller zero-point fluctuations (grey line) lead to a comparably larger locking potential [c.f. Eq. (4.63)] and better fidelities (compare to blue curve) for small ϵ. However, the destruction of the cat state with increasing ϵ occurs faster for smaller zero-point fluctuations, [compare the Wigner functions from Fig. 4.5 corresponding to the position of the crosses on the grey line]. (c) Wigner densities of the averaged quantum state (above the axis Re κ) can be directly compared to the reference state (below the axis Re κ), shown for three parameters marked in (b).
[Methods: Also here, the quantum state is averaged over a time interval $\Delta t_{\rm avg}\gamma_b$, and a running average over noise fluctuations with averaging time $\delta t_{\rm RA}\gamma_b = 2$ was used for the equations of motion (compare Fig. 4.5).
Other parameters: $\kappa_0 = 0.15$, $r_0 = 2/250$, $\beta_0 = 0.3$ (except where stated otherwise), all detunings are zero. (See Fig. 1.5 for color scale of Wigner functions.)]

quantum state still clearly shows two peaks (far from origin) and coherence fringes, parasitic terms in the locking signal introduce distortions leading to the imperfect cat state shown in Fig. 4.6(c) (right plot). In any case, a strongly reduced fidelity is a clear sign that the original goal, to stabilize a cat state by injection locking, is not reached.

One way to improve phase stabilization for small locking amplitudes is to modify the zero-point fluctuations. Keeping $E_J^*\beta_0\kappa_0^2 = E_{mw}$ fixed (which results in a fixed radial position of the cat-state peaks), smaller zero-point fluctuations increase the potential well for the Adler phase, c.f. Eq. (4.63). Given the same noise strength, smaller locking amplitudes can thus be used for phase stabilization [grey curve in Fig. 4.6(b)]. Nevertheless, an effective increase of this locking term in the Hamiltonian will introduce cat-state distortions faster with growing ϵ (compare the marked

points on the grey line with Fig. 4.5).
The fidelity compares the injection locked quantum state, which is subject to noise, to a perfect reference cat state. Quantum computation may instead only require two basis states that are (quasi-)orthogonal and well separated in the phase space (to exponentially suppress bit flip errors) [78]. Fulfilling these conditions, an analysis of the bit-flip and phase-flip rate [76, 208], which goes beyond the calculation of the distance to cat states, may show that weakly distorted cat-like states could still be useful for quantum computation.

In summary, we have shown that the phase-space angle of cat states can be stabilized by a locking signal in presence of Johnson-Nyquist noise. This instructive approach explains how classical noise affects quantum systems. A clear guideline for experiments is provided by a fidelity tongue which we calculated from our simulations. This model can be directly extended to study other in-series impedances such as a low-pass filter (c.f. Sec. 4.1.2) in regimes of classical noise. Furthermore, injection locking of cat states in presence of shot noise can be implemented directly by following the procedure of Secs. 4.2.1 and 4.2.2 when using an in-series impedance.

4.2.4 Alternative: Reconstruction of Diffused Quantum States

The previous results have explained how to stabilize the phase of Josephson-photonics devices by injecting a locking signal. Here, we present an alternative approach that reconstructs the quantum state and recovers information about the diffused phase-space angle. We perform this reconstruction based solely on the knowledge of a few experimentally accessible expectation values and the applied resonance condition.

Here, we especially focus on the reconstruction of 3-fold symmetric single-mode states (compare Sec. 1.4.1.3). The expectation values

$$\vec{n}_{\mathrm{ref}} = \begin{pmatrix} \langle \hat{n} \rangle_{\mathrm{st}} \\ \langle \hat{n}^2 \rangle_{\mathrm{st}} \\ |\langle \hat{a}^3 \rangle_{\mathrm{st}}| \end{pmatrix} \tag{4.71}$$

are either experimentally accessible or can be recovered despite a diffusing phase-space angle:

- The steady-state occupation $\langle \hat{n} \rangle_{\mathrm{st}}$

  The steady-state occupation can be obtained from the output power spectrum.

- The second moment $\langle \hat{n}^2 \rangle_{\mathrm{st}}$

  The (unnormalized) two-time second-order intensity correlation function

  $$G^{(2)}(t+\tau, t) = \langle \hat{a}^\dagger(t) \hat{a}^\dagger(t+\tau)\, \hat{a}(t+\tau) \hat{a}(t) \rangle \tag{4.72}$$

  yields, at some time t in the steady state and for zero time delay $\tau = 0$, the second moment

  $$\langle \hat{n}^2 \rangle_{\mathrm{st}} = G^{(2)}(t_{\mathrm{st}}, t_{\mathrm{st}}) + \langle \hat{n} \rangle_{\mathrm{st}} \,. \tag{4.73}$$

- The expectation value $|\langle \hat{a}^3 \rangle_{\mathrm{st}}|$

  For the reconstruction of a $\mathbb{Z}^{k=3}$-fold symmetric state, we need the expectation value that reflects that symmetry. Therefore, we propose a measurement of the two-time correlation function

  $$G_k^{(\phi)}(t+\tau, t) = \langle \hat{a}^{\dagger k}(t+\tau) \hat{a}^k(t) \rangle \,. \tag{4.74}$$

  The steady state long-time limit

  $$G_k^{(\phi)}(t_{\mathrm{st}} + \tau, t_{\mathrm{st}}) \to |\langle \hat{a}^k \rangle|^2 \quad (\text{for } \tau \to \infty) \tag{4.75}$$

  yields a third accessible expectation value. In Sec. 1.7, we have shown how for two-mode squeezed states, the expectation value $|\langle \hat{a}\hat{b} \rangle|^2$ for a system without phase diffusion can be recovered from a measurement of the two-time phase correlation function $G_\phi^{(2)}$. In the same way, the expectation value $|\langle \hat{a}^k \rangle|^2$ without phase diffusion can be recovered from a experimental measurement of the corelation function $G_k^{(\phi)}$ when there is sufficiently weak phase diffusion. We note in passing that the reconstruction of stationary single-mode states with a different symmetry ($k \neq 3$) as well as of two-mode squeezed states follows the same principles.

To reconstruct the quantum state, we take an ansatz, either for the Wigner function $W_{\mathrm{opt}}(\alpha, \vec{c})$ or for the density matrix $\hat{\rho}_{\mathrm{opt}}(\vec{c})$ with free variables $\vec{c}$ and follow the procedure below with a Nelder-Mead optimization algorithm [209].

(1) Take an initial guess of the parameters, $\vec{c}_0$, in the ansatz.

(2) Calculate the expectation values with the given ansatz, by which we obtain the vector

$$\vec{n}_{\mathrm{opt}}(\vec{c}_0) = \begin{pmatrix} \langle \hat{n} \rangle(\vec{c}_0) \\ \langle \hat{n}^2 \rangle(\vec{c}_0) \\ |\langle \hat{a}^3 \rangle(\vec{c}_0)| \end{pmatrix} \tag{4.76}$$

(3) We choose to calculate one possible distance measure

$$L_{\mathrm{opt}}(\vec{c}_0) = |\vec{n}_{\mathrm{opt}}(\vec{c}_0) - \vec{n}_{\mathrm{ref}}|^2 \tag{4.77}$$

between the expectation values obtained from the ansatz and the physical steady-state expectation values from experiments.

(4) The Nelder-Mead algorithm updates $\vec{c}_0$ and repeats steps (2) to (4) until convergence is reached.

The presented procedure reconstructs the stationary quantum states of Josephson-photonics devices using only two assumptions:

- The symmetry of the quantum state is known from the applied resonance condition.
- Three expectation values can be measured.

After convergence of the optimization procedure, the optimized ansatz matches the experimentally measured (and recovered) expectation values. However, the goal is to reconstruct the full quantum state. The ability of the ansatz to reconstruct the full quantum state can be measured by the overlap between two mixed states

$$F_M(W_{\mathrm{ref}}, W_{\mathrm{opt}}) = 1 - \left| \frac{\int_{-\infty}^{\infty}\int_{-\infty}^{\infty} W_{\mathrm{ref}}(x,p) W_{\mathrm{opt}}(x,p)\, \mathrm{d}x\mathrm{d}p}{\int_{-\infty}^{\infty}\int_{-\infty}^{\infty} [W_{\mathrm{ref}}(x,p)]^2\, \mathrm{d}x\mathrm{d}p} - 1 \right| \tag{4.78}$$

$$= 1 - \left| \frac{\mathrm{tr}\left[\hat{\rho}_{\mathrm{ref}}\hat{\rho}_{\mathrm{opt}}\right]}{\mathrm{tr}\left[\hat{\rho}_{\mathrm{ref}}^2\right]} - 1 \right| . \tag{4.79}$$

This measure yields an approximate distance between two quantum states, where we note that $\mathrm{tr}\left[\hat{\rho}_{\mathrm{ref}}\hat{\rho}_{\mathrm{opt}}\right] = \mathrm{tr}[\hat{\rho}_{\mathrm{ref}}^2]$ if both states are identical, and $\mathrm{tr}\left[\hat{\rho}_{\mathrm{ref}}\hat{\rho}_{\mathrm{opt}}\right] \neq \mathrm{tr}[\hat{\rho}_{\mathrm{ref}}^2]$ otherwise. While the fidelity from Eq. (4.67) is more difficult to evaluate, the measure F_M can be readily computed for Wigner functions. As reference quantum state $\hat{\rho}_{\mathrm{ref}}$ and expectation values $\vec{n}_{\mathrm{ref}}$, we numerically simulate the theoretical stationary state without phase diffusion (as in Sec. 1.4.1.3). In this way, we can assess whether the optimized ansatz faithfully reconstructs the full quantum state.

4.2.4.1 Ansatz 1: Extension of a Gaussian Wigner Function for the Regime of Weak Driving

Attempting to find an ansatz for a $\mathbb{Z}^3$-symmetric Wigner function, we first briefly review the steady state of a driven damped parametric amplifier (c.f. Sec. 1.4.1.2). It shows a $\mathbb{Z}^2$-symmetry in phase space and is analytically solved by a Gaussian Wigner function

$$W_{\text{squ}}(x,p) \propto e^{-\frac{x^2}{2\sigma_x^2}-\frac{p^2}{2\sigma_p^2}} = \exp\left[-\frac{x^2+p^2}{2\sigma_p^2}\right]\exp\left[-\frac{x^2}{2}\left(\frac{1}{\sigma_x^2}-\frac{1}{\sigma_p^2}\right)\right] \tag{4.80}$$

where we have defined the (dimensionless) position and momentum variables[7]

$$x = \text{Re}\,\alpha = r\cos\phi_\alpha \tag{4.81}$$
$$p = \text{Im}\,\alpha = r\sin\phi_\alpha\,, \tag{4.82}$$

from the phase space variable $\alpha = re^{i\phi_\alpha}$ (with $r \in \mathbb{R}_+$ and $\phi_\alpha \in \mathbb{R}$). The standard deviations $\sigma_{x/p}$ indicate the amount and direction of squeezing and antisqueezing. The above Wigner function can be expressed in cylindrical coordinates r and ϕ_α (using $r^2 = x^2+p^2$ and $r^2\cos^2(\phi_\alpha) = x^2$)

$$W_{\text{squ}}(r,\phi_\alpha) \propto \exp\left[-\frac{r^2}{4}\left(\frac{1}{\sigma_x^2}+\frac{1}{\sigma_p^2}\right)\right]\exp\left[-\frac{r^2\cos(2\phi_\alpha)}{4}\left(\frac{1}{\sigma_x^2}-\frac{1}{\sigma_p^2}\right)\right]\,, \tag{4.83}$$

where we highlight two properties.

- For $\sigma_x = \sigma_p = 1/2$, the squeezed state reduces to a vacuum state

$$W_{\text{vac}}(r,\phi_\alpha) = \frac{2}{\pi}\exp\left[-2r^2\right]\,. \tag{4.84}$$

- The $\mathbb{Z}^{k=2}$-symmetry is reflected by the term $r^2\cos(2\phi_\alpha)$.

Extending the Gaussian Wigner function for a 3-fold symmetry, we make the ansatz

$$W_{\text{opt}}(r,\phi_\alpha,\vec{c}) \propto \exp[-c_2r^2]\exp[-c_4r^4]\exp[-c_3r^3\cos(3\phi_\alpha)] \tag{4.85}$$

using the trigonometric identity $r^3\cos(3\phi_\alpha) = x^3 - 3xp^2$. The ansatz contains the free parameters $\vec{c} = (c_2,c_3,c_4)^T$ that correspond to three terms with individual roles:

- The contribution $e^{-c_2r^2}$ ensures that the ansatz can be reduced to the vacuum state when $c_2 = 2$ and $c_3 = c_4 = 0$.
- The contribution $e^{-c_rr^3\cos(3\phi_\alpha)}$ yields the correct symmetry of the ansatz.
- The contribution $\propto e^{-c_4r^4}$ decays exponentially with a higher power of r than r^3 (which accounted for the correct symmetry), ensuring that the ansatz is normalizable.

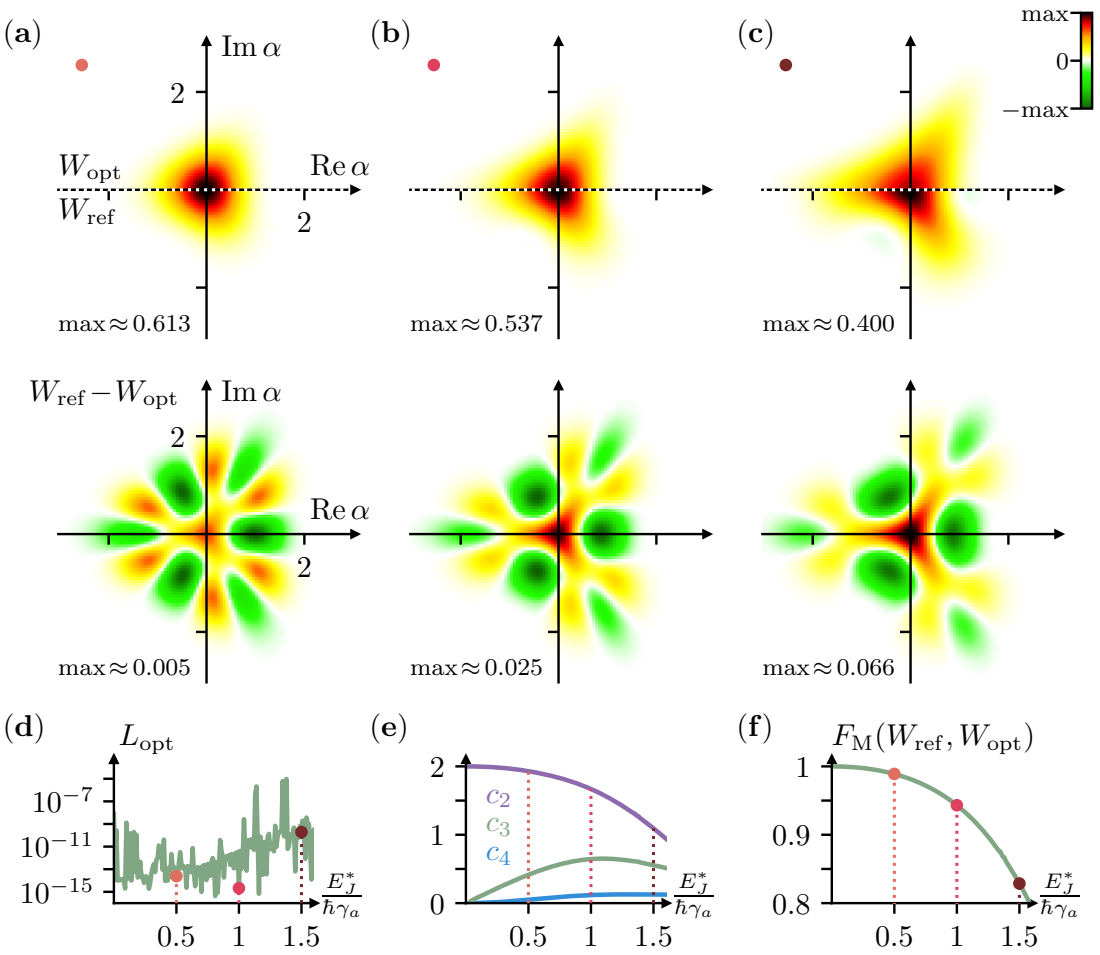

Figure 4.7: Quantum-state reconstruction with few accessible expectation values using an exponential Wigner ansatz. (a-c) Top: A comparison between the optimized exponential ansatz (above the axis $\mathrm{Re}\,\alpha$) from Eq. (4.85) and the reference state (below the axis $\mathrm{Re}\,\alpha$) for three different driving strengths that are marked in plots (d-f). The difference between the Wigner functions (bottom plots) grows in absolute and relative values for (a-c). (d) The optimized distance L_{opt} between the theoretical reference for the expectation values and the expectation values obtained by the ansatz converges and stays small for all driving energies E_J^* considered, meaning that in all cases the optimized ansatz faithfully describes three expectation values. (e) The optimized parameters of the ansatz exhibit a decreasing vacuum-state contribution $\propto e^{-c_2 r^2}$ and an increasingly dominant contribution $\propto e^{-c_3 r^3 \cos(3\phi_\alpha)}$ associated with the 3-fold symmetry as the driving energy is increased. Since this contribution decreases after reaching its maximum, whereas the Wigner function is expected to exhibit an even more pronounced $\mathbb{Z}^3$-symmetry with increasing driving energy, this indicates that the ansatz requires improvement. (e) The fidelity, Eq. (4.78), between reference state and optimized state confirms that the ansatz works in the limit of weak drive, but drops strongly in the regime of stronger driving. [Parameters: $\alpha_0 = 1$, $\omega_{\text{dc}} = 3\omega_a$]

To calculate expectation values, we use the Wigner-Weyl transformation[8]

$$(\hat{A})_W(x,p) = \sqrt{2}x_0 \int_{-\infty}^{\infty} e^{-2ipy} \left\langle \sqrt{2}x_0 \left(x + \frac{y}{2}\right) \middle| \hat{A} \middle| \sqrt{2}x_0 \left(x - \frac{y}{2}\right) \right\rangle \mathrm{d}y \qquad (4.86)$$

[8] $x_0 = \sqrt{\hbar/(m\omega_a)}$ are the zero-point fluctuations in a harmonic oscillator with mass m.

of a general operator $\hat{A}$. The measurement operators are then straightforwardly Weyl-transformed to

$$(\hat{n})_W(r,\phi_\alpha) = r^2 - \frac{1}{2} \tag{4.87}$$

$$(\hat{n}^2)_W(r,\phi_\alpha) = r^4 - r^2 \tag{4.88}$$

$$(\hat{a}^3)_W(r,\phi_\alpha) = r^3\cos(\phi_\alpha)\left[1-4\sin^2(\phi_\alpha)\right] - ir^3\sin(\phi_\alpha)\left[1-4\cos^2(\phi_\alpha)\right]\,. \tag{4.89}$$

Then, quantum mechanical expectation values $\vec{n}_{\mathrm{opt}}(\vec{c})$ can be easily evaluated using the general relation

$$\langle\hat{A}\rangle = \int_{-\infty}^{\infty}\int_{-\infty}^{\infty}(\hat{A})_W(x,p)\cdot W(x,p)\,\mathrm{d}x\mathrm{d}p\,, \tag{4.90}$$

where $W = (\hat{\rho})_W/\pi$ is the (dimensionless) Wigner function [210].

A Nelder-Mead algorithm is employed to minimize the distance L_{opt} between the expectation values $\vec{n}_{\mathrm{opt}}(\vec{c})$ and the reference expectation values $\vec{n}_{\mathrm{ref}}$ obtained from numerical simulations. Through this procedure, we obtain an ansatz Wigner function whose free parameters $\vec{c}$ are optimized to correctly reproduce three physical expectation values that are experimentally accessible (see Fig. 4.7).
In the case of weak driving, as in Fig. 4.7(a), the extended Gaussian ansatz correctly describes the correct quantum state up to minor differences. As the next step, we also try to find optimized parameters in the regime of stronger driving. We observe that the Nelder-Mead algorithm converges in all cases [c.f. Fig. 4.7(d)]. While for $E_J^* = 0$, the ansatz is correctly optimized and gives the vacuum state (with $c_2 = 2$ and $c_3 = c_4 = 0$), increasing the driving strength yields a growing contribution of c_3 that describes an emerging and more pronounced 3-fold symmetry [see Fig. 4.7(e)]. However, even larger driving leads to a decreasing parameter c_3, and serves as a hint that a faithful reconstruction of the full quantum state is not guaranteed by a converging small distance L_{opt}. A comparison of the optimized Wigner function with the reference state in the intermediate driving regime, Fig. 4.7(b), reveals larger deviations $W_{\mathrm{ref}} - W_{\mathrm{opt}}$ (relative errors still remain below 5%) than in the weak-driving regime, although the exponential ansatz provides a reasonable visual fit. However, the reconstruction does not capture the correct quantum state for strong driving, where Fig. 4.7(c) shows a clear difference between the optimized ansatz and the reference state. In particular, the exponential ansatz does not reproduce the emerging rounded peaks at finite amplitude and angles $\phi_\alpha = \pi, \pm\pi/3$ and the sharper indentation at angles $\phi_\alpha = 0, \pm 2\pi/3$.
The fidelity F_M [see Fig. 4.7(f)] serves as a measure that summarizes the results of the quantum-state reconstruction. It decreases only slightly in the weak driving regime and confirms that the ansatz performs well. However, for stronger driving, F_M drops significantly and reveals the need for an improved ansatz.

4.2.4.2 Ansatz 2: Coherent-State Ansatz for the Regime of Strong Driving

An established ansatz to describe nontrivial quantum states and their dynamics is to use coherent states [211, 212]. Here, we present a second ansatz to reconstruct the quantum state of strongly driven Josephson-photonics devices

$$\hat{\rho}_{\mathrm{opt}}(\vec{c}) = \sum_{l=0}^{k-1} e^{2\pi i \frac{l}{k}\hat{n}} \left(\sum_{n=0}^{N_\beta-1} \sum_{m=0}^{N_\beta-1} p_{n,m} \left|\beta_n\right\rangle \left\langle\beta_m\right| \right) e^{-2\pi i \frac{l}{k}\hat{n}}, \tag{4.91}$$

which is a sum of N_β coherent states with complex coherent-state amplitudes $\beta_n = |\beta_n| e^{i\phi_\beta}$ and coefficients $p_{n,m} = |p_{n,m}| e^{i\xi_{n,m}}$. The ansatz must reflect a $\mathbb{Z}^{k=3}$-symmetry, which is ensured by rotating each coherent-state contribution by the angles $\theta = 2\pi l/3$ $(l = 0, .., k-1)$.

At first sight, the ansatz is more complicated and does not have a simple analytical expression for the Wigner function, in contrast to the exponential ansatz studied above. Here, we use $N_\beta = 4$ coherent states for the ansatz. Because symmetry is ensured by additional rotations of the density matrix, these four coherent states will only describe one single branch of the Wigner function (covering an angle of $\Delta\phi_\alpha = 2\pi/3$ in phase space). The optimization contains in total $N_\beta^2 + 2N_\beta$ real

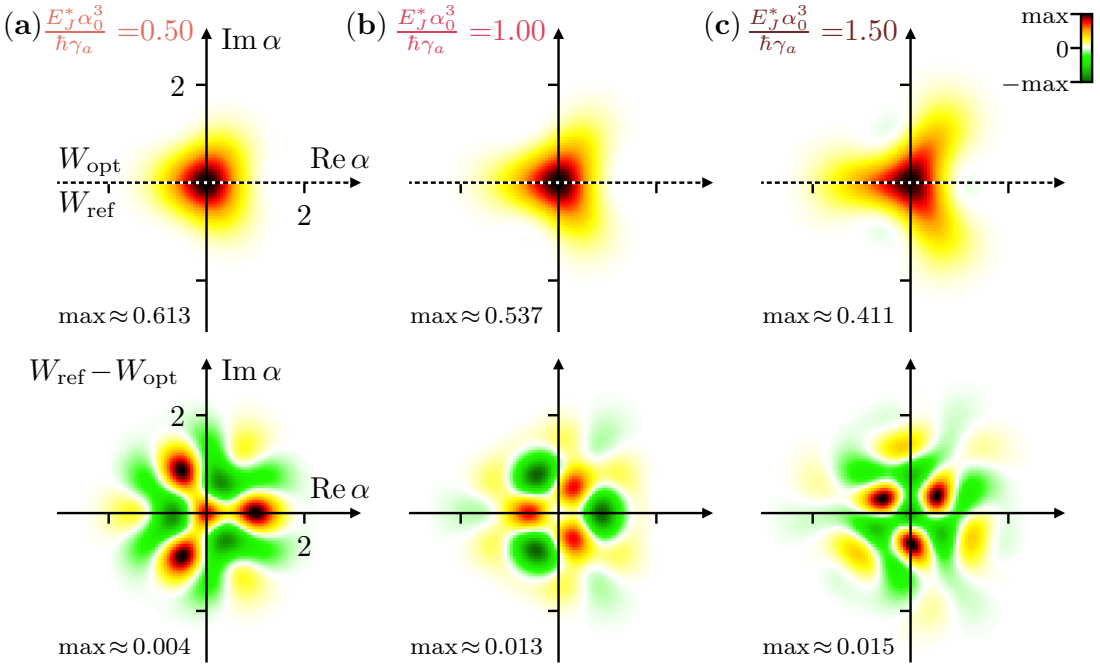

Figure 4.8: Quantum-state reconstruction with few accessible expectation values using the coherent-state ansatz. A comparison between the optimized ansatz (above the axis $\mathrm{Re}\,\alpha$) from Eq. (4.91) and the reference state (below the axis $\mathrm{Re}\,\alpha$) for the three different driving strengths from Fig. 4.7(a-c). The difference between the Wigner functions (bottom plot) has relative errors that now stay well below 5%. In all cases shown, the fidelity (calculated with Eq. (4.67) or Eq. (4.78) exceeds 0.998, yielding a clear improvement of reconstruction results.
[Parameters: $\alpha_0 = 1$, $\omega_{\mathrm{dc}} = 3\omega_a$, $N_\beta = 4$]

free parameters grouped in the vector

$$\vec{c} = (p_{0,0}, ..., p_{N_\beta-1,N_\beta-1}, \beta_0, ..., \beta_{N_\beta-1})^T \tag{4.92}$$

and thus is strongly under-determined when four coherent states are used. Except for the direct calculation of expectation values in the Hilbert space, an analogous optimization as shown in Sec. 4.2.4.1 is performed here.

The optimization results and the absolute differences from Fig. 4.8(a)-(c) can be directly compared to the optimization results using an exponential ansatz from Fig. 4.7(a-c) of Sec. 4.2.4.1. While for the weak driving regime, both the coherent-state ansatz and the exponential Wigner function yield satisfying results, the latter clearly outperforms the exponential ansatz in the regime of strong driving, where a simple analytic form seems inapplicable.

In summary, we have shown how to reconstruct the steady state of a single-mode Josephson-photonics device driven at the three-photon resonance $\omega_{\mathrm{dc}} = 3\omega_a$. A simple analytical function is able to approximate the quantum state in the limit of weak driving, whereas a more complicated ansatz with coherent states yields significantly improved results for stronger driving.
Using other resonance conditions, the protocol and ansatzes can be adapted to reconstruct other quantum states with different steady-state symmetries. One crucial requirement is that at least one expectation value should be experimentally observable that reflects the respective symmetry of the quantum state in phase space. For instance, the protocol can be applied to reconstruct the full Wigner function of a two-mode squeezed state when using the accessible expectation value $|\langle \hat{a}\hat{b} \rangle|$ instead of $|\langle a^3 \rangle|$.

5 Amplification and Detection of Microwave Photons

Many of the core quantum technological applications of the second quantum revolution demand reliable single photon detectors. Because the energy of a single microwave photon is in the order of gigahertz, and thus multiple orders of magnitude smaller than that of optical photons, the detection of single microwave photons remains a challenging task. Although recently a few schemes for microwave detectors [123–125] (also compare Sec. 1.6) have been proposed or realized, they all suffer from some limitations. Detectors of single photons with unknown arrival time that can also distinguish the number of impinging photons have not yet been achieved.

Some time ago, a scheme to amplify and detect single microwave photons with Josephson-photonics devices has been proposed [41]. Using a dc-voltage biased Josephson junction that is connected in series with two microwave resonators, a resonance condition $2eV_{\mathrm{dc}}/\hbar \approx n\omega_b - \omega_a$ transfers a single excitation in cavity $\hat{a}$ to n photons in cavity $\hat{b}$. When a photon impinges on cavity $\hat{a}$ from an input transmission line, the photon number can be multiplied such that n photons leak from cavity $\hat{b}$ into an output transmission line and can subsequently be detected. While deterministic photon multiplication can be achieved, experiments have so far demonstrated the working principle for classical input, i.e. continuous coherent-wave signals [13]. A complete analysis of a full single-photon detection scheme has heretofore not yet been performed.

5.1 Amplification and Detection with Josephson-Photonics Devices

Pub. (*iv*) studies the amplification and detection of single itinerant microwave photons with Josephson-photonics devices. Using Mølmer's approach to model single pulses of light (see Sec. 3), we theoretically describe true quantum input for the Josephson-photonics device. Specifically, we show how a Gaussian temporal mode of length T containing the Fock state $|1\rangle$ (which impinges from an input transmission line) is absorbed and multiplied to n excitations that leak into an output transmission line. The platform is carefully characterized and analyzed in different parameter regimes. A photon detection scheme is developed based on heterodyne quadrature measurement of the output.
As a central result, photon detection efficiency is increased in a parameter regime where a single output mode of the device is highly occupied. Realistic parameters that use a multiplication to $n = 16$ photons promise to outperform existing devices for the detection of single microwave photons, achieving a detection efficiency of 84.5% with dark count rates of $10^{-3}/T$.

5.1.1 Publication (*iv*): *Amplification and Detection of Single Itinerant Microwave Photons*

5.1.1.1 Bibliographic Data and Author's Contribution

Title	Amplification and Detection of Single Itinerant Microwave Photons
Authors	Lukas Danner, Max Hofheinz, Nicolas Bourlet, Ciprian Padurariu, Joachim Ankerhold, and Björn Kubala
Journal	arXiv
Volume	–
Number	arXiv:2510.08030
Year	2025
DOI	https://doi.org/10.48550/arXiv.2510.08030
Copyright	©2025 The Author(s). Published by arXiv under the terms of the Creative Commons Attribution 4.0 International license (CC BY 4.0) [9]

The author is the first author. He carried out analytical calculations and implemented and performed numerical calculations. He contributed considerably to the interpretation of the results of this publication. The author created the figures and assumed the primary role in the preparation of the manuscript. The author is the main author.

[9] https://creativecommons.org/licenses/by/4.0/

5.1.1.2 Summary of Publication (*iv*)

The publication *Amplification and Detection of Single Itinerant Microwave Photons* studies how single itinerant microwave photons can be detected using Josephson-photonics devices. Here, we first introduce the device and its basic working principle, where photon multiplication from one incoming photon to n outgoing photons can be achieved by the energy provided by the dc voltage. Then, the Mølmer approach can be applied to theoretically describe itinerant photon pulses. We proceed by presenting a tool, the two-time coherence function $G^{(1)}$, to characterize the system's output containing n photons in several modes. As a central part, we develop a full detection scheme based on heterodyne detection. Crucially, a high detection efficiency can be achieved when the Josephson-photonics device responds with a highly occupied output. Finally, we extend the analysis to a novel and more complex device, where multiplication is performed in two stages.

The Inelastic Cooper Pair tunneling Photon Multiplier (ICTPM)

A quantum pulse containing a single microwave photon impinges on a Josephson-photonics device from an input transmission line and is absorbed by a resonator $\hat{a}$ of the device [Fig. 1 of Pub. (*iv*)]. When the two-mode Josephson-photonics device, dubbed ICTPM, is dc-voltage biased with the resonance condition $2eV_{\mathrm{dc}}/\hbar \approx n\omega_b - \omega_a$, the energy of a Cooper pair coherently transfers a single excitation in cavity $\hat{a}$ to n photons in cavity $\hat{b}$. These photons then leak into an output transmission line. In experimental setups, the signal of the output transmission line is amplified by a quantum-limited amplifier, and a heterodyne signal records the quadratures of cavity $\hat{b}$ with measurement noise.
Photon multiplication can be achieved in multiple stages. Here, we consider either a single-stage device that consists of two cavities, where each photon from cavity $\hat{a}$ can be multiplied to n (with $n \in \mathbb{N}$) photons in cavity $\hat{b}$. Alternatively, photon multiplication can happen in two or more stages. Two-stage ICTMPs use in total two Josephson junctions, two dc-voltage drives, and three microwave cavities. In the first stage, each photon in cavity $\hat{a}$ is multiplied to n_1 photons in a central cavity $\hat{c}$. The second stage multiplies each photon in $\hat{c}$ to n_2 photons in cavity $\hat{b}$. In practice, a larger multiplication factor $n = n_1 \cdot n_2$ can be reached in this manner.

Modeling itinerant photon pulses with Mølmer's approach

We use Mølmer's approach [see Sec. 3 and Figs. 1 and 2 of Pub. (*iv*)] to describe the interaction of a quantum pulse in a temporal mode with the system using auxiliary cavities with time-dependent loss rates [189–193] (c.f. Sec. 3.2.3). To be precise, we restrict the analysis to a Gaussian input pulse of length T that contains a single photon in Fock state $|1\rangle$.
Until now, the interaction of the ICTPM was theoretically analyzed for pulses of coherent microwave input [41], i.e. classical coherent-state signals. Two immediate advantages arise when combining Mølmer's approach with the ICTPM.

- The interaction of the ICTPM with true quantum input can be investigated. Here, we specifically describe an itinerant pulse that contains a single input photon in Fock state $|1\rangle$. This is a truly quantum mechanical state in contrast to coherent-state input.

- Due to the coherent microwave input (with low mean occupation $\langle \hat{n}_{in} \rangle = 1$), also the quantum state of cavity $\hat{a}$ is close to a coherent state and exhibits relevant occupations of higher Fock states. Photon multiplication with large factors n, especially for two-stage setups, dramatically increases the Hilbert space dimensions needed for the simulation of a full system and makes a numerical analysis extremely challenging. However, for a quantum pulse in Fock state $|1\rangle$, the Hilbert space of the single-stage ICTPM is restricted to dimension $2_a \times (n+1)_b$, which can be efficiently modeled.

Device characterization: Output modes of the ICTPM

Pub. (*iv*) analyzes the output of a single-stage amplifier for a resonant Gaussian temporal input pulse in different parameter regimes. To do so, we diagonalize and analyze the first-order two-time correlation function,

$$G^{(1)}(t_1, t_2) = \langle \hat{b}^\dagger_{\text{out}}(t_2) \hat{b}_{\text{out}}(t_1) \rangle = \sum_k n_k v_k^*(t_2) v_k(t_1)\,, \tag{5.1}$$

which yields eigenmodes v_k with mean occupation n_k [see Fig. 3 of Pub. (*iv*)]. We start by finding a physical interpretation of specific directions in the two-time correlation function: For highly resonant input pulses, which are long in time, $T \gg \gamma_a^{-1}, \gamma_b^{-1}$, the coherence function approaches a long extent in the diagonal direction $t_+ = (t_1 + t_2)/2$. In the limiting case of continuous-wave input, i.e. an infinitely long input pulse, the diagonal direction of $G^{(1)}$ is also infinitely extended. Further, vertical cuts for $G^{(1)}$ when $t_2 \geq t_1$ can be interpreted as Fourier transforms of the instantaneous spectrum.
Proceeding to analyze specific examples, we consider the case of direct photon conversion, $n = 1$. Here, the frequency of the output photon corresponds to the spectral distribution of the input signal by the resonance condition $\omega_b = \omega_{\text{dc}} + \omega_{\text{in}}$. Then $G^{(1)}$ exhibits a circular shape in both vertical and diagonal directions with the same broadening (given by T). For larger multiplication factors $n > 1$, we find that the vertical direction can be confined. Now, the resonance condition only fixes the sum of the frequencies of all n outgoing photons. When the output spectrum is life-time broadened by the single-photon loss rate $\gamma_b \gg T^{-1}$ of cavity $\hat{b}$, the instantaneous inverse spectrum [i.e. the vertical direction of $G^{(1)}$] is consequently confined by $\gamma_b^{-1} \ll T$. In this case, we observe multiple output eigenmodes with similar mode occupations.
However, when the pulse duration becomes comparable to the inverse bandwidth of the instantaneous spectrum, $T \approx \gamma_b^{-1}$, the $G^{(1)}$-function becomes triangular and is diagonalized into a few dominant eigenmodes, where a single mode is highly occupied. This turns out to be desirable for achieving a high detection efficiency with the scheme described below.

Detection scheme for single microwave photons

The Josephson energy can be tuned to achieve perfect photon multiplication for resonant input photons, i.e. for continuous and coherent microwave input [41].
As a central result, Pub.(*iv*) shows that achieving high photon conversion is not sufficient for efficient subsequent photon detection.
Our theoretical model of the experimental scenario uses the stochastic Schrödinger equation (see Sec. 3.3.1) which simulates a heterodyne quadrature measurement

of the output of cavity $\hat{b}$. Despite n outgoing photons, the measured heterodyne signal is dominated by noise [see Fig. 4 of Pub. (*iv*)]. As shown in Sec. 3.3.2, the integration of the signal with a temporal mode as kernel function yields a complex number β_k. When repeating the same experiment multiple times, a histogram of the sampled numbers converges to the Husimi-Q distribution of the quantum state of that temporal mode. A highly occupied output mode has a Husimi-Q function with contributions at large radial distances from the origin. Such a quantum state can be clearly distinguished from vacuum. We define a photon detection event if $|\beta_k|$ is larger than a threshold r_0. This threshold should be set to achieve high detection efficiencies at a small dark count rate. Since in a real experimental setup the arrival time of the photons is unknown, we calculate the convolution of the signal with a temporal mode. In this way, we obtain a time trace $\beta_{\mathrm{conv},k}(t)$ for a single-shot experiment. To reduce dark counts (by reducing the number of measurement points under consideration) and to avoid artificially induced correlations by the convolution in $\beta_{\mathrm{conv},k}(t)$, we apply the photon-detection scheme stroboscopically and measure only once in a given time interval.
The best-case scenario [see Fig. 5 of Pub. (*iv*)] for our setup is when most of the n outgoing photons are emitted into a single highly occupied output mode. Then, its quantum state can be distinguished best from vacuum. In the worst possible case [compare Fig. 6 of Pub. (*iv*)], the outgoing photons are distributed among multiple output modes of the system. Then, their quantum states can be barely distinguished from vacuum, which complicates the search for an integration kernel to detect photons.

Photon detection in a two-Stage ICTPM

For single-photon input into a single-stage device, the only resonance process driven by the Hamiltonian is the coherent transition between $|1_a\rangle\,|0_b\rangle \leftrightarrow |0_a\rangle\,|n_b\rangle$. The Hamiltonian transition matrix element depends only trivially on the zero-point fluctuations of both cavities [compare Sec. 1.5.1 and Appendix A.1 of Pub. (*iv*)]. Further, the analysis can be simplified after a single photon is leaked from the system. Then, the Hamiltonian processes are off-resonant, showing no effect. Specifically, if the cavity $\hat{b}$ loses the first photon, all other $n-1$ photons will subsequently leak to the output transmission line.
For two-stage devices, the dynamics is much more complicated. After the first photon has leaked from cavity $\hat{b}$, there is a variety of possible system states

$$\begin{cases} |0\rangle_a\,|n_1-1\rangle_c\,|n_2-1\rangle_b\,, \\ |0\rangle_a\,|n_1-2\rangle_c\,|2n_2-1\rangle_b\,, \\ ..., \\ |0\rangle_a\,|0\rangle_c\,|n_1n_2-1\rangle_b\ . \end{cases} \tag{5.2}$$

The Hamiltonian processes are not suppressed, resulting in a potentially complex internal dynamics with multiple photon transfer processes between cavitites $\hat{c}$ and $\hat{b}$ before the next photon is emitted from $\hat{b}$. Adding further complexity, all internal transitions depend non-trivially on the zero-point fluctuations of cavity $\hat{b}$ and $\hat{c}$. Due to an increased parameter space, we do not pursue a complete analysis of the output modes in all possible regimes. Instead, Pub. (*iv*) identifies a regime in which a single output mode is highly occupied. The internal dynamics can be simplified

by delaying the second multiplication process from $\hat{c}$ to $\hat{b}$ until $\hat{b}$ is empty. This can be achieved by specifically engineering $\beta_0 \approx 1.66$ as the root of the Laguerre polynomial that appears in the nonlinear corrections of the Hamiltonian matrix elements. For a 3×3 photon multiplication scheme in two stages, it corresponds to blocking the transfer

$$(m_a, m_b = 2, m_c) \leftrightarrow (m_a, 5, m_c - 1)\,. \tag{5.3}$$

A two-stage device with multiplication of $n = 4\times4$ photons can realistically achieve a detection probability of 84.5% with a low dark-count rate of $10^{-3}/T$. It promises to outperform existing detection schemes for single microwave photons.

In summary, Pub. (*iv*) uses the Mølmer approach to theoretically describe single itinerant microwave photons (in Gaussian temporal pulses of length T) that interact with a Josephson-photonics device. Using appropriate resonance conditions, the device achieves photon multiplications of a single impinging photon to n outgoing photons. Based on heterodyne quadrature measurement, we have developed a scheme for the detection of itinerant microwave photons. Crucially, we have identified parameter regimes with highly occupied output modes such that subsequent photon detection can be enhanced. In a setup with two multiplication stages, a detection efficiency of 84.5% can be achieved while keeping the dark-count rate $10^{-3}/T$ sufficiently small. Thus, Josephson-photonics devices are anticipated to outperform existing detection schemes for single microwave photons with unknown arrival time.

Amplification and Detection of Single Itinerant Microwave Photons

Lukas Danner,[1,2,*] Max Hofheinz,[3] Nicolas Bourlet,[3] Ciprian Padurariu,[2] Joachim Ankerhold,[2] and Björn Kubala[1,2]

[1] *German Aerospace Center (DLR), Institute of Quantum Technologies, 89081 Ulm, Germany*
[2] *Institute for Complex Quantum Systems and IQST, University of Ulm, 89069 Ulm, Germany*
[3] *Institut Quantique, Université de Sherbrooke, Sherbrooke, Québec J1K 2R1, Canada*

(Dated: October 10, 2025)

Single-photon detectors are an essential part of the toolbox of modern quantum optics for implementing quantum technologies and enabling tests of fundamental physics. The low energy of microwave photons, the natural signal path for superconducting quantum devices, makes their detection much harder than for visible light. Despite impressive progress in recent years and the proposal and realization of a number of different detector architectures, the reliable detection of a single itinerant microwave photon remains an open topic.

Here, we investigate and simulate a detailed protocol for single-photon multiplication and subsequent amplification and detection. At its heart lies a Josephson-photonics device which uses inelastic Cooper-pair tunneling driven by a dc bias in combination with the energy of an incoming photon to create multiple photons, thus compensating for the low-energy problem. Our analysis provides clear design guidelines for utilizing such devices, which have previously been operated in an amplifier mode with a continuous wave input, for counting photons. Combining a formalism recently developed by Mølmer to describe the full quantum state of in- and outgoing photon pulses with stochastic Schrödinger equations, we can describe the full multiplication and detection protocol and calculate performance parameters, such as detection probabilities and dark count rates. With optimized parameters, a high population of a single output mode can be achieved that can then be easily distinguished from vacuum noise in heterodyne measurements of quadratures with a conventional linear amplifier. Realistic devices with two multiplication stages with multiplication of 16 reach for an impinging Gaussian pulse of length T a detection probability of 84.5% with a dark count rate of $10^{-3}/T$, and promise to outperform competing schemes.

I. INTRODUCTION

The ability to reliably detect radiation on the single-photon level is an indispensable ingredient for numerous protocols and technologies in quantum information processing, quantum sensing, and quantum communication. Devices such as avalanche photodiodes and superconducting nanowire single-photon detectors [1, 2] provide this capability at frequencies above infrared, thus enabling quantum key distribution, ranging, heralded preparation of non-Gaussian states, boson sampling, and many more [3–8]. However, other quantum technological devices, most prominently those based on superconducting circuits, naturally operate on energy scales compatible with microwave photons so that their efficient amplification, detection, and characterization is highly requested.

To meet the challenge of detecting itinerant microwave photons on the single-photon level, a considerable variety of schemes has been proposed previously [9–15]. After a number of breakthrough experimental realizations[16–18], the last decade has seen impressive progress in the field, see e.g. brief reviews in [19–21]. Among the schemes are threshold detectors, where photon absorption switches a current biased Josephson junction to the resistive state [22–27] or induces a phase transition in a Josephson parametric amplifier [28], and various ways to capture an incoming photon in a cavity [16–18, 29, 30], where it interacts with a local system whose modified state is subsequently detected. Demonstrated applications include the improved sensing of signals from electron spin resonance [31, 32], the detection of Josephson radiation[33], the measurement-based remote entanglement of superconducting qubits [34] as well as their readout [35, 36], and, perhaps most prominently in recent years, in the fundamental physics quest for detecting axions [24, 37, 38].

However, these realizations also have their significant limitations. Those that operate in regimes of maximal nonlinearity and non-unitarity, map all incoming non-zero photon number states onto the same output state. Further, they are typically gated or have a blind time after each detection event where the detector is reset which implies that these detectors saturate quickly. On the other hand, more linear power sensors either lack single photon sensitivity, as in the case of bolometers [33, 36, 39–41], or achieve true number resolving single photon detection only for precisely known incoming modes sufficiently far apart in time [42].

A first step towards counting photons arriving at unknown times has recently been achieved in the form of a photon number amplifier based on inelastic Cooper pair tunneling [43, 44]. This Inelastic-Cooper-pair-Tunneling Photon Multiplier (ICTPM) multiplies the photon number by an integer factor without added photon noise, at the expense of deamplifying or losing phase information. However, this fundamentally novel mode of amplification has so far only been investigated for classical

* lukas.danner@dlr.de

(coherent continuous-wave) input. Here we theoretically analyze true quantum input (single-photon wavepackets) and describe how such a photon-number amplifier is then read out using a quantum-limited amplifier to detect and count individual photons. The ICTPM uses the energy $2eV_{\rm dc}$ of a Cooper pair tunneling inelastically through a Josephson junction biased at a voltage $2eV_{\rm dc} \approx n\hbar\omega_b - \hbar\omega_a$ to power a photon conversion process between one excitation from a microwave cavity $\hat{a}$ to n excitations in a cavity $\hat{b}$ which are both connected in series to the junction, see Fig. 1. We utilize Mølmer's approach [45–49] to describe a resonant Gaussian single-photon pulse impinging on the ICTPM. While near-perfect photon conversion with negligible input-photon reflection can be achieved by adjusting the Josephson energy, a key challenge is that, because of the inherent nonlinearity of the photon number amplification process, a single incoming temporal mode may be mapped to multiple outgoing modes, each containing less than n photons. We analyze and characterize different regimes of the output, identifying parameters where a single temporal output mode is highly occupied. Numerically, we employ quantum trajectories based on the stochastic Schrödinger equation to carefully model the experimental readout of heterodyne quadrature measurement using a quantum-limited amplifier with large gain G. Thereby, we provide a scheme to analyze the output signal in order to detect the single input photon. Crucially, the detection efficiency can be optimized for parameter regimes exhibiting few output modes, where one is highly populated and can be distinguished from vacuum.

However, achieving a large multiplication factor n in order to improve detection efficiency would, in experiments where ω_b and ω_b are fixed, lead to a large dc-voltage. In this situation, the ICTPM can access higher-order processes, resulting in emission without an incoming signal [44] which, in turn, would trigger false detection events, i.e. dark counts. To avoid this limitation, we also analyze photon multiplication in a setup with two stages. Physically, internal processes here strongly differ from a single-stage setup, which strongly influences the system dynamics and the structure of the output signal.

II. MODEL DESCRIPTION AND SIMULATIONS

We consider a single itinerant microwave photon in a superconducting input transmission line [cf. Fig. 1(a)], which is the signal pulse to be detected. Before detection, the signal is amplified by an Inelastic-Cooper-Pair-Tunneling Photon Multiplier (ICTPM). First, we introduce the ICTPM [43, 44], which consists of a dc-biased Josephson junction connected in series to two microwave cavities (realized as LC-oscillators). The ICTPM is described by the Hamiltonian $\hat{H}_1 = \hbar\omega_a\hat{a}^\dagger\hat{a} + \hbar\omega_b\hat{b}^\dagger\hat{b} + \hat{H}_J$, where two harmonic oscillators with eigenfrequencies $\omega_\xi = (L_\xi C_\xi)^{-1/2}$ $(\xi = a, b)$ are driven nonlinearly by

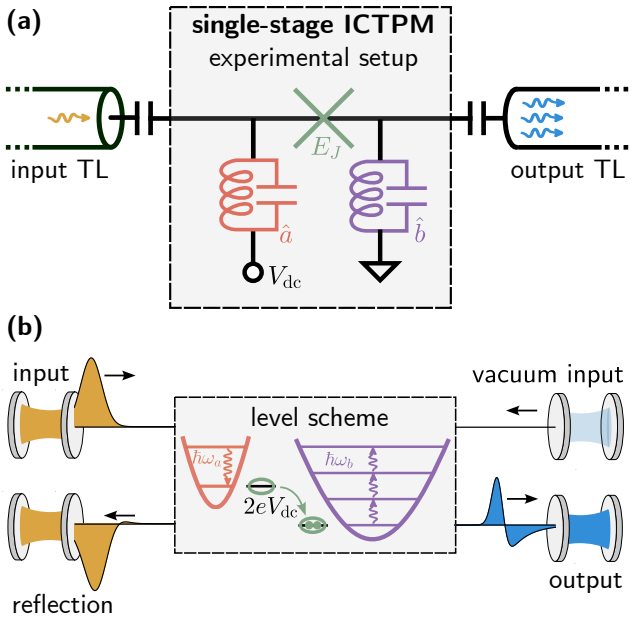

FIG. 1. Inelastic-Cooper-pair-Tunneling Photon Multiplier. (a) The system consists of a dc-biased Josephson junction (with tunable Josephson energy E_J), connected in series with two microwave modes, that are realized as LC-resonators and capacitively coupled to transmission lines (TLs). A single-photon pulse impinging on cavity $\hat{a}$ from the input transmission line will be absorbed by the ICTPM, which then leaks n photons into the output transmission line. (b) A Cooper pair can inelastically tunnel through the junction if the microwave modes absorb its energy of $2eV_{\rm dc}$. By setting the dc-voltage on the resonance $2eV_{\rm dc}/\hbar + \omega_a = n\omega_b$, the Cooper pairs drive the transition where one cavity-$\hat{a}$ excitation is coherently transferred to $n \in \mathbb{N}$ cavity $\hat{b}$-excitations. Time-dependent input-, output- and reflected pulses moving along transmission lines which are absorbed or emitted from the ICTPM can be numerically modeled by Mølmer's approach [45–49]. Therein, the transmission lines are mimicked by auxiliary cavities which emit (absorb) modes $u(t)$ $(v(t))$ for appropriately chosen time-dependent loss rates $g_u(t)$ $(g_v(t))$.

the Josephson junction

$$\hat{H}_J = -E_J \cos\left[\frac{2e}{\hbar}V_{\rm dc}t + \alpha_0(\hat{a}^\dagger + \hat{a}) + \beta_0(\hat{b}^\dagger + \hat{b})\right] \quad (1)$$

with driving energy E_J. Here, we have introduced the zero-point fluctuations $\alpha_0 = (\pi Z_a/R_Q)^{1/2}$ (and β_0 analogously) of the cavities determined by their characteristic impedance $Z_\xi = (L_\xi/C_\xi)^{1/2}$ and the quantum of resistance, $R_Q = h/4e^2$. The phase argument of the Josephson junction then follows from a Kirchhoff's loop rule for the (time-integrated) voltages of the circuit shown in Fig. 1(a). Both cavities are capacitively coupled to respective input or output transmission lines, leading to an effective loss rate γ_ξ, so that the ICTPM can be modeled by a Lindblad master equation with dissipation operators $\hat{L}_\xi = \sqrt{\gamma_\xi}\hat{\xi}$. The coherent coupling Hamiltonian, $\hat{H}_J$,

describing Cooper-pair tunneling across the dc-biased Josephson junction, only becomes effective at certain resonances, where the energy provided by the voltage bias to a tunneling pair, $2eV_{\mathrm{dc}}$, can be exactly absorbed by changing the occupation of the electromagnetic modes of the circuit. Here, we tune the dc-voltage to a resonance condition $2eV_{\mathrm{dc}}/\hbar + \omega_a \approx n\omega_b$ ($n \in \mathbb{N}$), such that each tunneling Cooper pair creates n excitations in cavity $\hat{b}$ by annihilating one excitation from cavity $\hat{a}$.

This photon process is indeed selected by a rotating wave approximation (RWA) of the coupling Hamiltonian (1) (see Appendix A 1), i.e.,

$$\hat{H}_{J,\mathrm{RWA}} \approx \frac{E_J^* \alpha_0 \beta_0^n}{2n!}(\hat{a}\hat{b}^{\dagger n} + \hat{a}^\dagger \hat{b}^n) \qquad (2)$$

where $E_J^* = E_J e^{-(\alpha_0^2+\beta_0^2)/2}$ (see below for higher-order corrections to (2)).

When an itinerant microwave photon in the input transmission line is resonantly absorbed by cavity $\hat{a}$, the Josephson junction drives a multiplication process, where one excitation from cavity $\hat{a}$ is coherently transferred into n excitations in cavity $\hat{b}$. These n photons eventually leak into the output transmission line, where they can be detected more easily.

Theoretically, the system's interaction with incoming and outgoing itinerant few-photon pulses can be conveniently modeled by a cascaded Master equation approach [45–49]. Within input-output theory, one defines an incoming temporal mode of the input field by the annihilation operator $\hat{a}_u = \int_0^\infty u(t)\hat{a}_{\mathrm{in}}(t)dt$ (where the mode envelope $u(t)$ is normalized, $\int_0^\infty |u(t)|^2 dt = 1$). This itinerant pulse is modeled by an auxiliary cavity coupled directly to the input cavity with time-dependent loss-rate $g_u(t) = u^*(t)/\sqrt{1 - \int_0^t |u(\tau)|^2 d\tau}$. Such an auxiliary cavity will emit its initial quantum state $\hat{\rho}_u$ (where $\hat{\rho}_u$ should be chosen to be the quantum state of the mode $\hat{a}_u$) into a temporal mode with envelope $u(t)$. Analogously, another auxiliary cavity with loss rate $g_v(t) = -v^*(t)/\sqrt{\int_0^t |v(\tau)|^2 d\tau}$ will perfectly absorb the reflected itinerant quantum pulse with mode envelope $v(t)$, where its final state $\hat{\rho}_v$ is the quantum state of the mode $\hat{a}_v = \int_0^\infty v(t)\hat{a}_{\mathrm{out}}(t)dt$. In the same manner, an auxiliary output cavity can be introduced for the right transmission line where we assume vacuum input. The resulting cascaded Master equation (see Appendix B) then contains interaction terms between the auxiliary cavities and the system, as well as modified Lindblad operators $\hat{L}_a \to \sqrt{\gamma_a}\hat{a} + g_u(t)\hat{a}_u + g_v(t)\hat{a}_v$ (and analogously for cavity $\hat{b}$). In that manner, the interaction of the ICTPM with a small number of input and output pulses can be described. One big advantage of this method is that true quantum input, i.e. a single photon Fock state $\hat{\rho}_u = |1_u\rangle\langle 1_u|$ (which behaves inherently differently than simple coherent input), can be simulated. The second advantage is that this simulation is also more efficient: To describe a single-photon Fock state, we need

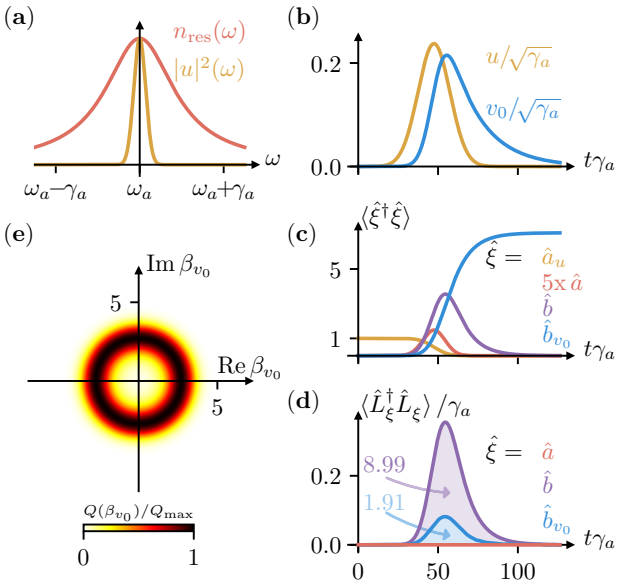

FIG. 2. Simulation of the amplification of an incoming single-photon pulse. (a) The impinging pulse in the frequency domain, $u(\omega)$, is Gaussian and smaller than the width of the resonance curve n_{res} of cavity $\hat{a}$ (occupation of a single cavity biased at $2eV_{\mathrm{dc}} = \hbar\omega$), so that it can be absorbed. (b) Pulse $u(t)$ in time domain and an output mode $v_0(t)$ of the right transmission [compare Fig. 1(a, c)]. They are modeled by auxiliary cavities with time-dependent loss rates $g_u(t)$ and $g_v(t)$ (not shown) and frequency ω_a and ω_b. (c) Occupation numbers gained from the simulation show how the input pulse loses its photon to the input cavity $\hat{a}$. The multiplication process driven by the Josephson junction transfers excitations from cavity $\hat{a}$ to cavity $\hat{b}$, which subsequently leaks photons into the output transmission line. Part of this output is in mode $v_0(t)$ and thus absorbed by the auxiliary cavity modeling that mode. (d) Integrating the rate of lost photons (from $\hat{a}$: 0 lost photons (red), from $\hat{b}$: $n = 9$ lost photons) yields a perfect multiplication to n photons when choosing the optimal Josephson driving strength E_J. The explicitly modeled auxiliary cavity v_0 from the right transmission line retains $\langle\hat{n}\rangle = 7.1$ photons [cf. blue line in (c) approaching that constant], but loses 1.91 photons, which are contained in other, not explicitly simulated modes. (e) The mode v_0 is found in a mixture of Fock states as shown by its Husimi-Q function. [Parameters: $n = 9$, $\gamma_b = \sigma_\omega = \gamma_a/10$, $E_J^* = E_{J,\mathrm{opt}}^*$].

2 states for the auxiliary input cavity while the amplifier dimension is then rigorously restricted to the dimension $2 \times (n+1)$ within RWA, Eq. (2). A coherent input with mean occupation of a $\langle\hat{a}_u^\dagger\hat{a}_u = 1\rangle$ numerically requires a considerably larger Hilbert space dimension.

As an introductory example of the simulation and its typical observables for this setting, we consider in Fig. 2 a single-photon Fock state $|1_u\rangle$ in a Gaussian temporal pulse envelope $u(t)$ as incoming quantum pulse of the in-

put transmission line. This itinerant pulse is resonant with cavity $\hat{a}$ [compare Fig. 2(a, b)], such that it will be completely absorbed. In the output transmission line, we model a single outgoing pulse in a mode $v_0(t)$ specified in Fig. 2(b). Our results [Fig. 2(c)] show how the photon leaks from the auxiliary cavity (i.e., the input transmission line) and is absorbed by cavity $\hat{a}$. Subsequently, the transfer process with a multiplication factor $n = 9$, driven by the Josephson junction, starts to accumulate photons in $\hat{b}$. Some of the photons emitted from cavity $\hat{b}$ into the output transmission line are absorbed by the auxiliary cavity, indicating that they are emitted into mode $v_0(t)$ of the output transmission line. Its final state, is characterized by the Husimi-Q function in Fig. 2(d), corresponds to the quantum state of that mode, which in our case is a diagonal mixture of Fock states $|0\rangle, ...|n\rangle$.

In general, the transfer process is not perfect. First, note that a photon loss of cavity $\hat{a}$ to the left transmission line prevents any photon multiplication. Since the Cooper-pair driven multiplication process between the microwave cavities of the ICTPM is coherent, i.e. a Hamiltonian term, the reverse process is also possible, further increasing the probability of a loss of an $\hat{a}$ excitation into the input transmission line. There is, however, a specific driving strength, $E^*_{J,\mathrm{opt}} = \hbar\sqrt{\gamma_a\gamma_b}\sqrt{nn!}/\alpha_0\beta_0^n$ [43], where one can achieve (near-)perfect conversion [Nominally, it becomes perfect for an incoming single photon in a delta-pulse mode with $\omega_{\mathrm{in}} = \omega_a$]. For $E^*_{J,\mathrm{opt}}$ all portions of the input pulse that are well within the frequency-dependent bandwidth $T(\omega)$ [43] of the amplifier are converted. In fact, the conversion probability, $p_{\mathrm{conv}} = 1 - \int\langle\hat{L}_a^\dagger\hat{L}_a\rangle dt = \int\langle\hat{L}_b^\dagger\hat{L}_b\rangle dt/n$, which can be defined via the integral with respect to time over the lost photons from either $\hat{a}$ or $\hat{b}$, cf. Fig. 2(d), can be expressed as $p_{\mathrm{conv}} = \int T(\omega)|u(\omega)|^2 d\omega$. Notably, the optimal driving strength can also be intuitively derived by matching the rates γ_a of the absorption of the input photon into cavity $\hat{a}$ to a golden-rule rate $\Gamma_{\mathrm{gr}} \propto |\langle 0_a, n_b|\hat{H}_{J,\mathrm{RWA}}|1_a, 0_b\rangle|^2/n\gamma_b$. The golden rule rate, which is formally valid only in the perturbative regime, describes the transition probability of the multiplication process followed by the subsequent loss of the first excitation from the lifetime-broadened level $|n_b\rangle$. Matching this first photon loss process is sufficient for a perfect conversion, since the loss of the first photon from cavity $\hat{b}$ effectively brings the coherent dynamics to an abrupt end, as the Josephson drive is not resonant anymore.

III. PHOTON DETECTION IN SINGLE-STAGE AMPLIFIER

In fact, a simple optimization of the conversion probability is not sufficient for an eventual heterodyne detection of microwave photons. Of more importance than the total number of photons in the output, is a high occupation of a single mode: as apparent from Fig. 2(e), the quantum state of the highly-occupied simulated mode can be quite clearly distinguished from a vacuum mode by comparing the Husimi-Q functions. Before analyzing the full photon detection schemes in a heterodyne measurement setup, we therefore first start to investigate parameter regimes of the ICTPM possessing different output modes.

A. Regimes of Output Modes

In general, the photons leaking from cavity b are distributed among several (eigen-) modes in the output transmission line. An eigenmode decomposition can be found by diagonalizing the first-order two-time correlation function [45, 46, 50, 51],

$$G^{(1)}(t_1, t_2) = \langle\hat{b}^\dagger_{\mathrm{out}}(t_2)\hat{b}_{\mathrm{out}}(t_1)\rangle = \sum_k n_k v_k^*(t_2)v_k(t_1)\ , \tag{3}$$

which yields the mean occupation $n_k = \langle\hat{b}^\dagger_{v_k}\hat{b}_{v_k}\rangle$ of the k-th eigenmode $\hat{b}_{v_k} = \int_0^\infty \hat{b}_{\mathrm{out}}(t)v_k(t)dt$ in the output transmission line.

It will turn out to be advantageous for detection to dominantly occupy a single output mode. To understand how to achieve a single-mode output, we can preliminarily consider the simplest scenario of this type, which can be realized in our amplifier for a multiplication factor $n = 1$. For that case, the bilinear Hamiltonian (2) can be solved analytically, and a scattering matrix connects input and output modes at frequencies linked by the biasing condition. Assuming vacuum input into the output transmission line and a single-photon input into the input transmission line, we find a single output mode, which, at optimally chosen Josephson driving strength, carries the full occupation $n_0 = 1$ [see Fig. 3(a)]. Approaching the limit of continuous-wave input (i.e., a very sharp pulse shape in Fourier space with a frequency spread σ_ω smaller than all other rates), the extent of the coherence function in the diagonal direction $t_+ = (t_1 + t_2)/2$ grows to a correspondingly long time $T_{\mathrm{out}} \sim 1/\sigma_\omega$. An understanding of other directions in the $G^{(1)}(t_1, t_2)$ map can be gained by considering vertical and horizontal cuts starting at the diagonal as the Fourier transform of the instantaneous spectrum at time $t_1 = t_2$. In Fig. 3(a), the long extent of the correlation function in these directions, $T_{\mathrm{spec}} \sim 1/\sigma_\omega$, and the corresponding circular shape of $G^{(1)}(t_1, t_2)$ thus reflects the fact that the frequency of the outgoing photon for $n = 1$ is fixed by the resonance condition $\omega_b = \omega_{\mathrm{dc}} + \omega_{\mathrm{in}}$, up to a broadening arising from the input photon bandwidth σ_ω. Crucially, just as in a linearly driven damped harmonic oscillator, the instantaneous spectrum is not lifetime broadened by $\gamma_b \gg \sigma_\omega$. Such broadening would result in a $G^{(1)}$ more strongly confined along the diagonal.

Such a confinement indeed occurs in the nontrivial cases of photon amplification with $n > 1$, see e.g. Fig. 3(b). The resonance condition $\omega_{\mathrm{in}} = \omega_{\mathrm{dc}} + n\omega_b$

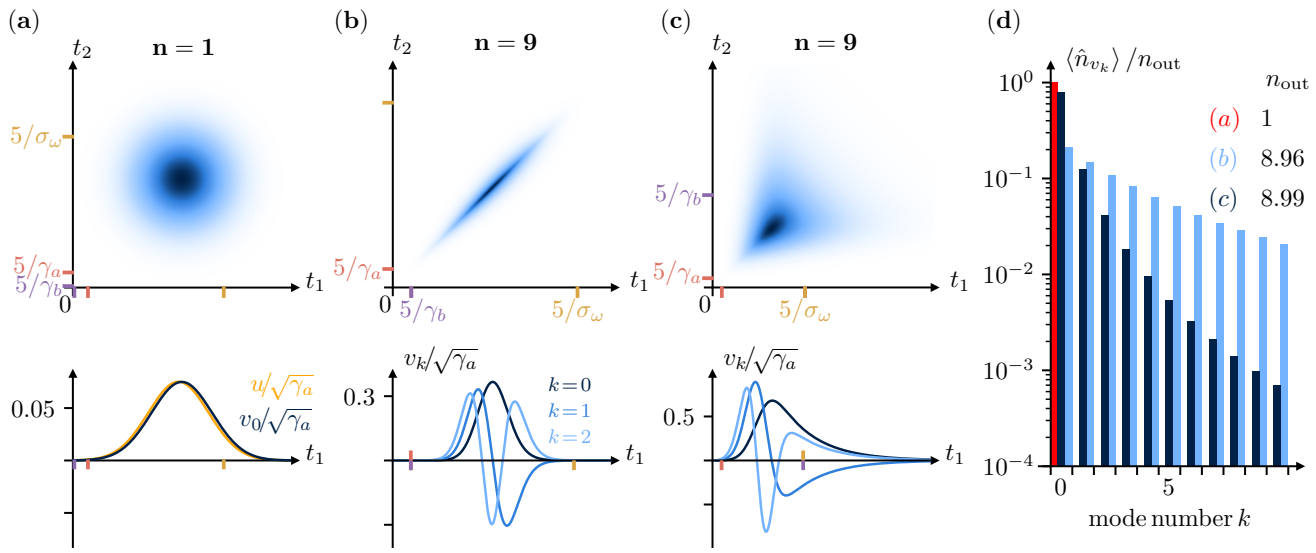

FIG. 3. Two-time first order correlation functions of the output field, $G^{(1)} = \langle \hat{b}^\dagger_{\text{out}}(t_2)\hat{b}_{\text{out}}(t_1)\rangle$ with eigenmodes and their occupations $\langle \hat{n}_k \rangle = \langle \hat{b}^\dagger_k \hat{b}_k \rangle$. In all cases, we simulate a single input mode centered around ω_a in a Gaussian envelope with $\sigma_\omega = \gamma_a/10$ in the quantum state $|1\rangle_{\text{in}}$ impinging on and being resonantly absorbed by cavity $\hat{a}$, and $E_J^* = E_{J,\text{opt}}^*$, for optimal conversion to n output photons on resonance. (a) Linear conversion, $n = 1$ and $\gamma_b = 10\gamma_a$, results in one output mode with occupation $\langle \hat{b}^\dagger_0 \hat{b}_0 \rangle = 1$, cf. (d). (b) For nonlinear multiplication $n = 9$ and $\gamma_b = \gamma_a$, the duration of the outgoing pulse (the extent of $G^{(1)}$ along the diagonal) is much longer than the inverse instantaneous bandwidth of the amplifier (off-diagonal extent). $G^{(1)}$ becomes elliptical and possesses multiple eigenmodes with similar occupations. (c) For $\gamma_a = 10\gamma_b$, the pulse duration of the output pulse is comparable to the inverse bandwidth of the instantaneous spectrum, yielding a triangular $G^{(1)}$ diagonalizable to very few dominant eigenmodes, see (d). Ticks mark different time scales that help to characterize $G^{(1)}$.

now only requires the sum of the frequencies of all n output photons to match the frequency distribution of the input photon. The spectral distribution of output photons is now lifetime-broadened by γ_b adding to the spectral broadening of the input σ_ω, so that, in the time domain, $G^{(1)}$ can become substantially sharper in the off-diagonal directions.

Choosing a rather large (but still realizable) multiplication factor of $n = 9$, we will now discuss parameter regimes with different relations between T_{out} and T_{spec} of the $G^{(1)}$ function [Fig. 3(b)-(d)] and the resulting complex multimode structure.

We start by considering a resonant Gaussian single-photon input pulse (i.e., it contains frequencies $\omega_{\text{in}} \sim \omega_a \pm \sigma_\omega$ where $\sigma_\omega \ll \gamma_a, \gamma_b$ and choose the optimal Josephson driving energy (fixed by the rate matching argument to achieve the best possible photon multiplication). We are then left with one parameter to vary, namely the ratio of the loss rates γ_a/γ_b [52].

At $\gamma_b = \gamma_a$, Fig. 3(b), we find an elongated elliptic-like shape of $G^{(1)}$. In this regime, the frequency distribution of the output photons is spectrally broadened by $\gamma_b \gg \sigma_\omega$, resulting in a short time extent away from the diagonal, $T_{\text{spec}} \sim 1/\gamma_b$, as compared to the long duration of the output pulse along the diagonal, $T_{out} \sim 1/\sigma_\omega$. Diagonalization of such elliptic shapes with principal axes of strongly different lengths [53] ultimately yields a large number of eigenmodes with similar mean occupations, cf. Fig. 3(b).

Following what we learned from the $n = 1$ case, we turn to the regime where $\gamma_b \ll \gamma_a$ [Fig. 3(c)], where we expect the reduced γ_b to increase T_{spec} and thus a $G^{(1)}$ with comparable extent along and off the diagonal. Indeed, the $G^{(1)}$ function is of triangular shape with two similar timescales and can be diagonalized into very few eigenmodes with one strongly occupied main eigenmode carrying $\sim 75\,\%$ of the emitted photons. Its quantum state can thus be easily distinguished from vacuum [cf. Fig. 2(e)]. It is this regime, where $G^{(1)}$ is as 'symmetric' as possible and yields only one highly occupied mode, that will prove well-suited for the eventual detection of microwave photons.

B. Heterodyne Detection with a highly occupied eigenmode

In a typical experiment [43, 44, 54], a signal from the transmission line will first be amplified by a linear phase-preserving amplifier with gain G before recording both quadratures with a classical device. For a quantum-limited amplifier, the noise mode $\hat{r}$ can additionally be assumed to be in a vacuum state, so that the minimal noise required by quantum mechanics is added. For $G \gg 1$,

the signal after amplification, $\hat{J}^{(b)}(t) = \sqrt{G}\hat{b}_{\rm out}(t) + \sqrt{G-1}\hat{r}^\dagger$ can be treated as a classical variable in the subsequent signal processing [55]. The sketched experimental scenario corresponds to a quantum-optical heterodyne detection scheme, which can theoretically be described with a stochastic Schrödinger equation [56]. From the time-evolution (compare Appendix B), we obtain single trajectories $J_k^{(b)}(t) = \langle \hat{b}_{\rm out}\rangle_k + \xi_k(t)$. The stochastic white noise term $\xi_k(t)$ with mean $\mathrm{E}[\xi_k(t)] = 0$ is delta-correlated $\mathrm{E}[\xi_k(t+\tau)\xi_k(t)] \propto \delta(\tau)$ and simulates vacuum noise. The simulated $J_k^{(b)}(t)$ for a single trajectory then corresponds to the classical record of $J^{(b)}(t)/\sqrt{G}$ measured in a single run in its signal-to-noise ratio and all other statistical properties.

If vacuum is sent through the input transmission line to the ICTPM, cavity $\hat{b}$ will remain in its ground state with $\langle \hat{b}\rangle = 0$. If, on the other hand, a single-photon pulse is sent, the information acquired by the weak heterodyne measurement induces a feedback on the system's time evolution, such that cavity $\hat{b}$ will explore its phase-space and $\langle \hat{b}\rangle \neq 0$ during the response time of the ICTPM. Note that the modification of the system's time evolution by the quadrature measurement merely reflects our incrementally increasing knowledge about the system's state. Experimentally, circulators prevent any physical signal backflow from the detection apparatus to the system. Only in a numerical simulation is the quantity $\langle \hat{b}\rangle_k$ known for any single noise realization. In an experiment, the only accessible observable is $J_k^{(b)}$, which is dominated by noise, see Fig. 4(a). It is thus a crucial task to develop a reliable scheme for detecting the small signal created by an incoming photon in each single noise-dominated trajectory $J_k^{(b)}$. This will be provided in the sequel.

Assuming we knew that for a certain trajectory $J_k^{(b)}(t)$ a single-photon pulse impinged on the system at a certain arrival time, we could integrate the measured signal with the dominant output eigenmode corresponding to that arrival time, $\beta_k = \int_0^\infty v_0(t) J_k^{(b)}(t) dt$, to get one complex-valued number. If the same experiment is repeated multiple times, the mode-matched values β_k can be plotted in a histogram [see Fig. 4(a)]. This histogram samples the Husimi-Q function of the quantum state of the corresponding mode $\hat{b}_{v_0} = \int_0^\infty v_0(t)\hat{b}_{\rm out}(t)dt$ [55, 57–59]. When v_0 represents a highly occupied mode, the probability $p(\beta_k|\,1_{\rm in})$ to find $|\beta_k|$ at larger absolute values is greatly enhanced for a single-photon input compared to the corresponding probability $p(\beta_k|\,0_{\rm in})$ for a vacuum state [Fig. 4(b)]. By defining a click threshold, r_0, a simple decision process identifies photons in a trajectory k if $\beta_k > r_0$. For this scheme, it is therefore crucial to fabricate an ICTPM device which exhibits one highly occupied output mode, cf. Sec. III A. Then r_0 can be defined large enough to suppress dark counts, $p_{\rm dark} = p(|\beta_k| > r_0|\,0_{\rm in}) \ll 1$, while keeping the photon detection probability $p_{\rm click} = p(\beta_k > r_0|\,1_{\rm in})$ sufficiently large.

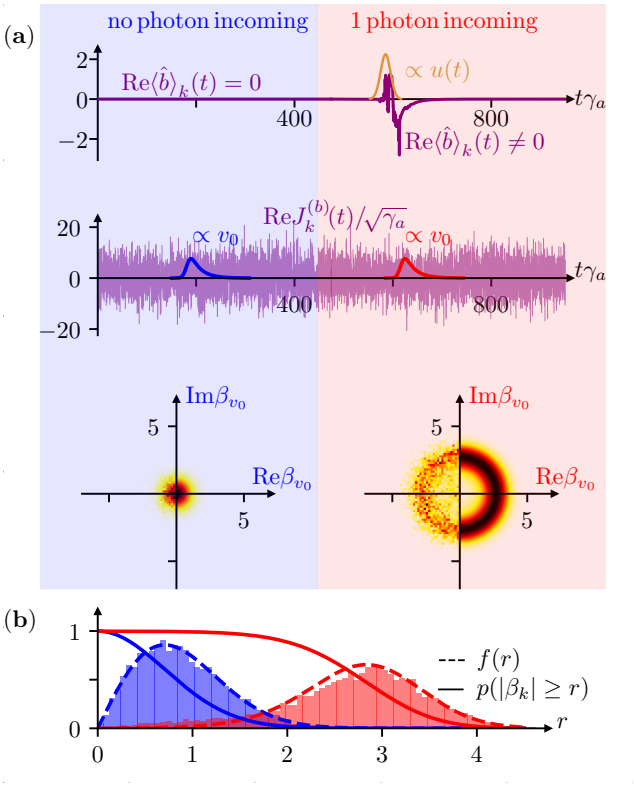

FIG. 4. (a) Weak measurement of the output from cavity $\hat{b}$ by heterodyne detection. A single trajectory of the numerical simulation yields $\langle \hat{b}\rangle = 0$, without incoming photon, and $\langle \hat{b}\rangle \neq 0$ during the photon multiplication process of the ICTPM when a single photon (Gaussian input mode in Fock state $|1\rangle_{\rm in}$, orange curve) impinges on cavity $\hat{a}$. Experimentally observable, however, is only the measured signal J_β dominated by noise, where information about photon arrivals seems lost. Integrating the measured signal with a mode envelope v_0 results in a single complex number, which samples the Husimi-Q function of v_0 at the specific integration time. (b) The probability density $f(r)$ for the radial component, $|\beta_k| = r$, clearly discriminates cases without an incoming photon (blue histogram and dashed theory curve) from the highly occupied output mode of the ICTPM after a photon arrival (red histogram and dashed theory curve). Defining a photon detection event, as $|\beta_k| > r$, for any chosen threshold r, the integrals $p(|\beta_k| \geq r) = \int_r^\infty d|\beta_k|\, f(|\beta_k|\,|1_{\rm in})$ (solid red line), $1 - p(|\beta_k| \geq r)$, and $\int_r^\infty d|\beta_k|\, f(|\beta_k|\,|0_{\rm in})$ (solid blue line) are the probability for correct, false negative, and false positive detection. [Parameters: $N_{\rm traj} = 10^4$ trajectories simulated, $\sigma_\omega = \gamma_b = \gamma_a/10$, $n = 9$, $E_J^* = E_{J,\rm opt}^*$].

In a real experimental setup, which tries to identify the arrival of single microwave photons at unknown arrival times within a long measurement trajectory, the obvious idea is now to replace the integration with the mode v_0 by a convolution, $\beta_k \to \beta_k(t) = \int_0^\tau v_0(t-\tau) J_k^{(b)}(\tau) d\tau$. This will introduce correlations between the values $\beta_k(t)$ within a correlation time $\tau_{\rm c}$ set by the mode shape v_0 (beyond any correlations that may be present within the

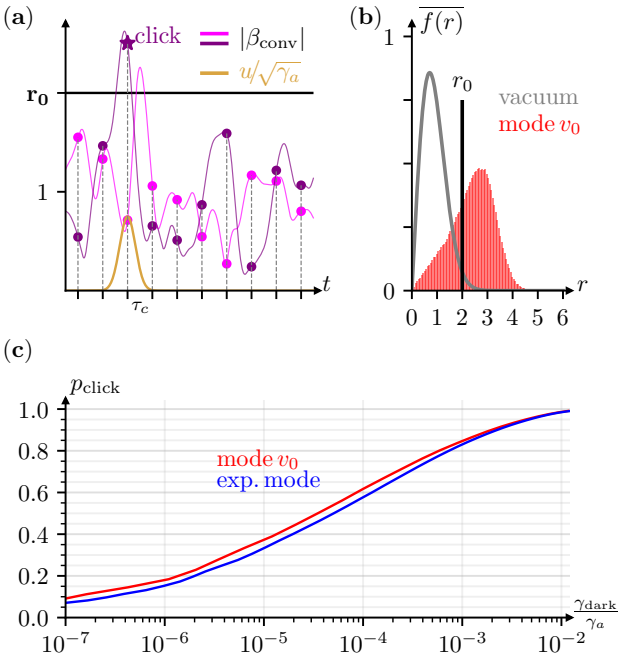

FIG. 5. (a) Convolution $\beta_{\rm conv}$ of two recorded trajectories with a single mode v_0, for a simulation with an input photon in a Gaussian mode $u(t)$. The convolution induces correlations within a correlation time $\tau_{\rm c}$. Measuring stroboscopically once within $\tau_{\rm c}$ (circles) avoids induced two-time correlations and reduces the effective number of measurement points. A photon detection event at time t is defined when $|\beta_{\rm conv}| > R_0$. (b) The resulting probability distributions, where averaging the instances of stroboscopic measurement over an interval of length $\tau_{\rm c}$ for an unbiased comparison to experiment results in a slight deterioration compared to Fig. 4(b). (c) The resulting performance curve showing detection probability versus the dark-count rate for convolution with the dominant eigenmode v_0 and an exponential mode $v_{\rm exp}(t) \propto \exp[-\gamma_b t/2]$. The comparison with an exponential mode with comparable timescales demonstrates that a small mismatch between detection mode and eigenmode (or similarly between assumed and actual input mode) only slightly degrades the performance. [Parameters see Fig. 4].

dynamics of $\hat{b}_{\rm out}$). One simple adequate method to get roughly uncorrelated discrete measurement points and thereby avoid double-counting a single photon while also keeping the dark count rate low is to stroboscopically take one measurement point within each time interval $\tau_{\rm c}$, cf. Fig. 5(a).

The stroboscopic scheme focuses on detecting single photons and more elaborate schemes will be needed to detect two (or more) nearly coincidental photons. To avoid such a scenario of overlapping modes, the mean rate of incoming photons in an experiment should be kept sufficiently small, $\gamma_{\rm ph} < \tau_{\rm c}^{-1}$. Employing the presented scheme, each chosen threshold value will result in a pair of numbers: t The photon detection probability and the associated dark count rate, which can be combined in a single performance curve, see Fig. 5(c). Here, we report, for instance, an achieved photon detection probability of $p_{\rm click} \approx 0.85$ for a dark count rate $\gamma_{\rm dark} = 5 \cdot 10^{-4}\gamma_a$, where filtering with the highest occupied eigenmode induced a correlation time $\tau_{\rm c} \approx 30/\gamma_a$. For an experiment with an average photon rate of $\gamma_{\rm ph} = \gamma_a/150 \approx 1/(5\tau_{\rm c})$, this means that within a time $\Delta t = 15{\cdot}10^3/\gamma_a$ our scheme will correctly detect 78.3 while producing 7.5 dark counts, where we expect an average of 100 incoming photons. We explain specific steps how these numbers can be improved further below in Sec. IV.

C. Detection in the multi-mode regime

The detection scheme of Sec. III B crucially relies on an output, where one eigenmode has a high occupation. That allows us to clearly distinguish the radial distribution of the Husimi-Q function of that mode from the vacuum one. Turning now to a parameter regime, where there are *many* eigenmodes, each with low occupation, cf. Fig. 3(b), the question arises: How to detect the signature of an impinging photon?

Technically, this means to retrieve a finite expectation value $\sqrt{\gamma_b}\langle\hat{b}\rangle$ in the background of a noisy measurement trajectory $J_k^{(b)}(t) = \sqrt{\gamma_b}\langle\hat{b}\rangle_k + \xi_k(t)$. To identify a suitable photon-detection mode, the expectation values $\langle\hat{b}\rangle$ of numerically simulated trajectories, see Fig. 6(a), can be used. Their shape can be approximated by an exponential function, $f(t) \propto \exp[-\gamma_b(t-t_0)/2]$ (blue curve) for times larger than the arrival time, $t \geq t_0$. If the recorded measurement is filtered with $f(t)$, we can thus expect that the filtered measurement peaks at the arrival times of photons. The fact that the highest-occupied eigenmode [with a Gaussian shape, cf. red curve in Fig. 6(a)] does not match the typical shape of $\langle\hat{b}\rangle$, and therefore yields an imperfect overlap, makes filtering with this eigenmode unfavorable in this parameter regime. Fig. 6(b) confirms this reasoning: Filtering the measurement with an exponential mode yields noticeably better probabilities for photon detection. Nonetheless, compared to the example given in Sec. III B, we will now only detect 53.3 of 100 incoming photons (given the same number of 7.5 dark counts for a photon rate of $\gamma_{\rm ph} = \gamma_a/150$).

To draw preliminary conclusions from the scenarios presented above, it clearly is beneficial to design a detector in such manner that it produces *one highly-occupied output eigenmode*. Moreover, the detection probability is obviously enhanced if the multiplication factor n is increased. Experimentally, multiplication factors are probably limited to $n \lesssim 5{-}10$, as either Josephson energy E_J, or zero-point fluctuations, α_0, β_0, have to be increased to achieve a sufficiently large transition matrix element for the multiplication process, which brings about such complications as the breakdown of the rotating wave approximation and the appearance of undesired competing

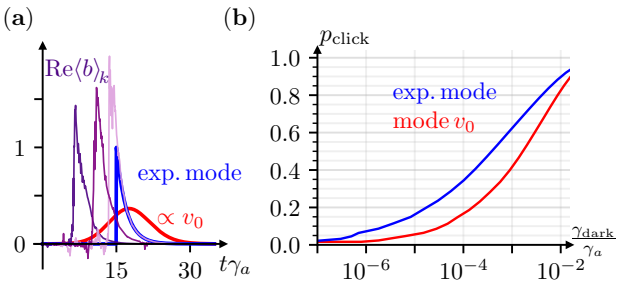

FIG. 6. (a) The expectation value $\langle\hat{b}\rangle$ for individual trajectories (shades of purple), which (while not measurable) is available from numerical simulations, can be used to find a suitable detection mode [here, a simple exponential mode $v_{\exp}(t) = \sqrt{\gamma_b}\theta(t-t_c)\exp[-\gamma_b(t-t_c)/2]$ (blue)]. In a regime of multi-mode output, that mode performs better than the highest-occupied eigenmode v_0 (red) as seen by comparing the curves of detection probability vs. dark count rate in (b). [Parameters: $N_{\rm traj} = 10^4$ trajectories simulated, $\sigma_\omega = \gamma_a/10$, $\gamma_b = \gamma_a$, $n = 9$, $E_J^* = E_{J,\rm opt}^*$].

resonances. One way to overcome such experimental limitations is a cascaded version of the ICTPM, where the multiplication process happens in two stages as will be discussed in the remainder of this paper.

IV. PHOTON DETECTION IN TWO-STAGE AMPLIFIER

The idea of photon multiplication in two stages is straightforward. The two-stage ICTPM [compare Appendix A 2, Fig. 9(a)] incorporates a third central cavity $\hat{c}$ without input or output lines, so that $\gamma_c \approx 0$, and with zero-point fluctuations κ_0. Two dc-driven processes through two Josephson junctions now drive multiplication in two separate stages, if resonance conditions are met: $2eV_{\rm dc,1} = \hbar(n_1\omega_c - \omega_a)$, transfers one impinging photon from cavity $\hat{a}$ to n_1 photons in cavity $\hat{c}$, and $2eV_{\rm dc,2} = \hbar(n_2\omega_b - \omega_c)$, transfers each photon from cavity $\hat{c}$ to n_2 photons in cavity $\hat{b}$. While the basic working scheme has been easily generalized to two (or even more) stages, the internal dynamics of a multi-stage amplifier becomes more complex. For the single-stage ICTPM and single-photon input, there is a single relevant coherent process, namely $|1\rangle_a|0\rangle_b \leftrightarrow |0\rangle_a|n\rangle_b$. Specifically, after the first photon has leaked from cavity $\hat{b}$ to the output transmission line, coherent back-transfer to cavity $\hat{a}$ (and subsequent loss to the left output) becomes impossible. For the two-stage ICTPM only the first multiplication stage behaves similarly (coupling only the two states $|1\rangle_a|0\rangle_c \leftrightarrow |0\rangle_a|n_1\rangle_c$.)

The complete transfer of n_1 photons in cavity $\hat{c}$ to cavity $\hat{b}$ in the second amplification stage involves transitions other than the one between $|n_1\rangle_c|0\rangle_b \leftrightarrow |n_1-1\rangle_c|n_2\rangle_b$. To be specific, let us consider an example where one photon from cavity $\hat{c}$ has been multiplied to n_2 photons in cavity $\hat{b}$ arriving at a state $|n_1-1\rangle_c|n_2\rangle_b$. Cavity $\hat{b}$ may now lose one or more photons, so that the consecutive multiplication process may involve the transitions $|n_1-1\rangle_c|m\rangle_b \leftrightarrow |n_1-2\rangle_c|m+n_2\rangle_b$ with $m = 0\ldots, n_2$. In fact, many of these coherent forward and backward photon-transfer processes in the second multiplication stage compete with the progressive loss of photons from the output cavity $\hat{b}$ until all but $n_2 - 1$ photons have leaked out.

The nonlinearity of the Josephson junction and the values of the zero-point fluctuations, β_0, κ_0, affect the Hamiltonian matrix elements of these transitions of the second stage. To understand how, consider the two parts of the driving Hamiltonian in the lab frame $\hat{H}_J = \hat{H}_{J1} + \hat{H}_{J2}$,

$$\begin{aligned}\hat{H}_{J1} &= -E_{J1}\cos\left[\frac{2e}{\hbar}V_{\rm dc,1}t + \alpha_0(\hat{a}^\dagger + \hat{a}) + \kappa_0(\hat{c}^\dagger + \hat{c})\right]\\ \hat{H}_{J2} &= -E_{J2}\cos\left[\frac{2e}{\hbar}V_{\rm dc,2}t + \kappa_0(\hat{c}^\dagger + \hat{c}) + \beta_0(\hat{b}^\dagger + \hat{b})\right].\end{aligned} \tag{4}$$

After moving to a rotating frame (using the resonance condition), we arrive for the second stage at $\hat{H}_{{\rm RWA},J2} = \hat{h}_2^\dagger + \hat{h}_2$ with

$$\hat{h}_2 = \frac{\epsilon_{J,2}}{2n_2!} : \hat{c}\hat{b}^{\dagger n_2}\frac{J_1\left(2\kappa_0\sqrt{\hat{c}^\dagger\hat{c}}\right)}{\kappa_0\sqrt{\hat{c}^\dagger\hat{c}}}\frac{J_{n_2}\left(2\beta_0\sqrt{\hat{b}^\dagger\hat{b}}\right)\cdot n_2!}{\left(\beta_0\sqrt{\hat{b}^\dagger\hat{b}}\right)^{n_2}} : \tag{5}$$

which now contains normal-ordered Bessel functions (cf. Appendix A 2), while the first-stage term $\hat{H}_{J1}$ turns into Eq. (2) with $(\beta_0, \hat{b}^{(\dagger)})$ replaced by $(\kappa_0, \hat{c}^{(\dagger)})$. The Josephson energies are parametrized as $\epsilon_{J,1} = E_{J,1}^*\alpha_0\kappa_0^{n_1}$ and $\epsilon_{J,2} = E_{J,2}^*\kappa_0\beta_0^{n_2}$, where we will also denote values $\epsilon_{J,1}^{\rm opt} = \hbar\sqrt{\gamma_a\gamma_b}\sqrt{n_1\cdot n_1!}$ and analogously $\epsilon_{J,2}^{\rm opt} = \hbar\sqrt{\gamma_a\gamma_b}\sqrt{n_2\cdot n_2!}$, which would give optimal conversion in a single-stage ICTPM.

Remarkably, for a single resonant impinging photon, perfect photon multiplication to $n_1\cdot n_2$ outgoing photons is still possible. Indeed, for the linear case, $n_1 = n_2 = 1$, one finds the condition [43],

$$\sqrt{\gamma_a}\frac{\epsilon_{J,2}}{\epsilon_{J,2}^{\rm opt}} = \sqrt{\gamma_b}\frac{\epsilon_{J,1}}{\epsilon_{J,1}^{\rm opt}}\,. \tag{6}$$

This expression also gives the correct scaling for the case of general multiplication factors and small zero-point fluctuations, see Fig. 7(a) where $n_1 = n_2 = 3$ and $\gamma_a = 100\gamma_b$.

However, contrary to the single-stage case, where the rate-matching expression holds throughout, the dynamics of the two-stage ICTPM for generic multiplication factors is more complex, and the strictly linear relation (6) is replaced by the line of optimal conversion in Fig. 7(a). In general, both the zero-point fluctuations, β_0, κ_0, via their effect on the transition matrix elements between higher

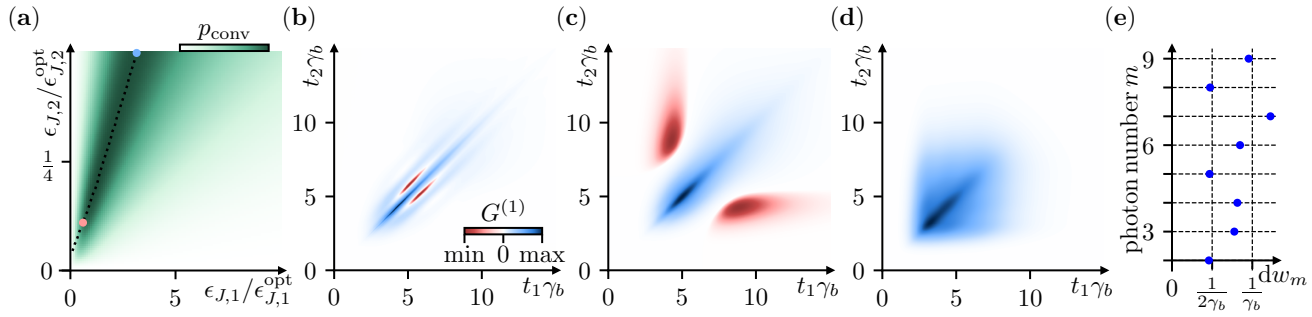

FIG. 7. (a) Probability of photon conversion for the two-stage ICTPM for multiplication factors $n_1 = n_2 = 3$ (max. 9 output photons). Given ϵ_{J1}, best conversion is achieved for ϵ_{J2} along the black dotted line. (b-d) Two-time first-order coherence functions $G^{(1)}$ yield a coherence pattern due to Rabi-oscillations in (b) [parameters marked with blue dot in (a)] with multiple weakly occupied eigenmodes (max. mean photon occupation is $\langle \hat{b}_{v_0}^\dagger \hat{b}_{v_0} \rangle = 1.52$ photons). (c) Reducing ϵ_{J2} [red dot in (a)] improves the occupation $\langle \hat{b}_{v_0}^\dagger \hat{b}_{v_0} \rangle = 2.89$ of the largest-occupied eigenmode, which is however insufficient due to poor overall photon conversion. (d) Zero-point fluctuations $\kappa_0 = 0.2$ and $\beta_0 \approx 1.66$ can suppress internal ICTPM processes to obtain a few-mode regime with one dominant eigenmode, $\langle \hat{b}_{v_0}^\dagger \hat{b}_{v_0} \rangle = 6.42$. (e) Mean waiting times $dw_m = w_{m,m-1}$ of the m-th photon emitted from cavity $\hat{b}$ for parameters in (d), obtained by a quantum jump approach (explanation given in main text). [Parameters: $\sigma_\omega = \gamma_b = \gamma_a/100$ (a-c): $\kappa_0, \beta_0 \ll 1$ limit; (d): $\epsilon_{J,1}/\epsilon_{J,1}^{\mathrm{opt}} = 0.9$, $\epsilon_{J,2}/\epsilon_{J,2}^{\mathrm{opt}} = 0.1$; color scales in (b)-(d) stretched, where [min, max] is (b) [-0.224, 2.233] (c) [-0.031, 1.852] (d) [0, 1.388] in units of γ_b].

Fock-states, and the two Josephson energies $\epsilon_{J,1/2}$ affect the conversion probability. In consequence, we will have to refrain from a complete systematic exploration of the full parameter space in our goal of finding a regime of a highly occupied eigenmode of the output field, which can be used for detecting photons analogously to the scheme presented in Sec. III B. Instead, drawing on the lessons from the single-stage case and our understanding of the impact of nonlinearities and zero-point fluctuations, we will show how to locate a favorable regime with a highly occupied output mode in Sec. IV A, before analyzing achievable detection efficiencies in Sec. IV B.

A. Output Modes for the two-stage ICTPM

We first analyze the output modes in the limit of zero-point fluctuations, $\kappa_0, \beta_0 \ll 1$, where the Bessel functions in (5) and thus any nontrivial dependence of the results on κ_0 and β_0 can be neglected. Following the lessons learned in Sec. III A, we first choose $\gamma_b = \sigma_\omega \ll \gamma_a$ and pick a rather large value $\epsilon_{J,2} = \epsilon_{J,2}^{\mathrm{opt}}/2$, on the line of optimal overall conversion in Fig. 7(a) to analyze the $G^{(1)}$-function in Fig. 7(b).

The coherence function reveals a multi-mode structure with pronounced coherence fringes. The number of photons leaked to the output line, $\int_0^t dt' G^{(1)}(t', t')$, indicates that the time interval, when pronounced coherence fringes occur, starts once about three photons have leaked and lasts until less than three photons remain in the ICTPM cavities. Simulating quantum jump trajectories furthermore confirms that after three photons have leaked the system is preferentially found with all 6 remaining photons in cavity $\hat{b}$. Taking into account the various timescales one can identify in the system, this suggests an evolution, where a coherent dynamic between a highly occupied cavity $\hat{b}$ and $\hat{c}$ sets in only after several multiplication processes from $\hat{c}$ to $\hat{b}$ have taken place and some photons have leaked, and that this dynamics stops once only a few photons are left.

Apparently, the interplay of different processes with drastically different timescales leads to a multi-mode emission, which (as learned above) is not conducive to detection. To avoid the scenario described above, we hence try to reduce the rate of photon accumulation in $\hat{b}$. Achieving this by quenching the Josephson coupling strength by a factor of ten to $\epsilon_{J,2} = \epsilon_{J,2}^{\mathrm{opt}}/20$ should yield similar rates for the conversion to cavity $\hat{b}$ and the decay rate from it, thus avoiding the piling up of a large occupation in $\hat{b}$. However, for such a small $\epsilon_{J,2}$, the rate matching expression of Eq. (6) fails and we find photon reflection into the input transmission line and poor photon conversion, cf. the regime for small $\epsilon_{J,2}$ in Fig. 7(a). Although now the $G^{(1)}$ function shows fewer fringes, see Fig. 7(c), and the dominant eigenmode carries more photons than before (2.9 of 7.7 outgoing photons), the distinguishability from a vacuum state is still too weak for a satisfying photon detection.

A second option to avoid large photon accumulation in $\hat{b}$ involves finite zero-point fluctuations. To delay the second photon multiplication process from $\hat{c}$ to $\hat{b}$, until $\hat{b}$ has emptied, we can fix $\beta_0^2 \approx 1.66$ to a root of the Laguerre polynomial appearing in the nonlinear corrections of the Hamiltonian matrix elements $\propto L_2^{(3)}(\beta_0^2)$, corresponding to the transfer $(m_a, m_b = 2, m_c) \leftrightarrow (m_a, 5, m_c - 1)$, see Eqs. (A13), (A14). The waiting-time distributions of the leaking photons in Fig. 7(f), which can be obtained

by simulations with a quantum jump approach, nicely confirm this picture: As we expect, the photons number two, five and eight leak out after a mean waiting time of $1/(2\gamma_b)$, while the photons number three, six and nine leak after $\sim 1/\gamma_b$, where these two different waiting times match the average decay time of the states $|2\rangle_b$ and $|1\rangle_b$, respectively. The waiting times of the other photons (number four and seven) are associated with the conversion of a cavity $\hat{c}$-photon into cavity $\hat{b}$-photons and one subsequent decay, for which similar timescales γ_b^{-1} are observed. In this regime, we find the desired $G^{(1)}$-function, which is dominated by a highly occupied single mode, cf. Fig. 7(d) with mean occupation of 6.42 out of 8.87 transmitted photons.

B. Heterodyne Detection for the two-stage ICTPM

In the last subsection, despite the more complex two-stage dynamics, we found a regime with dominant single-mode occupation. Since that occupation for the 3×3 amplifier is not quite as high as for the single-stage $n = 9$ case, we turn to a 4×4 scenario, where we similarly identify a good regime of $\epsilon_{J,1/2}$ for a finite β_0. The Husimi-Q function of the dominant output eigenmode is shown in Fig. 8(a). The corresponding occupation distribution, Fig. 8(b), confirms large occupation of higher Fock-states with a curious (and as yet not understood) suppression of states $|15\rangle$ and $|13\rangle$. Crucially, separability from the vacuum, Fig. 8(c), is good. Proceeding in the same analysis scheme as for the single stage, cf. Sec. III B, we arrive at the performance curve shown in Fig. 8(d) and can, for instance for a photon rate of $\gamma_{\rm ph} = 1/(5\tau_c) = \gamma_a/3000$, detect 84.5 out of 100 photons correctly with 3 dark counts. This corresponds to a dark count rate of $\gamma_{\rm dark} = 10^{-5}\gamma_a$, or one dark count in a time equivalent to 1000 times the length of the impinging Gaussian pulse. While the investigated two-stage ICTPM only slightly outperforms the single-stage device [c. f. Fig. 4(d) and 5(d)], it uses more easily achievable parameters for Josephson driving strengths and photon multiplication factors ($n_1 \times n_2 = 4^2$ versus $n = 9$). Moreover, one expects very favorable improvements even upon increasing only to $n_{1/2} = 5$, which, however, may already reach the limits of a comprehensive numerical analysis. The parameters assumed in our schemes for zero-point fluctuations, quality factors and Josephson energies are experimentally accessible. While Josephson energies can be tuned in-situ using a SQUID geometry, large zero-point fluctuations such as $\beta_0 \approx 1.67$ can be engineered when increasing the inductance-to-capacitance ratio of the resonator (e.g. zero-point fluctuations of $\mathcal{O}(1)$ have been achieved in [60, 61]).

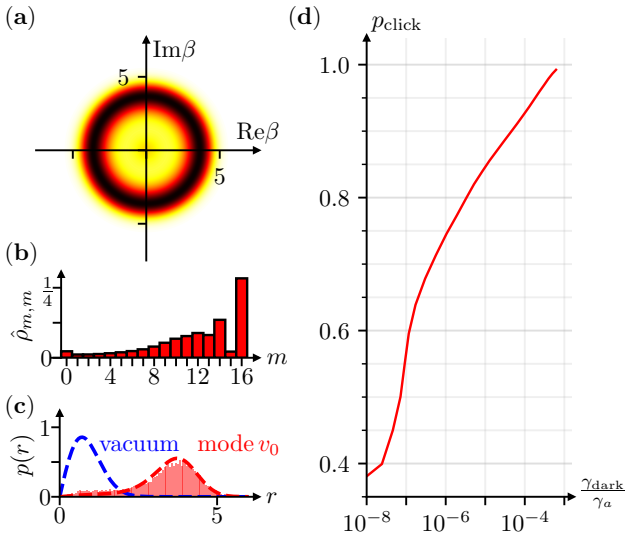

FIG. 8. (a) The quantum state $\hat{\rho}$ of the dominant eigenmode for the two-stage ICTPM device of Fig. 7(d) yields a ring-shaped Husimi-Q distribution with large $\langle|\beta|\rangle$ corresponding to (b) large occupations of high Fock states. (c) The resulting histogram of $|\beta| = r$ can clearly be distinguished from the vacuum distribution (theory curves with dashed lines) and (d) a similar detection scheme as before yields improved detection probabilities. [Parameters: $n_1 = n_2 = 4$, $\sigma_\omega = \gamma_b = \gamma_a/100$, $\kappa_0 = 0.2$, $\beta_0 = 1.67$, $\epsilon_{J,1} = 0.89\epsilon_{J,1}^{\rm opt}$, $\epsilon_{J,2} = 0.1\epsilon_{J,2}^{\rm opt}$, $\tau_c = 60$].

V. CONCLUSION

We have demonstrated that an inelastic Cooper pair tunneling photon multiplier can be used to detect a single impinging microwave photon. In such a system, two microwave modes are connected in-series to a dc-driven Josephson junction which drives a photon multiplication process to convert one photon from mode $\hat{a}$ to n photons in cavity $\hat{b}$. When the Josephson energy fulfills an impedance-matching condition, a resonant Gaussian photon pulse impinging from the left transmission line is absorbed by cavity $\hat{a}$ and (quasi-)deterministically converted to n photons leaking from cavity $\hat{b}$ into the right transmission line, where they can be detected by a heterodyne detection scheme which models the experimental scenario of a weak quadrature measurement after quantum-limited amplification of the output signal. The detection scheme relies not only on a high conversion probability, but on a highly-occupied output mode, whose Husimi-Q function can be well discriminated from vacuum. We have therefore characterized the multi-mode output of the ICTPM in different parameter regimes and identified optimal parameter ranges that ensure both near-perfect photon conversion and high photon occupation in a single output pulse.

Our detection scheme can be modified or extended for other scenarios, like detection and counting of the simultaneous arrival of several input photons or optimized for different expected pulse shapes.

We have presented a single-stage setup with a multiplication factor of $n \approx 9$, which is experimentally chal-

lenging due to unwanted cavity excitations from higher resonances due to the required large dc voltage, as well as a two-stage extension. While in principle three multiplication stages are possible, the two-stage device with multiplication of $n = 4\cdot4$ yields sufficient detection probabilities for low dark counts: Realistic simulations of the experimental scenario with an impinging Gaussian pulse of length T yield a photon detection probability of 84.5% with $10^{-3}/T$ dark count rate, which is competitive with existing microwave detectors. Combining the ICTPM with other setups for microwave-photon amplification or augmenting the two stage multiplication to $n > 4$ will significantly improve the detection efficiency beyond the numbers reported here. The ICTPM based on photon number amplification realizes a detector for single itinerant microwave photons without dead times, with low dark counts and detection efficiencies well beyond 80%.

VI. ACKNOWLEDGEMENTS

JA acknowledges financial support from the German Science Foundation (DFG) through grants AN336/13-1, AN336/18-1; JA, CP, BK through the Center for Integrated Quantum Science and Technology (IQST), and MH and NB from the Natural Sciences and Engineering Research Council of Canada (NSERC) through grants RGPIN-2025-06130, ALLRP 565748-22 and from the Québec government through Prompt Quebec grant 05_AQ22.001-V3.

Appendix A: Hamiltonians in rotating Rotating-Wave Approximation

In this Appendix, we provide the derivation for the rotating-wave Hamiltonians of the ICTPM devices studied in the main text.

1. Single-Stage Amplifier

The circuit from Fig. 1(a), consisting of two microwave cavities connected in series with a dc-biased Josephson junction, can be described by the Hamiltonian

$$\hat{H}_1 = \hat{H}_{\rm res} + \hat{H}_J \tag{A1}$$

consisting of a free resonator Hamiltonian which is driven by the Josephson junction,

$$\hat{H}_{\rm res} = \hbar\omega_a \hat{a}^\dagger\hat{a} + \hbar\omega_b \hat{b}^\dagger\hat{b} \tag{A2}$$

$$\hat{H}_J = -E_J \cos\left[\omega_{\rm dc}t + \alpha_0(\hat{a}^\dagger + \hat{a}) + \beta_0(\hat{b}^\dagger + \hat{b})\right]. \tag{A3}$$

We assume that the dc-voltage associated with the frequency $\omega_{\rm dc} = 2eV_{\rm dc}/\hbar$ is applied at the resonance $\omega_{\rm dc} \approx n\omega_b - \omega_a$ and move to a rotating reference frame defined by the unitary transformation $\hat{U} = \hat{U}_a \otimes \hat{U}_b$ with

$$\hat{U}_r = \exp[i\phi_{{\rm rot},r}\hat{r}^\dagger\hat{r}] = \exp[i(\omega_{{\rm rot},r}t + \phi_r)\hat{r}^\dagger\hat{r}] \tag{A4}$$

for $r = a, b$. Fixing the sum of rotating-frame frequencies to the driving frequency, $\omega_{\rm dc} = n\omega_{{\rm rot},b} - \omega_{{\rm rot},a}$ transforms the free resonator Hamiltonian to

$$\hat{H}_{\rm res,rot} = \hbar(\omega_a - \omega_{\rm rot,a})\hat{a}^\dagger\hat{a} + \hbar(\omega_b - \omega_{\rm rot,b})\hat{b}^\dagger\hat{b}\,. \tag{A5}$$

Throughout the paper, we assume perfectly resonant driving, such that $\hat{H}_{\rm res,rot} = 0$. In the driving Hamiltonian, we now additionally perform a rotating wave approximation (keeping only slowly oscillating terms), which yields

$$\hat{H}_{J,\rm RWA} = \frac{E_J^*\alpha_0\beta_0^n}{2n!} : (\hat{a}\hat{b}^{\dagger n} + \hat{a}^\dagger\hat{b}^n)\frac{J_1\left(2\alpha_0\sqrt{\hat{a}^\dagger\hat{a}}\right)}{\alpha_0\sqrt{\hat{a}^\dagger\hat{a}}}\frac{J_n\left(2\beta_0\sqrt{\hat{b}^\dagger\hat{b}}\right)\cdot n!}{\left(\beta_0\sqrt{\hat{b}^\dagger\hat{b}}\right)^n} : \tag{A6}$$

Here, $E_J^* = E_J \cdot e^{-(\alpha_0^2+\beta_0^2)/2}$ is the renormalized Josephson energy, J_n are Bessel functions of the first kind, and the colons signal normal ordering of operators. The Hamiltonian contains only nonzero matrix elements in the entries $H^*_{m_a+1,m_b|m_a,m_b+n} = H_{m_a,m_b+n|m_a+1,m_b} = \langle m_a|\langle m_b+n|\hat{H}_{J,\rm RWA}|m_a+1\rangle|m_b\rangle$ (with $m_a, m_b \in \mathbb{N}_0$), where

$$H_{m_a,m_b+n|m_a+1,m_b} = \frac{E_J^*\alpha_0\beta_0^n}{2n!}\left[\sqrt{m_a+1}\frac{L^{(1)}_{m_a}(\alpha_0^2)}{L^{(1)}_{m_a}(0)}\right]\cdot\left[\sqrt{\frac{(m_b+n)!}{(m_b)!}}\frac{L^{(n)}_{m_b}(\beta_0^2)}{L^{(n)}_{m_b}(0)}\right] \tag{A7}$$

and $L_m^{(n)}$ are generalized Laguerre polynomials. For a single incoming photon pulse, the Hamiltonian dimension restricts $m_a = m_b = 0$, yielding only two nonzero matrix elements

$$H_{0,n|1,0} = H^*_{1,0|0,n} = \frac{E_J^* \alpha_0 \beta_0^n}{2n!} \langle 0_a|\hat{a}|1_a\rangle\langle n_b|\hat{b}^{\dagger n}|0_b\rangle = \frac{E_J^* \alpha_0 \beta_0^n}{2\sqrt{n!}}\,. \tag{A8}$$

Since only the lowest levels couple, we see that the fractions of Bessel functions in (A6) are not involved, which yields Hamiltonian (2) from the main text.

2. Two-Stage Amplifier

Starting now at the Hamiltonian $\hat{H}_2 = \hat{H}_{\rm res} + \hat{H}_{J1} + \hat{H}_{J2}$, where now

$$\hat{H}_{\rm res} = \hbar\omega_a \hat{a}^\dagger\hat{a} + \hbar\omega_b \hat{b}^\dagger\hat{b} + \hbar\omega_c \hat{c}^\dagger\hat{c} \tag{A9}$$

$$\hat{H}_{J1} = -E_{J1}\cos\left[\omega_{{\rm dc},1}t + \alpha_0(\hat{a}^\dagger + \hat{a}) + \kappa_0(\hat{c}^\dagger + \hat{c})\right] \tag{A10}$$

$$\hat{H}_{J2} = -E_{J2}\cos\left[\omega_{{\rm dc},2}t + \kappa_0(\hat{c}^\dagger + \hat{c}) + \beta_0(\hat{b}^\dagger + \hat{b})\right]\,. \tag{A11}$$

and $\omega_{{\rm dc},i} = 2eV_{{\rm dc},i}/\hbar$ such that $\omega_{\rm dc,1} = n_1\omega_c - \omega_a$ and $\omega_{\rm dc,2} = n_2\omega_b - \omega_c$, an analogous unitary transformation $\hat{U} = \hat{U}_a \otimes \hat{U}_b \otimes \hat{U}_c$ (with $\hat{U}_r$ defined as in Eq. A4) yields $\hat{H}_{\rm res} = 0$ on resonance. The rotating-wave approximation then yields

$$\begin{aligned}
\hat{H}_{{\rm RWA},J1} &= \frac{E^*_{J,1}\alpha_0\kappa_0^{n_1}}{2n_1!} : \hat{a}\hat{c}^{\dagger n_1} \frac{J_1\left((2\alpha_0\sqrt{\hat{a}^\dagger\hat{a}}\right)}{\alpha_0\sqrt{\hat{a}^\dagger\hat{a}}} \frac{J_{n_1}\left(2\kappa_0\sqrt{\hat{c}^\dagger\hat{c}}\right)\cdot n_1!}{\left(\kappa_0\sqrt{\hat{c}^\dagger\hat{c}}\right)^{n_1}} : + \text{h.c.} \\
\hat{H}_{{\rm RWA},J2} &= \frac{E_{J,2}\kappa_0\beta_0^{n_2}}{2n_2!} : \hat{c}\hat{b}^{\dagger n_2} \frac{J_1\left(2\kappa_0\sqrt{\hat{c}^\dagger\hat{c}}\right)}{\kappa_0\sqrt{\hat{c}^\dagger\hat{c}}} \frac{J_{n_2}\left(2\beta_0\sqrt{\hat{b}^\dagger\hat{b}}\right)\cdot n_2!}{\left(\beta_0\sqrt{\hat{b}^\dagger\hat{b}}\right)^{n_2}} : + \text{h.c.}
\end{aligned} \tag{A12}$$

with $E^*_{J1} = E_{J1}e^{-(\alpha_0^2+\kappa_0^2)/2}$ and $E^*_{J2} = E_{J2}e^{-(\kappa_0^2+\beta_0^2)/2}$. Here, nonlinear corrections by the Bessel functions must always included, modifying the Hamiltonian transition matrix entries. They are

$$H_{m_a,m_b,m_c+n_1|m_a+1,m_b,m_c} = \frac{E^*_{J1}\alpha_0\kappa_0^{n_1}}{2n_1!}\left[\sqrt{m_a+1}\frac{L^{(1)}_{m_a}(\alpha_0^2)}{L^{(1)}_{m_a}(0)}\right]\cdot\left[\sqrt{\frac{(m_c+n_1)!}{(m_c)!}}\frac{L^{(n_1)}_{m_c}(\kappa_0^2)}{L^{(n_1)}_{m_c}(0)}\right] \tag{A13}$$

$$H_{m_a,m_b+n_2,m_c|m_a,m_b,m_c+1} = \frac{E^*_{J2}\kappa_0\beta_0^{n2}}{2n_2!}\left[\sqrt{m_c+1}\frac{L^{(1)}_{m_c}(\kappa_0^2)}{L^{(1)}_{m_c}(0)}\right]\cdot\left[\sqrt{\frac{(m_b+n_2)!}{(m_b)!}}\frac{L^{(n_2)}_{m_b}(\beta_0^2)}{L^{(n_2)}_{m_b}(0)}\right] \tag{A14}$$

Appendix B: Cascaded Master Equation Including Quantum Pulses

The Lindblad master equation, that includes quantum pulses modeled as auxiliary cavities, is

$$\frac{d\hat{\rho}}{dt} = -\frac{i}{\hbar}[\hat{H}_{\rm tot},\hat{\rho}] + \mathcal{L}_a[\hat{\rho}] + \mathcal{L}_b[\hat{\rho}]\,. \tag{B1}$$

The dissipation (for $i = a, b$) exhibits the standard Lindblad form

$$\mathcal{L}_i[\hat{\rho}] = \hat{L}_i\hat{\rho}\hat{L}_i^\dagger - \frac{\hat{L}_i^\dagger\hat{L}_i\hat{\rho} + \hat{\rho}\hat{L}_i^\dagger\hat{L}_i}{2}\,. \tag{B2}$$

The total Hamiltonian $\hat{H}_{\rm tot} = \hat{H}_{\rm sys} + \hat{H}_{\rm int}$ now consists of the system Hamiltonian and coherent interactions

$$\begin{aligned}
\hat{H}_{\rm int} =& \frac{i\hbar}{2}\left[\sqrt{\gamma_a}g_{u_a}\hat{a}_u^\dagger\hat{a} + \sqrt{\gamma_a}g^*_{v_a}\hat{a}^\dagger\hat{a}_v + g_{u_a}g^*_{v_a}\hat{a}_u^\dagger\hat{a}_v - \text{h.c.}\right] \\
&+\frac{i\hbar}{2}\left[\sqrt{\gamma_b}g_{u_b}\hat{b}_u^\dagger\hat{b} + \sqrt{\gamma_b}g^*_{v_b}\hat{b}^\dagger\hat{b}_v + g_{u_b}g^*_{v_b}\hat{b}_u^\dagger\hat{b}_v - \text{h.c.}\right]
\end{aligned} \tag{B3}$$

between the auxiliary cavities and the system. The Hamiltonian together with now modified loss-operators

$$\hat{L}_a = \sqrt{\gamma_a}\hat{a} + g^*_{u_a}\hat{a}_u + g^*_{v_a}\hat{a}_v \tag{B4}$$

$$\hat{L}_b = \sqrt{\gamma_b}\hat{b} + g^*_{u_b}\hat{b}_u + g^*_{v_b}\hat{b}_v \tag{B5}$$

ensure in a cascaded manner [45, 46, 62] a directional influence between the subsystems: The input cavities $\hat{a}_u$

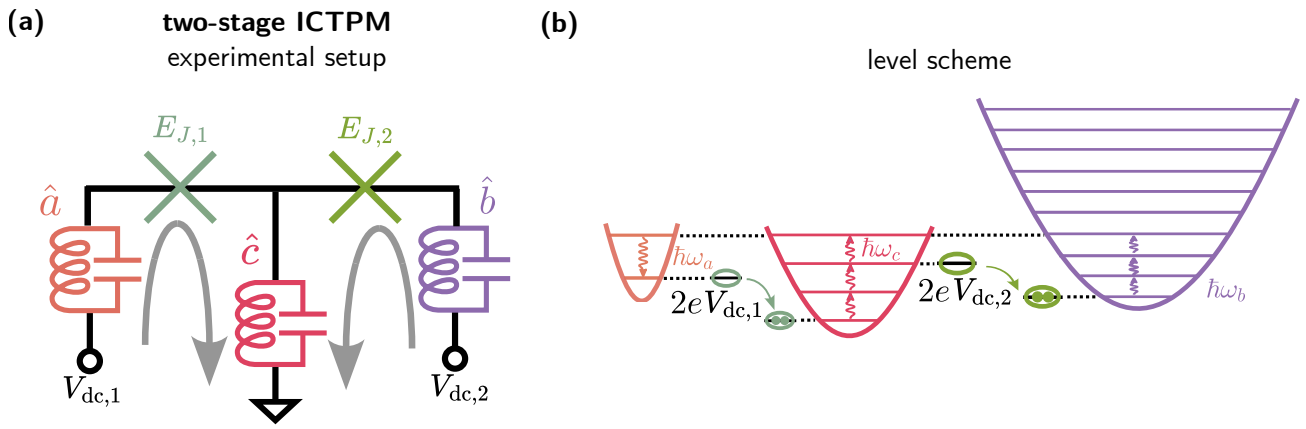

FIG. 9. Two-stage ICTPM as cascaded extension of the single-stage ICTPM. (a) In the first circuit loop, the microwave resonators $\hat{a}$ and $\hat{c}$ are connected in series to a Josephson junction with Josephson energy $E_{J,1}$. The second circuit loop couples the resonators $\hat{c}$ and $\hat{b}$ with the Josephson junction with energy $E_{J,2}$. Both circuits are dc-voltage biased and cavity $\hat{a}$ ($\hat{b}$) are coupled to an input (output) transmission line. (b) Setting the dc voltage in the first circuit to the resonance $2eV_{\mathrm{dc},1} \approx n_1\omega_c - \omega_a$ will result in photon multiplication of one cavity-$\hat{a}$ photon and n_1 cavity-$\hat{c}$ photons. A second multiplication stage between cavity $\hat{c}$ and $\hat{b}$ (with the resonance condition $eV_{\mathrm{dc},2} \approx n_2\omega_b - \omega_c$) will the ideally yield in total $n_1 \cdot n_2$ (here shown for $3 \cdot 3 = 9$) output photons, when appropriately choosing the Josephson energies to achieve perfect photon conversion.

and $\hat{b}_u$ influence the system's time evolution, but their time-evolution are not influenced by the system or the output cavities. Likewise, the time-evolution of the system is not influenced by the output cavities $\hat{a}_v$ and $\hat{b}_v$, but their time evolution is influenced by the input cavities and the system. The auxiliary input (output) cavities have mathematically constructed time-dependent loss rates, defined as

$$g_u(t) = \frac{u^*(t)}{\sqrt{1 - \int_0^t |u(\tau)|^2 d\tau}} \tag{B6}$$

$$g_v(t) = -\frac{v^*(t)}{\sqrt{\int_0^t |v(\tau)|^2 d\tau}}\,. \tag{B7}$$

In this way, they only emit (absorb) a quantum pulse given as initial (final) state of the specific mode envelope $u(t)$ ($v(t)$). A generalization of Molmer's approach involving multiple auxiliary cavities can be found in Ref. [46]. In this paper, we typically consider a Gaussian single-photon pulse into the system through the input (left) transmission line and do not specifically model the reflected output from cavity $\hat{a}$ (into the left transmission line), which here is formally achieved by setting $g_{v_a} = 0$ and by choosing $u_a(t)$ as a Gaussian mode envelope. Secondly, we always consider vacuum input into the system from the output (right) transmission line ($g_{u_b} = 0$). If we want to find the quantum state of a specific output mode $v_b(t)$, we include it with a accordingly defined $g_{v_b}(t)$, else we also set $g_{v_b}(t) = 0$.

REFERENCES

[1] L. You, "Superconducting nanowire single-photon detectors for quantum information," *Nanophotonics*, vol. 9, no. 9, pp. 2673–2692, 2020.

[2] I. Esmaeil Zadeh, J. Chang, J. W. N. Los, S. Gyger, A. W. Elshaari, S. Steinhauer, S. N. Dorenbos, and V. Zwiller, "Superconducting nanowire single-photon detectors: A perspective on evolution, state-of-the-art, future developments, and applications," *Applied Physics Letters*, vol. 118, no. 19, p. 190502, 2021.

[3] Y.-A. Chen, Q. Zhang, T.-Y. Chen, W.-Q. Cai, S.-K. Liao, J. Zhang, K. Chen, J. Yin, J.-G. Ren, Z. Chen, *et al.*, "An integrated space-to-ground quantum communication network over 4,600 kilometres," *Nature*, vol. 589, no. 7841, pp. 214–219, 2021.

[4] Y. Guan, H. Li, L. Xue, R. Yin, L. Zhang, H. Wang, G. Zhu, L. Kang, J. Chen, and P. Wu, "Lidar with superconducting nanowire single-photon detectors: Recent advances and developments," *Optics and Lasers in Engineering*, vol. 156, p. 107102, 2022.

[5] J. S. Neergaard-Nielsen, B. M. Nielsen, C. Hettich, K. Mølmer, and E. S. Polzik, "Generation of a superposition of odd photon number states for quantum information networks," *Physical Review Letters*, vol. 97, no. 8, p. 083604, 2006.

[6] T. Sonoyama, K. Takahashi, T. Sano, T. Suzuki, T. Nomura, M. Yabuno, S. Miki, H. Terai, K. Takase, W. Asa-

vanant, *et al.*, "Generation of multi-photon fock states at telecommunication wavelength using picosecond pulsed light," *Optics Express*, vol. 32, no. 18, pp. 32387–32395, 2024.

[7] P. Ercolano, A. Porzio, M. Ejrnaes, D. Salvoni, C. Bruscino, M. Peluso, J. Huang, C. Zhang, H. Li, L. You, *et al.*, "Photon statistics of one-and two-photon subtracted states at telecom wavelength reconstructed via direct detection," *Optics Express*, vol. 33, no. 16, pp. 33446–33455, 2025.

[8] H.-S. Zhong, H. Wang, Y.-H. Deng, M.-C. Chen, L.-C. Peng, Y.-H. Luo, J. Qin, D. Wu, X. Ding, Y. Hu, *et al.*, "Quantum computational advantage using photons," *Science*, vol. 370, no. 6523, pp. 1460–1463, 2020.

[9] G. Romero, J. J. García-Ripoll, and E. Solano, "Photodetection of propagating quantum microwaves in circuit qed," *Physica Scripta*, vol. 2009, no. T137, p. 014004, 2009.

[10] B. Peropadre, G. Romero, G. Johansson, C. M. Wilson, E. Solano, and J. J. García-Ripoll, "Approaching perfect microwave photodetection in circuit qed," *Physical Review A*, vol. 84, no. 6, p. 063834, 2011.

[11] F. Helmer, M. Mariantoni, E. Solano, and F. Marquardt, "Quantum nondemolition photon detection in circuit qed and the quantum zeno effect," *Physical Review A*, vol. 79, no. 5, p. 052115, 2009.

[12] I. Iakoupov, Y. Matsuzaki, W. J. Munro, and S. Saito, "Sequential nonabsorbing microwave single-photon detector," *Physical Review Research*, vol. 2, no. 3, p. 033238, 2020.

[13] P. Navez, A. Balanov, S. Savel'ev, and A. Zagoskin, "Quantum electrodynamics of non-demolition detection of single microwave photon by superconducting qubit array," *Journal of Applied Physics*, vol. 133, no. 10, 2023.

[14] B. Royer, A. L. Grimsmo, A. Choquette-Poitevin, and A. Blais, "Itinerant microwave photon detector," *Physical Review Letters*, vol. 120, p. 203602, 2018.

[15] S. He, P. Ouyang, H. Gao, Y. Li, J. He, and L. Wei, "Nonreciprocity detector arrays for high-efficiency detection of itinerant microwave photons," *Physical Review A*, vol. 109, no. 6, p. 062430, 2024.

[16] K. Inomata, Z. Lin, K. Koshino, W. D. Oliver, J.-S. Tsai, T. Yamamoto, and Y. Nakamura, "Single microwave-photon detector using an artificial λ-type three-level system," *Nature Communications*, vol. 7, no. 1, p. 12303, 2016.

[17] J.-C. Besse, S. Gasparinetti, M. C. Collodo, T. Walter, P. Kurpiers, M. Pechal, C. Eichler, and A. Wallraff, "Single-shot quantum nondemolition detection of individual itinerant microwave photons," *Physical Review X*, vol. 8, no. 2, p. 021003, 2018.

[18] S. Kono, K. Koshino, Y. Tabuchi, A. Noguchi, and Y. Nakamura, "Quantum non-demolition detection of an itinerant microwave photon," *Nature Physics*, vol. 14, no. 6, pp. 546–549, 2018.

[19] M. Casariego, E. Z. Cruzeiro, S. Gherardini, T. Gonzalez-Raya, R. André, G. Frazão, G. Catto, M. Möttönen, D. Datta, K. Viisanen, *et al.*, "Propagating quantum microwaves: towards applications in communication and sensing," *Quantum Science and Technology*, vol. 8, no. 2, p. 023001, 2023.

[20] X. Gu, A. F. Kockum, A. Miranowicz, Y.-x. Liu, and F. Nori, "Microwave photonics with superconducting quantum circuits," *Physics Reports*, vol. 718, pp. 1–102, 2017.

[21] S. R. Sathyamoorthy, T. M. Stace, and G. Johansson, "Detecting itinerant single microwave photons," *Comptes Rendus Physique*, vol. 17, no. 7, pp. 756–765, 2016.

[22] Y.-F. Chen, D. Hover, S. Sendelbach, L. Maurer, S. Merkel, E. Pritchett, F. Wilhelm, and R. McDermott, "Microwave photon counter based on josephson junctions," *Physical Review Letters*, vol. 107, no. 21, p. 217401, 2011.

[23] D. A. Ladeynov, A. L. Pankratov, L. S. Revin, A. V. Gordeeva, A. V. Chiginev, S. A. Razov, and E. V. Il'ichev, "Detection of 5 ghz photons using al josephson junctions at 0.7 k," *Academia Quantum*, vol. 2, no. 2, 2025.

[24] A. Pankratov, L. Revin, A. Gordeeva, A. Yablokov, L. Kuzmin, and E. Il'Ichev, "Towards a microwave single-photon counter for searching axions," *npj Quantum Information*, vol. 8, no. 1, p. 61, 2022.

[25] A. Rettaroli, D. Alesini, D. Babusci, C. Barone, B. Buonomo, M. M. Beretta, G. Castellano, F. Chiarello, D. Di Gioacchino, G. Felici, *et al.*, "Josephson junctions as single microwave photon counters: Simulation and characterization," *Instruments*, vol. 5, no. 3, p. 25, 2021.

[26] G. Oelsner, C. K. Andersen, M. Rehák, M. Schmelz, S. Anders, M. Grajcar, U. Hübner, K. Mølmer, and E. Il'ichev, "Detection of weak microwave fields with an underdamped josephson junction," *Physical Review Applied*, vol. 7, p. 014012, 2017.

[27] J.-X. He, P.-H. Ouyang, Y.-Q. Chai, H. Chang, Q. He, and L.-F. Wei, "Experimental demonstrations of josephson threshold detectors for broadband microwave photons detection," *Applied Physics Letters*, vol. 126, no. 20, 2025.

[28] J. Wang, K. Petrovnin, P. J. Hakonen, and G. S. Paraoanu, "Observing the poisson distribution of a coherent microwave field with a parametric photon detector," *IEEE Transactions on Quantum Engineering*, 2025.

[29] R. Lescanne, S. Deléglise, E. Albertinale, U. Réglade, T. Capelle, E. Ivanov, T. Jacqmin, Z. Leghtas, and E. Flurin, "Irreversible qubit-photon coupling for the detection of itinerant microwave photons," *Physical Review X*, vol. 10, no. 2, p. 021038, 2020.

[30] L. Balembois, J. Travesedo, L. Pallegoix, A. May, E. Billaud, M. Villiers, D. Estève, D. Vion, P. Bertet, and E. Flurin, "Cyclically operated microwave single-photon counter with sensitivity of 10- 22 w/hz," *Physical Review Applied*, vol. 21, no. 1, p. 014043, 2024.

[31] E. Albertinale, L. Balembois, E. Billaud, V. Ranjan, D. Flanigan, T. Schenkel, D. Estève, D. Vion, P. Bertet, and E. Flurin, "Detecting spins by their fluorescence with a microwave photon counter," *Nature*, vol. 600, no. 7889, pp. 434–438, 2021.

[32] E. Billaud, L. Balembois, J. Travesedo, M. Le Dantec, M. Rančić, E. Albertinale, R. Truong, S. Bertaina, T. Chanelière, P. Goldner, *et al.*, "Electron paramagnetic resonance spectroscopy of a scheelite crystal using microwave-photon counting," *Physical Review Research*, vol. 7, no. 1, p. 013011, 2025.

[33] B. Karimi, G. O. Steffensen, A. P. Higginbotham, C. M. Marcus, A. Levy Yeyati, and J. P. Pekola, "Bolometric detection of josephson radiation," *Nature Nanotechnology*, vol. 19, no. 11, pp. 1613–1618, 2024.

[34] A. Narla, S. Shankar, M. Hatridge, Z. Leghtas, K. M. Sliwa, E. Zalys-Geller, S. O. Mundhada, W. Pfaff,

L. Frunzio, R. J. Schoelkopf, *et al.*, "Robust concurrent remote entanglement between two superconducting qubits," *Physical Review X*, vol. 6, no. 3, p. 031036, 2016.
[35] A. Opremcak, I. Pechenezhskiy, C. Howington, B. Christensen, M. Beck, E. Leonard Jr, J. Suttle, C. Wilen, K. Nesterov, G. Ribeill, *et al.*, "Measurement of a superconducting qubit with a microwave photon counter," *Science*, vol. 361, no. 6408, pp. 1239–1242, 2018.
[36] A. M. Gunyhó, S. Kundu, J. Ma, W. Liu, S. Niemelä, G. Catto, V. Vadimov, V. Vesterinen, P. Singh, Q. Chen, *et al.*, "Single-shot readout of a superconducting qubit using a thermal detector," *Nature Electronics*, vol. 7, no. 4, pp. 288–298, 2024.
[37] A. V. Dixit, S. Chakram, K. He, A. Agrawal, R. K. Naik, D. I. Schuster, and A. Chou, "Searching for dark matter with a superconducting qubit," *Physical Review Letters*, vol. 126, p. 141302, 2021.
[38] C. Braggio, L. Balembois, R. Di Vora, Z. Wang, J. Travesedo, L. Pallegoix, G. Carugno, A. Ortolan, G. Ruoso, U. Gambardella, *et al.*, "Quantum-enhanced sensing of axion dark matter with a transmon-based single microwave photon counter," *Physical Review X*, vol. 15, no. 2, p. 021031, 2025.
[39] B. Karimi and J. P. Pekola, "Quantum trajectory analysis of single microwave photon detection by nanocalorimetry," *Physical Review Letters*, vol. 124, no. 17, p. 170601, 2020.
[40] R. Kokkoniemi, J. Govenius, V. Vesterinen, R. E. Lake, A. M. Gunyhó, K. Y. Tan, S. Simbierowicz, L. Grönberg, J. Lehtinen, M. Prunnila, *et al.*, "Nanobolometer with ultralow noise equivalent power," *Communications Physics*, vol. 2, no. 1, pp. 1–8, 2019.
[41] R. Kokkoniemi, J.-P. Girard, D. Hazra, A. Laitinen, J. Govenius, R. Lake, I. Sallinen, V. Vesterinen, M. Partanen, J. Tan, *et al.*, "Bolometer operating at the threshold for circuit quantum electrodynamics," *Nature*, vol. 586, no. 7827, pp. 47–51, 2020.
[42] R. Dassonneville, R. Assouly, T. Peronnin, P. Rouchon, and B. Huard, "Number-resolved photocounter for propagating microwave mode," *Physical Review Applied*, vol. 14, no. 4, p. 044022, 2020.
[43] J. Leppäkangas, M. Marthaler, D. Hazra, S. Jebari, R. Albert, F. Blanchet, G. Johansson, and M. Hofheinz, "Multiplying and detecting propagating microwave photons using inelastic cooper-pair tunneling," *Physical Review A*, vol. 97, p. 013855, 2018.
[44] R. Albert, J. Griesmar, F. Blanchet, U. Martel, N. Bourlet, and M. Hofheinz, "Microwave photon-number amplification," *Physical Review X*, vol. 14, p. 011011, 2024.
[45] A. H. Kiilerich and K. Mølmer, "Input-output theory with quantum pulses," *Physical Review Letters*, vol. 123, p. 123604, 2019.
[46] A. H. Kiilerich and K. Mølmer, "Quantum interactions with pulses of radiation," *Physical Review A*, vol. 102, p. 023717, 2020.
[47] V. R. Christiansen, A. H. Kiilerich, and K. Mølmer, "Interactions of quantum systems with pulses of quantized radiation: From a cascaded master equation to a traveling mode perspective," *Physical Review A*, vol. 107, p. 013706, 2023.
[48] M. Khanahmadi and K. Mølmer, "Qubit readout and quantum sensing with pulses of quantum radiation," *Physical Review A*, vol. 107, p. 013705, 2023.
[49] M. M. Lund, F. Yang, and K. Mølmer, "Perfect splitting of a two-photon pulse," *Physical Review A*, vol. 107, p. 023715, 2023.
[50] C. Fabre and N. Treps, "Modes and states in quantum optics," *Reviews of Modern Physics*, vol. 92, p. 035005, 2020.
[51] A. A. Clerk, M. H. Devoret, S. M. Girvin, F. Marquardt, and R. J. Schoelkopf, "Introduction to quantum noise, measurement, and amplification," *Reviews of Modern Physics*, vol. 82, pp. 1155–1208, 2010.
[52] It is easy to see, that the zero-point fluctuations α_0, β_0 merely enter as trivial prefactors of the Josephson driving energy, since for a single-photon input only the transition matrix element between two states $(n_a = 1, n_b = 0) \Leftrightarrow (n_a = 0, n_b = n)$ matters.
[53] C. E. Rasmussen and C. K. I. Williams, *Gaussian Processes for Machine Learning*. The MIT Press, 2005.
[54] U. Martel, R. Albert, F. Blanchet, J. Griesmar, G. Ouellet, H. Therrien, N. Nehra, N. Bourlet, A. Peugeot, and M. Hofheinz, "Influence of bias-voltage noise on the inelastic cooper-pair tunneling amplifier (icta)," *Applied Physics Letters*, vol. 126, no. 7, p. 074001, 2025.
[55] M. P. da Silva, D. Bozyigit, A. Wallraff, and A. Blais, "Schemes for the observation of photon correlation functions in circuit qed with linear detectors," *Physical Review A*, vol. 82, p. 043804, 2010.
[56] H. M. Wiseman and G. J. Milburn, *Quantum Measurement and Control*. Cambridge University Press, 2009.
[57] M. S. Kim, "Quasiprobability functions measured by photon statistics of amplified signal fields," *Physical Review A*, vol. 56, pp. 3175–3179, 1997.
[58] H. Nha, G. J. Milburn, and H. J. Carmichael, "Linear amplification and quantum cloning for non-gaussian continuous variables," *New Journal of Physics*, vol. 12, no. 10, p. 103010, 2010.
[59] C. Eichler, D. Bozyigit, C. Lang, L. Steffen, J. Fink, and A. Wallraff, "Experimental state tomography of itinerant single microwave photons," *Physical Review Letters*, vol. 106, p. 220503, 2011.
[60] C. Rolland, A. Peugeot, S. Dambach, M. Westig, B. Kubala, Y. Mukharsky, C. Altimiras, H. le Sueur, P. Joyez, D. Vion, P. Roche, D. Esteve, J. Ankerhold, and F. Portier, "Antibunched photons emitted by a dc-biased josephson junction," *Physical Review Letters*, vol. 122, p. 186804, 2019.
[61] G. C. Ménard, A. Peugeot, C. Padurariu, C. Rolland, B. Kubala, Y. Mukharsky, Z. Iftikhar, C. Altimiras, P. Roche, H. le Sueur, P. Joyez, D. Vion, D. Esteve, J. Ankerhold, and F. Portier, "Emission of photon multiplets by a dc-biased superconducting circuit," *Physical Review X*, vol. 12, p. 021006, 2022.
[62] C. W. Gardiner and P. Zoller, *Quantum Noise. A Handbook of Markovian and Non-Markovian Quantum Stochastic Methods with Applications to Quantum Optics*, vol. 2 of *Springer Series in Synergetics*. Springer-Verlag Berlin Heidelberg New York, 2000.

Conclusion and Outlook

At the heart of a Josephson-photonics device, where a dc-voltage biased Josephson junction is connected in series with a few microwave resonators, lies the interplay between microwave optical photonics and superconducting electronics. This versatile platform creates microwave excitations in the resonators by accessing various resonances that enable inelastic Cooper-pair tunneling. In this way, it elegantly connects microscopic-scale properties of microwave photons to macroscopic superconducting circuits. Properties of the created microwave light range from the classical to the deep quantum. This establishes the platform as a powerful tool for quantum technological applications, such as potential quantum radars using two-mode squeezed light or quantum computing with dissipative cat qubits.

In this thesis, we have developed the field of Josephson photonics in two directions, setting new impulses for experimental realizations and technological applications:

- We established tools for phase stabilization of Josephson-photonics devices and reconstruction of diffused quantum states.
- We investigated Josephson-photonics devices as detectors for single microwave photons.

Because a dc voltage does not provide a stable reference, Josephson-photonics devices have suffered from diffusion of the neutrally stable phase of the photonic quantum states. However, quantum technological applications strongly rely on a stable phase of the quantum states of light.
As a solution that stabilizes the diffusing phase-space angle, we have presented techniques of injection locking and synchronization. We have amended the theoretical model by a low-frequency impedance connected in series, which is in the simplest case an in-series resistor R_0 [47, 49, 50]. Such an impedance is a crucial part of Josephson-photonics devices that enables a physically correct theoretical description of self-sustained oscillations that can be synchronized and injection locked to external signals. The superconducting and nonlinear Josephson-photonics devices serve as an ideal platform to study fundamental properties of the synchronization dynamics. By bridging the gap between classical and quantum, these devices

enable the study of foundational principles and phenomena of synchronization, where they beautifully highlight similarities and differences between the classical and quantum regime. Specifically, our analysis comprises paradigmatic examples that stabilize the phase of coherent states [49], single- and two-mode squeezed states [50], and cat states (Sec. 4.2.3). Ongoing experiments currently implement circuit designs based on our proposals to stabilize the phase of cat qubits. Specifically, incorporating a low-pass filter (i.e. a parallel R_0C_0-circuit) as in-series impedance could reduce the noise entering the systems while still functioning as a low-frequency environment that enables phase stabilization by injection locking. At the same time, such a device provides a natural platform for studying hysteresis effects in the synchronization dynamics.
An alternative solution that partially mitigates the issue of the neutrally stable phase of microwave light is to reconstruct the quantum state without phase diffusion from experimental data. By measuring a few experimentally accessible expectation values, an ansatz for the quantum state can be optimized. The resulting optimized ansatz yields the physically correct expectation values and then serves as a neat approximation of the full physical quantum state. An illustrative case is a simple exponential Wigner function that accurately reconstructs and describes a complicated $\mathbb{Z}^3$-symmetric stationary state of a weakly driven Josephson-photonics device.

As a second part, we have studied the amplification and detection of single microwave photons in a Josephson-photonics platform, dubbed the Inelastic Cooper Pair tunneling Photon Multiplier (ICTPM), that contains two microwave cavities $\hat{a}$ and $\hat{b}$. By tuning the dc voltage accordingly, $2eV_{\mathrm{dc}}/\hbar = n\omega_b - \omega_a$, a resonance can be accessed that involves the difference of two resonator eigenfrequencies. The ICTPM then multiplies an excitation of cavity $\hat{a}$ to $n \in \mathbb{N}$ photons in cavity $\hat{b}$. In this way, an input can be resonantly absorbed by the ICTPM and amplified. Until now, deterministic photon number multiplication has been experimentally demonstrated for a classical and continuous coherent-wave input signal.
Our work [51] progresses towards the multiplication and detection of single microwave photons, i.e. true quantum input pulses. Using Mølmer's approach, we efficiently model itinerant quantum pulses containing single microwave photons that interact with the ICTPM. We have analyzed the setup for Gaussian pulses of length T. Typically, the n outgoing photons are emitted into multiple outgoing modes with similar occupations. However, we have identified a specific parameter regime in which the outgoing photons are emitted into a few modes, one of which has a high occupation. Most crucially, we find that merely achieving perfect photon multiplication is not sufficient for the detection of single microwave photons. Instead, the detection efficiency is enhanced in regimes where the ICTPM contains a highly occupied output mode. On the basis of these insights, we have developed a photon detection scheme by heterodyne measurement of the ICTPM. The quantum state of a highly occupied mode can be distinguished well from vacuum, enabling the detection of the output signatures in a signal dominated by noise. In a setup with two multiplication stages, large multiplication factors $n = 16$ can be reached. Realistic devices achieve a detection efficiency of 84.5% with a dark count rate of $10^{-3}/T$ and promise to outperform existing schemes for the detection of single microwave photons with unknown arrival times.

Looking ahead, we can already state that this work drives research for other novel schemes that rely on our results and developed mechanisms. For instance, resonance conditions similar to those for the ICTPM mimic avalanche photodiodes from optics. Another scheme involves an undriven resonator $\hat{a}$ that absorbs the itinerant pulse and a second driven microwave cavity that observes the state of $\hat{a}$. In particular, the combination of these proposals with the ICTPM holds the promise of even stronger detection performances.

References

[1] M. H. Devoret, J. M. Martinis, D. Esteve, and J. Clarke, "Resonant Activation from the Zero-Voltage State of a Current-Biased Josephson Junction", *Physical Review Letters* **53**, 1260–1263 (1984), DOI: 10.1103/PhysRevLett.53.1260.

[2] J. M. Martinis, M. H. Devoret, and J. Clarke, "Energy-Level Quantization in the Zero-Voltage State of a Current-Biased Josephson Junction", *Physical Review Letters* **55**, 1543–1546 (1985), DOI: 10.1103/PhysRevLett.55.1543.

[3] M. H. Devoret, J. M. Martinis, and J. Clarke, "Measurements of Macroscopic Quantum Tunneling out of the Zero-Voltage State of a Current-Biased Josephson Junction", *Physical Review Letters* **55**, 1908–1911 (1985), DOI: 10.1103/PhysRevLett.55.1908.

[4] A. L. Cullen, "A Travelling-Wave Parametric Amplifier", *Nature* **181**(4605), 332–332 (1958), DOI: 10.1038/181332a0.

[5] K. G. Fedorov, M. Renger, S. Pogorzalek, R. D. Candia, Q. Chen, Y. Nojiri, et al., "Experimental quantum teleportation of propagating microwaves", *Science Advances* **7**(52), eabk0891 (2021), DOI: 10.1126/sciadv.abk0891.

[6] S. Storz, J. Schär, A. Kulikov, P. Magnard, P. Kurpiers, J. Lütolf, et al., "Loophole-free Bell inequality violation with superconducting circuits", *Nature* **617**(7960), 265–270 (2023), DOI: 10.1038/s41586-023-05885-0.

[7] R. Assouly, R. Dassonneville, T. Peronnin, A. Bienfait, and B. Huard, "Quantum advantage in microwave quantum radar", *Nature Physics* **19**(10), 1418–1422 (2023), DOI: 10.1038/s41567-023-02113-4.

[8] M. Hofheinz, F. Portier, Q. Baudouin, P. Joyez, D. Vion, P. Bertet, et al., "Bright side of the Coulomb blockade", *Physical Review Letters* **106**(21), 217005 (2011), DOI: 10.1103/PhysRevLett.106.217005.

[9] F. Chen, A. J. Sirois, R. W. Simmonds, and A. J. Rimberg, "Introduction of a dc bias into a high-Q superconducting microwave cavity", *Applied Physics Letters* **98**(13), 132509 (2011), DOI: 10.1063/1.3573824.

[10] C. Rolland, A. Peugeot, S. Dambach, M. Westig, B. Kubala, Y. Mukharsky, et al., "Antibunched Photons Emitted by a dc-Biased Josephson Junction", *Physical Review Letters* **122**, 186804 (2019), DOI: 10.1103/PhysRevLett.122.186804.

[11] A. Peugeot, G. Ménard, S. Dambach, M. Westig, B. Kubala, Y. Mukharsky, et al., "Generating Two Continuous Entangled Microwave Beams Using a dc-Biased Josephson Junction", *Physical Review X* **11**, 031008 (2021), DOI: 10.1103/PhysRevX.11.031008.

[12] T. Aissaoui, A. Murani, R. Lescanne, and A. Sarlette, "A cat qubit stabilization scheme using a voltage biased Josephson junction", arXiv:2411.08132 (2024).

[13] R. Albert, J. Griesmar, F. Blanchet, U. Martel, N. Bourlet, and M. Hofheinz, "Microwave Photon-Number Amplification", *Physical Review X* **14**, 011011 (2024), DOI: 10.1103/PhysRevX.14.011011.

[14] D. V. Averin, Y. V. Nazarov, and A. A. Odintsov, "Incoherent tunneling of the cooper pairs and magnetic flux quanta in ultrasmall Josephson junctions", *Physica B: Condensed Matter* **165-166**, 945–946 (1990), DOI: 10.1016/S0921-4526(09)80058-6.

[15] S. M. Girvin, L. I. Glazman, M. Jonson, D. R. Penn, and M. D. Stiles, "Quantum fluctuations and the single-junction Coulomb blockade", *Physical Review Letters* **64**, 3183–3186 (1990), DOI: 10.1103/PhysRevLett.64.3183.

[16] M. H. Devoret, D. Esteve, H. Grabert, G.-L. Ingold, H. Pothier, and C. Urbina, "Effect of the electromagnetic environment on the Coulomb blockade in ultrasmall tunnel junctions", *Physical Review Letters* **64**, 1824–1827 (1990), DOI: 10.1103/PhysRevLett.64.1824.

[17] T. Holst, D. Esteve, C. Urbina, and M. H. Devoret, "Effect of a Transmission Line Resonator on a Small Capacitance Tunnel Junction", *Physical Review Letters* **73**, 3455–3458 (1994), DOI: 10.1103/PhysRevLett.73.3455.

[18] J. Basset, H. Bouchiat, and R. Deblock, "Emission and Absorption Quantum Noise Measurement with an On-Chip Resonant Circuit", *Physical Review Letters* **105**, 166801 (2010), DOI: 10.1103/PhysRevLett.105.166801.

[19] M. Westig, B. Kubala, O. Parlavecchio, Y. Mukharsky, C. Altimiras, P. Joyez, et al., "Emission of Nonclassical Radiation by Inelastic Cooper Pair Tunneling", *Physical Review Letters* **119**, 137001 (2017), DOI: 10.1103/PhysRevLett.119.137001.

[20] S. Jebari, F. Blanchet, A. Grimm, D. Hazra, R. Albert, P. Joyez, et al., "Near-quantum-limited amplification from inelastic Cooper-pair tunnelling", *Nature Electronics* **1**, 223–227 (2018), DOI: 10.1038/s41928-018-0055-7.

[21] S. Jebari, "The Inelastic Cooper pair Tunneling Amplifier (ICTA)", (University Grenoble Alpes, Grenoble, 2017).

[22] A. Grimm, F. Blanchet, R. Albert, J. Leppäkangas, S. Jebari, D. Hazra, et al., "Bright On-Demand Source of Antibunched Microwave Photons Based on Inelastic Cooper Pair Tunneling", *Physical Review X* **9**, 021016 (2019), DOI: 10.1103/PhysRevX.9.021016.

[23] G. C. Ménard, A. Peugeot, C. Padurariu, C. Rolland, B. Kubala, Y. Mukharsky, et al., "Emission of Photon Multiplets by a dc-Biased Superconducting Circuit", *Physical Review X* **12**, 021006 (2022), DOI: 10.1103/PhysRevX.12.021006.

[24] U. Martel, R. Albert, F. Blanchet, J. Griesmar, G. Ouellet, H. Therrien, et al., "Influence of bias-voltage noise on the inelastic cooper-pair tunneling amplifier (ICTA)", *Applied Physics Letters* **126**(7), 074001 (2025), DOI: 10.1063/5.0240842.

[25] V. Gramich, B. Kubala, S. Rohrer, and J. Ankerhold, "From Coulomb-Blockade to Nonlinear Quantum Dynamics in a Superconducting Circuit with a Resonator", *Physical Review Letters* **111**, 247002 (2013), DOI: 10.1103/PhysRevLett.111.247002.

[26] J. Leppäkangas, G. Johansson, M. Marthaler, and M. Fogelström, "Nonclassical Photon Pair Production in a Voltage-Biased Josephson Junction", *Physical Review Letters* **110**, 267004 (2013), DOI: 10.1103/PhysRevLett.110.267004.

[27] A. D. Armour, M. P. Blencowe, E. Brahimi, and A. J. Rimberg, "Universal Quantum Fluctuations of a Cavity Mode Driven by a Josephson Junction", *Physical Review Letters* **111**, 247001 (2013), DOI: 10.1103/PhysRevLett.111.247001.

[28] S. Meister, M. Mecklenburg, V. Gramich, J. T. Stockburger, J. Ankerhold, and B. Kubala, "Resonators coupled to voltage-biased Josephson junctions: From linear response to strongly driven nonlinear oscillations", *Physical Review B* **92**, 174532 (2015), DOI: 10.1103/PhysRevB.92.174532.

[29] M. Trif and P. Simon, "Photon cross-correlations emitted by a Josephson junction in two microwave cavities", *Physical Review B* **92**, 014503 (2015), DOI: 10.1103/PhysRevB.92.014503.

[30] B. Kubala, V. Gramich, and J. Ankerhold, "Non-classical light from superconducting resonators coupled to voltage-biased Josephson junctions", *Physica Scripta* **T165**, 014029 (2015), DOI: 10.1088/0031-8949/2015/T165/014029.

[31] S. Dambach, B. Kubala, V. Gramich, and J. Ankerhold, "Time-resolved statistics of nonclassical light in Josephson photonics", *Physical Review B* **92**, 054508 (2015), DOI: 10.1103/PhysRevB.92.054508.

[32] J. Leppäkangas, M. Fogelström, A. Grimm, M. Hofheinz, M. Marthaler, and G. Johansson, "Antibunched Photons from Inelastic Cooper-Pair Tunneling", *Physical Review Letters* **115**, 027004 (2015), DOI: 10.1103/PhysRevLett.115.027004.

[33] A. D. Armour, B. Kubala, and J. Ankerhold, "Josephson photonics with a two-mode superconducting circuit", *Physical Review B* **91**, 184508 (2015), DOI: 10.1103/PhysRevB.91.184508.

[34] J. Leppäkangas, M. Fogelström, M. Marthaler, and G. Johansson, "Correlated Cooper pair transport and microwave photon emission in the dynamical Coulomb blockade", *Physical Review B* **93**, 014506 (2016), DOI: 10.1103/PhysRevB.93.014506.

[35] J.-R. Souquet and A. A. Clerk, "Fock-state stabilization and emission in superconducting circuits using dc-biased Josephson junctions", *Physical Review A* **93**, 060301(R) (2016), DOI: 10.1103/PhysRevA.93.060301.

[36] S. Dambach, B. Kubala, and J. Ankerhold, "Generating entangled quantum microwaves in a Josephson-photonics device", *New Journal of Physics* **19**(2), 023027 (2017), DOI: 10.1088/1367-2630/aa5bb6.

[37] S. Dambach, B. Kubala, and J. Ankerhold, "Time-resolved statistics of photon pairs in two-cavity Josephson photonics", *Fortschritte der Physik* **65**(6-8), 1600061 (2017), DOI: 10.1002/prop.201600061.

[38] A. D. Armour, B. Kubala, and J. Ankerhold, "Noise switching at a dynamical critical point in a cavity-conductor hybrid", *Physical Review B* **96**, 214509 (2017), DOI: 10.1103/PhysRevB.96.214509.

[39] H. Wang, M. P. Blencowe, A. D. Armour, and A. J. Rimberg, "Quantum dynamics of a Josephson junction driven cavity mode system in the presence of voltage bias noise", *Physical Review B* **96**, 104503 (2017), DOI: 10.1103/PhysRevB.96.104503.

[40] J. Leppäkangas and M. Marthaler, "Inelastic scattering of microwave radiation in the dynamical Coulomb blockade", *Physical Review B* **98**, 224511 (2018), DOI: 10.1103/PhysRevB.98.224511.

[41] J. Leppäkangas, M. Marthaler, D. Hazra, S. Jebari, R. Albert, F. Blanchet, et al., "Multiplying and detecting propagating microwave photons using inelastic Cooper-pair tunneling", *Physical Review A* **97**, 013855 (2018), DOI: 10.1103/PhysRevA.97.013855.

[42] S. Dambach, P. Egetmeyer, J. Ankerhold, and B. Kubala, "Quantum thermodynamics with a Josephson-photonics setup", *The European Physical Journal Special Topics* **227**, 2053–2058 (2019), DOI: 10.1140/epjst/e2018-800062-8.

[43] L. Arndt and F. Hassler, "Statistics of radiation due to nondegenerate Josephson parametric down-conversion", *Physical Review B* **100**, 014505 (2019), DOI: 10.1103/PhysRevB.100.014505.

[44] S. Dambach, "Josephson Photonics and Josephson Scanning Tunneling Microscopy", (Ulm University, Ulm, 2019).

[45] B. Kubala, J. Ankerhold, and A. D. Armour, "Electronic and photonic counting statistics as probes of non-equilibrium quantum dynamics", *New Journal of Physics* **22**(2), 023010 (2020), DOI: 10.1088/1367-2630/ab6eb0.

[46] B. Lang and A. D. Armour, "Multi-photon resonances in Josephson junction-cavity circuits", *New Journal of Physics* **23**(3), 033021 (2021), DOI: 10.1088/1367-2630/abe483.

[47] L. Danner, C. Padurariu, J. Ankerhold, and B. Kubala, "Injection locking and synchronization in Josephson photonics devices", *Physical Review B* **104**, 054517 (2021), DOI: 10.1103/PhysRevB.104.054517.

[48] T. Aissaoui, "Cat Qubit Stabilization with dc-biased Josephson Junctions", (Sorbonne Université, Paris, 2025).

[49] F. Höhe, L. Danner, C. Padurariu, B. I. C. Donvil, J. Ankerhold, and B. Kubala, "Quantum synchronization in presence of shot noise", *New Journal of Physics* **27**(2), 023039 (2025), DOI: 10.1088/1367-2630/adb777.

[50] L. Danner, F. Höhe, C. Padurariu, J. Ankerhold, and B. Kubala, "Quantum microwaves: Stabilizing squeezed light by phase locking", *Physical Review B* **111**, 184519 (2025), DOI: 10.1103/PhysRevB.111.184519.

[51] L. Danner, M. Hofheinz, N. Bourlet, C. Padurariu, J. Ankerhold, and B. Kubala, "Amplification and Detection of Single Itinerant Microwave Photons", arXiv:2510.08030 (2025).

[52] S. Sengupta, B. Kubala, J. Ankerhold, and C. Padurariu, "Optomechanical Cooling without Residual Heating", arXiv:2511.10318 (2025).

[53] M. Tinkham, "Introduction to Superconductivity", vol. **2** (Dover Publications, 2004).

[54] J. Bardeen, L. N. Cooper, and J. R. Schrieffer, "Theory of Superconductivity", *Physical Review Journals* **108**, 1175–1204 (1957), DOI: 10.1103/PhysRev.108.1175.

[55] B. D. Josephson, "Possible new effects in superconductive tunnelling", *Physics Letters* **1**(7), 251–253 (1962), DOI: 10.1016/0031-9163(62)91369-0.

[56] G.-L. Ingold and Y. V. Nazarov, "Charge Tunneling Rates in Ultrasmall Junctions", in: "Single Charge Tunneling: Coulomb Blockade Phenomena In Nanostructures", ed. by H. Grabert and M. H. Devoret, vol. **294** (Springer, 1992).

[57] G.-L. Ingold, "Ladungseffekte in ultrakleinen Tunnelkontakten", (2007).

[58] M. P. Blencowe, A. D. Armour, and A. J. Rimberg, "Quantum-classical correspondence for a dc-biased cavity resonator–Cooper-pair transistor system", in: "Fluctuating Nonlinear Oscillators: From Nanomechanics to Quantum Superconducting Circuits", ed. by M. Dykman, (Oxford University Press, 2012).

[59] M. C. Cassidy, A. Bruno, S. Rubbert, M. Irfan, J. Kammhuber, R. N. Schouten, et al., "Demonstration of an ac Josephson junction laser", *Science* **355**(6328), 939–942 (2017), DOI: 10.1126/science.aah6640.

[60] S.-H. Tan, B. I. Erkmen, V. Giovannetti, S. Guha, S. Lloyd, L. Maccone, et al., "Quantum Illumination with Gaussian States", *Physical Review Letters* **101**, 253601 (2008), DOI: 10.1103/PhysRevLett.101.253601.

[61] S. Lloyd, "Enhanced Sensitivity of Photodetection via Quantum Illumination", *Science* **321**(5895), 1463–1465 (2008), DOI: 10.1126/science.1160627.

[62] F. Chen, J. Li, A. D. Armour, E. Brahimi, J. Stettenheim, A. J. Sirois, et al., "Realization of a single-Cooper-pair Josephson laser", *Physical Review B* **90**, 020506(R) (2014), DOI: 10.1103/PhysRevB.90.020506.

[63] A. Blais, A. L. Grimsmo, S. M. Girvin, and A. Wallraff, "Circuit quantum electrodynamics", *Reviews of Modern Physics* **93**, 025005 (2021), DOI: 10.1103/RevModPhys.93.025005.

[64] M. Abramowitz and I. A. Stegun, "Handbook of Mathematical Functions: With Formulas, Graphs, and Mathematical Tables", (Dover Publications, 1964).

[65] C. W. Gardiner and P. Zoller, "Quantum Noise. A Handbook of Markovian and Non-Markovian Quantum Stochastic Methods with Applications to Quantum Optics", vol. **2** (Springer, 2000).

[66] H. J. Carmichael, "Statistical Methods in Quantum Optics 2: Non-Classical Fields", vol. **2** (Springer, 2008).

[67] M. J. Collett and C. W. Gardiner, "Squeezing of intracavity and traveling-wave light fields produced in parametric amplification", *Physical Review A* **30**, 1386–1391 (1984), DOI: 10.1103/PhysRevA.30.1386.

[68] R. A. Fisher, M. M. Nieto, and V. D. Sandberg, "Impossibility of naively generalizing squeezed coherent states", *Physical Review D* **29**, 1107–1110 (1984), DOI: 10.1103/PhysRevD.29.1107.

[69] S. L. Braunstein and R. I. McLachlan, "Generalized squeezing", *Physical Review A* **35**, 1659–1667 (1987), DOI: 10.1103/PhysRevA.35.1659.

[70] M. Hillery, "Photon number divergence in the quantum theory of n-photon down conversion", *Physical Review A* **42**, 498–502 (1990), DOI: 10.1103/PhysRevA.42.498.

[71] R. Gordillo and R. Puebla, "Comment on "Properties and dynamics of generalized squeezed states"", arXiv:2507.12250 (2025).

[72] M. A. Nielsen and I. L. Chuang, "Quantum Computation and Quantum Information: 10th Anniversary Edition", (Cambridge University Press, 2010).

[73] P. W. Shor, "Scheme for reducing decoherence in quantum computer memory", *Physical Review A* **52**, R2493(R) (1995), DOI: 10.1103/PhysRevA.52.R2493.

[74] A. M. Steane, "Error Correcting Codes in Quantum Theory", *Physical Review Letters* **77**, 793–797 (1996), DOI: 10.1103/PhysRevLett.77.793.

[75] Z. Leghtas, G. Kirchmair, B. Vlastakis, R. J. Schoelkopf, M. H. Devoret, and M. Mirrahimi, "Hardware-Efficient Autonomous Quantum Memory Protection", *Physical Review Letters* **111**, 120501 (2013), DOI: 10.1103/PhysRevLett.111.120501.

[76] M. Mirrahimi, Z. Leghtas, V. V. Albert, S. Touzard, R. J. Schoelkopf, L. Jiang, et al., "Dynamically protected cat-qubits: a new paradigm for universal quantum computation", *New Journal of Physics* **16**(4), 045014 (2014), DOI: 10.1088/1367-2630/16/4/045014.

[77] Z. Leghtas, S. Touzard, I. M. Pop, A. Kou, B. Vlastakis, A. Petrenko, et al., "Confining the state of light to a quantum manifold by engineered two-photon loss", *Science* **347**(6224), 853–857 (2015), DOI: 10.1126/science.aaa2085.

[78] R. Lescanne, M. Villiers, T. Peronnin, A. Sarlette, M. Delbecq, B. Huard, et al., "Exponential suppression of bit-flips in a qubit encoded in an oscillator", *Nature Physics* **16**(5), 509–513 (2020), DOI: 10.1038/s41567-020-0824-x.

[79] A. Marquet, A. Essig, J. Cohen, N. Cottet, A. Murani, E. Albertinale, et al., "Autoparametric Resonance Extending the Bit-Flip Time of a Cat Qubit up to 0.3 s", *Physical Review X* **14**, 021019 (2024), DOI: 10.1103/PhysRevX.14.021019.

[80] H. Putterman, K. Noh, R. N. Patel, G. A. Peairs, G. S. MacCabe, M. Lee, et al., "Preserving Phase Coherence and Linearity in Cat Qubits with Exponential Bit-Flip Suppression", *Physical Review X* **15**, 011070 (2025), DOI: 10.1103/PhysRevX.15.011070.

[81] R. Rousseau, D. Ruiz, E. Albertinale, P. d'Avezac, D. Banys, U. Blandin, et al., "Enhancing dissipative cat qubit protection by squeezing", arXiv:2502.07892 (2025).

[82] U. Réglade, A. Bocquet, R. Gautier, J. Cohen, A. Marquet, E. Albertinale, et al., "Quantum control of a cat qubit with bit-flip times exceeding ten seconds", *Nature* **629**(8013), 778–783 (2024), DOI: 10.1038/s41586-024-07294-3.

[83] J. Guillaud and M. Mirrahimi, "Repetition Cat Qubits for Fault-Tolerant Quantum Computation", *Physical Review X* **9**, 041053 (2019), DOI: 10.1103/PhysRevX.9.041053.

[84] J. Guillaud and M. Mirrahimi, "Error rates and resource overheads of repetition cat qubits", *Physical Review A* **103**, 042413 (2021), DOI: 10.1103/PhysRevA.103.042413.

[85] L. Sun, A. Petrenko, Z. Leghtas, B. Vlastakis, G. Kirchmair, K. M. Sliwa, et al., "Tracking photon jumps with repeated quantum non-demolition parity measurements", *Nature* **511**(7510), 444–448 (2014), DOI: 10.1038/nature13436.

[86] F.-M. L. Régent, C. Berdou, Z. Leghtas, J. Guillaud, and M. Mirrahimi, "High-performance repetition cat code using fast noisy operations", *Quantum* **7**, 1198 (2023), DOI: 10.22331/q-2023-12-06-1198.

[87] S. Puri, A. Grimm, P. Campagne-Ibarcq, A. Eickbusch, K. Noh, G. Roberts, et al., "Stabilized Cat in a Driven Nonlinear Cavity: A Fault-Tolerant Error Syndrome Detector", *Physical Review X* **9**, 041009 (2019), DOI: 10.1103/PhysRevX.9.041009.

[88] A. Grimm, N. E. Frattini, S. Puri, S. O. Mundhada, S. Touzard, M. Mirrahimi, et al., "Stabilization and operation of a Kerr-cat qubit", *Nature* **584**(7820), 205–209 (2020), DOI: 10.1038/s41586-020-2587-z.

[89] M. Resch, C. Padurariu, B. Kubala, and J. Ankerhold, "Fast initialization of Bell states with Schrödinger cats in multi-mode systems", arXiv:2505.02497 (2025).

[90] A. Roy, Z. Leghtas, A. D. Stone, M. Devoret, and M. Mirrahimi, "Continuous generation and stabilization of mesoscopic field superposition states in a quantum circuit", *Physical Review A* **91**, 013810 (2015), DOI: 10.1103/PhysRevA.91.013810.

[91] A. A. Houck, D. I. Schuster, J. M. Gambetta, J. A. Schreier, B. R. Johnson, J. M. Chow, et al., "Generating single microwave photons in a circuit", *Nature* **449**(7160), 328–331 (2007), DOI: 10.1038/nature06126.

[92] M. Pechal, L. Huthmacher, C. Eichler, S. Zeytinoğlu, A. A. Abdumalikov, S. Berger, et al., "Microwave-Controlled Generation of Shaped Single Photons in Circuit Quantum Electrodynamics", *Physical Review X* **4**, 041010 (2014), DOI: 10.1103/PhysRevX.4.041010.

[93] Z. H. Peng, S. E. de Graaf, J. S. Tsai, and O. V. Astafiev, "Tuneable on-demand single-photon source in the microwave range", *Nature Communications* **7**(1), 12588 (2016), DOI: 10.1038/ncomms12588.

[94] Y. Zhou, Z. Peng, Y. Horiuchi, O. Astafiev, and J. Tsai, "Tunable Microwave Single-Photon Source Based on Transmon Qubit with High Efficiency", *Physical Review Applied* **13**, 034007 (2020), DOI: 10.1103/PhysRevApplied.13.034007.

[95] Y. Lu, A. Bengtsson, J. J. Burnett, B. Suri, S. R. Sathyamoorthy, H. R. Nilsson, et al., "Quantum efficiency, purity and stability of a tunable, narrowband microwave single-photon source", *npj Quantum Information* **7**(1), 140 (2021), DOI: 10.1038/s41534-021-00480-5.

[96] S. Hawaldar, S. S. Khaire, P. Delsing, and B. Suri, "On-demand single-microwave-photon source in a superconducting circuit with wideband frequency tunability", *Physical Review Applied* **23**, 044042 (2025), DOI: 10.1103/PhysRevApplied.23.044042.

[97] N. Bergeal, F. Schackert, L. Frunzio, and M. H. Devoret, "Two-Mode Correlation of Microwave Quantum Noise Generated by Parametric Down-Conversion", *Physical Review Letters* **108**, 123902 (2012), DOI: 10.1103/PhysRevLett.108.123902.

[98] B. Yurke, L. R. Corruccini, P. G. Kaminsky, L. W. Rupp, A. D. Smith, A. H. Silver, et al., "Observation of parametric amplification and deamplification in a Josephson parametric amplifier", *Physical Review A* **39**, 2519–2533 (1989), DOI: 10.1103/PhysRevA.39.2519.

[99] C. M. Caves, "Quantum limits on noise in linear amplifiers", *Physical Review D* **26**, 1817–1839 (1982), DOI: 10.1103/PhysRevD.26.1817.

[100] F. Fesquet, F. Kronowetter, M. Renger, Q. Chen, K. Honasoge, O. Gargiulo, et al., "Perspectives of microwave quantum key distribution in the open air", *Physical Review A* **108**, 032607 (2023), DOI: 10.1103/PhysRevA.108.032607.

[101] F. Fesquet, F. Kronowetter, M. Renger, W. K. Yam, S. Gandorfer, K. Inomata, et al., "Demonstration of microwave single-shot quantum key distribution", *Nature Communications* **15**(1), 7544 (2024), DOI: 10.1038/s41467-024-51421-7.

[102] L. Zhong, E. P. Menzel, R. Di Candia, P. Eder, M. Ihmig, A. Baust, et al., "Squeezing with a flux-driven Josephson parametric amplifier", *New Journal of Physics* **15**(12), 125013 (2013), DOI: 10.1088/1367-2630/15/12/125013.

[103] F. Kronowetter, F. Fesquet, M. Renger, K. Honasoge, Y. Nojiri, K. Inomata, et al., "Quantum Microwave Parametric Interferometer", *Physical Review Applied* **20**, 024049 (2023), DOI: 10.1103/PhysRevApplied.20.024049.

[104] R. Di Candia, K. Fedorov, L. Zhong, S. Felicetti, E. Menzel, M. Sanz, et al., "Quantum teleportation of propagating quantum microwaves", *EPJ Quantum Technology* **2**(1), 25 (2015), DOI: 10.1140/epjqt/s40507-015-0038-9.

[105] S. Pogorzalek, K. Fedorov, M. Xu, A. Parra-Rodriguez, M. Sanz, M. Fischer, et al., "Secure quantum remote state preparation of squeezed microwave states", *Nature Communications* **10**(1), 2604 (2019), DOI: 10.1038/s41467-019-10727-7.

[106] S. Barzanjeh, S. Guha, C. Weedbrook, D. Vitali, J. H. Shapiro, and S. Pirandola, "Microwave Quantum Illumination", *Physical Review Letters* **114**, 080503 (2015), DOI: 10.1103/PhysRevLett.114.080503.

[107] S. Barzanjeh, S. Pirandola, D. Vitali, and J. M. Fink, "Microwave quantum illumination using a digital receiver", *Science Advances* **6**(19), eabb0451 (2020), DOI: 10.1126/sciadv.abb0451.

[108] C. W. S. Chang, A. M. Vadiraj, J. Bourassa, B. Balaji, and C. M. Wilson, "Quantum-enhanced noise radar", *Applied Physics Letters* **114**(11), 112601 (2019), DOI: 10.1063/1.5085002.

[109] N. Messaoudi, C. W. S. Chang, A. M. Vadiraj, C. M. Wilson, J. Bourassa, and B. Balaji, "Practical Advantage in Microwave Quantum Illumination", in: "2020 IEEE Radar Conference (RadarConf20)", 1–5 (2020), DOI: 10.1109/RadarConf2043947.2020.9266556.

[110] D. Luong, B. Balaji, C. W. Sandbo Chang, V. M. Ananthapadmanabha Rao, and C. Wilson, "Microwave Quantum Radar: An Experimental Validation", in: "2018 International Carnahan Conference on Security Technology (ICCST)", 1–5 (2018), DOI: 10.1109/CCST.2018.8585630.

[111] M. Sanz, K. G. Fedorov, F. Deppe, and E. Solano, "Challenges in Open-air Microwave Quantum Communication and Sensing", in: "2018 IEEE Conference on Antenna Measurements & Applications (CAMA)", 1–4 (2018), DOI: 10.1109/CAMA.2018.8530599.

[112] L. You, "Superconducting nanowire single-photon detectors for quantum information", *Nanophotonics* **9**(9), 2673–2692 (2020), DOI: 10.1515/nanoph-2020-0186.

[113] I. Esmaeil Zadeh, J. Chang, J. W. N. Los, S. Gyger, A. W. Elshaari, S. Steinhauer, et al., "Superconducting nanowire single-photon detectors: A perspective on evolution, state-of-the-art, future developments, and applications", *Applied Physics Letters* **118**(19), 190502 (2021), DOI: 10.1063/5.0045990.

[114] E. Albertinale, L. Balembois, E. Billaud, V. Ranjan, D. Flanigan, T. Schenkel, et al., "Detecting spins by their fluorescence with a microwave photon counter", *Nature* **600**(7889), 434–438 (2021), DOI: 10.1038/s41586-021-04076-z.

[115] E. Billaud, L. Balembois, J. Travesedo, M. Le Dantec, M. Rančić, E. Albertinale, et al., "Electron paramagnetic resonance spectroscopy of a scheelite crystal using microwave-photon counting", *Physical Review Research* **7**, 013011 (2025), DOI: 10.1103/PhysRevResearch.7.013011.

[116] B. Karimi, G. O. Steffensen, A. P. Higginbotham, C. M. Marcus, A. Levy Yeyati, and J. P. Pekola, "Bolometric detection of Josephson radiation", *Nature Nanotechnology* **19**(11), 1613–1618 (2024), DOI: 10.1038/s41565-024-01770-7.

[117] A. Narla, S. Shankar, M. Hatridge, Z. Leghtas, K. M. Sliwa, E. Zalys-Geller, et al., "Robust Concurrent Remote Entanglement Between Two Superconducting Qubits", *Physical Review X* **6**, 031036 (2016), DOI: 10.1103/PhysRevX.6.031036.

[118] A. Opremcak, I. V. Pechenezhskiy, C. Howington, B. G. Christensen, M. A. Beck, E. Leonard, et al., "Measurement of a superconducting qubit with a microwave photon counter", *Science* **361**(6408), 1239–1242 (2018), DOI: 10.1126/science.aat4625.

[119] A. M. Gunyhó, S. Kundu, J. Ma, W. Liu, S. Niemelä, G. Catto, et al., "Single-shot readout of a superconducting qubit using a thermal detector", *Nature Electronics* **7**(4), 288–298 (2024), DOI: 10.1038/s41928-024-01147-7.

[120] A. V. Dixit, S. Chakram, K. He, A. Agrawal, R. K. Naik, D. I. Schuster, et al., "Searching for Dark Matter with a Superconducting Qubit", *Physical Review Letters* **126**, 141302 (2021), DOI: 10.1103/PhysRevLett.126.141302.

[121] C. Braggio, L. Balembois, R. Di Vora, Z. Wang, J. Travesedo, L. Pallegoix, et al., "Quantum-Enhanced Sensing of Axion Dark Matter with a Transmon-Based Single Microwave Photon Counter", *Physical Review X* **15**, 021031 (2025), DOI: 10.1103/PhysRevX.15.021031.

[122] A. Pankratov, L. Revin, A. Gordeeva, A. Yablokov, L. Kuzmin, and E. Il'ichev, "Towards a microwave single-photon counter for searching axions", *npj Quantum Information* **8**(1), 61 (2022), DOI: 10.1038/s41534-022-00569-5.

[123] M. Casariego, E. Zambrini Cruzeiro, S. Gherardini, T. Gonzalez-Raya, R. André, G. Frazão, et al., "Propagating quantum microwaves: towards applications in communication and sensing", *Quantum Science and Technology* **8**(2), 023001 (2023), DOI: 10.1088/2058-9565/acc4af.

[124] X. Gu, A. F. Kockum, A. Miranowicz, Y.-x. Liu, and F. Nori, "Microwave photonics with superconducting quantum circuits", *Physics Reports* **718-719**, 1–102 (2017), DOI: 10.1016/j.physrep.2017.10.002.

[125] S. R. Sathyamoorthy, T. M. Stace, and G. Johansson, "Detecting itinerant single microwave photons", *Comptes Rendus Physique* **17**(7), 756–765 (2016), DOI: 10.1016/j.crhy.2016.07.010.

[126] Y.-F. Chen, D. Hover, S. Sendelbach, L. Maurer, S. T. Merkel, E. J. Pritchett, et al., "Microwave Photon Counter Based on Josephson Junctions", *Physical Review Letters* **107**, 217401 (2011), DOI: 10.1103/PhysRevLett.107.217401.

[127] D. A. Ladeynov, A. L. Pankratov, L. S. Revin, A. V. Gordeeva, A. V. Chiginev, S. A. Razov, et al., "Detection of 5 GHz photons using Al Josephson junctions at 0.7 K", *Academia Quantum* **2**(2), (2025), DOI: 10.20935/AcadQuant7780.

[128] A. Rettaroli, D. Alesini, D. Babusci, C. Barone, B. Buonomo, M. M. Beretta, et al., "Josephson Junctions as Single Microwave Photon Counters: Simulation and Characterization", *Instruments* **5**(3), 25 (2021), DOI: 10.3390/instruments5030025.

[129] G. Oelsner, C. K. Andersen, M. Rehák, M. Schmelz, S. Anders, M. Grajcar, et al., "Detection of Weak Microwave Fields with an Underdamped Josephson Junction", *Physical Review Applied* **7**, 014012 (2017), DOI: 10.1103/PhysRevApplied.7.014012.

[130] J.-X. He, P.-H. Ouyang, Y.-Q. Chai, H. Chang, Q. He, and L.-F. Wei, "Experimental demonstrations of Josephson threshold detectors for broadband microwave photons detection", *Applied Physics Letters* **126**(20), 202601 (2025), DOI: 10.1063/5.0259463.

[131] K. Inomata, Z. Lin, K. Koshino, W. D. Oliver, J.-S. Tsai, T. Yamamoto, et al., "Single microwave-photon detector using an artificial Λ-type three-level system", *Nature communications* **7**(1), 12303 (2016), DOI: 10.1038/ncomms12303.

[132] J.-C. Besse, S. Gasparinetti, M. C. Collodo, T. Walter, P. Kurpiers, M. Pechal, et al., "Single-Shot Quantum Nondemolition Detection of Individual Itinerant Microwave Photons", *Physical Review X* **8**, 021003 (2018), DOI: 10.1103/PhysRevX.8.021003.

[133] S. Kono, K. Koshino, Y. Tabuchi, A. Noguchi, and Y. Nakamura, "Quantum non-demolition detection of an itinerant microwave photon", *Nature Physics* **14**(6), 546–549 (2018), DOI: 10.1038/s41567-018-0066-3.

[134] R. Lescanne, S. Deléglise, E. Albertinale, U. Réglade, T. Capelle, E. Ivanov, et al., "Irreversible Qubit-Photon Coupling for the Detection of Itinerant Microwave Photons", *Physical Review X* **10**, 021038 (2020), DOI: 10.1103/PhysRevX.10.021038.

[135] L. Balembois, J. Travesedo, L. Pallegoix, A. May, E. Billaud, M. Villiers, et al., "Cyclically Operated Microwave Single-Photon Counter with Sensitivity of $10^{-22}\,\mathrm{W}/\sqrt{\mathrm{Hz}}$", *Physical Review Applied* **21**, 014043 (2024), DOI: 10.1103/PhysRevApplied.21.014043.

[136] B. Karimi and J. P. Pekola, "Quantum Trajectory Analysis of Single Microwave Photon Detection by Nanocalorimetry", *Physical Review Letters* **124**, 170601 (2020), DOI: 10.1103/PhysRevLett.124.170601.

[137] R. Kokkoniemi, J. Govenius, V. Vesterinen, R. E. Lake, A. M. Gunyhó, K. Y. Tan, et al., "Nanobolometer with ultralow noise equivalent power", *Communications Physics* **2**(1), 124 (2019), DOI: 10.1038/s42005-019-0225-6.

[138] R. Kokkoniemi, J.-P. Girard, D. Hazra, A. Laitinen, J. Govenius, R. Lake, et al., "Bolometer operating at the threshold for circuit quantum electrodynamics", *Nature* **586**(7827), 47–51 (2020), DOI: 10.1038/s41586-020-2753-3.

[139] C. Huygens, "Oeuvres complètes de Christiaan Huygens. Publiées par la Société hollandaise des sciences", (La Haye, M. Nijhoff, 1888–1950).

[140] A. Pikovsky, M. Rosenblum, and J. Kurths, "Synchronization: A Universal Concept in Nonlinear Sciences", (Cambridge University Press, 2001).

[141] S. H. Strogatz and I. Stewart, "Coupled Oscillators and Biological Synchronization", *Scientific American* **269**(6), 102–109 (1993), DOI: 10.1038/scientificamerican1293-102.

[142] S. H. Strogatz, "Nonlinear Dynamics and Chaos: With Applications to Physics, Biology, Chemistry and Engineering", vol. **2** (Westview Press, 2000).

[143] Y. Kuramoto, "Chemical Oscillations, Waves, and Turbulence", (Dover Publications, 2003).

[144] L. Glass, "Synchronization and Rhythmic Processes in Physiology", *Nature* **410**(6825), 277–284 (2001), DOI: 10.1038/35065745.

[145] R. Sarfati, J. C. Hayes, and O. Peleg, "Self-organization in natural swarms of Photinus carolinus synchronous fireflies", *Science Advances* **7**(28), eabg9259 (2021), DOI: 10.1126/sciadv.abg9259.

[146] S. Mendjan, A. Deyett, and D. Yelon, "Coordination of cardiogenesis in vivo and in vitro", *Nature Reviews Molecular Cell Biology*, (2025), DOI: 10.1038/s41580-025-00878-5.

[147] A. B. L. Tort, D. A. Laplagne, A. Draguhn, and J. Gonzalez, "Global coordination of brain activity by the breathing cycle", *Nature Reviews Neuroscience* **26**(6), 333–353 (2025), DOI: 10.1038/s41583-025-00920-7.

[148] F. N. Buijs, L. León-Mercado, M. Guzmán-Ruiz, N. N. Guerrero-Vargas, F. Romo-Nava, and R. M. Buijs, "The Circadian System: A Regulatory Feedback Network of Periphery and Brain", *Physiology* **31**(3), 170–181 (2016), DOI: 10.1152/physiol.00037.2015.

[149] P. Mougkogiannis, A. Nikolaidou, and A. Adamatzky, "On Emergence of Spontaneous Oscillations in Kombucha and Proteinoids", *BioNanoScience* **15**(1), 65 (2024), DOI: 10.1007/s12668-024-01678-5.

[150] C. Buczek, R. Freiberg, and M. Skolnick, "Laser injection locking", *Proceedings of the IEEE* **61**(10), 1411–1431 (1973), DOI: 10.1109/PROC.1973.9294.

[151] G. H. van Tartwijk and G. P Agrawal, "Laser instabilities: a modern perspective", *Progress in Quantum Electronics* **22**(2), 43–122 (1998), DOI: 10.1016/S0079-6727(98)00008-1.

[152] B. Van der Pol, "A theory of the amplitude of free and forced vibrations", *Radio Review* **1**, 701–710 (1920).

[153] S. Walter, A. Nunnenkamp, and C. Bruder, "Quantum Synchronization of a Driven Self-Sustained Oscillator", *Physical Review Letters* **112**, 094102 (2014), DOI: 10.1103/PhysRevLett.112.094102.

[154] S. Walter, A. Nunnenkamp, and C. Bruder, "Quantum synchronization of two Van der Pol oscillators", *Annalen der Physik* **527**(1-2), 131–138 (2015), DOI: 10.1002/andp.201400144.

[155] E. Amitai, N. Lörch, A. Nunnenkamp, S. Walter, and C. Bruder, "Synchronization of an optomechanical system to an external drive", *Physical Review A* **95**, 053858 (2017), DOI: 10.1103/PhysRevA.95.053858.

[156] T. E. Lee and H. R. Sadeghpour, "Quantum Synchronization of Quantum van der Pol Oscillators with Trapped Ions", *Physical Review Letters* **111**, 234101 (2013), DOI: 10.1103/PhysRevLett.111.234101.

[157] T. E. Lee, C.-K. Chan, and S. Wang, "Entanglement tongue and quantum synchronization of disordered oscillators", *Physical Review E* **89**, 022913 (2014), DOI: 10.1103/PhysRevE.89.022913.

[158] T. Weiss, S. Walter, and F. Marquardt, "Quantum-coherent phase oscillations in synchronization", *Physical Review A* **95**, 041802(R) (2017), DOI: 10.1103/PhysRevA.95.041802.

[159] S. Dutta and N. R. Cooper, "Critical Response of a Quantum van der Pol Oscillator", *Physical Review Letters* **123**, 250401 (2019), DOI: 10.1103/PhysRevLett.123.250401.

[160] L. Ben Arosh, M. C. Cross, and R. Lifshitz, "Quantum limit cycles and the Rayleigh and van der Pol oscillators", *Physical Review Research* **3**, 013130 (2021), DOI: 10.1103/PhysRevResearch.3.013130.

[161] Y. Kuramoto, "International symposium on mathematical problems in theoretical physics", *Lecture Notes in Physics* **30**, 420 (1975), URL: https://cir.nii.ac.jp/crid/1570009750979995136.

[162] J. A. Acebrón, L. L. Bonilla, C. J. Pérez Vicente, F. Ritort, and R. Spigler, "The Kuramoto model: A simple paradigm for synchronization phenomena", *Review of Modern Physics* **77**, 137–185 (2005), DOI: 10.1103/RevModPhys.77.137.

[163] R. Adler, "A Study of Locking Phenomena in Oscillators", *Proceedings of the IRE* **34**(6), 351–357 (1946), DOI: 10.1109/JRPROC.1946.229930.

[164] A. Roulet and C. Bruder, "Synchronizing the Smallest Possible System", *Physical Review Letters* **121**, 053601 (2018), DOI: 10.1103/PhysRevLett.121.053601.

[165] Á. Parra-López and J. Bergli, "Synchronization in two-level quantum systems", *Physical Review A* **101**, 062104 (2020), DOI: 10.1103/PhysRevA.101.062104.

[166] M. Koppenhöfer, C. Bruder, and A. Roulet, "Quantum synchronization on the IBM Q system", *Physical Review Research* **2**, 023026 (2020), DOI: 10.1103/PhysRevResearch.2.023026.

[167] A. Roulet and C. Bruder, "Quantum Synchronization and Entanglement Generation", *Physical Review Letters* **121**, 063601 (2018), DOI: 10.1103/PhysRevLett.121.063601.

[168] N. Jaseem, M. Hajdušek, V. Vedral, R. Fazio, L.-C. Kwek, and S. Vinjanampathy, "Quantum synchronization in nanoscale heat engines", *Physical Review E* **101**, 020201(R) (2020), DOI: 10.1103/PhysRevE.101.020201.

[169] M. R. Hush, W. Li, S. Genway, I. Lesanovsky, and A. D. Armour, "Spin correlations as a probe of quantum synchronization in trapped-ion phonon lasers", *Physical Review A* **91**, 061401(R) (2015), DOI: 10.1103/PhysRevA.91.061401.

[170] A. W. Laskar, P. Adhikary, S. Mondal, P. Katiyar, S. Vinjanampathy, and S. Ghosh, "Observation of Quantum Phase Synchronization in Spin-1 Atoms", *Physical Review Letters* **125**, 013601 (2020), DOI: 10.1103/PhysRevLett.125.013601.

[171] V. R. Krithika, P. Solanki, S. Vinjanampathy, and T. S. Mahesh, "Observation of quantum phase synchronization in a nuclear-spin system", *Physical Review A* **105**, 062206 (2022), DOI: 10.1103/PhysRevA.105.062206.

[172] L. Zhang, Z. Wang, Y. Wang, J. Zhang, Z. Wu, J. Jie, et al., "Quantum synchronization of a single trapped-ion qubit", *Physical Review Research* **5**, 033209 (2023), DOI: 10.1103/PhysRevResearch.5.033209.

[173] S. Sonar, M. Hajdušek, M. Mukherjee, R. Fazio, V. Vedral, S. Vinjanampathy, et al., "Squeezing Enhances Quantum Synchronization", *Physical Review Letters* **120**, 163601 (2018), DOI: 10.1103/PhysRevLett.120.163601.

[174] N. Lörch, S. E. Nigg, A. Nunnenkamp, R. P. Tiwari, and C. Bruder, "Quantum Synchronization Blockade: Energy Quantization Hinders Synchronization of Identical Oscillators", *Physical Review Letters* **118**, 243602 (2017), DOI: 10.1103/PhysRevLett.118.243602.

[175] S. E. Nigg, "Observing quantum synchronization blockade in circuit quantum electrodynamics", *Physical Review A* **97**, 013811 (2018), DOI: 10.1103/PhysRevA.97.013811.

[176] N. Es'haqi-Sani, G. Manzano, R. Zambrini, and R. Fazio, "Synchronization along quantum trajectories", *Physical Review Research* **2**, 023101 (2020), DOI: 10.1103/PhysRevResearch.2.023101.

[177] Y. Shen, H. Y. Soh, L.-C. Kwek, and W. Fan, "Fisher Information as General Metrics of Quantum Synchronization", *Entropy* **25**(8), 1116 (2023), DOI: 10.3390/e25081116.

[178] F. Schmolke and E. Lutz, "Measurement-Induced Quantum Synchronization and Multiplexing", *Physical Review Letters* **132**, 010402 (2024), DOI: 10.1103/PhysRevLett.132.010402.

[179] T. Kehrer, T. Nadolny, and C. Bruder, "Quantum synchronization through the interference blockade", *Physical Review A* **110**, 042203 (2024), DOI: 10.1103/PhysRevA.110.042203.

[180] L. Chen, H.-X. Li, Y. Lu, C. W. Warren, C. J. Križan, S. Kosen, et al., "Transmon qubit readout fidelity at the threshold for quantum error correction without a quantum-limited amplifier", *npj Quantum Information* **9**(1), 26 (2023), DOI: 10.1038/s41534-023-00689-6.

[181] C. J. Axline, L. D. Burkhart, W. Pfaff, M. Zhang, K. Chou, P. Campagne-Ibarcq, et al., "On-demand quantum state transfer and entanglement between remote microwave cavity memories", *Nature Physics* **14**(7), 705–710 (2018), DOI: 10.1038/s41567-018-0115-y.

[182] C. Fabre and N. Treps, "Modes and states in quantum optics", *Reviews of Modern Physics* **92**, 035005 (2020), DOI: 10.1103/RevModPhys.92.035005.

[183] R. Dändliker, "The concept of modes in optics and photonics", in: "Education and Training in Optics and Photonics", paper GP193 (Optica Publishing Group, 1999).

[184] M. G. Raymer and I. A. Walmsley, "Temporal modes in quantum optics: then and now", *Physica Scripta* **95**(6), 064002 (2020), DOI: 10.1088/1402-4896/ab6153.

[185] U. M. Titulaer and R. J. Glauber, "Density Operators for Coherent Fields", *Physical Review* **145**, 1041–1050 (1966), DOI: 10.1103/PhysRev.145.1041.

[186] J. Wenner, Y. Yin, Y. Chen, R. Barends, B. Chiaro, E. Jeffrey, et al., "Catching Time-Reversed Microwave Coherent State Photons with 99.4% Absorption Efficiency", *Physical Review Letters* **112**, 210501 (2014), DOI: 10.1103/PhysRevLett.112.210501.

[187] C. W. Gardiner and M. J. Collett, "Input and output in damped quantum systems: Quantum stochastic differential equations and the master equation", *Physical Review A* **31**, 3761–3774 (1985), DOI: 10.1103/PhysRevA.31.3761.

[188] J. Combes, J. Kerckhoff, and M. Sarovar, "The SLH framework for modeling quantum input-output networks", *Advances in Physics: X* **2**(3), 784–888 (2017), DOI: 10.1080/23746149.2017.1343097.

[189] A. H. Kiilerich and K. Mølmer, "Input-Output Theory with Quantum Pulses", *Physical Review Letters* **123**, 123604 (2019), DOI: 10.1103/PhysRevLett.123.123604.

[190] A. H. Kiilerich and K. Mølmer, "Quantum interactions with pulses of radiation", *Physical Review A* **102**, 023717 (2020), DOI: 10.1103/PhysRevA.102.023717.

[191] V. R. Christiansen, A. H. Kiilerich, and K. Mølmer, "Interactions of quantum systems with pulses of quantized radiation: From a cascaded master equation to a traveling mode perspective", *Physical Review A* **107**, 013706 (2023), DOI: 10.1103/PhysRevA.107.013706.

[192] M. Khanahmadi and K. Mølmer, "Qubit readout and quantum sensing with pulses of quantum radiation", *Physical Review A* **107**, 013705 (2023), DOI: 10.1103/PhysRevA.107.013705.

[193] M. M. Lund, F. Yang, and K. Mølmer, "Perfect splitting of a two-photon pulse", *Physical Review A* **107**, 023715 (2023), DOI: 10.1103/PhysRevA.107.023715.

[194] A. A. Clerk, M. H. Devoret, S. M. Girvin, F. Marquardt, and R. J. Schoelkopf, "Introduction to quantum noise, measurement, and amplification", *Reviews of Modern Physics* **82**, 1155–1208 (2010), DOI: 10.1103/RevModPhys.82.1155.

[195] M. P. da Silva, D. Bozyigit, A. Wallraff, and A. Blais, "Schemes for the observation of photon correlation functions in circuit QED with linear detectors", *Physical Review A* **82**, 043804 (2010), DOI: 10.1103/PhysRevA.82.043804.

[196] H. M. Wiseman and G. J. Milburn, "Quantum Measurement and Control", (Cambridge University Press, 2009).

[197] N. Gisin and I. C. Percival, "The quantum-state diffusion model applied to open systems", *Journal of Physics A: Mathematical and General* **25**(21), 5677 (1992), DOI: 10.1088/0305-4470/25/21/023.

[198] M. S. Kim, "Quasiprobability functions measured by photon statistics of amplified signal fields", *Physical Review A* **56**, 3175–3179 (1997), DOI: 10.1103/PhysRevA.56.3175.

[199] C. Eichler, D. Bozyigit, C. Lang, M. Baur, L. Steffen, J. M. Fink, et al., "Observation of Two-Mode Squeezing in the Microwave Frequency Domain", *Physical Review Letters* **107**, 113601 (2011), DOI: 10.1103/PhysRevLett.107.113601.

[200] C. Yan, J. Hassel, V. Vesterinen, J. Zhang, J. Ikonen, L. Grönberg, et al., "A low-noise on-chip coherent microwave source", *Nature Electronics* **4**(12), 885–892 (2021), DOI: 10.1038/s41928-021-00680-z.

[201] S. H. Simon and N. R. Cooper, "Theory of the Josephson Junction Laser", *Physical Review Letters* **121**, 027004 (2018), DOI: 10.1103/PhysRevLett.121.027004.

[202] B. Lang, G. F. Morley, and A. D. Armour, "Discrete time translation symmetry breaking in a Josephson junction laser", *Physical Review B* **107**, 144509 (2023), DOI: 10.1103/PhysRevB.107.144509.

[203] H. Kramers, "Brownian motion in a field of force and the diffusion model of chemical reactions", *Physica* **7**(4), 284–304 (1940), DOI: 10.1016/S0031-8914(40)90098-2.

[204] W. C. Stewart, "CURRENT-VOLTAGE CHARACTERISTICS OF JOSEPHSON JUNCTIONS", *Applied Physics Letters* **12**(8), 277–280 (1968), DOI: 10.1063/1.1651991.

[205] D. E. McCumber, "Effect of ac Impedance on dc Voltage-Current Characteristics of Superconductor Weak-Link Junctions", *Journal of Applied Physics* **39**(7), 3113–3118 (1968), DOI: 10.1063/1.1656743.

[206] C. Xu and M. G. Vavilov, "Full counting statistics of photons emitted by a double quantum dot", *Physical Review B* **88**, 195307 (2013), DOI: 10.1103/PhysRevB.88.195307.

[207] H. Risken, "The Fokker-Planck equation", vol. **2** (Springer, 1996).

[208] R. Gautier, A. Sarlette, and M. Mirrahimi, "Combined Dissipative and Hamiltonian Confinement of Cat Qubits", *PRX Quantum* **3**, 020339 (2022), DOI: 10.1103/PRXQuantum.3.020339.

[209] J. A. Nelder and R. Mead, "A Simplex Method for Function Minimization", *The Computer Journal* **7**(4), 308–313 (1965), DOI: 10.1093/comjnl/7.4.308.

[210] U. Leonhardt, "Essential Quantum Optics: From Quantum Measurements to Black Holes", vol. **1** (Cambridge University Press, 2012).

[211] M. Werther and F. Großmann, "Apoptosis of moving nonorthogonal basis functions in many-particle quantum dynamics", *Physical Review B* **101**, 174315 (2020), DOI: 10.1103/PhysRevB.101.174315.

[212] Y. Zhao, K. Sun, L. Chen, and M. Gelin, "The hierarchy of Davydov's Ansätze and its applications", *WIREs Computational Molecular Science* **12**(4), e1589 (2022), DOI: 10.1002/wcms.1589.

PART C

Back Matter

Acknowledgements

This content has been intentionally omitted for privacy reasons.

Curriculum Vitae

This content has been intentionally omitted for privacy reasons.

This content has been intentionally omitted for privacy reasons.

List of Talks and Poster Contributions

Talks

2022 **Characterization of Josephson Photonics Devices as Microwave Sources for a Quantum Radar**
Quantum Alliance PhD Conference
Munich, April 27th, 2022

2024 **Nonlinear Dynamics in Josephson Photonics Devices: Injection Locking and Interactions with Single Photons**
Sherbrooke, August 15th, 2024

2025 **Amplification and Detection of Single Itinerant Microwave Photons**
2nd DPG Fall Meeting: 100 Years of Quantum Physics
Göttingen, September 8th, 2025

Posters

2021 **Injection Locking and Synchronization in Josephson Photonics Devices**
DPG Fall Meeting (SKM)
online conference, September 27th - October 1st, 2021

2022 **Characterization of Josephson Photonics Devices as Microwave Sources for a Quantum Radar**
Summerschool Nanotechnology meets Quantum Information (NanoQI)
Donostia-San Sebastián, August 30th - September 2nd, 2022

Characterization of Josephson Photonics Devices as Microwave Sources for a Quantum Radar
DPG Fall Meeting (SKM)
Regensburg, September 4th - September 9th, 2022

2023 **Characterization of Josephson Photonics Devices as Sources of Microwave Light in Presence of Shot Noise**
Wilhelm and Else Heraeus School on Open Quantum Systems and Mesoscopic Physics 2023
Hyytiälä, June 4th - June 9th, 2022

2024 **Amplification of Single-Photon Pulses in Josephson Photonics Devices**
"A journey through the quantum world: from chemistry to circuits" on the occasion of Joachim Ankerhold's jubilee birthday
Ulm, June 24th - June 26th, 2024

Declaration of Academic Honesty

Hereby, I declare that

- I have prepared this thesis independently
- I have explicitly cited all passages where I quoted or referred to works and contents by other people and that I have not used any other sources than those which are indicated by me
- I have not applied for admission, nor submitted this thesis in any other dissertation procedure
- I comply with the *Statutes of Ulm University on Safeguarding Good Scientific Practice* in the currently valid version of February 12th, 2025
- I agree that the dissertation may also be used for the purpose of verifying compliance with generally accepted scientific standards, in particular by using electronic data processing programs.

Ulm, November 26th, 2025

Lukas Danner

List of Figures

List of Tables

List of Abbreviations

BCS Bardeen–Cooper–Schrieffer

ICTPM Inelastic Cooper Pair Tunneling Photon Multiplier

qubit quantum bit

RCSJ Resistively and Capacitively Shunted Junction

RWA rotating-wave approximation

SQUID Superconducting Quantum Interference Device

SSO self-sustained oscillator